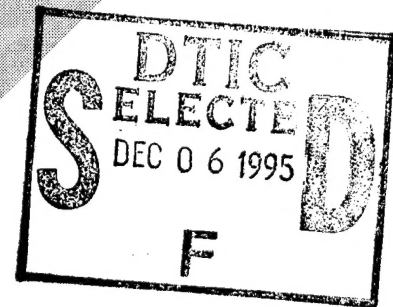


N94-36175

CONFIDENTIAL



DTIC QUALITY INSPECTED 5

19951121 085

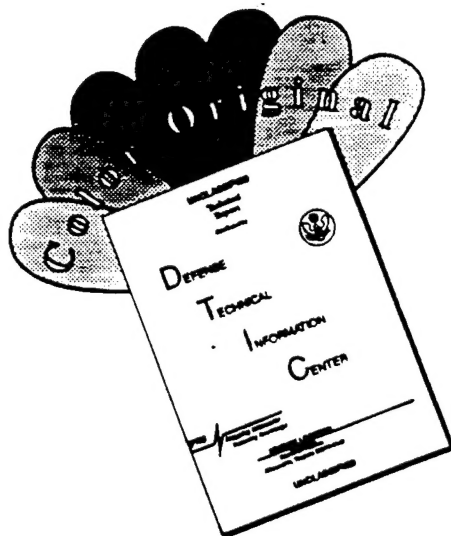
A Service of:



National Aeronautics and
Space Administration

Scientific and Technical
Information Office

DISCLAIMER NOTICE



THIS DOCUMENT IS BEST QUALITY AVAILABLE. THE COPY FURNISHED TO DTIC CONTAINED A SIGNIFICANT NUMBER OF COLOR PAGES WHICH DO NOT REPRODUCE LEGIBLY ON BLACK AND WHITE MICROFICHE.

**This microfiche was
produced according to
ANSI / AIM Standards
and meets the
quality specifications
contained therein. A
poor blowback image
is the result of the
characteristics of the
original document.**



111-6
16371
153F

Natural Orbital Environment Guidelines for Use in Aerospace Vehicle Development

Jeffrey Anderson, Editor and Robert E. Smith, Compiler

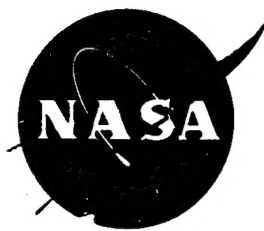
(NASA-TM-4527) NATURAL ORBITAL
ENVIRONMENT DEFINITION GUIDELINES
FOR USE IN AEROSPACE VEHICLE
DEVELOPMENT (NASA, Marshall Space
Flight Center) 158 p

N94-36175

Unclass

H1/46 0016371

June 1994



Natural Orbital Environment Guidelines for Use in Aerospace Vehicle Development

B. Jeffrey Anderson, Editor
Marshall Space Flight Center • MSFC, Alabama

Robert E. Smith, Compiler
Physitron, Inc. • Huntsville, Alabama

Accession For	
NTIS CRA&I	<input checked="" type="checkbox"/>
DTIC TAB	<input type="checkbox"/>
Unannounced	<input type="checkbox"/>
Justification	
By	
Distribution/	
Availability Codes	
Dist	Avail and/or Special
A-1	

National Aeronautics and Space Administration
Marshall Space Flight Center • MSFC, Alabama 35812

June 1994

ACKNOWLEDGMENT

This document was developed from SSP 30425, Space Station Program Natural Environment Definition for Design, with added analyses and work developed in support of the space station and other NASA programs. Thus, it has benefited from the comments, experience, and work of many individuals within NASA and its contractor community. The significant contributions of the following individuals in the disciplines noted are gratefully acknowledged:

NEUTRAL ATMOSPHERE

Dr. Michael Hickey, UAH
Mr. Orvel E. Smith, NTI

SOLAR

Dr. John Davis, MSFC
Mr. Robert Wilson, MSFC
Dr. Rob Suggs, NASA Headquarters

PLASMA

Dr. Dave Snyder, LeRC
Dr. Kai-Shen Hwang, Grumman
Dr. Nobie Stone, MSFC
Dr. Craig Pollock, MSFC
Dr. Thomas Moore, MSFC

PENETRATING CHARGED PARTICLES

Mr. John Watts, MSFC

METEOROIDS/ORBITAL DEBRIS

Mr. Don Kessler, JSC
Dr. Herb Zook, JSC

THERMAL

Ms. Bonnie James, MSFC
Mr. Wade Batts, NTI

GRAVITATION

Dr. J. Marsh, GSFC

GENERAL and EDITORIAL

Dr. William Vaughan, UAH
Ms. Margaret Alexander, MSFC

FOREWORD

This document provides a description of the near-Earth natural space environment that is recommended for space vehicle development applications. It is intended to provide general guidance on the conditions space systems will encounter and must successfully withstand during their lifetime on orbit. It will be particularly useful for preliminary design analyses. While these data and models are considered to be accurate and the best available for general engineering applications, their suitability for use for final program decisions depends upon the specific design problem involved.

The natural environment is characterized by many complex and frequently subtle processes, many more than it is possible to treat in a general description such as this. In many cases the characteristics and interactions among these processes are poorly understood or adequate measurements have never been made. In addition, it is often impossible to define a limiting (e.g., maximum possible) extreme value for environmental parameters. Likewise, it may not be technically or economically feasible to design a system to withstand an extreme value when it can be defined if the probability is small that such a value will occur during the mission lifetime.

For these reasons, good engineering judgment must be exercised in the application of environment data to space vehicle design analyses. When environmental considerations become significant design or cost drivers, environmental specialists should be consulted to assure that the environment was correctly understood and used and that subtle or infrequent effects, those not addressed by the general purpose information provided here, are not present in a form that would compromise the vehicle. Assessments made early in the development program will prove advantageous in maintaining an economical program and obtaining a vehicle with minimal operational sensitivity to the environment. For those parameters that need accurate and timely monitoring prior to or during operations, this early planning will permit development of the necessary measurement and communication systems.

This document is a follow-on to NASA TM-82478, Space and Planetary Environment Criteria Guidelines for Use in Space Vehicle Development, 1982 Revision (Volume 1), January 1983, which is still useful for many applications. In case of conflict, the data in this document should be used. There is no intent to automatically replace references to NASA TM-82478 or other previous documents in any contract Scope of Work by the issuance of this document.

Questions or requests for assistance in the application of these natural environment guidelines to aerospace vehicle programs should be addressed to the Chief, Electromagnetics and Environments Branch, EL54, Systems Analysis and Integration Laboratory, Science and Engineering Directorate, Marshall Space Flight Center, AL 35812.

TABLE OF CONTENTS

Section	Page
I. SCOPE AND PURPOSE	1-1
1.1 Format and Use of the Document	1-1
II. GENERAL INFORMATION	2-1
2.1 Sun-Earth Constants	2-1
2.2 Terrestrial Space	2-2
2.2.1 Fields	2-2
2.2.2 Plasma and Particles	2-3
2.2.3 Variability	2-3
III. NEUTRAL ATMOSPHERE	3-1
3.1 Thermosphere Region	3-1
3.2 Variations	3-2
3.2.1 Variations With Solar Activity	3-2
3.2.2 Variations During Periods of Increased Solar Activity	3-2
3.2.3 The Diurnal Variation	3-4
3.2.4 Semiannual Variation	3-5
3.2.5 Seasonal-Latitudinal Variations of the Lower Thermosphere Density	3-5
3.2.6 Seasonal-Latitudinal Variations of Helium	3-5
3.2.7 Thermospheric Waves	3-5
3.2.8 Thermospheric Winds	3-6
3.2.9 Thermospheric Tides	3-6
3.3 Solar and Geomagnetic Indices	3-10
3.4 Orbital and Suborbital Neutral Atmosphere Model	3-14
3.5 Marshall Engineering Thermosphere Model	3-16
3.5.1 Statistical Analysis Mode	3-16
IV. PLASMA ENVIRONMENT	4-1
4.1 Spacecraft-Plasma Interactions	4-2
4.2 Ionospheric Plasma	4-3
4.2.1 Density	4-3
4.2.2 Temperature	4-4
4.2.3 Dynamics	4-5
4.2.4 International Reference Ionosphere 90 (IRI90)	4-5
4.3 Auroral Oval Plasma	4-5
4.3.1 Global Morphology	4-6
4.3.2 Aurora Morphology	4-7
4.4 Polar Cap Plasma	4-8
4.4.1 Ionosphere and Polar Wind	4-8
4.5 Geosynchronous Altitude Plasma	4-9
4.6 Transient Fluxes in Low Earth Polar or Geosynchronous Orbit	4-9

TABLE OF CONTENTS (CONTINUED)

Section	Page
V. PENETRATING CHARGED PARTICLES	5-1
5.1 Magnetospheric Particles	5-1
5.1.1 Trapped Radiation	5-9
5.1.2 Nonisotropic Effects	5-9
5.2 Cosmic Rays	5-9
5.2.1 Galactic Cosmic Rays	5-10
5.2.2 Solar Particle Events	5-10
5.2.3 Geomagnetic Shielding and Cutoff Rigidity	5-10
VI. ELECTROMAGNETIC RADIATION	6-1
6.1 Galactic Radio Noise	6-1
6.2 Solar Electromagnetic Radiation	6-11
6.3 Natural Environmental Electromagnetic Radiation	6-11
6.4 Manmade Noise	6-11
VII. METEORIODS AND ORBITAL DEBRIS	7-1
7.1 Meteoroids	7-1
7.1.1 Uncertainty in the Meteoroid Environment	7-3
7.2 Orbital Debris	7-4
7.2.1 Background	7-4
7.2.2 Orbital Debris Flux to a Tumbling Surface	7-6
7.2.3 Average Shape and Mass Density	7-7
7.2.4 Velocity and Direction Distribution	7-7
7.2.5 Limitations and Uncertainty in the Debris Flux Model	7-10
7.3 Evaluation of Directionality Effects	7-16
VIII. MAGNETIC FIELD	8-1
IX. THERMAL ENVIRONMENT	9-1
9.1 General Discussion	9-1
9.1.1 Solar Constant	9-1
9.1.2 Albedo	9-1
9.1.3 Outgoing Longwave Radiation	9-2
9.1.4 The Earth Radiation Budget Experiment	9-2
9.2 Thermal Environment Criteria	9-2
9.2.1 Temporal Variations	9-2
9.2.2 Solar Zenith Angle Correction for Albedo	9-3
9.2.3 Correlation Analysis	9-4
X. GRAVITATIONAL FIELD	10-1

TABLE OF CONTENTS (CONTINUED)

Section	Page
APPENDIX A – ABBREVIATIONS AND ACRONYMS	A-1
APPENDIX B –	B-1
1.0 GALACTIC COSMIC RAYS (GCRs).....	B-1
2.0 SOLAR FLARE PARTICLE EVENTS	B-9
3.0 GEOMAGNETIC CUTOFFS	B-13
APPENDIX C	C-1
APPENDIX D – REFERENCES	D-1
APPENDIX E – BIBLIOGRAPHY	E-1

LIST OF ILLUSTRATIONS

Figure	Title	Page
2-1.	Schematic view of terrestrial space.....	2-2
2-2.	Solar cycle as represented by yearly mean sunspot number for the period 1700 to 1992	2-4
3-1.	Number density of atmospheric constituents versus altitude.....	3-3
3-2.	Typical atmospheric mass density profiles at high and low solar activity.....	3-4
3-3.	Schematic diagram of the zonal mean meridional circulation in the thermosphere at equinox for various levels of magnetic (auroral) activity	3-7
3-4.	Schematic diagram of the zonal mean meridional circulation in the thermosphere at solstice for various levels of magnetic (auroral) activity	3-8
3-5.	13-month smoothed values of $F_{10.7}$ over the mean solar cycle	3-15
3-6.	13-month smoothed values of geomagnetic activity index (A_p) over the mean solar cycle	3-15
4-1.	Plasma density (m^{-3}) at 400 km for June 21 and solar minimum conditions ($F_{10.7} = 70$, 0:0:0 G.m.t., results from IRI90 with default options selected)	4-10
4-2.	Electron energies (eV) at 400 km for June 21 and solar minimum conditions ($F_{10.7} = 70$, 0:0:0 G.m.t., IRI90 results with default options selected)	4-10
4-3.	Noon-midnight cross section view of plasma density (m^{-3}) as a function of altitude from 150 to 700 km for June 21 and solar minimum conditions ($F_{10.7} = 70$, contours in the 0° and 180° longitude plane, IRI90 results with default options selected).....	4-11
4-4.	Noon-midnight cross section view of electron energy (eV) as a function of altitude from 150 to 700 km for June 21 and solar minimum conditions ($F_{10.7} = 70$, contours in the 0° and 180° longitude plane, IRI90 results with default options selected).....	4-11
4-5.	Ionospheric electron density in an aurora ($\times 10^4 n_e/cm^3$).....	4-12
4-6.	Global plots of the average integral energy flux ($keV/cm^2 s sr$) of precipitating electrons are presented in polar spectrogram format, in a magnetic local time corrected geomagnetic latitude coordinate system, for four levels of K_p . Plots apply globally to both poles	4-13

LIST OF ILLUSTRATIONS (Continued)

Figure	Title	Page
4-7.	Global plots of the average energy (keV) of precipitating electrons are presented in polar spectrogram format, in a magnetic local time corrected geomagnetic latitude coordinate system, for four levels of K_p . Plots apply globally to both poles	4-15
4-8.	Time history of model substorm-geosynchronous plasma environment.....	4-17
4-9.	Auroral electron intensity (center of the arc).....	4-18
4-10.	Distribution functions of electrons (left) and ions (right) for very intense auroral fluxes	4-18
5-1.	Proton flux densities at an altitude of 296 km in the South Atlantic Anomaly. This is a region of low magnetic field strength	5-2
5-2.	Omnidirectional isoflux contours of 1-MeV electrons: R - λ projection.....	5-3
5-3.	AP8Min R - λ plot of isoflux contours of protons with an energy of ≥ 50 MeV.....	5-3
5-4.	AP8Min equatorial omnidirectional radial profiles of proton flux at energies between 0.1 and 400 MeV	5-4
5-5.	AP8Min and AP8Max B - L plot of constant intensity flux contours of protons with an energy of ≥ 50 MeV	5-4
5-6.	Characteristics of GCRs. Differential energy spectra for GCRs outside the magnetosphere at maximum and minimum solar activity (as defined by sunspot number).....	5-11
5-7a.	Differential energy spectrum of hydrogen (mostly protons). The data are selected to show the solar maximum and solar minimum fluxes. The dashed curve is a worst-case spectrum	5-12
5-7b.	Differential energy spectrum of helium (mostly alphas). The data are selected to show the solar maximum and solar minimum fluxes. The dashed curve is a worst-case spectrum.....	5-13
5-7c.	Differential energy spectrum of iron. The data are selected to show the solar maximum and solar minimum fluxes. The dashed curve is a worst-case spectrum	5-14
5-8.	Event-integrated proton fluxes above 30 MeV for the major solar events of the 19th and 20th solar cycles	5-15
5-9.	Event-integrated proton differential energy spectra. For F_m , a typical ordinary event; F_w , a worst-case ordinary event (90-percent confidence level); and F_a , an anomalously large solar event	5-16

LIST OF ILLUSTRATIONS (Continued)

Figure	Title	Page
6-1.	Levels of galactic radio noise as a function of frequency	6-
6-2.	Median values of average noise power expected from various sources (omnidirectional antenna near surface)	6-
6-3.	Normally incident solar radiation at sea level on very clear days, solar spectral irradiance outside the Earth's atmosphere at 1 AU, and blackbody spectral irradiance curve at $T = 5762$ K (normalized to 1 AU).....	6-
6-4.	Power flux levels for various frequency ranges of naturally occurring electromagnetic and plasma waves.....	6-1
7-1.	Normalized meteoroid velocity distribution from equation (7-3)	7-
7-2.	Comparison of meteoroid and orbital debris fluxes, F_r , as a function of size	7-
7-3.	Normalized collision velocity distribution as function of debris velocity for a spacecraft with orbital inclinations of 28.5° , 57° , and 98°	7-
7-4.	Orbital debris reference frame	7-1
7-5.	Comparison of model flux, F_c , with catalog flux not corrected for GEODSS results	7-1
7-6a.	K factor for single-sided flat plates for 28.5° inclination orbit	7-1
7-6b.	K factor for single-sided flat plates for 28.5° , 57° , and 98° inclination orbits	7-1
7-7.	K factor for a right circular cylinder, length to diameter ratio = 3.1, $\theta = 90^\circ$	7-1
9-1.	Albedo correction term	9-
9-2.	Statistical summary of albedo (top) and OLR (bottom) observations for a 30° inclination orbit.....	9-
9-3.	Statistical summary of albedo (top) and OLR (bottom) observations for a 60° inclination orbit.....	9-1
9-4.	Statistical summary of albedo (top) and OLR (bottom) observations for a 90° inclination orbit.....	9-1
9-5.	Orbit-average solar zenith angles for 30° , 60° , and 90° inclination orbits, daylight side only	9-1
9-6.	Albedo-OLR correlated pairs for 30° inclination orbits	9-1

LIST OF ILLUSTRATIONS (Continued)

Figure	Title	Page
9-7.	Albedo-OLR correlated pairs for 60° inclination orbits	9-1
9-8.	Albedo-OLR correlated pairs for 90° inclination orbits	9-1
C-1.	Probability of meeting or exceeding a given time interval without exceeding the 95th percentile density (top) or 99th percentile density (bottom). The bins represent a range of $F_{10.7}$: (1) 66-102, (2) 102-138, (3) 138-174, (4) 174-210, and (5) 210-246.....	C-1

LIST OF TABLES

Table	Title	Page
2-1.	Sur.-Earth physical constants	2
3-1.	Maximum, mean, and minimum values of the 13-month smoothed 10.7-cm solar radio noise flux and geomagnetic activity index over the mean solar cycle	3-
3-2.	Pressure parameters in Earth orbit	3-
4-1.	Worst-case plasma environment in geosynchronous Earth orbit	4
5-1.	Spherical harmonic coefficients of the International Geomagnetic Reference Field (IGRF) 1965	5-
5-2.	Spherical harmonic coefficients of the IGRF 1970	5-
6-1.	Solar electromagnetic radiation	6-
6-2.	Parameters for estimating irradiance variability over the 11-year solar cycle	6-
6-3.	Reference solar irradiance, Rayleigh scattering, oxygen, ozone cross sections, and energy flux	6-
7-1.	Uncertainties and accuracy limitations	7-1
8-1.	Spherical harmonic coefficients of the IGRF 1991	8-
8-2.	Schmidt coefficients	8-5
9-1.	Thermal parameters for LEO	9-4
9-2.	Running mean albedo and OLR percentile data for 30° inclination orbits	9-5
9-3.	Running mean albedo and OLR percentile data for 60° inclination orbits	9-6
9-4.	Running mean albedo and OLR percentile data for 90° inclination orbits	9-7
10-1.	Gravitational coefficients (4x4)	10-2
B1-1.	Constants used in equations (B1-4) through (B1-5) to compute the differential energy spectra of H, He, and Fe at solar maximum and solar minimum	B-2
B1-2.	The ratio of the abundance of various nuclei to helium	B-2
B1-3.	The ratios of the abundance of various elements to iron	B-2
B1-4.	Relative fractions of Li, Be, and B in the combined total abundance Li+Be+B	B-3

LIST OF TABLES

Table	Title	Page
B1-5.	Ratios of Mg, Si, and S to an adjusted helium spectrum	B-3
B1-6.	Fractional abundance of each element in the subiron group	B-4
B1-7.	Ratio of the abundances of various nuclei to iron	B-4
B2-1.	Mean and worst-case flare compositions.....	B-11
B2-2.	Mean flare compositions.....	B-12
C-1.	Median value of global maximum densities for altitude and $F_{10.7}$ bin with differences between global maximum density and median value for several percentile ranges. Densities in kg/m^3	C-1
C-2.	Probabilities of achieving a time interval without encountering a thermospheric density level above a given percentile value	C-6

TECHNICAL MEMORANDUM

NATURAL ORBITAL ENVIRONMENT GUIDELINES FOR USE IN AEROSPACE VEHICLE DEVELOPMENT

I. SCOPE AND PURPOSE

The purpose of this document is to provide definitions of the natural near-Earth space environment suitable for use in the initial development/design phase of any space vehicle. The natural environment includes the neutral atmosphere, plasma, charged particle radiation, electromagnetic radiation (EMR), meteoroids, orbital debris, magnetic field, physical and thermal constants, and gravitational field. Communications and other unmanned satellites operate in geosynchronous Earth orbit (GEO), therefore, some data are given for GEO, but emphasis is on altitudes from 200 km to 1000 km (low-Earth orbit (LEO)).

This document covers neither the environment below 100 km altitude (see NASA TM-4511, Terrestrial Environment (Climatic) Criteria Guidelines for Use in Aerospace Vehicle Development, 1993 Revision) nor the induced environment and other effects resulting from the presence of the space vehicle at orbital altitudes. Man-made factors are included as part of the ambient natural environment, i.e., orbital debris and radio frequency (RF) noise generated on Earth, because they are not caused by the presence of the space vehicle but form part of the ambient environment that the space vehicle experiences. It is very important to take induced environments into account because the net effect can be quite different from the unperturbed ambient natural environment. This document does not provide techniques or engineering solutions to permit operation in the natural environments described herein.

1.1 Format and Use of the Document

The format of this document is such that each section contains an explanation and description of the natural environment phenomenon to which it is devoted. In general, the descriptions include the mean and limiting values of each parameter. It is intended that these data will be sufficient for most space vehicle general design purposes; however, for systems which preliminary analyses show are sensitive to the environmental parameter being used, users should contact personnel of the Electromagnetics and Environments Branch, EL54, Marshall Space Flight Center (MSFC), AL 35812. For additional information, the user is referred to the reference section of this document. Background material appears in references 1, 2, and 3.

II. GENERAL INFORMATION

This section provides frequently used physical constants and describes the general character of terrestrial space.

2.1 Sun-Earth Constants

The values given in table 2-1 define the Sun-Earth parameters for aerospace vehicle design performance analyses.

Table 2-1. Sun-Earth physical constants.

Distance to the Sun	= 1.4959787E ⁸ km (equals 1 AU by definition)
Solar Constant (Note 1)	= 1,371 ⁺¹⁰ ₋₁₀ W/m ² at 1 AU
Eccentricity of Orbit (Note 2)	= 0.0167295
Orbital Period (Sidereal) (Note 3)	= 365.25636 days
Radius of the Earth (equatorial)	= 6378.140 km
Mass of the Earth	= 5.977E ²⁴ kg
Earth Rotation Rate	= 0.72921E ⁻⁴ (rads)/s
Gravitational Constant for the Earth (μ_E)	= 3.986012E ¹⁴ N m ² /kg
Inclination of the Equator (Note 4)	= 23.45°
Period of Rotation (Sidereal)	= 23.934 h (86 162.4 s)
Space Sink Temperature	= 3 K (absolute)
Solar Radiation Pressure at 1 AU	= 9.02×E ⁻⁶ N/m ² (100-percent reflecting)

- Notes:
1. The spectrum of the Sun is a blackbody spectrum with a characteristic temperature of 5762 K. The +10 and -10 W/m² are due to the natural variability of the solar output and measurement uncertainty.
 2. The eccentricity gives the noncircular nature of an orbit. The maximum distance from the Sun is (1+ecc) times the average radius; the minimum distance is (1-ecc) times the average radius.
 3. The sidereal period is measured with respect to the "fixed" stars rather than with respect to the Sun.
 4. The inclination of the Equator is with respect to the Earth's orbital plane.

CAUTION: The above are accepted values for general use. However, the various gravitational and other models may have been developed using other values. When this is the case, the values associated with the model should be used.

2.2 Terrestrial Space

This region of space extends from the base of the ionosphere at about 60 km above the surface of the Earth to the boundary of the magnetosphere beyond which interplanetary space is unaffected by the Earth. This distance is about 95 000 km above the surface of the Earth (16 radii of the Earth (R_E)) in the sunward direction and several times this in the anti-sunward direction. This region is loosely referred to as the magnetosphere, although more strictly speaking, this term means the (major) part of terrestrial space into which the Earth's magnetic field extends.

The morphology is roughly axisymmetric within $4 R_E$ of the Earth's center, but at greater distances it becomes very unsymmetric, with a long tail extending in the anti-sunward direction. The principal regions and their interacting phenomena are described below and illustrated in figure 2-1.

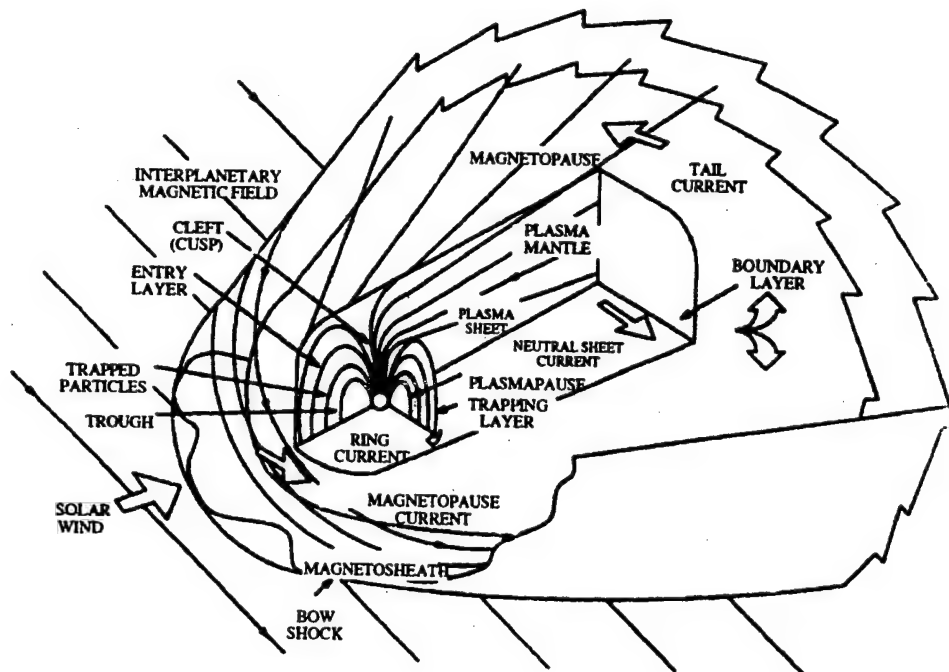


Figure 2-1. Schematic view of terrestrial space.⁴

2.2.1 Fields. The gravitational field results from the mass of the solid Earth and reflects the distribution of that mass. It traps the neutral atmosphere, constrains its motion, and influences the motions of meteoroids and debris. However, it has little effect on the rest of terrestrial space because electrical forces are so much stronger. The magnetic field has two sources: (1) currents inside the Earth that produce about 99 percent of the field at the surface and (2) currents in the magnetosphere. The latter becomes relatively more important beyond a few Earth radii because the internal field decreases as the inverse distance cubed from the Earth's center.

For many purposes, the Earth's field may be regarded as a dipole tilted 11.7° from the rotation axis and offset from the geometric center of the Earth by 430 km in the direction of southeast Asia.

Many phenomena are related to magnetic latitude which, as a result of the tilt, is 11.7° greater than geographic latitude in the longitude of eastern North America and 11.7° less on the opposite side of the world. The offset puts the surface of the Earth, or a circular orbit, at a higher altitude with respect to the geomagnetic field in the region of the South Atlantic off the coast of Brazil than it is elsewhere. This region is called the South Atlantic Anomaly. Since both the tilt and the offset are changing slowly, the South Atlantic Anomaly is drifting slowly to the west. For some applications, it may be necessary to include the magnitude and direction of this drift. If it is necessary, contact the personnel of the Electromagnetics and Environments Branch, EL54, Marshall Space Flight Center, AL 35812.

There are also electric fields that result from the motion of the magnetospheric plasma. In the ionosphere, these electric fields are perpendicular to the magnetic field and have magnitudes up to 0.1 to 0.5 V/m.

2.2.2 Plasma and Particles. The neutral atmosphere extends from the surface to 2500-km altitude or more, where its density has dropped to approximately 10^{-17} kg m $^{-3}$. Its density continues to decrease at greater altitudes, so an outer limit is not rigorously defined.

Sunlight and, to a lesser extent, fast charged particles ionize some of the neutral atmosphere, creating a plasma consisting of equal number densities of ions and electrons. In the altitude range of about 60 to 1000 km, this is called the ionosphere. The number density of the plasma is less than that of the neutral atmosphere below about 1000 km. However, collisions between plasma and neutrals are infrequent enough above about 150 km that the two are decoupled and electrical forces dominate the behavior of the ionosphere and other plasma. Between about 60 and 150 km, the neutral atmosphere and ionosphere are coupled in a complicated way.

Plasma fills the rest of terrestrial space as well and is given various names in different regions. The region out to the field lines at ($L = 4.5$) is sometimes referred to as the outer ionosphere and sometimes as the plasmasphere. Beyond that, the plasma density declines to its interplanetary value of about 10^7 ions m $^{-3}$. The plasma is electrically neutral (equal ion and electron number densities), and the energy distribution of its particles may be described by one or more temperatures (Maxwellian distributions). The plasma may have a bulk streaming velocity as well.

In addition, there are fluxes of fast moving particles, such as the trapped radiation (Van Allen belts), the aurora, and cosmic rays that have very nonthermal energy distributions. These are called penetrating charged particles. The shape of the magnetosphere, the motion of the plasma, and the acceleration of the fast particles are caused by the interactions of the Earth's magnetic field rotating with the Earth, the ionosphere, and the solar wind plasma flowing past the magnetic field. The solar wind is a very tenuous plasma that flows radially outward from the Sun through interplanetary space.

2.2.3 Variability. Processes within terrestrial space are partially controlled by the level of solar activity. The solar activity varies more or less cyclically with an average period of 11 years. The electromagnetic radiation (EMR) emitted by the Sun varies (although not much in the visible portion of the spectrum) as does the solar wind, the solar magnetic field, and the production of solar cosmic rays. The exact level of solar activity cannot be predicted very accurately, although the phase within the 11-year period can be established. Figure 2-2 shows solar activity from 1700 to 1992. In addition, plasma, radio noise, and energetic particles tend to be emitted from localized regions on the Sun's surface. These localized active regions and some coronal features persist longer than the solar rotation period of 27 days, and since they only affect the Earth when they face it, enhanced solar activity can be estimated 27 or more days in advance.

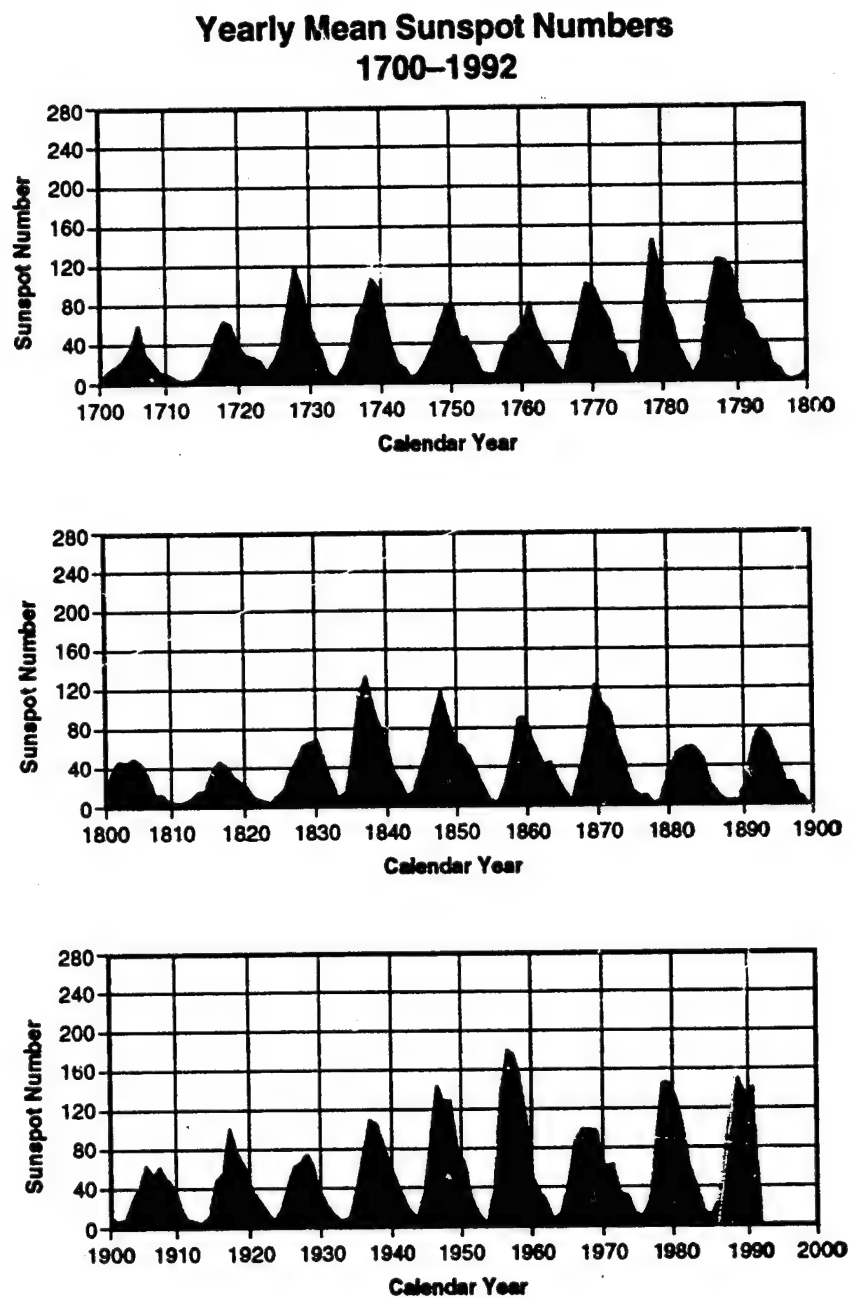


Figure 2-2. Solar cycle as represented by yearly mean sunspot number for the period 1700 to 1992.

III. NEUTRAL ATMOSPHERE

The state of the neutral atmosphere is most conveniently described in terms of a mean, with spatial and temporal variations about that mean. For space vehicle operations, the neutral atmosphere is significant because (1) even at its low density, it produces torques and drags on the vehicle; (2) the density height profile of the atmosphere above 100 km altitude modulates the flux of trapped radiation encountered, as explained in section V of this document, and the orbital debris, as explained in section VII of this document; and (3) the atomic oxygen both erodes and chemically changes those surfaces which are exposed to it.

3.1 Thermosphere Region

The region of the Earth's atmosphere lying between about 90 and 500 km is known as the thermosphere, while that region lying above 500 km is known as the exosphere. The temperature in the lower thermosphere increases rapidly with increasing altitude from a minimum at 90 km. Eventually it becomes altitude independent at upper thermospheric altitudes. This asymptotic temperature, known as the exospheric temperature, is constant with altitude due to the extremely short thermal conduction time.

The thermospheric gases are heated by the absorption of the solar extreme ultraviolet (EUV) radiation. At the lowest thermospheric altitudes, the absorption of ultraviolet (UV) radiation is also important. The EUV and UV radiation initially heats only the dayside thermosphere, and although conductive and convective processes act to redistribute some of this energy, a large temperature gradient always exists between the daytime and the nighttime thermosphere. An average daytime exospheric temperature is 1060 K, and an average nighttime exospheric temperature is 840 K. The longitudinal temperature gradient causes a wind to flow from the dayside to the nightside thermosphere, with speeds typically reaching 100 m/s.

An additional heat source for the thermosphere is the interaction of the Earth's magnetic field at very great distances (several Earth radii), in the region known as the magnetopause, with the solar wind. The solar wind is a stream of high speed plasma emanating from the Sun. This interaction causes energetic particles to penetrate down into the lower thermosphere at high geographic latitudes and directly heat the thermospheric gas. These energetic particles are also responsible for the aurora seen at these high latitudes. In addition, electric fields mapped down from the magnetosphere onto the high latitude ionosphere cause electric currents to flow. The ionosphere is a small fraction of the thermosphere that remains ionized due to the solar radiation. It never totally disappears at night, and during daylight hours the ionization density never exceeds more than 1 percent of the neutral density. These electrical currents lose energy through ohmic or joule dissipation and heat the neutral thermospheric gas. The ions also collide directly with the neutral gas, setting the whole gas into motion. At these high latitudes, the wind speeds generated by this process can be very large, at times as large as 1.5 km/s. Eventually viscous effects dissipate these winds, and their lost kinetic energy provides an additional heat source for the neutral thermospheric gas.

The high-latitude heat sources are effective during both the day and night. Although an intermittent source of energy for the thermosphere, they can at times exceed the global EUV energy absorbed by the thermosphere. In addition, although the energy is deposited at high latitudes (greater than 60° or so), the disturbance effects are transmitted to lower latitudes through the actions of winds and waves. However, the disturbance effects at low latitudes are significantly smaller than they are at higher

latitudes. The high-latitude ionospheric currents that flow perturb the geomagnetic field, so that such disturbances, which can be detected by ground-based magnetometers, are referred to as geomagnetic storms.

Whenever the neutral thermospheric gas is heated, it expands radially outward. Because the undisturbed thermospheric density decreases with increasing altitude, an outward expansion of the gas results in an increase of density at high altitudes. Thus, the daytime thermospheric density is greater than the nighttime density, while during times of geomagnetic storms, the high-latitude density is greater than it is during undisturbed periods. This anisotropic heating leads to the so-called diurnal and polar bulges, which were first inferred from the increased drag experienced by orbiting satellites.

Below the turbopause (located at about 105 km altitude), the atmosphere is well mixed by turbulence, so that the composition of the atmosphere does not vary with altitude. Above the turbopause, however, diffusion becomes so rapid that the altitude variation of the various species becomes dependent on molecular mass, with the result that composition varies with altitude. Thus, the number densities of the heavier thermospheric species (N_2 and O_2) decrease with increasing altitude much faster than those of the lighter species (H and He). This means that the heavier molecular species predominate in the lower thermosphere, while the lighter atomic species predominate in the upper thermosphere. A typical altitude profile for the individual thermospheric constituents is shown in figure 3-1. Lifting of the thermosphere will cause the mean molecular weight at a given altitude to increase, while a sinking motion will cause it to decrease.

3.2 Variations

In addition to the diurnal variation in the neutral mass density at orbital altitudes, there is a semi-annual variation, a seasonal-latitudinal variation in the lower thermosphere, and a seasonal-latitudinal variation in the helium number density as well as nonperiodic perturbations associated with variations in solar activity, atmospheric waves, and thermospheric winds. All of these variations are discussed in the paragraphs that follow.

3.2.1 Variations With Solar Activity. The short wavelength solar electromagnetic radiation (EUV and UV) changes substantially with the overall level of solar activity, with the result that the thermospheric density, especially at orbital altitudes, is strongly dependent on the level of solar activity. Thus, there is an 11-year variation in the thermospheric mass density, corresponding to the mean 11-year variation in solar activity. Similarly, there is also, on the average, a 27-day variation in density that is related to the mean 27-day solar rotation period, although the variation tends to be slightly longer than 27 days early in the cycle when active regions occur more frequently at higher latitude and slightly shorter than 27 days later in the cycle when active regions occur more frequently closer to the Sun's equator. The appearance of coronal holes and active longitudes also affects this average 27-day variation. Changes in the thermospheric density related to changes in the solar output during active periods associated with flares, eruptions, coronal mass ejections (CMEs) and coronal holes (CHs) can begin almost instantaneously (minutes to hours), although more often a day or more lag is seen. Figure 3-2 shows typical neutral densities for periods of high and low solar activity.

3.2.2 Variations During Periods of Increased Solar Activity (Flares, Coronal Mass Ejections, and Coronal Holes). As previously described, during periods of increased solar activity, the enhanced interaction of the solar wind with the Earth's magnetosphere leads to a high-latitude heat and momentum source for the thermospheric gases. Some of this heat and momentum is convected to low latitudes. This

episodic type of increased solar activity that usually causes variations in the Earth's magnetic field varies over the solar cycle and usually has two or more major peaks, one during the rise of the cycle and the other with larger peaks during the decline of the cycle. Also, more intense solar cycles seem to have more intense episodic type activity. Finally, there is a seasonal variation associated with this episodic type activity with the density usually being greatest in March (± 1 month) and September (± 1 month) of each year. This variation is possibly related to the path of the Earth in its rotation around the Sun.

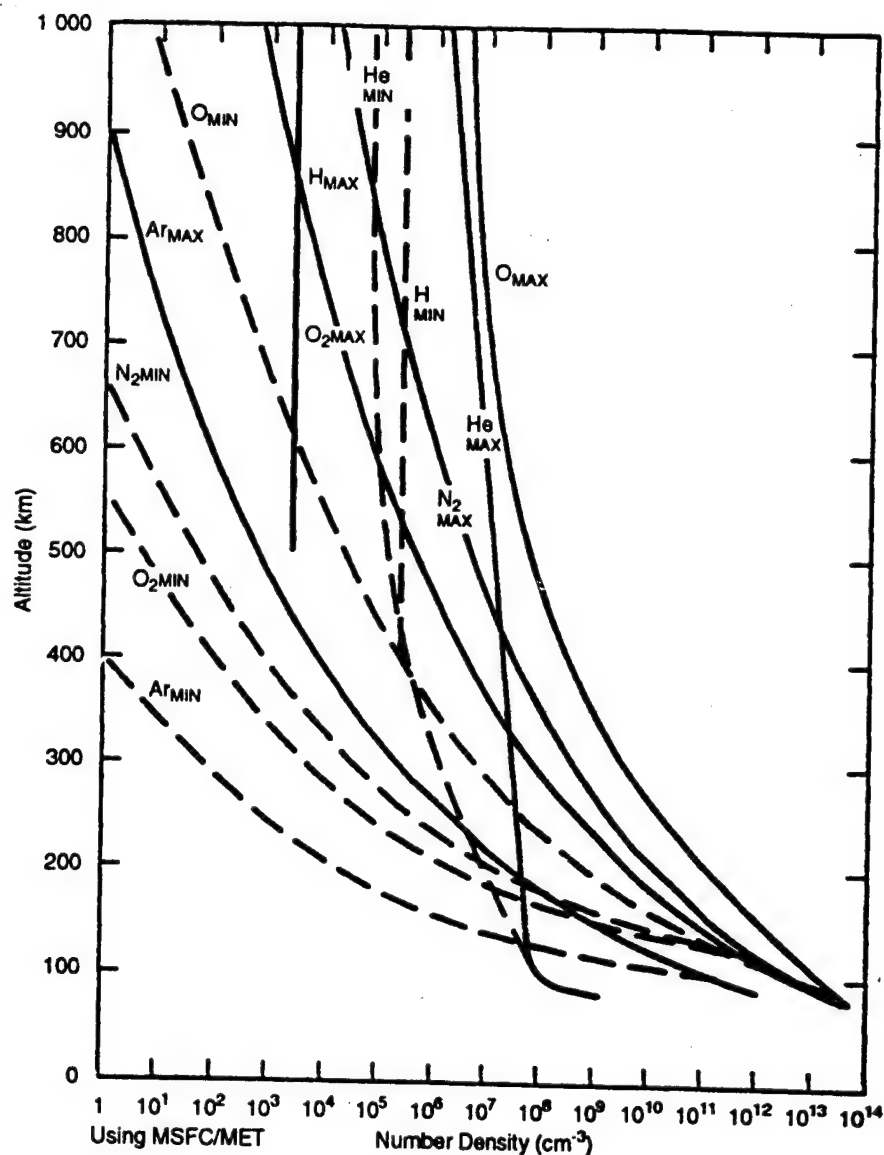


Figure 3-1. Number density of atmospheric constituents versus altitude.

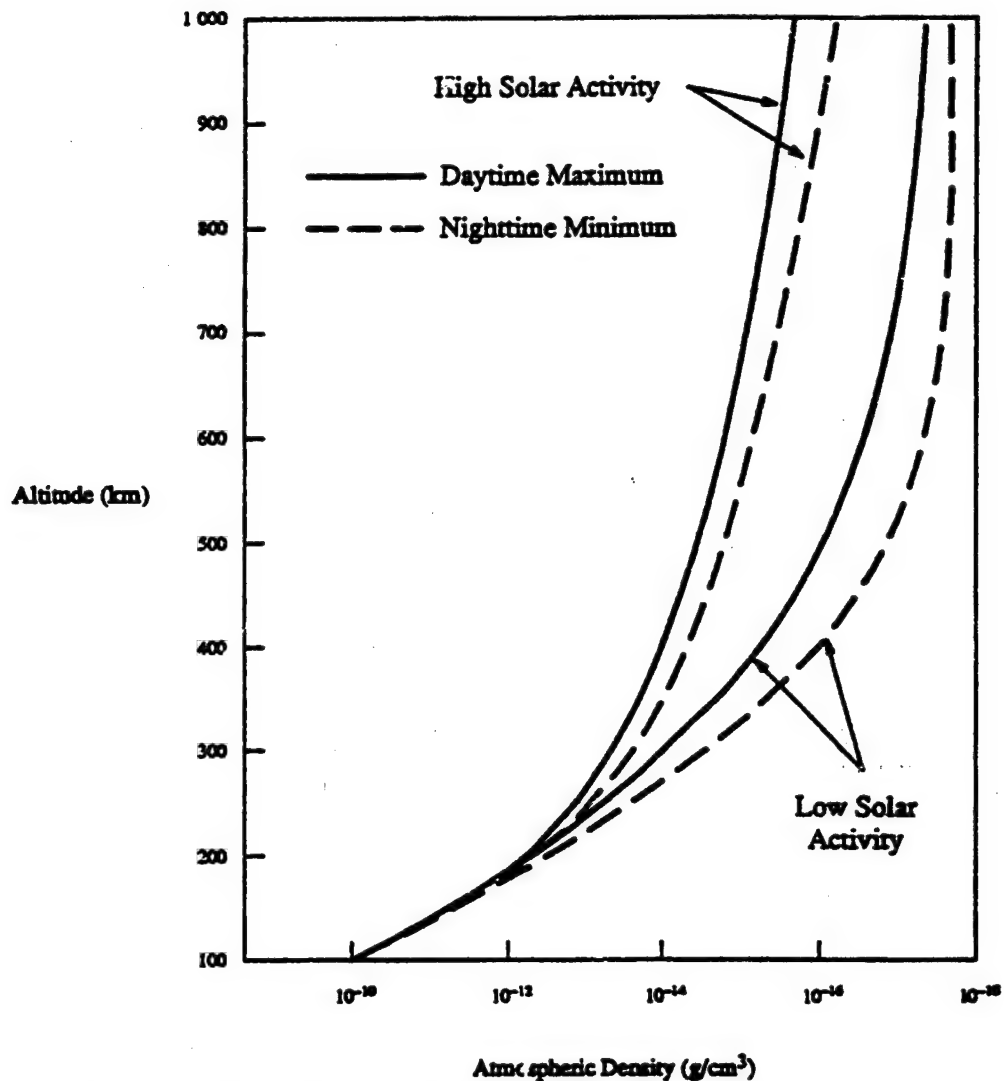


Figure 3-2. Typical atmospheric mass density profiles at high and low solar activity.
(For information only; not for design use.)

3.2.3 The Diurnal Variation. The rotation of the Earth with respect to the solar EUV heat source induces a diurnal (24-hour period) variation (or diurnal tide) in the thermospheric temperature and density. Due to a lag in the response of the thermosphere to the EUV heat source, the density at orbital altitudes maximizes around 2 p.m. local solar time at a latitude approximately equal to that of the sub-solar point. The lag, which is a function of altitude, decreases with decreasing altitude. Similarly, the density minimum occurs between 3 and 4 a.m. local solar time at about the same latitude in the opposite hemisphere. In the lowest regions of the thermosphere (120 km and below) where the characteristic thermal conduction time is on the order of a day or more, the diurnal variation is not a predominant effect.

The various constituents of the thermosphere do not all respond to the diurnal variation of the solar EUV heat source with the same amplitude and phase. The time lag is longer, by as much as 2 hours at orbital altitudes, for the heavier constituents (N_2 , O_2 , and Ar) than for O. By contrast, the lighter species number densities maximize in the early morning hours (3 a.m. and 7 a.m. local solar time, for H and He, respectively). This is due to dynamical (buoyancy) effects.

Harmonics of the diurnal tide are also induced in the Earth's atmosphere. In particular, a semi-diurnal tide (period of 12 h) and a terdiurnal tide (period of 8 h) are important in the lower thermosphere (below some 160 km for the semidiurnal tide and much lower for the terdiurnal tide). These tides are not important at orbital altitudes.

3.2.4 Semiannual Variation. This variation is believed to be a conduction mode of oscillation driven by a semiannual variation in joule heating in the high-latitude thermosphere (because of a semiannual variation in the effects on the Earth-atmosphere system of episodic-type variations in solar activity). The variation is latitudinally independent and is modified by composition effects. The amplitude of the variation is height-dependent (30 to 20 percent and asymmetric about the mean density at 350 km) and variable from year to year, with a primary minimum in July, primary maximum in October, and a secondary minimum in January followed by a secondary maximum in April. It has been found that the magnitude and altitude dependence of the semiannual oscillation vary considerably from one solar cycle to the next. This variation is important at orbital altitudes.

3.2.5 Seasonal-Latitudinal Variations of the Lower Thermosphere Density. This variation is driven in the thermosphere by the dynamics of the lower atmosphere (mesosphere and below). The amplitude of the variation maximizes in the lower thermosphere somewhere between about 105 and 120 km, diminishing to zero at altitudes around 170 km. Although the temperature oscillation amplitude is quite large, the corresponding density oscillation amplitude is small. This variation is not important at orbital altitudes.

3.2.6 Seasonal-Latitudinal Variations of Helium. Satellite mass spectrometers have measured a strong increase of helium above the winter pole. Over a year, the helium number density varies by a factor of 42 at 275 km, 12 at 400 km, and 3 or 4 above 500 km. The formation of this winter helium bulge is primarily due to the effects of global scale winds that blow from the summer to the winter hemisphere. The amplitude of the bulge decreases with increasing levels of solar activity, due to the increased effectiveness of exospheric transport above 500 km that carries helium back to the summer hemisphere. There is also a very weak dependence of the helium bulge amplitude on the magnitude of the lower thermospheric eddy diffusivity.

3.2.7 Thermospheric Waves. Fluctuations have been detected in temperature and density measurements throughout the atmosphere from the ground up to at least 510 km. Some of these fluctuations are caused by gravity waves, so named because they are primarily oscillations of the neutral gas for which the restoring force is gravity. A thermospheric gravity wave produces a corresponding wave in the ionosphere known as a traveling ionospheric disturbance.

Thermospheric gravity waves oscillate with periods typically in the range of 30 min to several hours, and have horizontal wavelengths in the range of hundreds of kilometers up to about 4000 km. The density amplitudes of the larger scale waves are larger at higher latitudes and diminish toward the equator. At about 200 km altitude, typical values of these amplitudes are 15 percent of the mean at auroral latitudes and 5 percent of the mean at equatorial latitudes. The smaller scale waves have amplitudes that are essentially independent of latitude. Gravity wave amplitudes generally decrease at greater

altitudes in the thermosphere due to dissipation by molecular processes. The larger scale waves survive to greater altitudes than do the smaller scale waves.

3.2.8 Thermospheric Winds. Figures 3-3 and 3-4 show the general flow patterns of thermospheric winds between 100 and 700 km, as they are currently known. The wind speeds range from 100 to 200 m/s at low latitudes (less than 28.5°), while at high latitudes (greater than about 65°) they can be as large as 1500 m/s or more. Rapid (minutes) changes in wind direction (of up to 180°), probably driven by gravity waves, have also been observed.

3.2.8.1 Austral (South Polar Region) Thermospheric Winds. Ground-based observations with Fabry-Perot interferometers have shown that there is a direct relationship between austral thermospheric winds at F-layer altitudes and the interplanetary magnetic field (IMF), particularly in the midnight magnetic local time (MLT) sector. The strength of the zonal component of the austral neutral wind in the MLT midnight sector is directly correlated with the strength and direction of the B_y component of the IMF. The zonal wind in the MLT midnight sector changes direction when the sign of the B_y component of the IMF changes, and the speed of the zonal wind in the MLT midnight sector is directly proportional to the strength of the B_y component. Conversely, the meridional wind in the MLT midnight sector is correlated with the B_z component of the IMF. The meridional wind decreases as the B_z component turns northward. When B_z is positive, sunward winds develop in the MLT midnight sector and exceed the strength of the zonal winds.⁶

3.2.9 Thermospheric Tides. Models of the tides in the lower thermosphere (90 to 140 km) show the midlatitude semidiurnal tide in the wind has an amplitude of tens of m/s, maximizing at 50 to 70 m/s around 110 km. Temperature tide amplitudes typically reach a maximum of 10 to 20 K; however, the models do not always agree with observations since a semidiurnal oscillation of about 70 K has been measured at low latitudes at 120 km altitude. The best agreement occurs at midlatitudes, but in general, the models underestimate both the wind and temperature tidal amplitudes. Phase differences are relatively small for the temperature tide, but are large for the tidal winds, as much as 3 h.

Radar measurements of midlatitude semidiurnal wind tides show maximum amplitudes of 60 to 70 m/s in the 110 to 120 km altitude range. Values of the maximum midlatitude, annual mean semidiurnal amplitudes and the altitudes at which they occur are: (a) temperature, 25 K at 115 km; (b) northward wind, 50 m/s at 125 km altitude; and (c) eastward wind, 50 m/s at 125 km altitude. The local times of these maxima generally decrease with increasing altitude; temperature leads the meridional wind by about 6 h, while the zonal wind leads the temperature by a few hours.

At middle-thermospheric altitudes (300 km), the mean winds are poleward in winter and equatorward in summer. The amplitude of the diurnal component of the mean wind is much greater at solar minimum than at solar maximum, showing that the influence of ion drag more than compensates for the greater EUV input at solar maximum. A typical seasonally averaged wind amplitude for the diurnal tide is about 50 m/s. The mean semidiurnal wind tide amplitude averaged over all seasons and solar cycle conditions is about 41 m/s.

3.2.9.1 Solar Storm Induced Effects in the Thermosphere. During magnetic storms and substorms, particle precipitation and the joule dissipation of the high-latitude ionospheric currents heat the neutral gas at altitudes above some 110 km. The thermosphere then expands and densities above about 120 km increase. The energy deposited in the high-latitude thermosphere at such times is significant and can exceed the global EUV absorbed by the thermosphere. It remains an important heat source locally at night in the auroral zones.

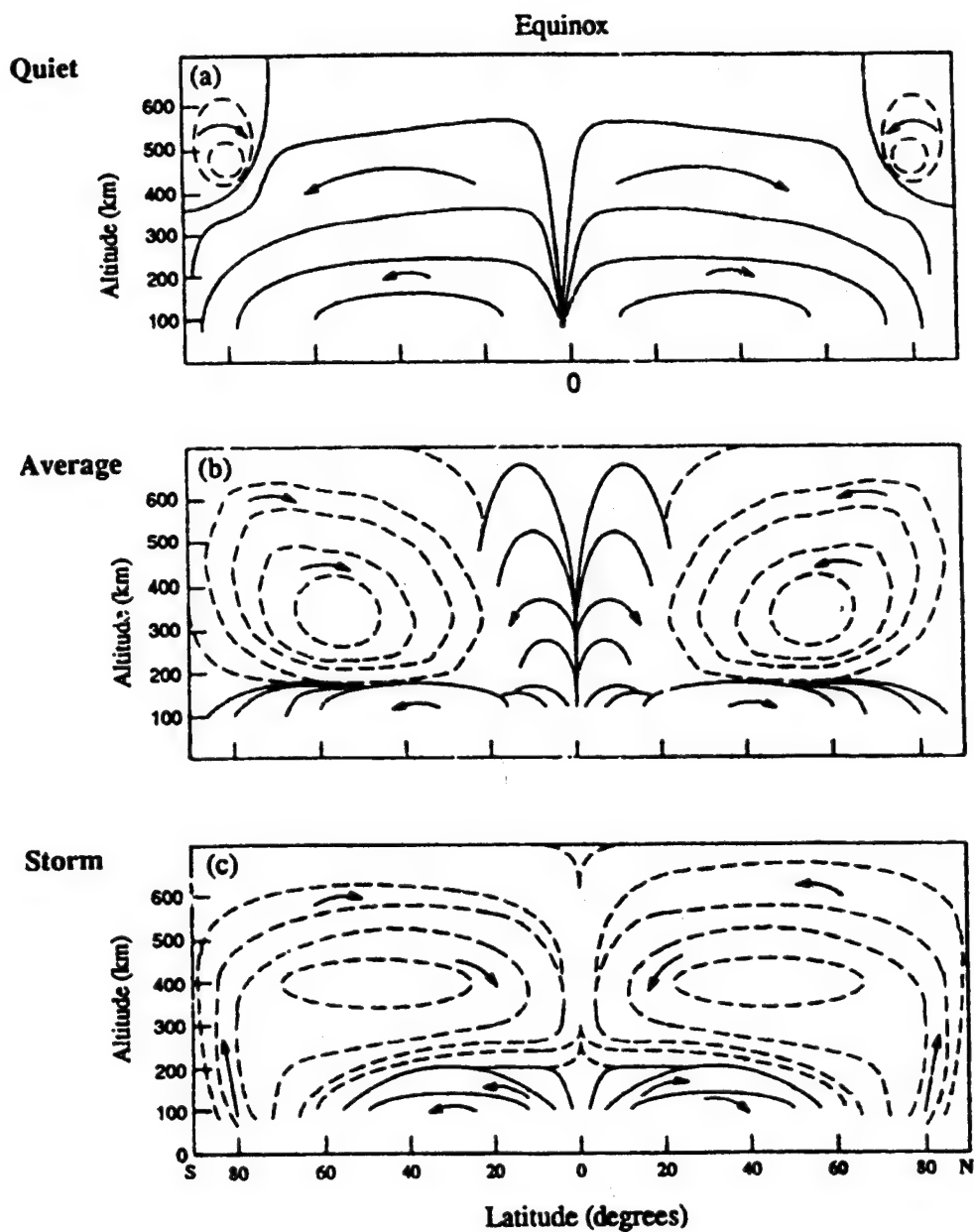


Figure 3-3. Schematic diagram of the zonal mean meridional circulation in the thermosphere at equinox for various levels of magnetic (auroral) activity.⁵ (Maximum velocities are typically hundreds of meters per second.)

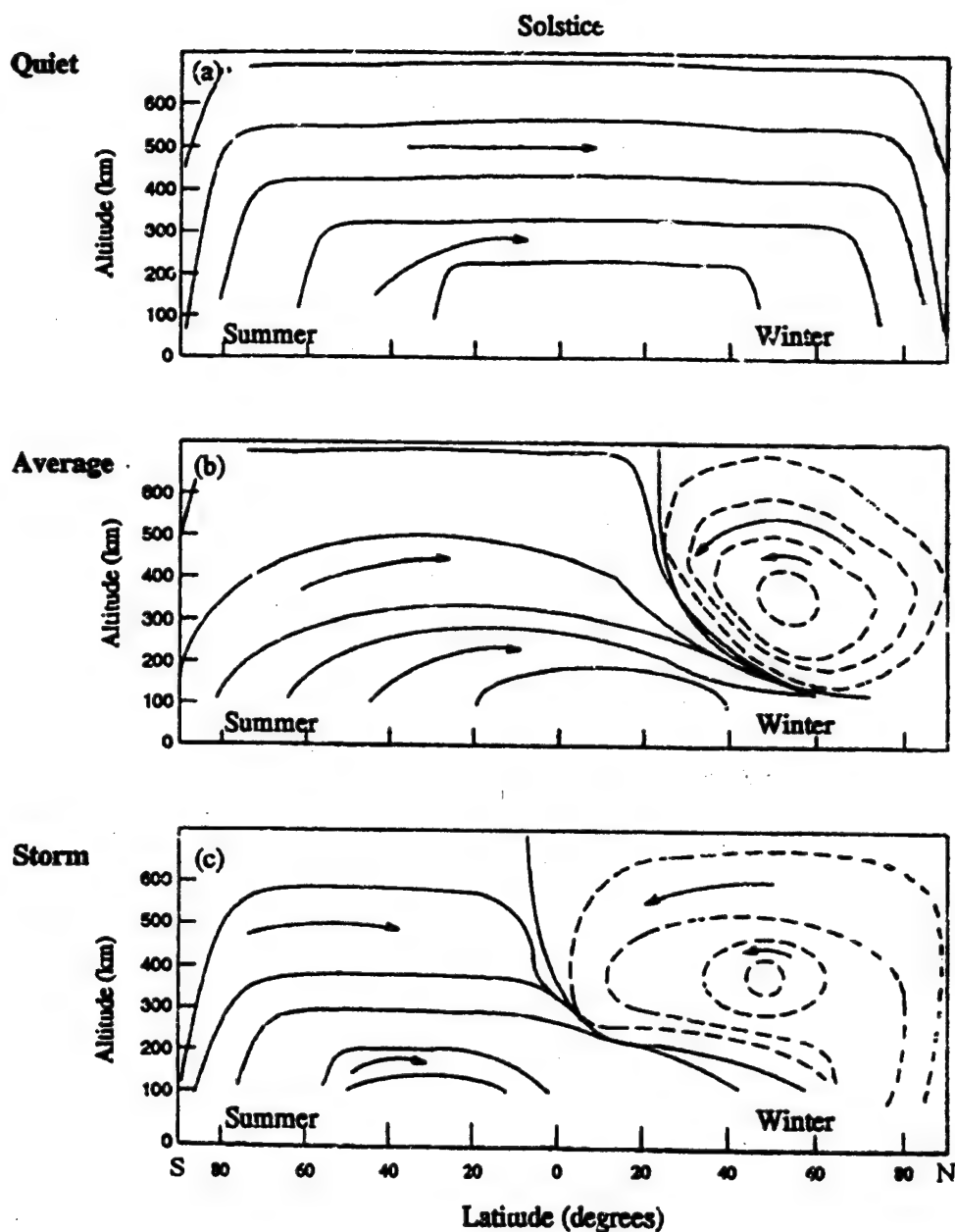


Figure 3-4. Schematic diagram of the zonal mean meridional circulation in the thermosphere at solstice for various levels of magnetic (auroral) activity.⁵ (Maximum velocities are typically hundreds of meters per second.)

The energy generated during a substorm is transferred from high to low latitudes principally by the meridional winds assisted by gravity waves. This high-latitude heating sets up a circulation cell in which gas is lifted in the auroral zone, flows equatorward, sinks at middle to low latitudes, and then returns to the heating region at low altitudes. The sinking causes compressional heating (figs. 3-3 and 3-4).

Since the mean molecular weight decreases with altitude, lifting of the gas at auroral latitudes leads to increases in the mean molecular weight at a fixed altitude. Compositional changes also accompany geomagnetic storms and these changes are even observed at middle and low latitudes. In general during a geomagnetic storm, there is a large depletion in O and an enhancement in O_2 within the auroral ovals. The magnitude of both the O depletion and the O_2 enhancement is underestimated in current models, with the misrepresentation increasing with the use of daily values of A_p instead of the 3-hourly values.⁷ Analyses which require instantaneous values of either atomic or molecular oxygen within the auroral ovals should take special precautions in using the available models of the thermosphere.

In one numerical simulation of a geomagnetic substorm, it was found that at both 200 and 450 km the latitudinal variations in the mass density during the substorm were relatively insignificant and did not at all reflect the total heat input into the auroral zone. In particular, it was apparent that the global density response was relatively significant (60 percent) when compared with the 40-percent increase between the equator and the pole at 450 km. This predominance in the global component was even more pronounced at 200 km and appeared to be in substantial agreement with the satellite drag data. The maximum in the density occurred at 0200 u.t. at high latitudes and shifted toward 0800 u.t. at the equator, with the average time lag of 6 h deduced from satellite drag data.

In other simulations of geomagnetic substorms, one finds that the thermosphere at high latitudes is significantly perturbed by the heat and momentum deposited there, with wind speeds approaching 1 km/s in the region of the polar cap and temperatures elevated some 500 K in the auroral zones. At lower latitudes the effects are far less dramatic, but are nonetheless still significant. The response is asymmetric with respect to longitude, reflecting the asymmetry of the high-latitude heat sources. Large-scale disturbances propagate from each auroral region toward equatorial latitudes with a time delay of about 2 h at 330 km altitude and about 5 h at 125 km altitude. At 330 km altitude, the equatorial thermosphere is influenced mainly by the interactions of two converging gravity waves, while at 125 km it is influenced mainly by the mean motion. Equatorial temperature oscillations of magnitude 100 to 200 K occurred at 330 km altitude driven by oscillations in the mean meridional wind of about 200 m/s. Temperature enhancements at 125 km were much smaller (60 K) as were the meridional wind speed enhancements (8 m/s). The zonally averaged zonal wind enhancements were found to be confined primarily to the high latitudes.

3.2.9.1.1 Ionospheric Storm Effects. During and following a geomagnetic substorm, the ionosphere is altered as a consequence of several competing effects. Some of these will lead to increases in the ionization density of the F2-region (positive storm effects), and others will lead to decreases in the F2-peak (negative storm effects). These are briefly summarized for the subauroral ionosphere:

- **Positive Storm Effects:**

- (1) Traveling atmospheric disturbances such as gravity waves will cause a sudden uplifting of the F-layer. Through collisions the neutral disturbances impart to the ions a motion parallel to the geomagnetic field lines. These effects propagate equatorward at speeds of many hundreds of meters

per second. The duration of the upward drift is about 1 h and is particularly pronounced in the noon/afternoon local time sector.

(2) The large-scale wind circulation will also impart a motion to the ions that is parallel to the geomagnetic field. This effect may last a whole day and is more likely to occur in the daytime.

(3) The expansion of the polar ionization enhancement toward lower latitudes, due, for example, to particle precipitation, will directly increase ionization densities. It is typically a nighttime phenomenon.

- Negative Storm Effects:

(1) Changes in the neutral gas composition, and particularly an increase in the N_2/O ratio, will lead to a depletion of ionization. This is most clearly observed in the morning sector, with an anomalously low rate of ionization after sunrise. The effect may last from many hours to days.

(2) The displacement and expansion of the ionospheric trough region toward lower latitudes creates a steep ionization density drop and is typically observed in the afternoon/evening sector.

Another ionospheric effect of geomagnetic disturbances is the propagation of disturbance effects known as traveling ionospheric disturbances (TIDs). They are characterized by oscillations in the ionization density at the height of the F-layer, driven by gravity wave-driven oscillations in the neutral density and neutral winds.

3.3 Solar and Geomagnetic Indices

Various surrogate indices are used to quantitatively assess the levels of solar activity. One of these is the 10.7 cm (2800 MHz) solar radio noise flux, designated $F_{10.7}$. Although it is the EUV radiation that heats the thermosphere, it cannot be measured at the ground. The $F_{10.7}$ can be measured from the ground, and it also correlates quite well with the EUV radiation. Although there are instances when the correlation is not good, it appears unlikely that the $F_{10.7}$ radio flux will be replaced by another index in the foreseeable future.

An index that is used as a measure of episodic type solar activity is the planetary geomagnetic activity index a_p (or k_p , which is essentially the logarithm of a_p). It is based on magnetic field fluctuation data reported every 3 h at 12 stations between geomagnetic latitudes 48° and 63° and selected for good longitudinal coverage. Although it is the high latitude ionospheric current fluctuations that drive the magnetic field fluctuations as observed at these stations, it is not the magnetic field fluctuations which are driving the thermosphere. Therefore, the correlations between observed density changes and the a_p index are not always good. The daily planetary geomagnetic index, A_p , is the average of the eight 3-hourly a_p values for that particular day.

Table 3-1 lists the maximum, mean, and minimum 13-month smoothed values for $F_{10.7}$ and A_p throughout a mean 11-year solar cycle. Figures 3-5 and 3-6 show data from this table. The $F_{10.7}$ data are derived from sunspot records for the period 1749 to 1947 with direct $F_{10.7}$ measurements thereafter. Table 3-1 covers a mean duration cycle length of 11 years. The standard deviation about the mean length is 1.23 years in the historical record. "Max" and "min" are the historical extremes for each point in the cycle and have been determined after the data have been 13-month smoothed and constrained to the

mean duration cycle. The A_p values in table 3-1 and figure 3-6 are derived in a similar fashion based on a data record that goes back to 1932.

Table 3-1. Maximum, mean, and minimum values of the 13-month smoothed 10.7 cm solar radio noise flux and geomagnetic activity index over the mean solar cycle (page 1 of 4).

Cycle P_t	$F_{10.7}$			A_p		
	Max	Mean	Min	Max	Mean	Min
1	73.3	69.6	67.0	11.5	9.5	7.6
2	73.4	69.7	67.0	11.7	9.6	7.7
3	74.0	70.0	67.0	11.8	9.7	7.7
4	74.5	70.4	67.0	11.9	9.7	7.6
5	74.9	70.7	67.0	11.9	9.7	7.4
6	76.2	71.1	67.1	12.2	9.9	7.3
7	78.4	71.6	67.2	12.5	10.0	7.2
8	79.8	72.2	67.3	12.9	10.3	7.3
9	81.5	72.8	67.4	13.3	10.6	7.8
10	84.1	73.6	67.5	14.1	10.9	8.1
11	87.7	74.5	67.7	15.1	11.2	8.2
12	93.4	75.7	67.9	15.7	11.5	8.3
13	97.9	77.0	68.0	15.9	11.8	8.3
14	101.7	78.4	68.0	16.4	12.0	8.3
15	107.7	80.1	68.0	17.4	12.3	8.5
16	114.5	82.0	68.0	18.4	12.7	8.4
17	121.1	84.0	68.1	18.7	12.9	8.5
18	129.1	86.2	68.4	18.8	13.1	8.7
19	137.6	88.5	68.5	18.6	13.2	9.0
20	143.4	91.0	68.6	18.3	13.2	9.3
21	147.6	93.7	68.8	18.1	13.2	9.7
22	151.7	96.3	68.7	18.4	13.4	9.5
23	155.7	98.9	68.8	18.4	13.5	9.3
24	160.1	101.6	69.2	17.6	13.5	9.1
25	164.8	104.4	69.7	17.1	13.6	9.0
26	169.1	107.2	70.1	17.4	13.6	9.1
27	173.0	110.2	70.6	17.4	13.6	9.4
28	177.1	113.2	70.7	18.5	13.8	9.8
29	186.1	116.2	71.3	19.9	14.0	10.0
30	191.5	119.3	72.2	19.9	14.1	10.0
31	194.3	122.0	72.6	19.9	14.1	10.1
32	196.9	124.3	73.3	20.1	14.1	10.4
33	199.6	126.5	73.9	20.4	14.2	10.2
34	204.2	128.6	74.1	20.8	14.2	10.3
35	210.6	131.0	74.4	20.9	14.1	10.6

Table 3-1. Maximum, mean, and minimum values of the 13-month smoothed 10.7 cm solar radio noise flux and geomagnetic activity index over the mean solar cycle (page 2 of 4).

Cycle P_i	$F_{10.7}$			A_p		
	Max	Mean	Min	Max	Mean	Min
36	214.8	133.3	74.5	21.0	14.0	10.6
37	217.2	135.6	74.6	21.2	14.0	10.5
38	221.6	137.6	74.5	21.6	14.1	10.4
39	226.9	139.6	74.1	22.1	14.1	10.6
40	229.9	141.4	73.6	22.2	14.0	10.8
41	231.7	143.2	73.5	21.0	13.7	10.7
42	233.7	144.6	73.6	20.1	13.4	10.4
43	235.6	145.6	74.0	19.8	13.3	10.5
44	238.8	146.7	75.1	19.3	13.3	10.7
45	242.8	147.2	75.8	19.2	13.3	10.8
46	245.2	147.7	76.5	19.0	13.4	11.0
47	244.5	148.1	78.1	18.8	13.3	10.7
48	243.3	148.4	80.1	18.6	13.4	10.8
49	244.7	148.7	82.5	18.6	13.4	10.6
50	245.7	148.2	84.0	18.3	13.4	10.2
51	243.3	146.8	85.5	18.2	13.5	10.6
52	239.4	145.7	87.9	18.7	13.8	11.3
53	235.0	145.1	89.5	19.2	14.1	11.4
54	232.9	144.9	92.2	19.6	14.2	11.3
55	233.3	144.9	93.8	20.3	14.4	11.3
56	233.1	144.7	94.9	21.0	14.6	11.5
57	231.2	144.2	95.0	21.4	14.8	11.6
58	229.1	143.5	94.7	21.2	14.8	11.6
59	228.1	142.7	94.9	20.4	14.7	11.8
60	227.6	142.3	96.5	20.7	14.8	12.1
61	226.7	142.1	97.3	21.9	15.1	12.2
62	225.6	141.3	96.8	22.7	15.2	12.0
63	223.0	140.1	96.0	22.7	15.1	11.6
64	218.6	138.4	96.0	22.3	15.1	11.2
65	215.3	136.8	96.6	21.7	15.1	11.2
66	212.0	135.5	96.7	21.5	15.1	11.2
67	206.9	134.3	95.1	22.1	15.1	11.2
68	204.0	133.0	95.0	23.1	15.5	11.3
69	203.6	131.6	96.3	23.5	15.6	11.3
70	200.4	129.8	96.5	23.4	15.6	11.2
71	196.8	128.3	94.7	23.3	15.7	11.1
72	195.7	127.3	93.6	23.1	15.5	10.8

Table 3-1. Maximum, mean, and minimum values of the 13-month smoothed 10.7 cm solar radio noise flux and geomagnetic activity index over the mean solar cycle (page 3 of 4).

Cycle P_t	$F_{10.7}$			A_p		
	Max	Mean	Min	Max	Mean	Min
73	194.8	126.5	93.5	22.2	15.7	10.9
74	191.5	125.1	91.9	22.1	15.6	11.1
75	187.4	123.5	88.7	22.2	15.6	11.7
76	182.9	122.3	86.6	22.5	15.8	11.6
77	178.6	121.5	87.8	22.6	15.9	11.5
78	176.3	120.5	86.5	22.5	15.8	11.3
79	174.9	119.5	85.9	21.6	15.7	11.3
80	171.1	117.9	85.0	21.0	15.4	11.3
81	164.5	116.3	83.6	21.1	15.2	11.2
82	158.1	114.6	82.3	21.6	15.2	11.2
83	154.4	112.9	81.6	22.2	15.4	11.4
84	152.7	111.1	81.5	22.0	15.3	11.3
85	150.8	109.5	81.9	22.0	15.2	11.4
86	148.1	108.0	81.6	22.2	15.0	11.3
87	145.0	106.4	81.4	22.5	14.9	11.3
88	141.1	104.9	80.2	22.8	14.7	11.2
89	137.0	103.4	80.3	23.5	14.7	11.1
90	132.4	101.9	80.0	24.2	14.7	11.0
91	125.4	100.3	78.9	24.7	14.8	11.3
92	119.5	98.9	77.6	25.0	14.8	11.3
93	118.4	97.7	76.6	24.9	14.8	11.2
94	118.7	96.6	74.8	24.5	14.8	11.4
95	119.4	95.6	74.0	23.6	14.7	11.6
96	119.8	94.8	73.4	22.8	14.7	11.3
97	119.0	93.9	73.2	22.1	14.7	11.1
98	117.7	92.8	73.1	21.8	14.8	11.1
99	116.4	91.8	72.7	21.4	14.8	11.2
100	114.6	90.6	71.7	21.1	14.8	11.2
101	110.8	89.6	71.1	20.5	14.7	10.5
102	105.4	88.4	70.6	19.7	14.4	9.9
103	103.2	87.3	70.1	19.7	14.3	9.5
104	102.0	86.5	69.9	19.8	14.1	9.2
105	100.0	85.7	70.0	19.5	14.0	9.0
106	98.2	84.3	69.9	19.1	13.8	8.9
107	96.6	83.6	69.7	18.6	13.8	8.8
108	94.6	82.5	69.5	17.9	13.8	8.7
109	93.8	81.8	69.4	17.0	13.7	8.7

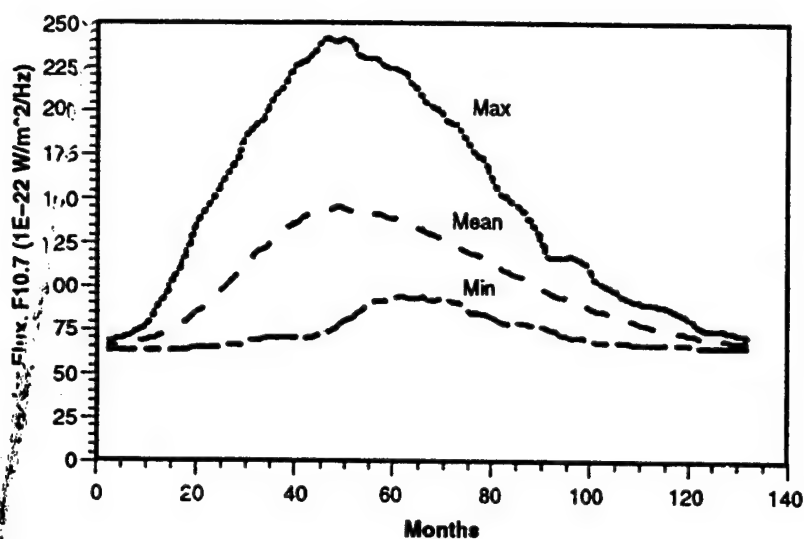
Table 3-1. Maximum, mean, and minimum values of the 13-month smoothed 10.7 cm solar radio noise flux and geomagnetic activity index over the mean solar cycle (page 4 of 4).

Cycle P_t	$F_{10.7}$			A_p		
	Max	Mean	Min	Max	Mean	Min
110	92.7	81.1	69.3	16.5	13.6	8.8
111	92.0	80.3	69.0	16.7	13.5	8.9
112	91.8	79.6	68.8	16.9	13.4	9.0
113	91.4	78.9	68.5	17.1	13.3	9.0
114	90.8	78.2	68.2	17.4	13.3	9.0
115	90.1	77.5	68.2	17.7	13.1	9.0
116	89.1	76.9	68.2	17.6	12.9	9.2
117	88.2	76.4	68.2	17.4	12.7	9.3
118	87.0	75.9	68.3	16.9	12.5	9.2
119	85.4	75.3	68.3	16.1	12.2	9.1
120	83.2	74.8	68.3	14.7	11.8	9.1
121	80.5	74.2	68.3	13.6	11.5	9.1
122	78.5	73.5	67.9	13.7	11.2	8.9
123	77.6	72.9	67.6	13.4	10.9	8.5
124	77.1	72.3	67.4	13.0	10.6	8.1
125	76.9	72.0	67.4	12.7	10.5	8.0
126	76.7	71.6	67.2	12.4	10.3	8.0
127	76.5	71.3	67.1	11.7	10.1	8.0
128	76.2	70.9	67.0	11.2	9.9	8.0
129	75.2	70.6	67.0	11.0	9.8	7.9
130	74.2	70.3	67.0	10.9	9.1	7.2
131	74.0	70.1	67.0	11.1	9.2	7.4
132	73.5	69.9	67.0	11.4	9.4	7.6

This table may be extended by repetition of the 11-year cycle.

3.4 Orbital and Suborbital Neutral Atmosphere Model

The MSFC Global Reference Atmosphere Model (GRAM) provides a single continuous representation of the neutral atmosphere from the Earth's surface to 2500 km altitude. GRAM consists of a four-dimensional (latitude, longitude, altitude, and time) model of the atmosphere from the surface to 25 km that is faired to a Barnett model of the atmosphere from 30 to 115 km, which is then faired to a modified MSFC/J70 model that extends from 90 to 2500 km. There is a description of this model in section 3.8.1 of references 2, G, and H. The computer program for the GRAM and the appropriate input parameters for the model, which depend upon the date assumed for application, are available upon request.



Note: The standard deviation about the mean period is 1.23 years in the historical record.

Figure 3-5. 13-month smoothed values of $F_{10.7}$ over the mean solar cycle (use table 3-1 for numerical values).

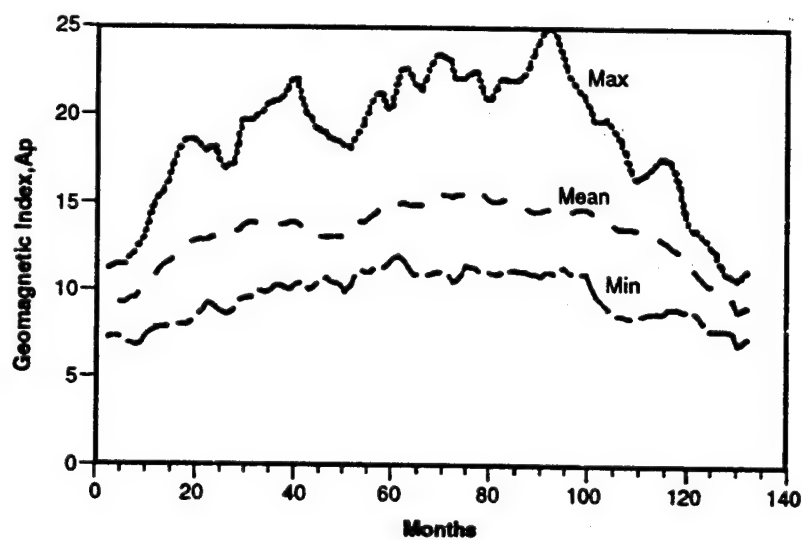


Figure 3-6. 13-month smoothed values of geomagnetic activity index (A_p) over the mean solar cycle (use table 3-1 for numerical values).

3.5 Marshall Engineering Thermosphere Model

The Marshall Engineering Thermosphere (MET) model has been developed to represent, in so far as is practical for engineering applications, the variability of the ambient mass density. It is the standard neutral atmospheric density model used for control and lifetime studies for most NASA spacecraft projects. A description of the model can be found in references 8, 9, and 10. The computer program for the MET orbital atmosphere model is available upon request.

The MET model is an empirical model whose coefficients were obtained from satellite drag analyses. It is a static diffusion model and is essentially the Smithsonian's Jacchia 1970 model with two additions from the Jacchia 1971 model. Inputs to the model are time (year, month, day, hour, and minute), position (altitude and geographic latitude and longitude), the previous day's solar radio flux ($F_{10.7}$), the centered solar radio flux averaged over six solar rotations ($F_{10.7B}$), and the a_p index 6 to 7 hours before the time in question (for some studies the daily planetary geomagnetic index, A_p , may be used instead of the 3-hourly a_p value).

With the exospheric temperature specified, the temperature can be calculated for any altitude between the lower boundary (90 km) and the upper level (2500 km) of the model from an empirically determined temperature profile. The density for all points on the globe at 90 km altitude is assumed constant, and mixing prevails to 105 km. Between these two altitudes, the mean molecular mass varies as a result of the dissociation of molecular to atomic oxygen. At 120 km altitude, the ratio of atomic to molecular oxygen is assumed to be 1.5. Density between 90 and 105 km is calculated by integration of the barometric equation. For altitudes above 105 km, the diffusion equation for each of the individual species (O_2 , O , N_2 , He , and Ar) is integrated upward from the 105 km level. For hydrogen, the integration of the diffusion equation proceeds upward from 500 km altitude. The total mass density is calculated by summing the individual specie mass densities.

The total density is then further modified by the effects of the seasonal-latitudinal density variation of the lower thermosphere below 170 km altitude and seasonal-latitudinal variations of helium above 500 km. These two effects have been incorporated in the MET model using equations developed by Jacchia for his 1971 thermospheric model.

The final output of the MET model is total mass density, temperature, pressure, individual specie number densities, mean molecular weight, scale height, specific heats, and the local gravitational acceleration.

The total mass density, the temperature, and the individual species all have the same phase variation in the MET model (i.e., they all maximize at the same local time). For some studies involving the effects of various species on an orbiting spacecraft where accurate phases of the various species within an orbit are required, it may be necessary to use the MSIS model.¹¹

The values given in table 3-2 define the Earth pressure parameters for space vehicle design performance analyses.

3.5.1 Statistical Analysis Mode. The statistical analysis mode (SAM) of the MET model was developed for use during those time periods when actual values of the daily and 162-day mean values of the 10.7 cm solar radio flux and the global geomagnetic index, a_p , are unknown or unavailable, e.g., when the time of application to a specific problem is sometime in the future. This is particularly true during the design, development, and testing phases of a space vehicle when there are only rough

estimates of the 13-month smoothed mean values of these three parameters and no guesses at all about how they should be combined. The procedure currently used in spacecraft development work is to assume that the daily and the 162-day mean values of the 10.7 cm solar radio flux are both equal to the 13-month smoothed value predicted using a technique developed through a statistical analysis of sunspot data from 1855 to the present (see ref. E for sunspot to F10.7 conversion). The 13-month smoothed values of a_p are predicted in the same manner. This procedure provides useful estimates of the long-term mean density, subject primarily to the accuracy of the predicted 13-month smoothed input data. For periods shorter than 90 days, the thermospheric properties defined by the use of the 13-month smoothed inputs are no longer representative of the original model outputs using the proper input parameters. For systems which are sensitive to thermospheric effects and variations over time periods of a few days or less (e.g., control and pointing systems), representative samples (ref. D) of the proper model inputs taken from the historical dataset should be used. Alternatively, for some applications the variations may be treated statistically.

Table 3-2. Pressure parameters in Earth orbit (ambient pressure in Pascal; Torr in parenthesis).*

Minimum	Nominal	Maximum	Altitude (km)
4.0E-5 (3.0E-7)	8.5E-5 (6.4E-7)	2.3E-4 (1.7E-6)	200
1.8E-7 (1.4E-9)	1.5E-6 (1.1E-8)	1.7E-5 (1.3E-7)	400
3.0E-8 (2.3E-10)	3.1E-7 (2.3E-9)	6.5E-6 (4.9E-8)	500
1.7E-8 (1.3E-10)	8.3E-8 (6.2E-10)	2.7E-6 (2.0E-8)	600
4.3E-9 (3.2E-11)	7.5E-9 (5.6E-11)	1.5E-7 (1.1E-9)	1000
1.0E-11 (7.5E-14)			Geosynchronous

*Low and high pressure values were computed from the MET model using an orbit average value and assuming a 28.5° orbit inclination. The following inputs were used: Low: date: August 8, 0400 u.t., $F_{10.7} = 70$, $A_p = 0$ High: date: October 27, 1400 u.t., $F_{10.7} = 230$, $A_p = 400$.

Nominal pressure values were taken from USSA 1976 (ref. A). Geosynchronous pressure values were taken from reference 1. To convert from Pascal to Torr multiply by $7.5E^{-3}$.

The MET-SAM is the initial step in developing the statistics of these shorter period perturbations in orbital altitude density in addition to providing limits on the magnitudes of the variations that are averaged out through the use of 13-month smoothed solar activity input parameters to the original MET model.

The MET-SAM also provides answers to another frequently asked question—what is the percent of time that the recommended density value will be exceeded during the operational phase of the vehicle? Or, how confident are you that the recommended density value will not be exceeded more than 5 percent of the time? The answers are crucial in the design of the guidance and control capability. the

selection of the altitude at which the vehicle will orbit and the reboost strategy for payloads put into LEO by the shuttle. The MET-SAM is also based on the premise that most applications during the development phase primarily require detailed knowledge about the maximum and minimum densities that will be encountered with limits on the magnitude of the variations that occur during monthly time periods. Research is in progress to develop a technique for including the perturbations within an orbit.

All available daily values of the 10.7 cm solar flux and the three hourly values of a_p from 1947 to 1991 were used to calculate values of the global minimum, mean, and maximum exospheric temperatures. The statistics of this new data set were calculated, and the results were indexed to five different levels of solar active as defined by the values of the 13-month smoothed 10.7 cm solar flux. This makes it possible to statistically include the 3-hour to 90-day variations in these three temperatures using only known or estimated values of the 13-month smoothed 10.7 cm solar flux. MET-SAM is not yet available for general release, so an output summary table of expected density variations is included in table C-1, appendix C. The data in this table present the statistics of the global (spatial) maximum densities for averaging periods as short as 3 hours, the temporal resolution of the a_p data set.

Use of the data in this table also makes it possible for the design engineers to easily accomplish any required trade studies while managers will be able to determine just what risks they will be taking. For applications which require density values other than the global maximum or for questions concerning the application of the data in engineering analyses contact personnel of the Electromagnetics and Environments Branch, EL54, MSFC, AL 35812. Table C-1 also shows the median value of the global maximum density for the altitude and the 10.7 cm solar flux bin indicated, computed over the period of record. It also gives the differences between the median value of the global maximum density and several other percentile levels of the global maximum density. "Percentile" refers to the fraction of time the density was equal to or less than the indicated value. These data may be used directly to indicate the magnitude of the variations in the global maximum density which occur over time periods of a few days. If appropriate for the application, an additional increment may be added to account for model inaccuracies and variations related to other sources. To obtain a conservative (upper limit) estimate, we recommend assuming these additional variations are gaussian with a standard deviation equal to 0.2 times the total density.

To understand the frequency of occurrence of these variations, table C-2 provides the probabilities of encountering intervals of 10 and 30 days without exceeding the indicated percentile level. (As with table C-1, only solar and geomagnetic variations are considered.) Probabilities for other time intervals can be estimated from figure C-1. If one of these higher percentile levels is exceeded, it typically drops back down within a short time period (hours, a few days at most). The distributions are highly skewed, and once a level has been exceeded, it is usually exceeded again within a few days. On the other hand, if the Sun is quiet, it may remain so for several months.

IV. PLASMA ENVIRONMENT

Slightly below the temperature transition region discussed in section III that marks the lower boundary of the thermosphere—and associated changes in composition of the neutral species—there is an important transition related to the electromagnetic properties of the gas. At roughly 80 km altitude, there is a division between the lower turbulent neutral gas mixture region where all the meteorological processes occur and the upper region where solar irradiation produces a partially ionized plasma composed of O, N₂, O₂, He, H, O⁺, H⁺, He⁺, NO⁺, O₂⁺, N₂⁺, and electrons. This upper region is electrically neutral, with the most abundant neutral being O and the most abundant ion being O⁺ up to about 1000 km altitude where H⁺ and He⁺ become dominant. A plasma is a quasi-neutral gas of charged and neutral particles that exhibits collective behavior. The particles' movements are controlled to a great extent by the Earth's magnetic field and the solar wind, but their collective behavior and movement generate electric and magnetic fields that, in turn, affect the particle's motion and the motion of other charged particles far away.

Plasmas are usually described by their density (expressed as electron number density, $n_e \text{ m}^{-3}$), the chemical composition of the ions (often expressed as percentage of total ions), and the electron and ion temperatures (expressed in Kelvin, T, or as energy in electron volts (eV)). The high energy particles which also may be present (megaelectron volts (MeV) range) cannot be so described and they interact differently with a vehicle than the plasma does. They are discussed in section V of this document.

The plasma environment may be conceptually divided into three regions: the ionosphere, which is contained within the magnetosphere; the magnetosphere; and the solar wind. The ionosphere is characterized by its low temperature and high density relative to the other regions, as well as its predominantly O⁺ composition. Frequently, this region is considered to extend to about 1000 km, the altitude where the ion density begins to exceed the neutral density. Alternately, an arbitrary density criterion of 10^9 m^{-3} places the "ionopause" at a few thousand kilometers altitude in the polar regions and at a few tens of thousands of kilometers in the equatorial regions. The equatorial extension of the ionosphere is predominantly composed of lighter ions, H⁺ and He⁺, and is usually referred to as the plasmasphere. Above the ionopause/plasmapause, but within the region of closed magnetic field lines, the plasma is still dominated by photoionized terrestrial particles, but the density decreases and the temperature increases owing to energy inputs from the solar wind.

Even as low as about 60 km altitude, there are sufficient long-lived free-charged particles to affect the propagation of electromagnetic waves, to support various modes of electrostatic waves, and to support detectable (or sometimes significant) currents in the presence of electric fields. As altitude increases, the charged densities increase through a series of layers to something on the order of 10^{12} m^{-3} (on the day side) at the peak density altitude (250 to 300 km). With additional increases in altitude, they decrease to the order of 10^7 m^{-3} in the solar wind and magnetospheric plasma sheet or to even lower densities which are found in the magnetospheric tail lobes, $\sim 10^5 \text{ m}^{-3}$ (fig. 2-1). At low altitudes, the temperatures of these plasmas are typically 300 K to 3500 K (0.05 to 0.3 eV) except in the polar auroral regions. In the auroral regions, an intense, energetic electron flux often precipitates from the plasma sheet. The high altitude plasma is much more energetic; typically 10^5 K (10 eV) for ions and 1 to $5 \times 10^5 \text{ K}$ (10 to 50 eV) for electrons in the solar wind, $\sim 3 \times 10^7 \text{ K}$ (3 kiloelectron volts (keV)) for electrons and $\sim 1 \times 10^8 \text{ K}$ (10 keV) for ions in the magnetospheric plasma sheet. However, the dynamics of the intervening region are such that temperatures can sometimes

be 1 to 2 orders of magnitude higher. Contact of this energetic plasma with the atmosphere produces the aurora.

The boundaries between the other regions are termed the "geopause," where the terrestrial plasma is replaced by the solar wind plasma leaking into the magnetosphere, and the "magnetopause" where the geomagnetic field is replaced by the interplanetary or solar wind magnetic field. At the subsolar point, the altitude of the geopause is just less than the altitude of the magnetopause; however, in the extended tail, the altitude of the geopause is much less than that of the magnetopause owing to the penetration of the solar wind as it moves along the flanks of the magnetosphere. The magnetopause ranges from 6 to 10 Earth radii in the sunward direction to hundreds of Earth radii in the antisunward direction.

4.1 Spacecraft-Plasma Interactions

Plasma interactions can be quite complicated, and there are significant differences between a space vehicle's interactions with the relatively cold, dense plasma of the ionosphere, the hot tenuous plasma at very high orbits, and interactions in the auroral regions where the higher energy plasma characteristic of higher altitudes penetrates to LEO. In all regimes, a spacecraft accumulates electric charge from the plasma in order to establish electrical equilibrium with the plasma, a process called spacecraft charging. Equilibrium requires that no net current be collected by the vehicle. Both the plasma properties and the spacecraft design and operating characteristics influence the process.

The plasma electrons have much less mass than the positive ions. Since, at a given energy, the thermal velocity is inversely related to the particle mass, the thermal electron flux to passive spacecraft surfaces and structure is greater than the corresponding thermal ion flux. As a result, surfaces tend to accumulate negative charge. At low latitudes in LEO, the plasma is relatively dense and of low energy, so equilibrium is established within a few volts negative of the reference plasma potential. Thus, charging of passive surfaces is usually not a problem in this regime. However, for active surfaces, e.g., solar arrays and structure tied electrically to them, arcing and related significant effects can occur, depending upon the grounding scheme and the magnitude of the spacecraft-imposed voltages.

Spacecraft passing through the auroral zone can be charged to large negative potentials by energetic electrons precipitating from the magnetosphere. This is because large surface potentials are required to retard this flux and allow equilibrium (no net current) to be achieved. Also in this region, conditions occur in the wake of large structures, or they may occur naturally so that the entire vehicle is involved, where the low energy plasma density is depleted. This makes it ineffective in balancing the current from the high energy electron flux, and the charging process is enhanced. This is similar to the situation in GEO where the plasma is very energetic but tenuous. In GEO, thermal current densities can be three orders of magnitude less than in LEO, so that photoelectron emission from surfaces can play a significant role in balancing currents to a spacecraft. Sun/shade effects become important to the point that potentials as large as several kilovolts can develop between sunlit and shaded surfaces (depending on geometry and material properties).

4.2 Ionospheric Plasma

The ionospheric plasma is generated principally by photo ionization of the ambient neutral atmosphere and by magnetospheric particles interacting with the thermosphere in the 100 to 200 km altitude region. The transport of the plasma is controlled by the geomagnetic field. Hence, as discussed in Smith and West,¹ the plasma characteristics vary with geomagnetic latitude, altitude, local time, season, and level of solar and geomagnetic activity, but only weakly with geomagnetic longitude. The plasma density drops at night due to the loss of solar UV to maintain the production of free ions and electrons. The plasma density tends to be higher in the equatorial regions than the polar regions, with a dip near the geomagnetic equator. The temperature tends to be about 1000 K during the day, but two to three times that in the morning and evening. The plasmas in the polar regions (above 60° geomagnetic latitude) have a significant contribution from the solar wind and can be more similar to the magnetospheric plasma than to the ionospheric plasma.

4.2.1 Density.¹² Ionospheric structure is generally discussed in terms of three fundamental altitude regimes which differ, in addition to differences in neutral gas properties, in the energy and source regions of the interacting particles precipitating from the magnetosphere. They are referred to as the D (50 to 90 km), E (90 to 160 km), and F (160 to 500+ km) regions. Above the D layer, the neutral gases are in diffusive equilibrium; however, layering of the electron density profile is exhibited within these regions due to competing particle production, loss, and transport processes. The highest electron densities are at the F2 layer peak, 250 to 350 km at midlatitudes and 350 to 500 km at equatorial latitudes. The density in the E layer, typically located at 100 to 120 km altitude, is an order of magnitude less than the F2 layer peak. Under certain conditions, a valley or an F1 ledge can be observed between these two layers. The density in the D layer, below the E layer peak, decreases rapidly with decreasing altitude. In the D layer, ionization is primarily caused by solar x rays and depends strongly upon the solar zenith angle. The highest values, 10^8 to 10^9 m⁻³, occur during summer noon. Below about 70 km altitude, ionization by cosmic rays is the major electron source; therefore, the electron density is negatively correlated with the solar cycle below 70 km and positively correlated above.

The E layer is composed primarily of AO ions and electrons, the result of ionization by solar EUV radiation. The daily maximum is near noon, the seasonal maximum is in the summer, and density varies directly with solar activity. The nighttime density is more than an order of magnitude less than the daytime due to recombination. Although thin and patchy, a sporadic E layer, Es, with a density that can exceed the E and F2 peaks, occurs irregularly.

The F region consists of the overlapping F1 and F2 layers. The F1 layer, at about 150 to 200 km altitude, is of lesser importance. It is under strong solar control. The density distribution in the F layer in general is determined by transport processes, ambipolar diffusion, electrodynamic drift, and neutral wind drag, because neutral densities decrease rapidly with increasing altitude. Therefore, the F2 layer peak and the topside ionosphere are highly variable, 10 to 30 percent day to day. The F2 layer peak density maximizes in the afternoon in winter. There are two crests at $\pm 15^\circ$ magnetic latitude with a minimum at the magnetic equator in a latitudinal profile of the F layer. At night and higher altitudes, the two crests merge into a single crest at the magnetic equator. The so-called "fountain effect" causes this "equatorial anomaly." The charged particles are pushed upwards by the equatorial electric field where they then drift downward along magnetic field lines.

At high latitudes, the ionosphere is strongly coupled to the magnetosphere and to the solar wind. The transition from closed to open field lines and the influx of energetic particles profoundly

affect the ionospheric plasma. The boundary region, the auroral oval, is marked by the beautiful display of auroras. Surrounding the magnetic poles, the oval extends to near 75° geomagnetic latitude noon and 65° at local midnight. On the night side, the oval is well marked by a depletion in electron density, the so-called trough. On the dayside, one finds a region of enhanced densities just inside the oval, the so-called magnetospheric cleft. The electron density at the tip of the cleft is almost an order of magnitude greater than it is at the bottom of the trough. During magnetic storms, the trough moves equatorward 2° per unit increase in K_p . The region inside the oval is called the polar cap.

A wide variety of ionospheric irregularities have been observed, predominantly at high latitudes and during the equatorial nighttime. The plasma fluctuations range in scale from hundreds of kilometers down to centimeters. Plasma instabilities play an important role in the generation of medium-scale (kilometers) and small-scale (meters) irregularities. Examples of irregularities are patches of enhanced ionization in the E region (sporadic E) and of depleted ionization in the F region (spread F). Spread F is most frequently observed in the equatorial nighttime ionosphere. The irregularities cause signal fluctuations in traversing radio waves, known as scintillations.

Influx of solar plasma into the tail of the magnetosphere, sometimes preceded by solar flare, can cause complex ionospheric disturbances (storms). The most consistent pattern is an enhancement in D region ionization. These effects are most dramatic at auroral latitudes, but significant modifications in the ionosphere occur at all latitudes. A particularly severe event, called a polar cap absorption (PCA) event, is due to protons arriving from the Sun and causing a radio communication blackout over a considerable time period.

4.2.2 Temperature. The main source of energy for the terrestrial ionosphere is EUV radiation from the Sun. The electrons are heated most efficiently, and their temperature exceeds the temperatures of the ions and neutrals. Electron temperatures increase from about 300 K at 100 km altitude to about 3500 K at 800 km altitude. Ion temperatures are close to the neutral temperature below about 400 km altitude and increase toward the electron temperature above that altitude. Below 150 km altitude, the high neutral densities and the high collision frequencies result in the same temperature for electrons, ions, and neutrals. During nighttime, the temperatures of all species are close together.

In general, plasma temperatures are lowest at the geomagnetic equator and increase toward higher latitudes, due to the increased influence of heating by precipitating particles at auroral latitudes. At low altitudes, however, the electron temperature peaks at the magnetic equator, reaches minimal values at about $\pm 20^\circ$, and then increases toward higher latitudes. This behavior is the mirror image of the equatorial anomaly of the electron density and illustrates the strong anticorrelation between electron density and temperature.

Roughly speaking, the temperatures increase from an almost constant nighttime value to an almost constant daytime value. The most significant departure from this behavior is the early morning peak in electron temperature. It is most pronounced at the magnetic equator at about 300 km altitude (the peak temperature exceeds the daytime value by a factor of 2 to 3); its magnitude decreases rapidly toward higher and lower altitudes and toward higher latitudes. The temperature peak is a result of the sharp increase in solar heating coupled with the still low electron densities from the preceding night.

The electron temperature is almost unaffected by the solar cycle, in contrast to the increase of almost all other neutral and ionized parameters. This again is a result of the close coupling with the

electron density which determines both energy gain and loss of the electron gas. The simultaneous increase of both terms leaves the electron temperature nearly unchanged.

4.2.3 Dynamics. The Sun-induced thermospheric winds provide the energy source needed to drive the so-called ionospheric dynamo which maintains the system of ionospheric currents and fields. On the sunlit side of the Earth, two large vortices of electric current exist in the quiet equinox ionosphere, the current flows counterclockwise in the northern hemisphere and clockwise in the southern hemisphere (Sq currents). The concentrated current at the magnetic equator represents the equatorial electrojet. Magnetic storms severely affect thermospheric winds and ionospheric currents. The thermospheric winds and ionospheric drifts are of the order of 100 m/s and can reach 1000 m/s and more during magnetic storms. Ionospheric current densities are of the order of $10 \mu\text{A m}^{-2}$ and electric fields are of the order of 10 mV m^{-1} . The Earth's magnetic field strength is typically 3×10^{-5} Tesla at ionospheric altitudes.

The solar wind blowing past the Earth's magnetic field creates a magnetospheric dynamo which drives plasma across the polar cap. The empirically found dependence of the auroral plasma convection on solar wind parameters illustrates the strong coupling between the solar wind and the high latitude ionosphere.

4.2.4 International Reference Ionosphere 90 (IRI90). A computer code, IRI90, that describes the ionosphere in the 85 to 1000 km altitude range for geomagnetic latitudes up to about 60° (the auroral zones) is available (ref. C). It calculates monthly mean electron and ion species (H^+ , He^+ , O^+ , NO^+ , and O_2^+) densities and temperatures as a function of latitude, longitude (geomagnetic or geocentric), time of day, day of year, altitude, and solar $F_{10.7}$ radio flux. (However, the model has not been extended to cover the ionosphere during the intense solar maximum of the current solar cycle.) The error bars on the model during quiet times are a factor of 2 to 4 of the indicated values at altitudes below the F2 peak, and these are primarily the result of small scale variations in the ionosphere. Above the F2 peak, problems with the scale height could lead to error bars of up to a factor of 10.

The IRI90 was used to generate figures 4-1 and 4-2 which show global density and temperature contours at 400 km altitude on June 21, approximately the summer solstice. Figures 4-3 and 4-4 show the variation of density and temperature with altitude. IRI90 is an updated version of earlier models (Bilitza, 1986) which adds several new options but retains the general character and range of parameters from the previous editions. Since the different options are suitable to different applications, care should be exercised in their selection.

4.3 Auroral Oval Plasma

As mentioned previously, the aurora is primarily produced by high-energy charged particles precipitating into the atmosphere along magnetic field lines. One result of these fluxes is the increase of local plasma density by factors of up to 100 over regions of tens of kilometers in latitudinal dimension and hundreds or thousands of kilometers in longitudinal dimension in the auroral regions (60° to 70° magnetic latitude). These enhancements occur between about 100 and 250 km altitude (fig. 4-5). Above 250 km, the thermal plasma may be depleted above intense auroral in the midnight sector, falling far below $1.0 \times 10^{10} \text{ m}^{-3}$. In this region, there is no clear distinction between magnetospheric and ionospheric phenomena. There is a very wide range of scales, both spatially and temporally, in the dynamics present. Small-scale (meters to decameters) irregularities exist and

move with the prevailing ambient plasma drifts. Ion-ion and ion-neutral collisions in the lower thermosphere tend to make the temperature distribution isotropic while anisotropies still remain at higher altitudes (near 600 km). Plasma property anisotropies are introduced by the geomagnetic field.

4.3.1 Global Morphology. The conditions in the magnetosphere depend on whether B_z , the component of the interplanetary magnetic field (IMF) normal to the ecliptic plane with positive values northward, is directed northward or southward. There are three distinct magnetospheric states: (1) the quiet state, (2) the active polar cap state, and (3) the active auroral oval state.

4.3.1.1 The Quiet Magnetosphere. In this state, the energy input from the solar wind is minimized by a configuration that minimizes magnetic recombination on the dayside. A weak but northward IMF B_z is typical. The auroral oval has the following characteristics:

- (a) Visually small in diameter and circular
- (b) Somewhat expanded near the dawn and dusk regions
- (c) Relatively thin near midnight.

4.3.1.2 The Active Polar Cap State. At this time, characteristics of this state are still controversial, and more detailed observational data are required before a consensus can be reached. However, it is believed that it occurs during strongly northward IMF B_z conditions and is characterized by the presence of:

- (a) Sun-aligned arcs
- (b) Additional magnetic-field-aligned current systems
- (c) Distortions or disruptions in the traditional two-cell polar convection patterns.

4.3.1.3 The Active Auroral Oval State. The southward IMF B_z plays a prominent role in this state. Auroral boundaries are active, with rapid poleward movement of the poleward boundary and less rapid equatorward movement of the equatorward boundary during the expansion phase of magnetic substorms. Although there is some controversy, it appears as if the optical signature of this poleward movement ends before the ground signature of the electrojet activity ceases. The equatorward particle precipitation boundaries move equatorward with increasing geomagnetic activity. The ion boundaries are equatorward of the electron boundaries in the disk/evening sector, while the electron boundaries are ahead in the morning sector. The electron boundaries are equatorward of the ion boundaries at all local times except the disk when the geomagnetic activity is very low—very quiet times.

Auroral features are also very active in this state. During the expansion phase of an auroral substorm, the poleward and equatorward motions of the nighttime auroral can begin at localized sites in local time, primarily between 2200 and 2400 h local time. Sometimes an "eye-shaped" structure with substantial north-south structures embedded can form as the expansion proceeds in the east-west as well as north-south directions. The configuration of the east-west expansion is a function of the condition of the IMF. At the most extreme portion of the poleward expansion, the arcs can intensify rapidly and form vortices along the arc's length. Westward traveling surges (WTSs)

have been observed to propagate nearly 7000 km. Sometimes WTS activity is the predominant auroral response to substorm activity.

4.3.1.4 Electrodynamics and Convection. There are many statistical or empirical, as well as several theoretical, models of the convection and/or electric fields in the auroral zones. Specific use will dictate which model should be used in engineering analyses. Most of these models stress the importance of the IMF B_y , the dawn-dark component of the IMF, in controlling the dayside convective patterns. Results of analyses have shown that substantial structure can be present within the distribution of field-aligned currents. Results of studies have also shown that:

(a) In the morning sector, the westward electrojet is dominated on the poleward side by strong electric fields (with low auroral luminosity and conductivity) and on the equatorward side by large conductivity values. The equatorward side is also the region of precipitating electrons (upward electrical currents).

(b) On the evening side in the eastward electrojet, the reverse trend is observed.

(c) The westward electrojet is also centered in the region of highest auroral luminosity, while the eastward electrojet is in the region of the lowest luminosity.

(d) The brightest auroral regions are associated with upward electrical currents, both in the evening and morning sectors.

(e) The polar cap potential is modified rapidly by changing IMF conditions; however, the nightside auroral zone response is delayed substantially.

(f) Conductivity gradients play crucial roles in the formation of auroral surges.

Once again, understanding of the characteristics of the global aurora is progressing rapidly. However, there are many differences between models and observational data, and the use of any empirical/statistical/theoretical model will be highly dependent upon the application. Care should be utilized in the selection of the "proper" model and experts in the field should be consulted.

4.3.2 Aurora Morphology. Aurora occur in all three altitude regimes, D, E, and F, with the E layer dominant in terms of total auroral precipitation energy. Electron density profiles in the auroral region are dependent upon the energy distribution of the incident precipitating particles, while the auroral emissions are dependent upon the photochemistry of the auroral ionosphere as well as the energy distribution of the precipitating particles. The spectrum of the precipitating particles determines the altitude at which the particle energy is deposited and, therefore, the applicable photochemistry, since neutral composition and density depend strongly on altitude. Enhanced electron densities are produced by impact ionization due to precipitating electron fluxes. The auroral E region extends about 2° farther equatorward than the F region, and this extension is formed by proton precipitation, in contrast to the mainly electron precipitation that forms the F region. There is a strong seasonal and universal time (UT) control of the auroral ionosphere.

The aurora occurs at all local times in the auroral ovals that are rings at about 65° magnetic latitude around each magnetic pole. The most intense and energetic fluxes occur near local midnight. The location of the aurora and its intensity vary with solar (and resulting magnetospheric) activity. Figures 4-6 and 4-7 illustrate the spatial distribution. Global plots of the average integral energy

flux and the average energy of precipitating electrons are presented in polar spectrogram format in a magnetic local time-corrected geomagnetic latitude coordinate system for each of four levels of K_p . Plots apply to both poles. A statistical analysis of the probability of encountering various levels of aurora particle flux may be found in McNeil et al.,¹³ and a detailed discussion of auroral morphology may be found in Jursa (ref. F).

In the dayside auroral zone, magnetic field lines extend to the dayside magnetopause and provide fairly direct access for the solar plasma to the topside ionosphere. The solar plasma strongly heats and drives winds in the day side auroral ionosphere, generally in the direction away from the Sun and across the polar cap toward the nightside. The strong ionospheric heating associated with this process generates the largest outflows of ionospheric plasma anywhere at the Earth and forms a global scale "ion fountain" across the polar cap. Global electric systems flow along magnetic field lines into and out of the auroral ionosphere. Where these are most intense and in the upward direction, they exceed the capacity of the plasma to carry them with thermal motions, and discharges occur in which electrons are accelerated downward and ions are accelerated upward. These discharges greatly enhance the brightness of the aurora where the electrons are incident and produce outward flowing ion beams which are far out of local thermodynamic equilibrium and unstable, generating natural plasma wave noise at a variety of frequencies.

4.4 Polar Cap Plasma

In the polar cap, the differences between magnetosphere configurations are more pronounced than in the auroral oval region. The configurations depend on whether B_z , the IMF component normal to the ecliptic plane with positive values northward, is directed northward or southward. Current understanding of the polar cap convection under southward IMF conditions is well developed even though the convection is complex and multiple flow entry regions exist. However, observed traveling convection vortices in the polar cleft region are inconsistent with present-day current-closed models.

4.4.1 Ionosphere and Polar Wind. Density structures in both the E and F regions show that in darkness the ratio of enhanced density to the background density remains constant for many tens of hours and that the vortices only disappeared when they were convected into regions of sunlight or auroral precipitation. There are systematic differences between the winter electron density signatures in the topside ionosphere in the southern and northern polar regions with the southern hemisphere having the lower densities. The region above the polar ionosphere contains mainly ionospheric plasma flowing generally away from the Sun across the polar cap and upward into the magnetosphere. Only weak fluxes of energetic components of the solar wind plasma enter the polar cap region, sometimes referred to as "polar rain." The light ion component of the ionospheric plasma, which flows upward into the magnetosphere even without solar wind energy inputs, is referred to as the polar wind. The heavy ion component responds to energy inputs from the solar wind, to heat-driven thermospheric dynamics, the solar cycle in UV inputs to the thermosphere, and magnetic activity. This combined light and heavy ion source of plasma to the magnetosphere provides much of the material from which the energetic particle populations are generated. Theoretical research on this area has shown that results are highly model dependent and that two-dimensional models produce different results than three-dimensional models. Caution in use of models is strongly advised.

The polar cap region becomes active with Sun-aligned auroral arcs when the IMF is northward. Field-aligned electrodynamic systems which close in the ionosphere are associated with

these arcs. Plasma drift inside the arcs is primarily antisunward, while outside the arcs both sunward and antisunward drifts occur.

Models of the ionosphere have not progressed to the point where they can be used for reliable forecasts of future conditions especially those related to magnetic storm and substorm dynamics. Major questions of convection patterns are still unanswered. Even the static conditions predicted by the IRI90 model frequently do not match observational data. Great care must be exercised in the use of all ionospheric models.

4.5 Geosynchronous Altitude Plasma

The geosynchronous altitude plasma environment is very complex and dynamic. The fluxes in GEO can be quite energetic and are highly variable with magnetic activity especially during geomagnetic substorms. The values given in table 4-1 are an estimate of the 90th percentile worst charging case environment assuming a single Maxwellian representation of the environment. Figure 4-8 provides a recommended time variation sequence suitable for modeling the worst effects of a geomagnetic storm.¹⁶

Table 4-1. Worst-case plasma environment in geosynchronous Earth orbit.

Electron number density, n_e m ⁻³	1.12 E ⁶
Electron temperature, T_e , eV	1.2 E ⁴
Ion number density, n_i m ⁻³	2.36 E ⁵
Ion temperature, T_i , eV	2.95 E ⁴

4.6 Transient Fluxes in Low Earth Polar or Geosynchronous Orbit

In polar LEO, the important transient and energetic fluxes occur in the auroral zone. Figure 4-9 shows typical aurora fluxes from rocket measurements at about 320 km, and figure 4-10 shows extreme values for space vehicle design derived from satellite measurements made at 840 km. Distribution functions of electrons (left) and ions (right) for very intense auroral fluxes are shown in figure 4-10. These particles are not very penetrating but may be significant for charging at altitudes above 250 km.

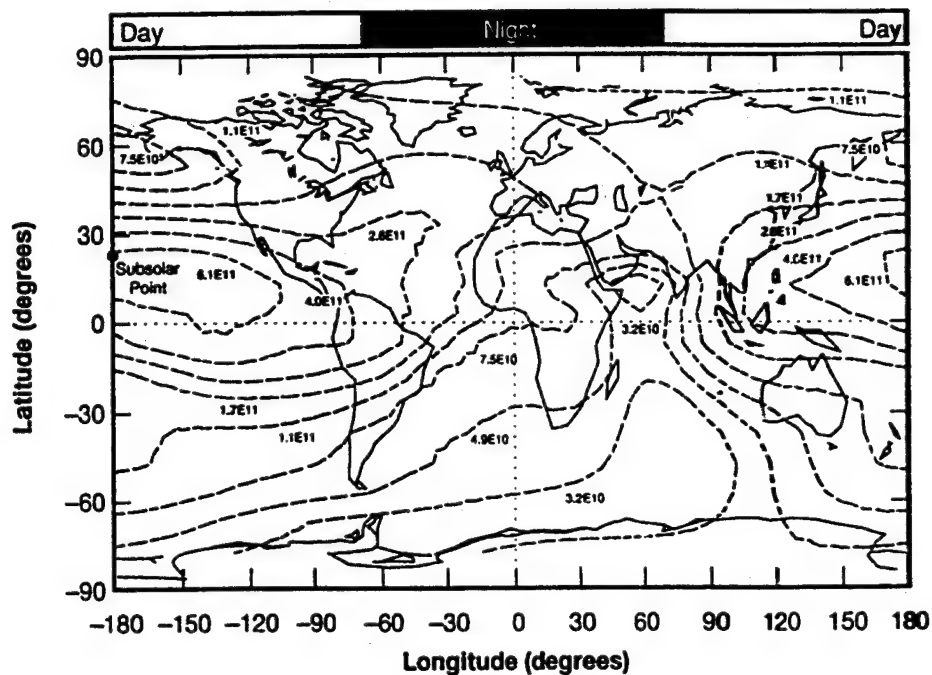


Figure 4-1. Plasma density (m^{-3}) at 400 km for June 21 and solar minimum conditions ($F_{10.7} = 70$, 0:0:0 G.m.t., results from IRI90 with default options selected).

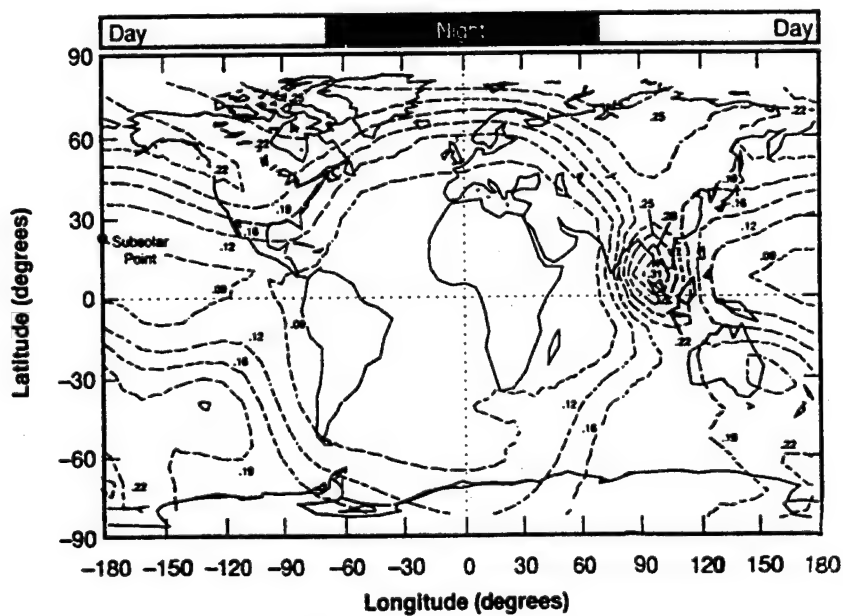


Figure 4-2. Electron energies (eV) at 400 km for June 21 and solar minimum conditions ($F_{10.7} = 70$, 0:0:0 G.m.t., IRI90 results with default options selected).

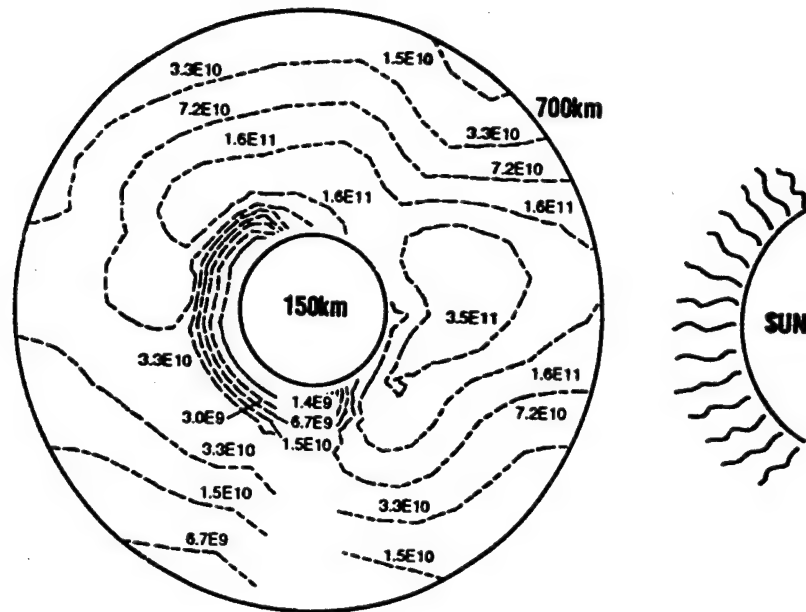


Figure 4-3. Noon-midnight cross section view of plasma density (m^{-3}) as a function of altitude from 150 to 700 km for June 21 and solar minimum conditions ($F_{10.7} = 70$, contours in the 0° and 180° longitude plane, IRI90 results with default options selected).

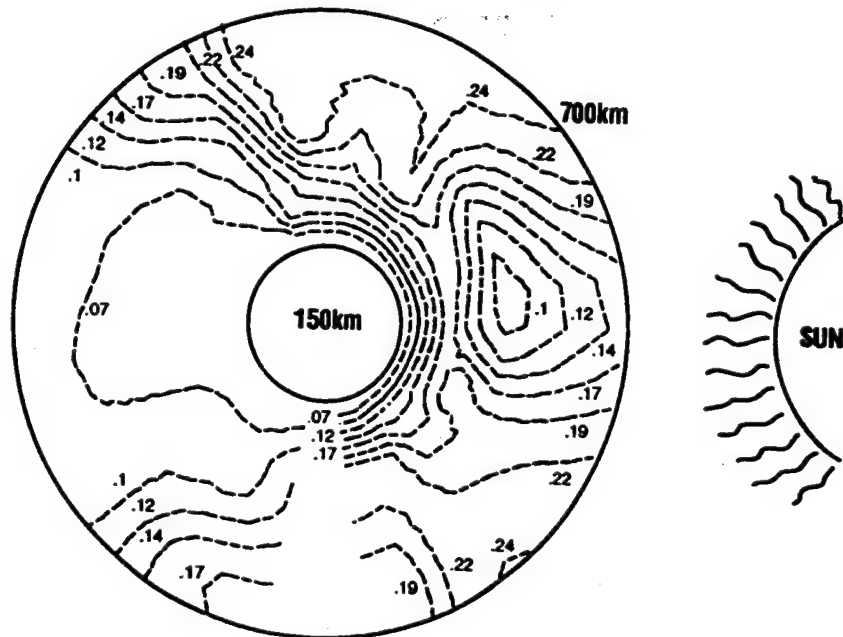


Figure 4-4. Noon-midnight cross section view of electron energy (eV) as a function of altitude from 150 to 700 km for June 21 and solar minimum conditions ($F_{10.7} = 70$, contours in the 0° and 180° longitude plane, IRI90 results with default options selected).

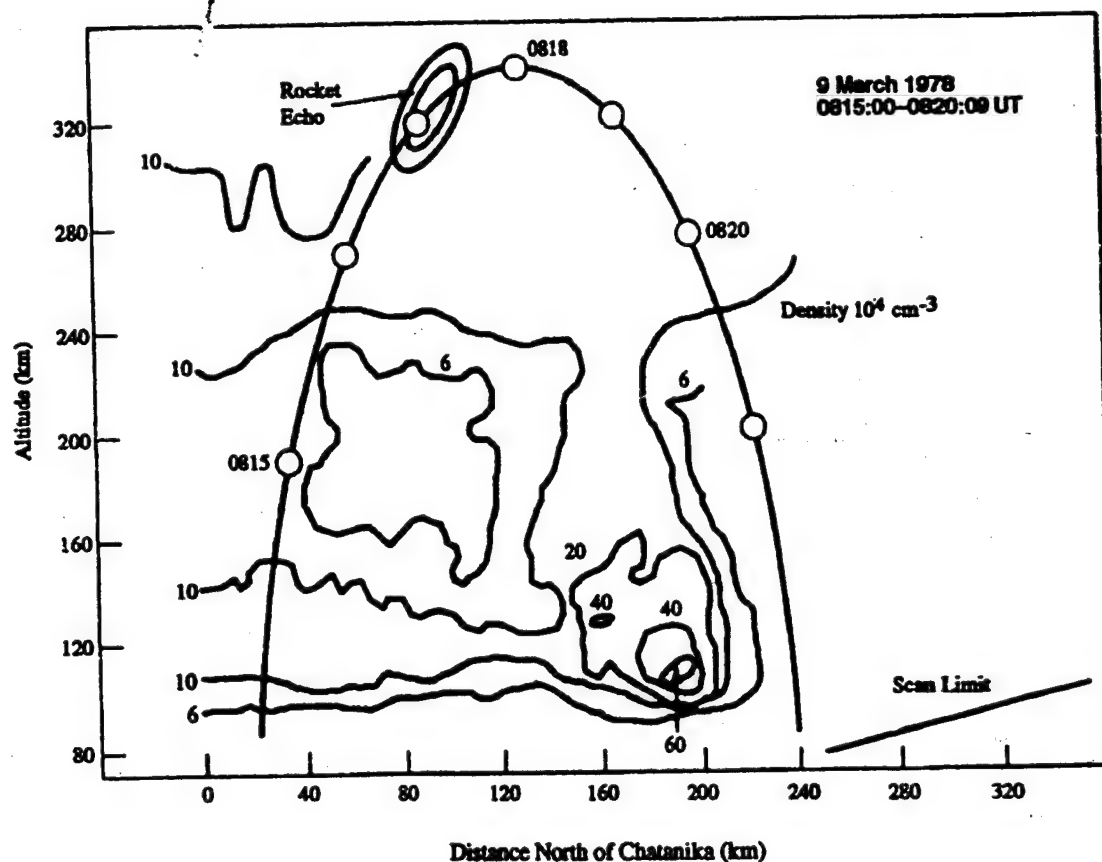


Figure 4-5. Ionospheric electron density in an aurora ($\times 10^4 n_e/\text{cm}^3$).¹⁴

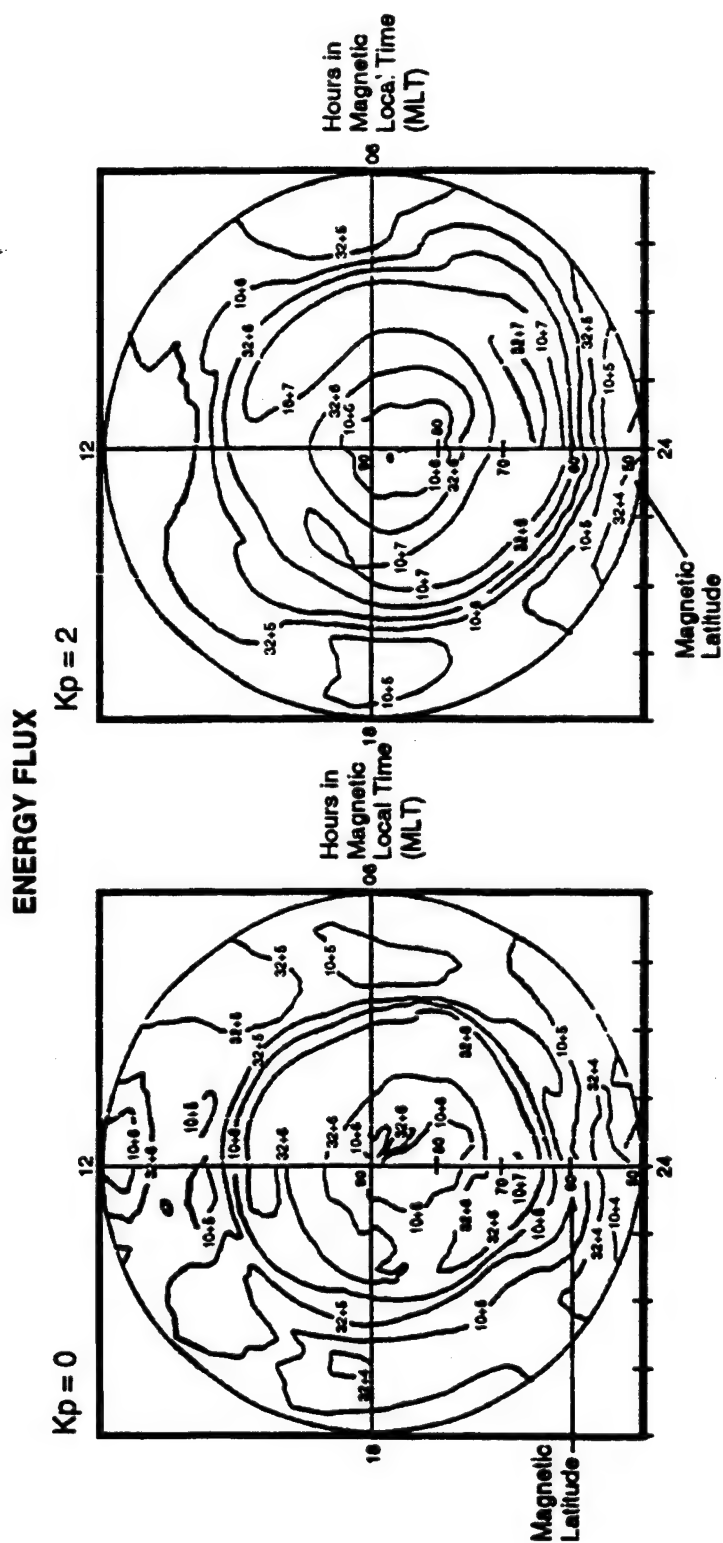


Figure 4-6. Global plots of the average integral energy flux ($\text{keV}/\text{cm}^2 \text{ s sr}$) of precipitating electrons are presented in polar spectrogram format, in a magnetic local time corrected geomagnetic latitude coordinate system, for four levels of K_p . Plots apply globally to both poles (page 1 of 2).¹⁵

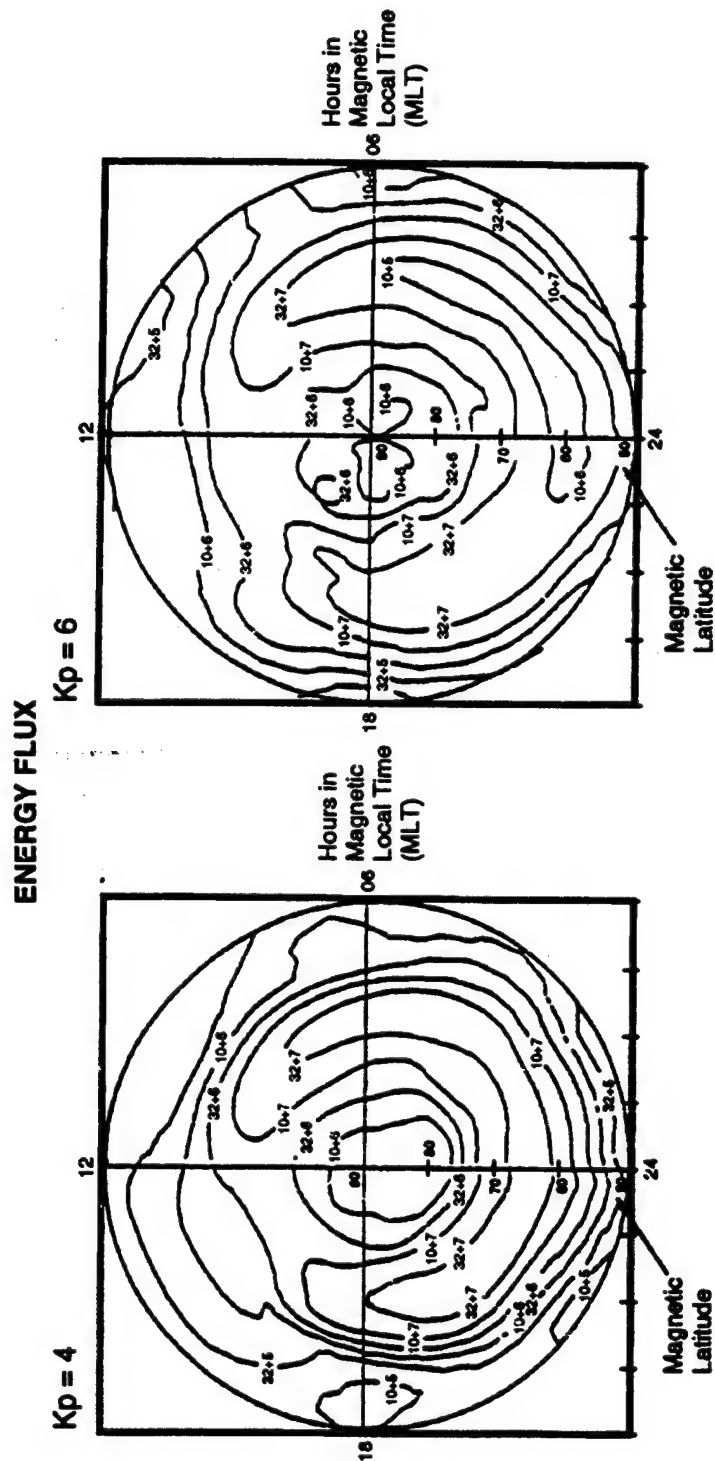


Figure 4-6. Global plots of the average integral energy flux ($\text{keV}/\text{cm}^2 \text{ s sr}$) of precipitating electrons are presented in polar spectrogram format, in a magnetic local time corrected geomagnetic latitude coordinate system, for four levels of K_p . Plots apply globally to both poles (page 2 of 2).¹⁵

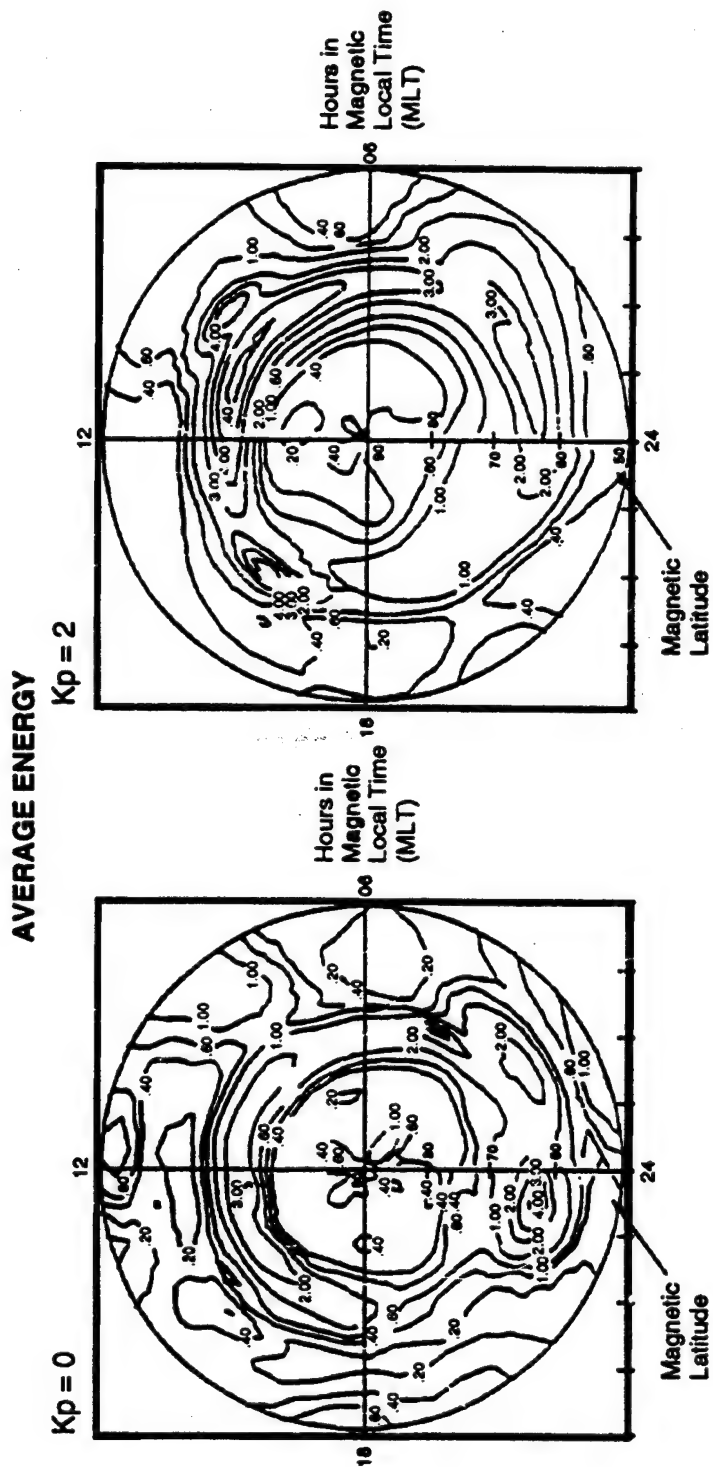


Figure 4-7. Global plots of the average energy (keV) of precipitating electrons are presented in polar spectrogram format, in a magnetic local time corrected geomagnetic latitude coordinate system, for four levels of K_p . Plots apply globally to both poles (page 1 of 2). 15

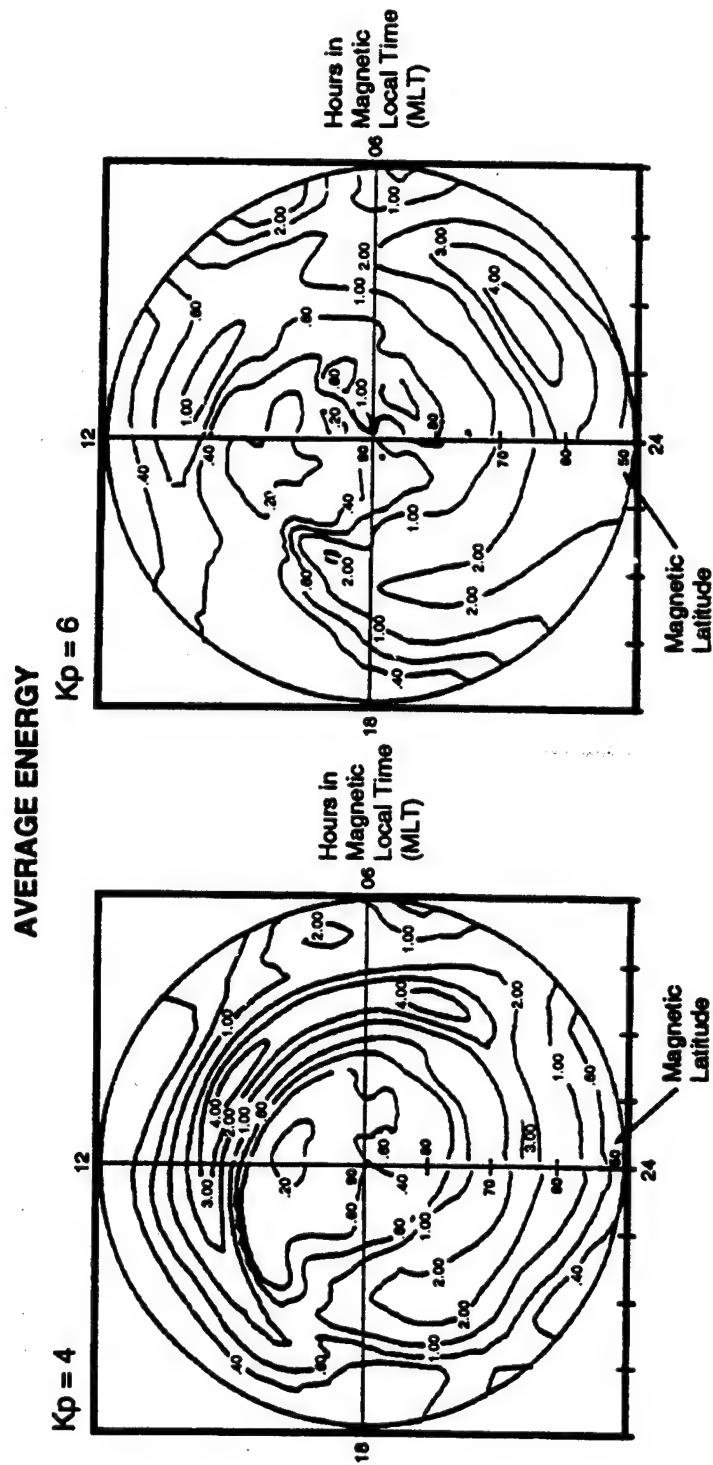


Figure 4-7. Global plots of the average energy (keV) of precipitating electrons are presented in polar spectrogram format, in a magnetic local time corrected geomagnetic latitude coordinate system, for four levels of K_p . Plots apply globally to both poles (page 2 of 2). 15

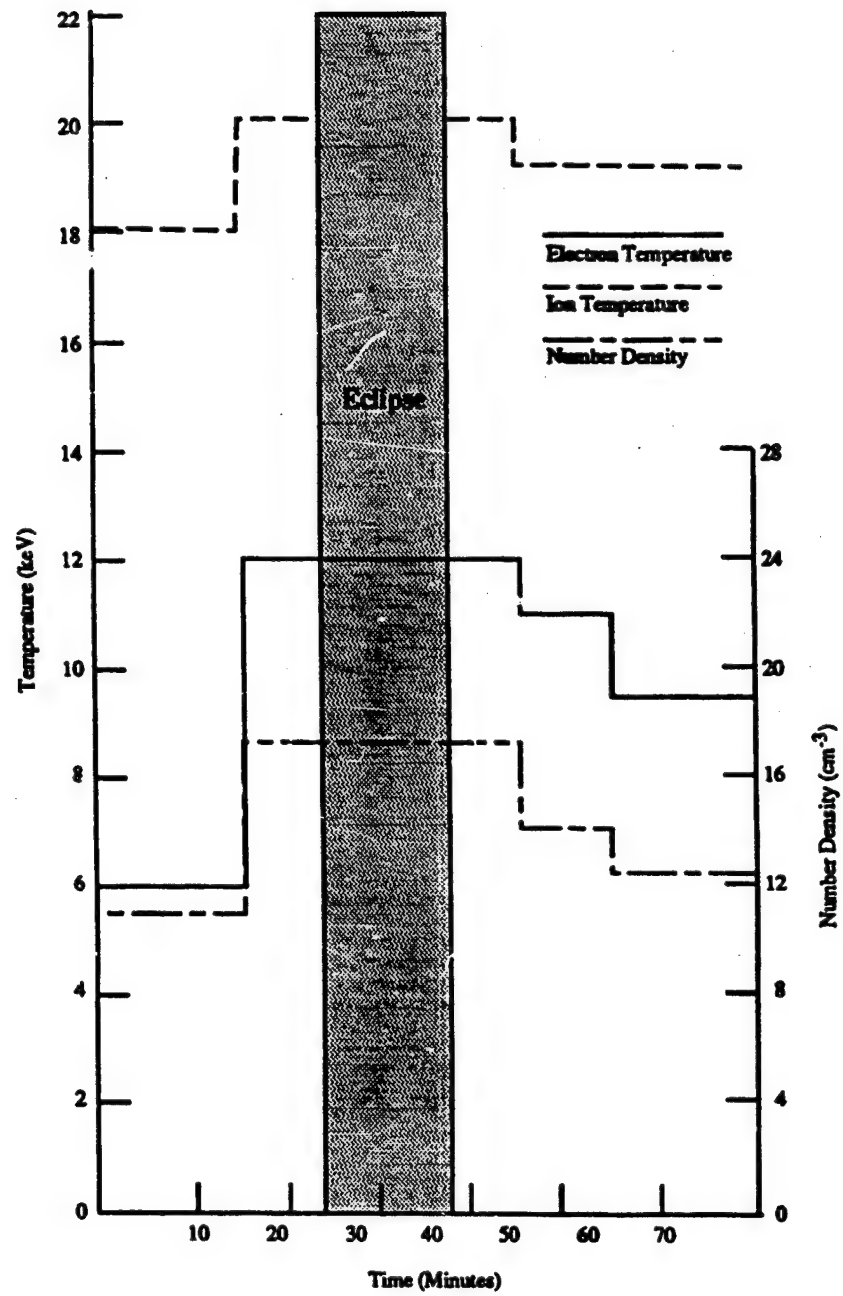
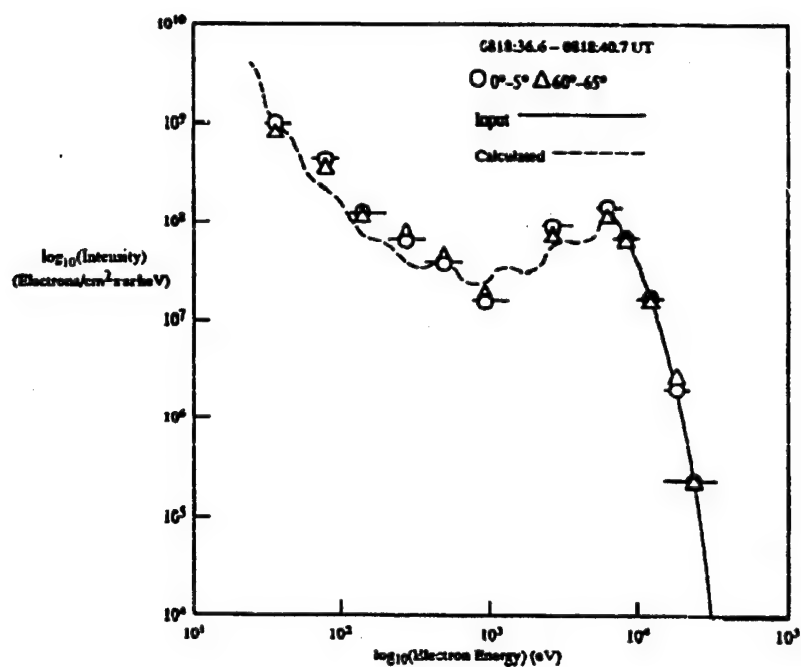
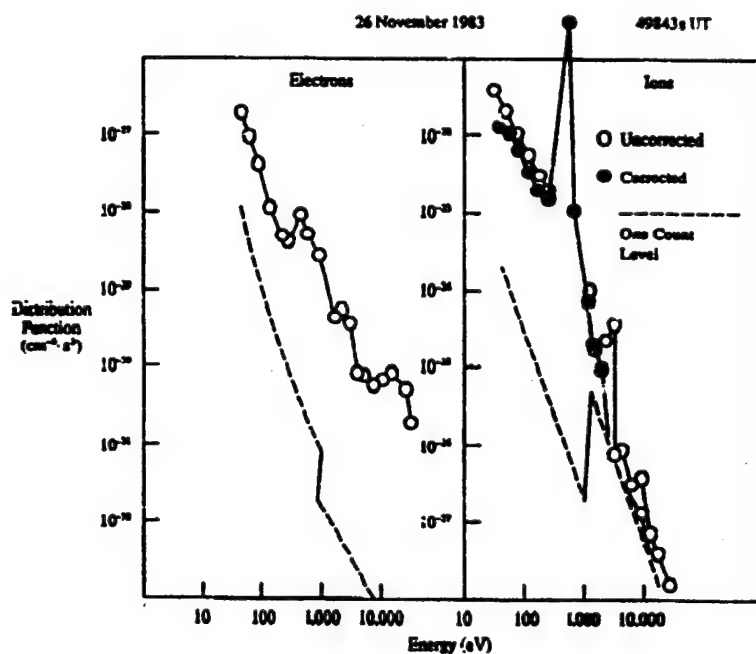


Figure 4-8. Time history of model substorm-geosynchronous plasma environment.¹⁶

Figure 4-9. Auroral electron intensity (center of arc).¹⁷Figure 4-10. Distribution functions of electrons (left) and ions (right) for very intense auroral fluxes.¹⁸

V. PENETRATING CHARGED PARTICLES

Penetrating charged particles, often referred to as charged-particle radiation or corpuscular radiation, presents a significant challenge to the design and operation of a spacecraft. This is because many of the particles have sufficient energy to penetrate several centimeters of metal and to produce significant levels of ionization inside the spacecraft. A high level of radiation will significantly affect materials, chemical processes, and living organisms, especially the crew. It will also affect electronics by (1) causing soft upsets (referred to as single event upsets (SEUs)), (2) degrading performance, and (3) producing permanent damage. In addition, ionizing radiation will affect the propagation of light through optical materials by altering their optical properties. The quantitative relationship between the amount of ionization and the effects depends upon the nature of the radiation in a complicated way.

It is convenient to divide the charged particles into two groups: magnetospheric particles and cosmic rays. Magnetospheric particles are accelerated from thermal, low-energy plasma by processes inside the magnetosphere and occur only within terrestrial space. Cosmic rays exist in interplanetary space and, therefore, enter terrestrial space from outside. Within terrestrial space, the motion of both kinds of charged particles is controlled by the geomagnetic field.

5.1 Magnetospheric Particles

5.1.1 Trapped Radiation. These particles are trapped in the geomagnetic field and perform many oscillations between hemispheres and around the Earth during their lifetime. (Other terms for these particles are durably trapped, geomagnetically trapped, or Van Allen radiation.) The range of energies is rather large and is centered in the tens of keV for electrons and MeV for protons. The fluxes are generally stable in time except during great magnetic storms, and the isoflux contours have axisymmetry around the Earth. (More precisely, the flux in three-dimensional space may be mapped into a function of two variables: field strength B and L or B and λ . The L -shell value is defined in section VIII of this document. This means that the flux contours in a meridian plane can represent the entire three-dimensional morphology.) Both protons and electrons occur (see reference 1 for a general discussion).

Trapped radiation is composed of both protons and electrons. These particles may originate on the Sun, in the atmosphere, or may be produced by cosmic ray albedo neutron decay. Decaying neutrons projected upward from the atmosphere are the major source for trapped protons. Once they have been generated, they are guided and transported by geomagnetic and electric fields. In the absence of fluctuations, the particles retain their energy and move in stable orbits on a constant L shell. Particles leave the radiation belts when they collide with the neutral atmosphere. This is more likely to occur the deeper an orbit penetrates into the neutral atmosphere.

The general shape of the Van Allen belts follows the shape of the geomagnetic field. This means that a space vehicle penetrates most deeply into the belts in the region of the South Atlantic Anomaly. Because the flux is increasing with altitude in the region of 300 to 1000 km, the most intense radiation is encountered in the anomaly, as shown in figure 5-1. The distributions of electron and proton fluxes in a meridional plane are shown in figures 5-2 and 5-3, and the profile of proton flux with altitude at solar minimum is shown in figure 5-4. The very steep inner gradient is controlled by the exact altitude dependence of the neutral atmospheric density which varies with solar activity. The atmosphere is more extended (higher density at a given altitude) when the Sun is active. Thus, at 500 km, the trapped proton flux is greater when the Sun is quiet. The profile at the inner edge is primarily controlled by the atmosphere modulated by solar activity. These changes do not show clearly on the figures listed above. However, they can be shown by a contour plot against B and L as shown in figure 5-5.

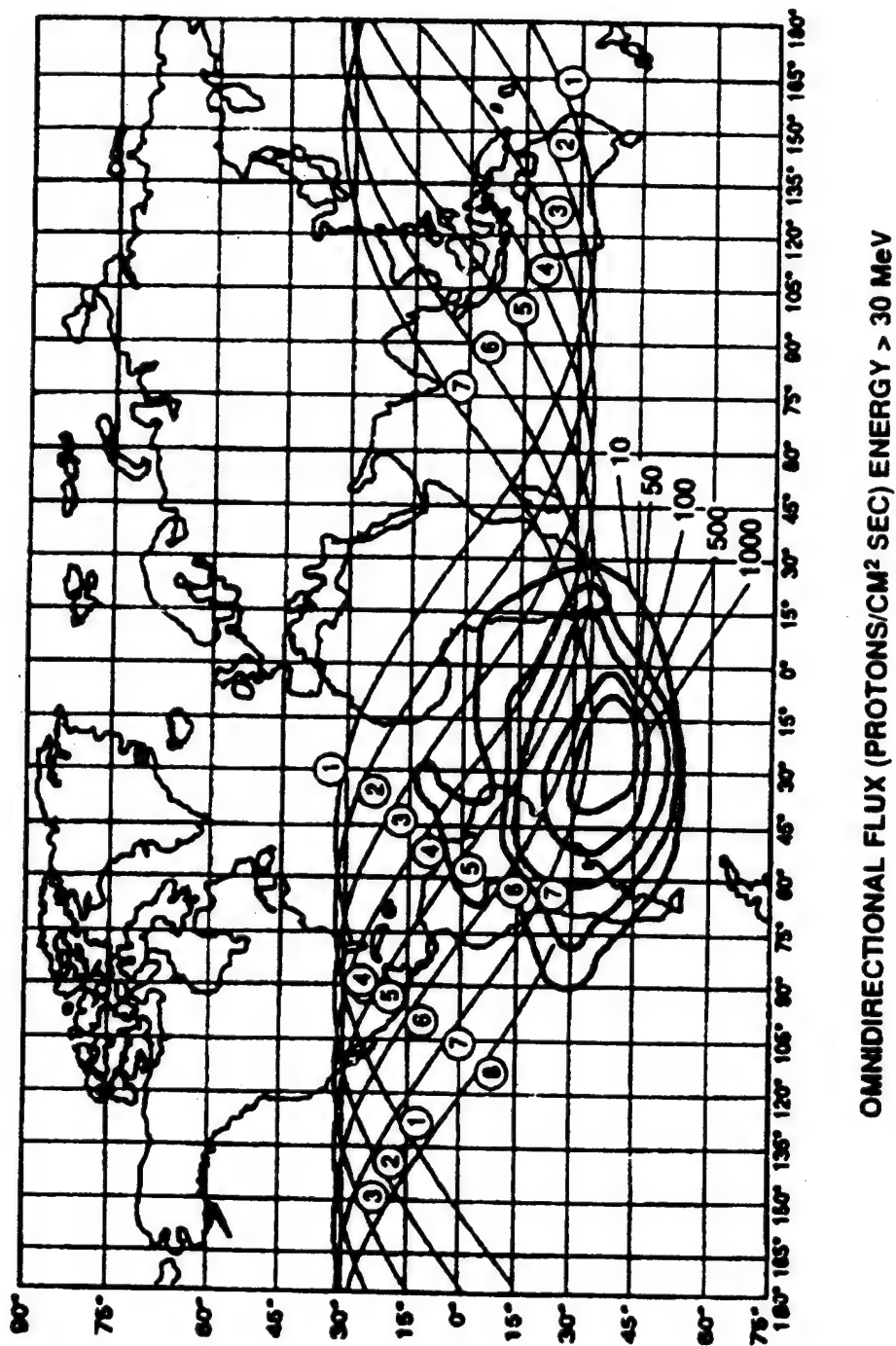


Figure 5-1. Proton flux densities at an altitude of 296 km in the South Atlantic Anomaly.
This is a region of low magnetic field strength.

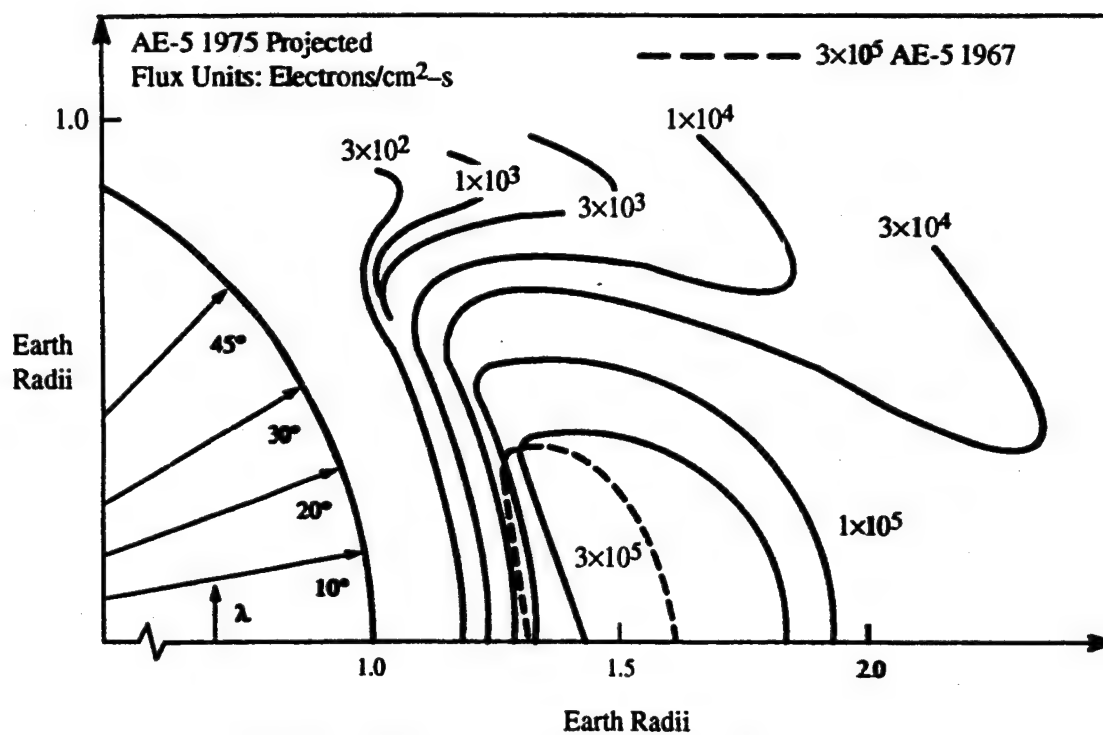


Figure 5-2. Omnidirectional isoflux contours of 1-MeV electrons: R - λ projection.

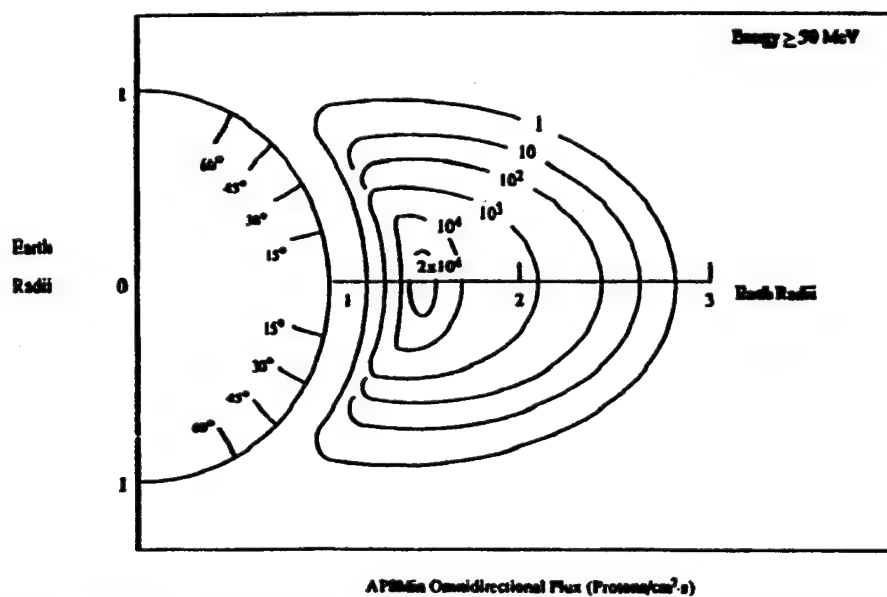


Figure 5-3. AP8Min R - λ plot of isoflux contours of protons with an energy of ≥ 50 MeV.

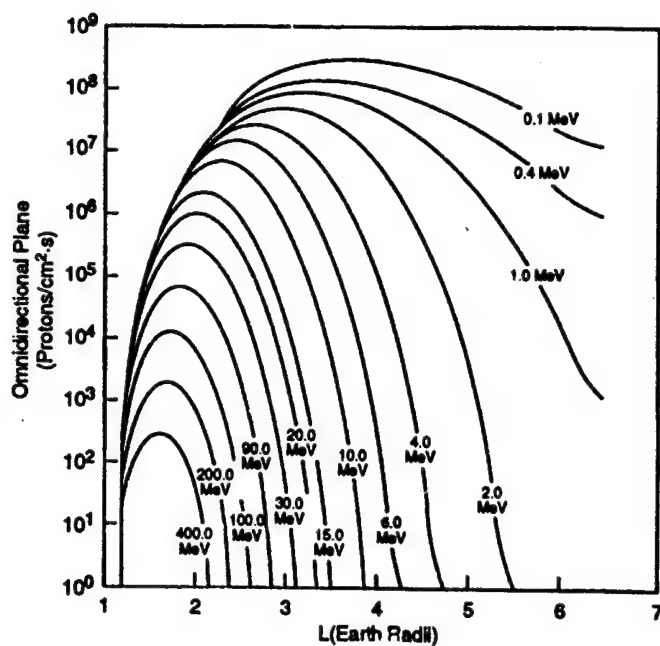


Figure 5-4. AP8Min equatorial omnidirectional radial profiles of proton flux at energies between 0.1 and 400 MeV.

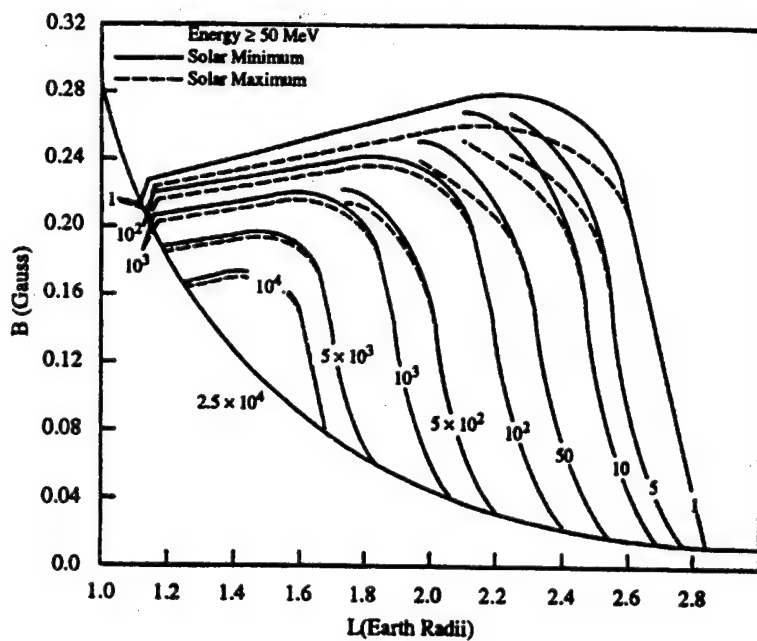


Figure 5-5. AP8Min and AP8Max B - L plot of constant intensity flux contours of protons with an energy of ≥ 50 MeV.

The trapped flux environment at solar maximum and minimum is defined by the computer codes AP8MAX and AP8MIN for protons and AE8MAX and AE8MIN for electrons.^{19 20} These computer codes are available upon request. It is essential that the magnetic field used with the proton models be the model of 1965 (Epoch, 1964), i.e., IGRF 1965 80-term projection to 1964 model using the coefficients in table 5-1, for solar minimum and 1970 (Epoch, 1970), i.e., the Hurwitz US C&GS 1970 field and the coefficients in table 5-2, for solar maximum.²¹ Use of current (1991 model) field values, or those projected for the 1990's, will give flux values far higher than real at projected operating altitudes. This is because the Earth's field is decaying, which lowers the mirror point altitudes, resulting in loss of particles to the atmosphere at these low altitudes. Since the magnetic moment value of 0.31165300 was only appropriate near 1960, the ALLMAG routines²¹ for computing B and L and the ORP program for looking up fluxes in the AP and AE models must be modified by replacing the constant magnetic moment value with the following:

$$M = (G_{12}^2 + G_{22}^2 + G_{21}^2)^{1/2} / 100\,000 \quad (5-1)$$

where G_{mn} are the field expansion coefficients. The revised computer code is available upon request.

In calculating total dose in LEO, it will be found that trapped protons contribute nearly the entire amount with three exceptions: at the lowest altitudes (below about 300 km), the contribution from trapped particles becomes so small that galactic cosmic rays (GCRs) make the largest contribution. For very thin shields (<0.3 g/cm²), trapped electrons are more important than trapped protons. At high inclination orbits, solar flare event particles make significant contributions. To repeat, because of the rapid variation with altitude, it is essential that the correct numerical models be used with the correct input parameters. It should be borne in mind that these models are correct only to within a factor of 3 for trapped proton fluxes and within a factor of 5 for trapped electrons. Variations can occur during very large magnetic storms that last a few days.

Table 5-1. Spherical harmonic coefficients of the International Geomagnetic Reference Field (IGRF) 1965 (page 1 of 2).

n	m	g_n^m	h_n^m	gt_n^m	ht_n^m
0	0	1		10	
1	0	-30 339		153	
1	1	-2 123	5 758	87	-23
2	0	-1 654		-244	
2	1	2 994	-2 006	3	-118
2	2	1 567	130	-16	-167
3	0	1 297		2	
3	1	-2 036	-403	-108	42
3	2	1 289	242	7	7
3	3	843	-176	-38	-77
4	0	958		-7	
4	1	805	149	2	-1
4	2	492	-280	-30	16

Table 5-1. Spherical harmonic coefficients of the IGRF 1965 (page 2 of 2).

n	m	g_n^m	h_n^m	gt_n^m	ht_n^m
4	3	-392	8	-1	29
4	4	256	-265	-21	-42
5	0	-223		19	
5	1	357	16	11	23
5	2	246	125	29	17
5	3	-26	-123	6	-24
5	4	-161	-107	0	8
5	5	-51	77	13	-3
6	0	47		-1	
6	1	60	-14	-3	-9
6	2	4	106	11	-4
6	3	-229	68	19	20
6	4	3	-32	-4	-11
6	5	-4	-10	-4	1
6	6	-112	-13	-2	9
7	0	71		-5	
7	1	-54	-57	-3	-11
7	2	0	-27	-7	3
7	3	12	-8	-5	4
7	4	-25	9	3	2
7	5	-9	23	0	4
7	6	13	-19	-2	2
7	7	-2	-17	-6	3
8	0	10		1	
8	1	9	3	4	1
8	2	-3	-13	6	-2
8	3	-12	5	0	-3
8	4	-4	-17	0	-2
8	5	7	4	-1	-3
8	6	-5	22	3	-4
8	7	12	-3	-3	-3
8	8	6	-16	-5	-3

Table 5-2. Spherical harmonic coefficients of the IGRF 1970 (page 1 of 2).

n	m	g_n^m	h_n^m
0	0	10	
1	0	-302 059	
1	1	-20 664	57 446
2	0	-17 917	
2	1	29 971	-20 582
2	2	16 086	430
3	0	12 899	
3	1	-20 708	-3 699
3	2	12 760	2 456
3	3	8 334	-1 880
4	0	9 475	
4	1	8 009	1 617
4	2	4 579	-2 758
4	3	-3 690	185
4	4	2 436	-2 788
5	0	-2 145	
5	1	3 595	157
5	2	2 490	1 420
5	3	-290	-1 310
5	4	-1 669	-911
5	5	-582	808
6	0	460	
6	1	651	-171
6	2	95	1 146
6	3	-2 188	625
6	4	20	-323
6	5	-22	-78
6	6	-1 125	38
7	0	734	
7	1	-546	-666
7	2	46	-265
7	3	175	-34
7	4	-210	81

Table 5-2. Spherical Harmonic coefficients of the IGRF 1970 (page 2 of 2).

n	m	g_n^m	h_n^m
7	5	-32	209
7	6	143	-240
7	7	41	-186
8	0	121	
8	1	77	121
8	2	-32	-160
8	3	-124	22
8	4	-44	-176
8	5	45	46
8	6	34	189
8	7	125	-46
8	8	94	-187
9	0	107	
9	1	57	-174
9	2	23	163
9	3	-110	14
9	4	131	-27
9	5	33	-32
9	6	2	80
9	7	15	137
9	8	9	-4
9	9	-4	14
10	0	-39	
10	1	-26	27
10	2	7	19
10	3	-19	0
10	4	-15	35
10	5	74	-45
10	6	46	22
10	7	6	-31
10	8	-8	56
10	9	22	-1
10	10	14	-63

5.1.2 Nonisotropic Effects. The proton flux is nonisotropic in the South Atlantic Anomaly region, a factor which will affect the results of calculations involving complex shielding geometry. The flux is nonisotropic because the protons follow a helical path about a magnetic field line. As the field intensity increases, both the diameter and the pitch of the helix decrease until the pitch becomes zero. The point with zero pitch angle is called the mirror point, and the center of the helical path is called the guiding center. From here the helix reverses direction and protons travel up the field line toward decreasing field intensity and away from the Earth. In the South Atlantic Anomaly, almost all the protons observed are near their mirror points. Thus, the flux is anisotropic, with most of the flux arriving from a narrow band perpendicular to the local geomagnetic field direction. Any protons there which are not near the mirror point will travel deep into the atmosphere and be scattered or stopped by atmospheric interactions.

Atmospheric interactions also affect the proton angular distribution in another fashion. Protons that are observed traveling eastward are following guiding centers above the observation point, and protons traveling westward are following guiding centers below the observation point. The gyroradius for energetic protons in the anomaly is on the same order as the atmospheric density scale height. Thus, westward traveling protons encounter a significantly denser atmosphere and are more likely to suffer atmospheric interactions and be lost. The resulting energy-dependent anisotropy is called the east-west effect. For typical values of the magnetic field parameters and atmospheric scale height in the anomaly, the ratio of eastward traveling to westward traveling flux is 3 for 50-MeV protons and 22 for 400-MeV protons. Evaluation of the anisotropic effects is complex, but a computer code for use in conjunction with the AP8MAX and AP8MIN models is available upon request.

5.2 Cosmic Rays

For the purpose of this document, the term "cosmic rays" applies to electrons, protons, and the nuclei of all elements. Outside the Earth's magnetosphere, all Galactic Cosmic Rays (GCRs) may be treated as isotropic (to within about 10 percent). Within the Earth's magnetic field, the less energetic nuclei are deflected by the field, and at lower altitudes, the flux becomes anisotropic while the energy spectrum, the total flux, and the directional characteristics are modified by geomagnetic shielding. For every space vehicle mission phase, this effect must be evaluated and integrated over many orbits.

The source of cosmic rays is either galactic or solar. GCRs originate outside the solar system and are thought to permeate our galaxy. Since the condition of the interplanetary medium through which cosmic rays propagate depends on solar activity, the number reaching the Earth's orbit is modulated by the 11-year solar cycle. During the maximum activity phase, the intensity near the Earth decreases, and during the minimum activity phase, it increases.

Solar particle events, in contrast, originate in the Sun and are produced in solar flares. They are lower in energy than GCRs (1 MeV to 1 GeV/nucleon) and are mostly protons and alpha particles. They are a significant hazard during years of maximum solar activity. Although the occurrence of large flares is not yet predictable, especially with long leads times, it is now known that large flares tend to occur in large, highly sheared, magnetically-complex active regions; so, prediction of events with <24-h notice may someday be possible.

5.2.1 Galactic Cosmic Rays. GCRs consist of the nuclei of the elements plus about 2 percent which are electrons. Their energies cover the range from 10 MeV per particle to above 10^{16} MeV per particle. The flux is highest during periods of minimum solar activity. At these energies, the nuclei are completely ionized. A small flux of x-rays and γ -rays from celestial sources is sometimes included in

GCRs, but for space vehicle design purposes, only cosmic-ray nuclei are significant, and this section will be confined to them. GCRs consist of the nuclei of the elements from hydrogen through iron in roughly the same proportions as are found in the solar system, but with the heavier nuclei more abundant in the cosmic rays. Nuclei heavier than nickel are extremely rare.

Figure 5-6 gives the relative abundances and energy spectra of GCRs of interest. The figure covers the energy range of importance in essentially all space vehicle radiation effects studies. In spite of their small number, the heavy elements are very important due to their densely ionizing tracks. They are responsible for many effects in detectors and microelectronics. From figure 5-6, it can be seen that the flux of each nuclear specie decreases rapidly with increasing energy. The lowest energies are observed outside the magnetosphere, where the flux is limited by magnetic fields carried by the solar wind. The energies observed and the flux at these energies vary inversely with the solar cycle.

Although the contribution from GCRs to the total dose in rads inside a spacecraft is typically less than 15 percent for most geocentric orbits, these nuclei are responsible for such effects as "SEUs" and "latch-up" in microcircuits (large-scale integrated (LSI) and very large-scale integrated devices (VLSIDs)). Along with the trapped radiation-belt protons, the nuclei are also responsible for the induced radioactivity in most materials in orbit. Noise induced directly by ionization in sensitive devices such as charge-coupled devices (CCDs) and via Cherenkov and fluorescence radiation in photomultiplier tubes are other effects of GCRs that must frequently be considered. The designer should also consider the possible effects of GCRs on materials as well as the probability of production of secondary particles and their effects.

The available data have been fit to an empirical model which is summarized in part 1, appendix B. Figures 5-7a, b, and c show the differential spectra of protons, α -particles, and iron nuclei at various levels of solar activity and the fit of the model. This model should be used to define the GCR environment.

5.2.2 Solar Particle Events. Solar particle events are sporadic phenomena with durations of a few days. They occur at irregular intervals from a few weeks to a few years depending on the intensity threshold considered. Their most significant components consist of protons at energies from a few MeV to a few hundred MeV. The proton spectra may exhibit intensities that vary over several orders of magnitude, both from event to event and within the time profile of an individual event. The solar particles will, however, envelop the Earth within minutes after a solar flare event, reach peak intensity in a few hours, and decay in 1 or 2 days. They are less likely to occur during solar cycle minima. Within the Earth's magnetosphere, the protons reach LEO most freely in the polar regions at magnetic latitudes above about 63° because the magnetic energetic cutoff goes to near zero at higher latitudes (see below).

An empirical representation of the probability of solar particle events has been summarized in part 2, appendix B. Figure 5-8 shows a history of solar proton events over two solar cycles, and figure 5-9 gives differential spectra integrated over various events.

5.2.3 Geomagnetic Shielding and Cutoff Rigidity. The Earth's magnetic field deflects incoming cosmic rays (solar and galactic) to a degree which depends on the energy of the particles, preventing those with lower energies from penetrating deep into the magnetosphere (cut-off rigidity). In LEO, the minimum rigidity, P/Z , that a particle can have and reach a latitude, λ , from the vertical is

$$P_{\min}/Z = 15 \text{ GV} \frac{\cos^4 \lambda}{(r/R_E)^2},$$

where rigidity is defined as momentum, P , divided by the charge, Z , on the particle (the usual unit is volts or billions of volts, GV), r/R_E is the radial distance from the center of the Earth in units of Earth radii, and λ is the latitude. The minimum cutoff drops to near zero somewhat faster than the formula predicts at magnetic latitudes above about 65° . The rigidity is also less at high altitude for a given latitude, as can be seen from the r/R_E dependence. Thus, spacecraft orbiting the Earth may either be continuously exposed to the unattenuated interplanetary cosmic ray intensities (e.g., high-altitude polar orbits, geostationary orbits, etc.), may be intermittently exposed (e.g., low-altitude polar orbits), or may be completely shielded up to an energy of approximately 10 MeV for low-inclination, low-altitude orbits, and to about 10 gigaelectron volt (GeV) for equatorial orbits. To approximate the average exposure of a space vehicle to cosmic rays, calculations must be performed over many orbital revolutions. An approach to this is summarized in part 3, appendix B.

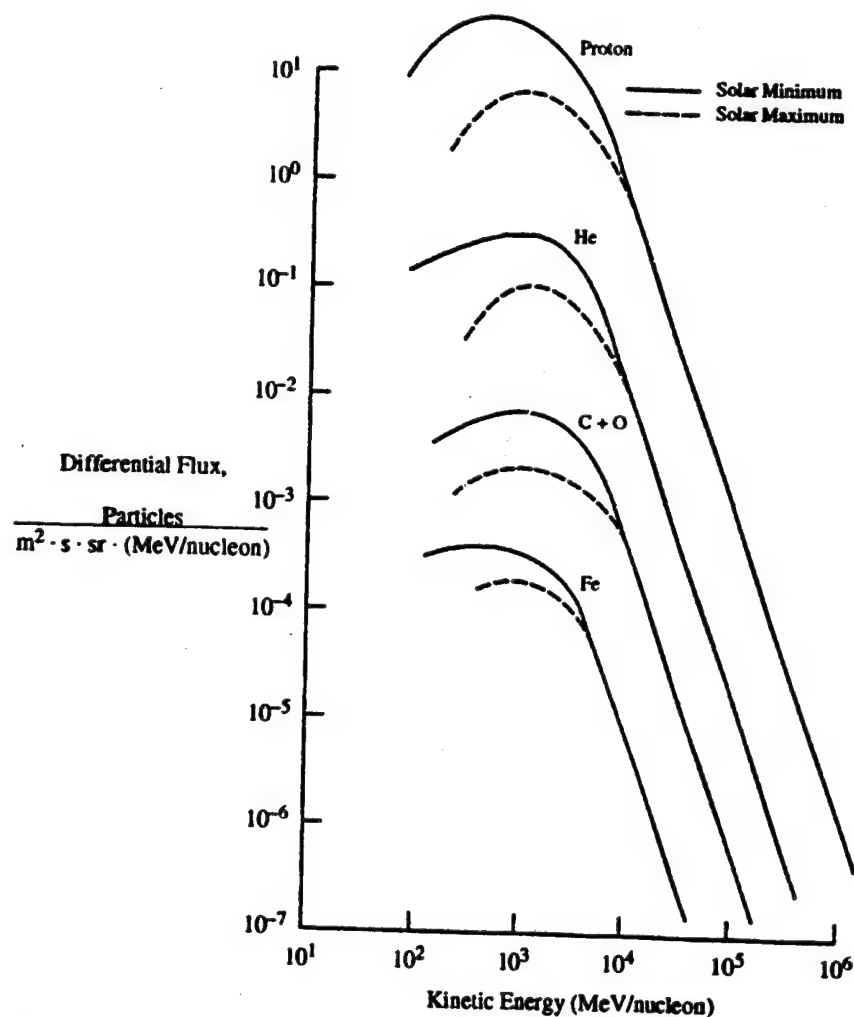


Figure 5-6. Characteristics of GCRs. Differential energy spectra for GCRs outside the magnetosphere at maximum and minimum solar activity (as defined by sunspot number).

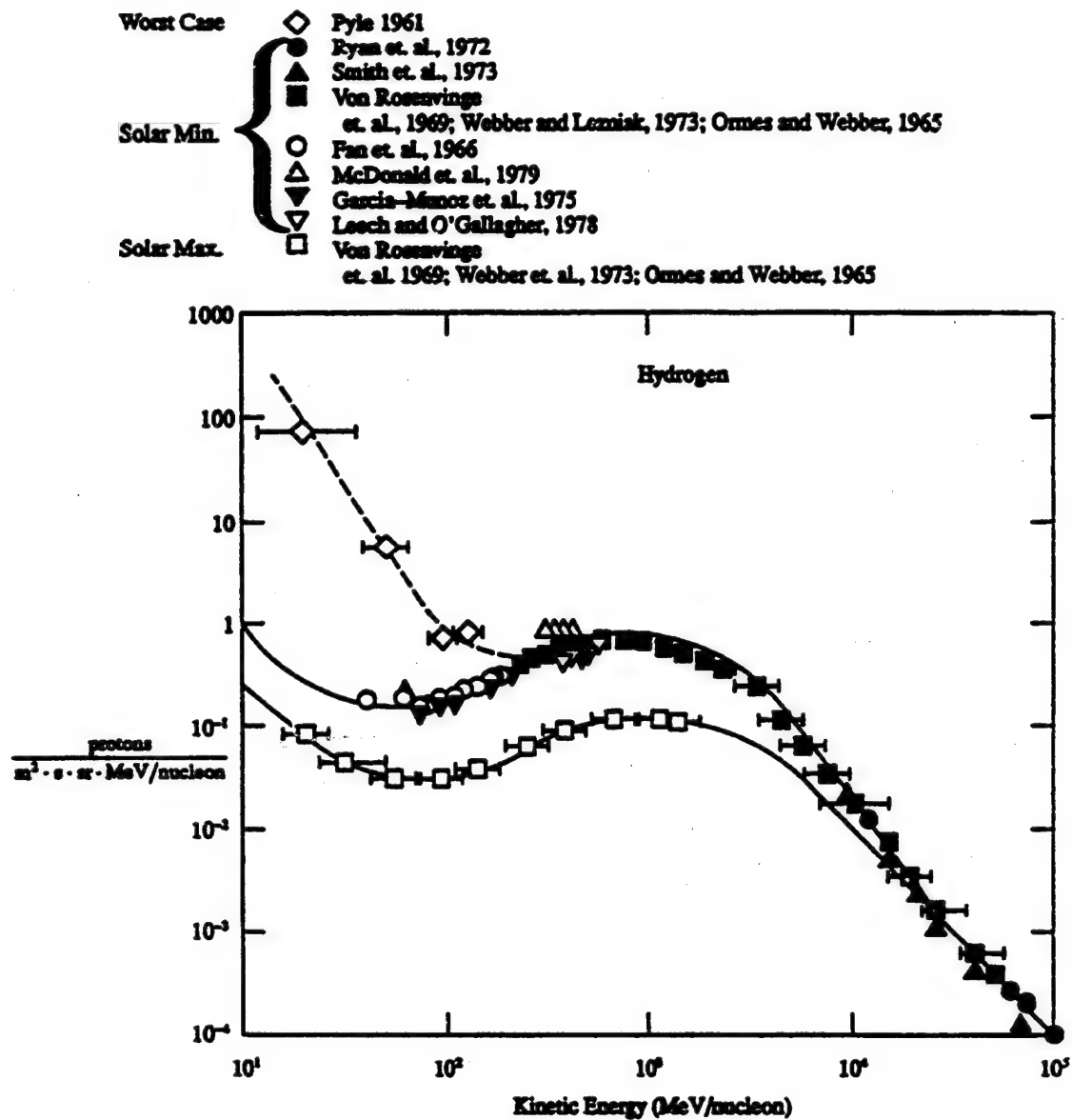


Figure 5-7a. Differential energy spectrum of hydrogen (mostly protons). The data are selected to show the solar maximum and solar minimum fluxes. The dashed curve is a worst-case spectrum.

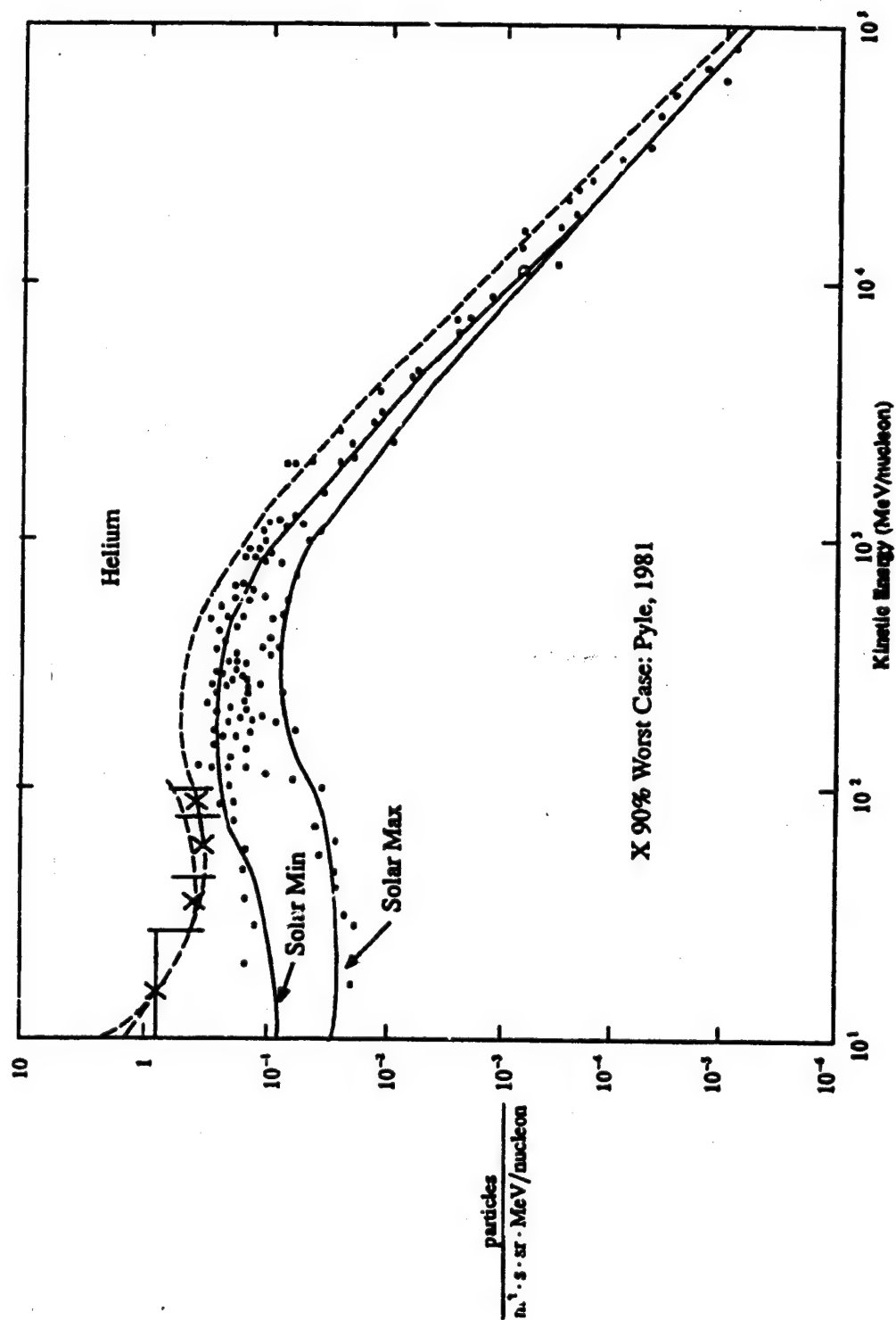


Figure 5-7b. Differential energy spectrum of helium (mostly alphas). The data are selected to show the solar maximum and solar minimum fluxes. The dashed curve is a worst-case spectrum.

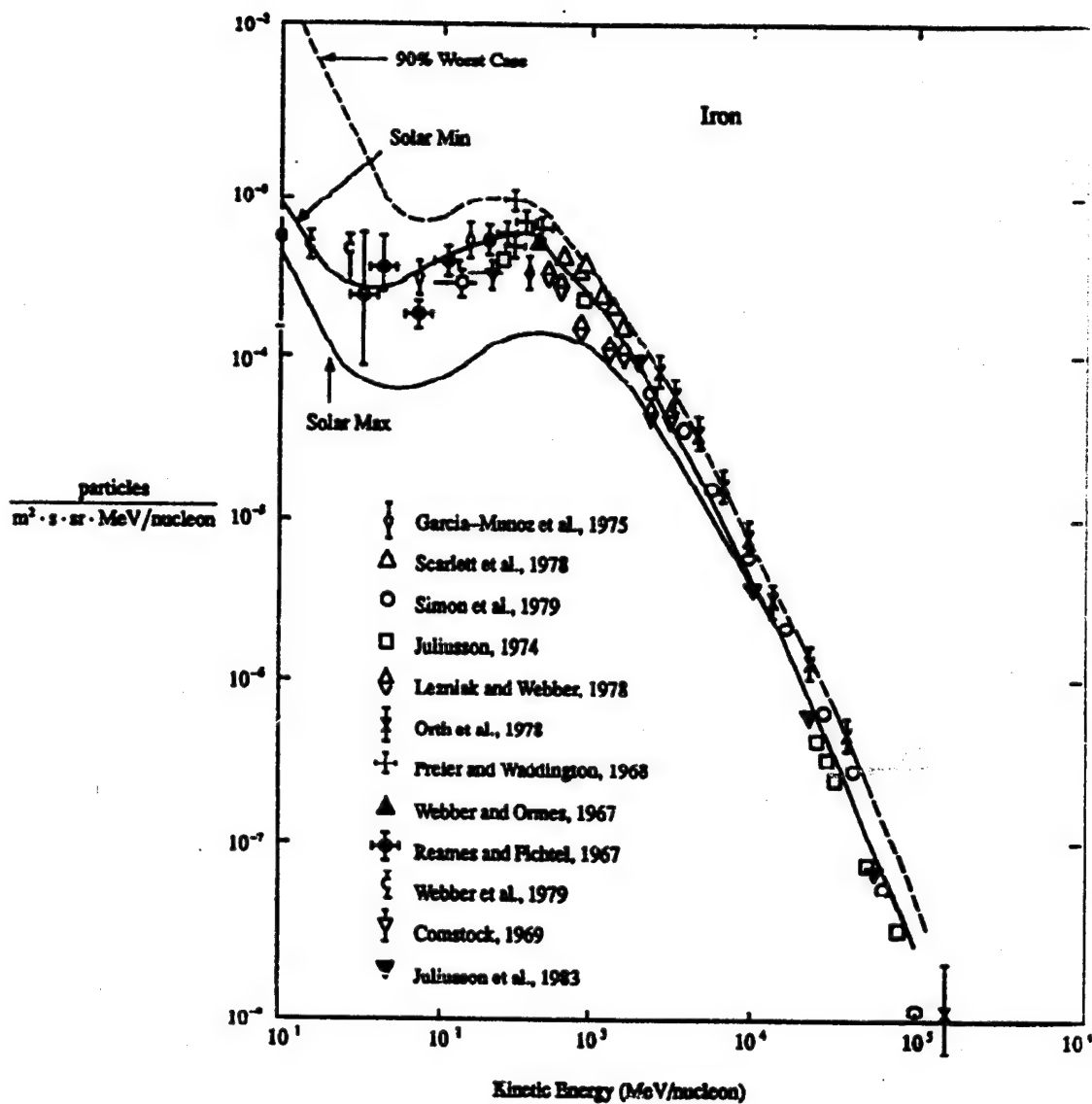


Figure 5-7c. Differential energy spectrum of iron. The data are selected to show the solar maximum and solar minimum fluxes. The dashed curve is a worst-case spectrum.

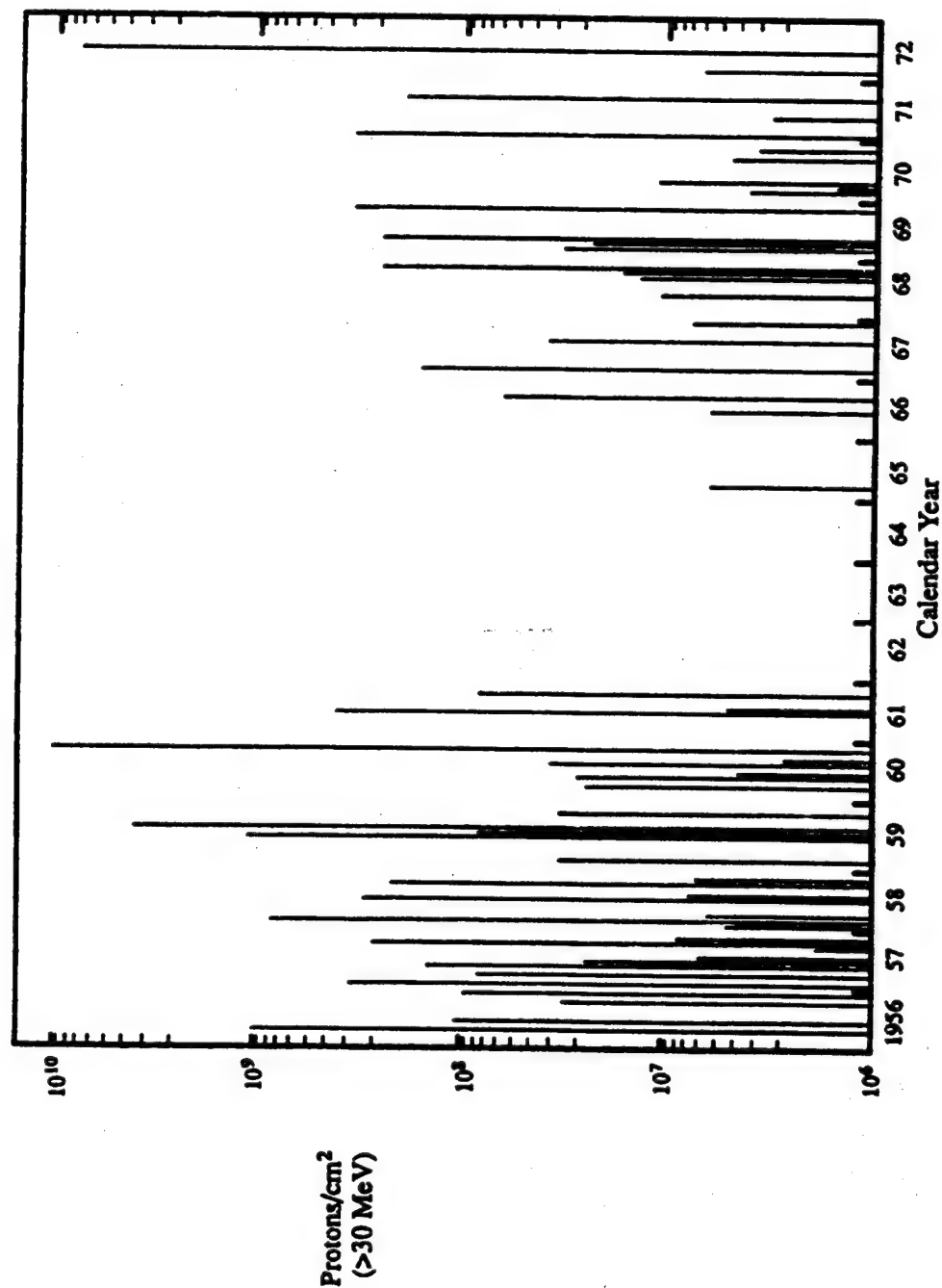


Figure 5-8. Event-integrated proton fluxes above 30 MeV for the major solar events of the 19th and 20th solar cycles.

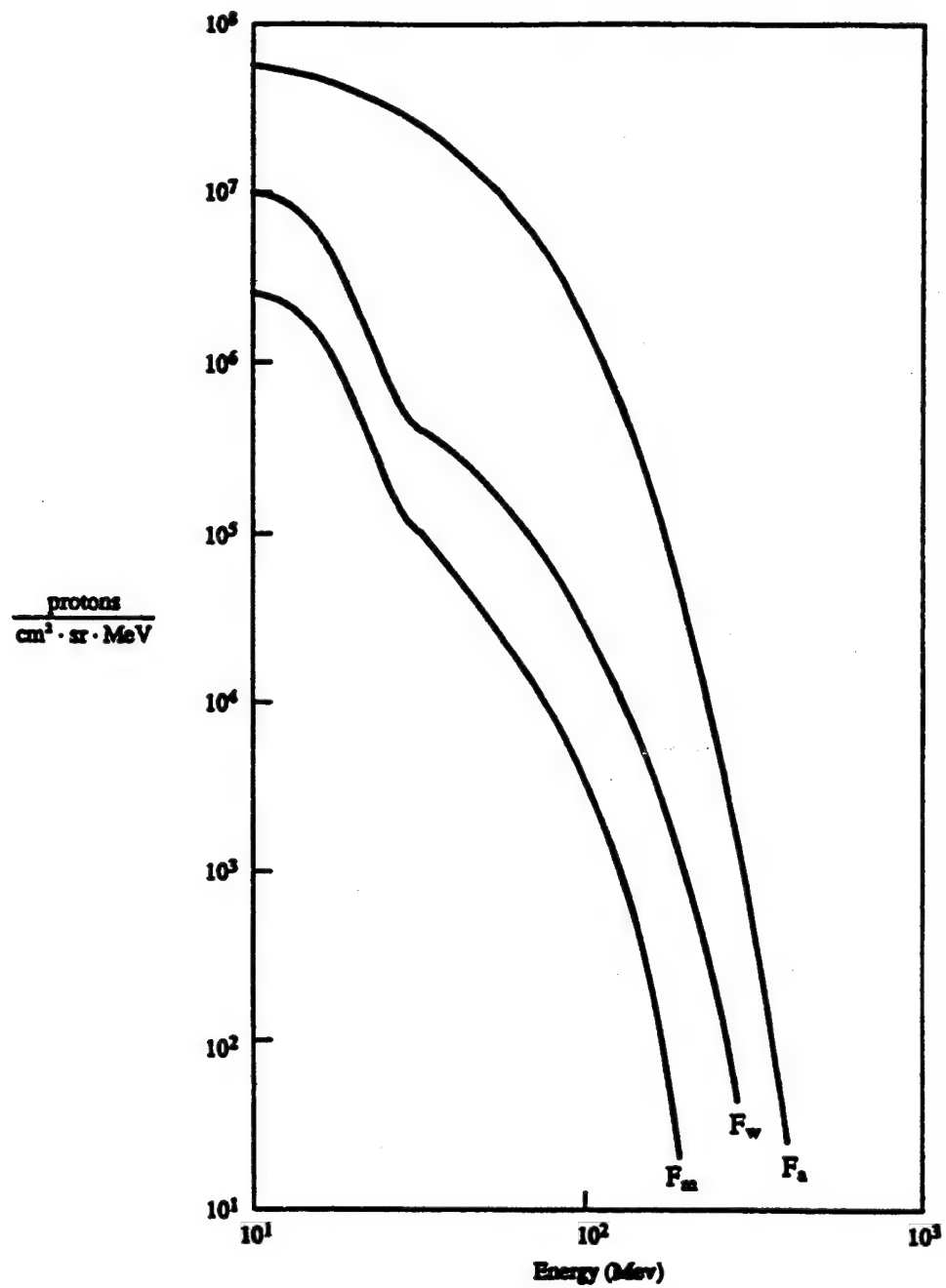


Figure 5-9. Event-integrated proton differential energy spectra. For F_m , a typical ordinary event; F_w , a worst-case ordinary event (90-percent confidence level); and F_a , an anomalously large solar event.

VI. ELECTROMAGNETIC RADIATION

Important sources of electromagnetic noise exist over the entire frequency spectrum from direct current (dc) to x-ray at low-Earth orbital altitudes. These noise sources broadly separate into four categories: galactic, solar, near-Earth natural plasma, and manmade radio noise. The highest power density occurs at the visible and IR frequencies and amounts to the solar constant of 1371_{-10}^{+10} W/m². This section discusses the nature of these noise sources and the manner in which the natural ionospheric environment may affect the propagation of these signals to the space vehicle. Only natural and remote manmade electromagnetic radiations (EMR's) are considered.

The peak of the ionosphere with an electron density of $n_e = 10^{10}$ to 10^{12} m⁻³ occurs at 200 to 300 km altitude (see section IV of this document). These densities correspond to a peak in the natural electron plasma frequency (Langmuir oscillations) of about 0.8 to 8 MHz. EMR below this frequency cannot propagate through the peak electron density region without strong attenuation. Thus, sub-ionospheric and ground-based sources below this frequency will generally not reach orbiting space vehicles except for ducted propagation for some plasma waves. Note, however, that the density and position of this peak electron density vary significantly with solar activity and time of day.

High levels of power in the RF spectral region are primarily a result of Earth-based and space vehicle onboard radiation sources that are manmade. The major ground-based transmitters resulting in high power levels in the ionosphere are in the 100 MHz to 5 GHz range used by radars. They generally have very narrow spatial distributions.

Galactic Radio Noise

Galactic noise reaching orbital altitudes extends from frequencies of 15 MHz to 100 GHz. The source is broadly directional toward and perpendicular to the galactic plane and varies by about 10 W/Hz. Figure 6-1 is a spectrum of the galactic noise as a function of frequency. Space vehicle radio engineers will find that this galactic noise is a dominant factor for a typical radio receiver operating between 40 and 250 MHz (fig. 6-2). For comparison between cosmic noise levels and natural near-Earth noise, see section 6.3.

Solar Electromagnetic Radiation

Solar electromagnetic energy flux near the Earth but outside the atmosphere (at 1 AU) is about 1371_{-10}^{+10} W/m². The irradiance spectrum approximates a black body curve, $T = 5762$ K, which peaks in the visible frequency range (fig. 6-3). The integrated irradiance of the near UV portion of the electromagnetic flux ($0.18 \mu\text{m} < \lambda < 0.4 \mu\text{m}$) is approximately 118 W/m², i.e. about 8.6 percent of the solar constant. The far UV portion ($\lambda < 0.18 \mu\text{m}$) contributes about 0.023 W/m². Irradiance levels for the extreme high energy spectrum are summarized in table 6-1.

The UV portion ($\lambda < 0.3 \mu\text{m}$) of the electromagnetic spectrum is of particular importance in determining the effects of solar radiation on material properties. For "terrestrial space," the UV radiation is independent of orbit geometry above the atmosphere; however, the spacecraft surface geometry, orientation, and orbit geometry will affect the exposure level over a given orbital lifetime.

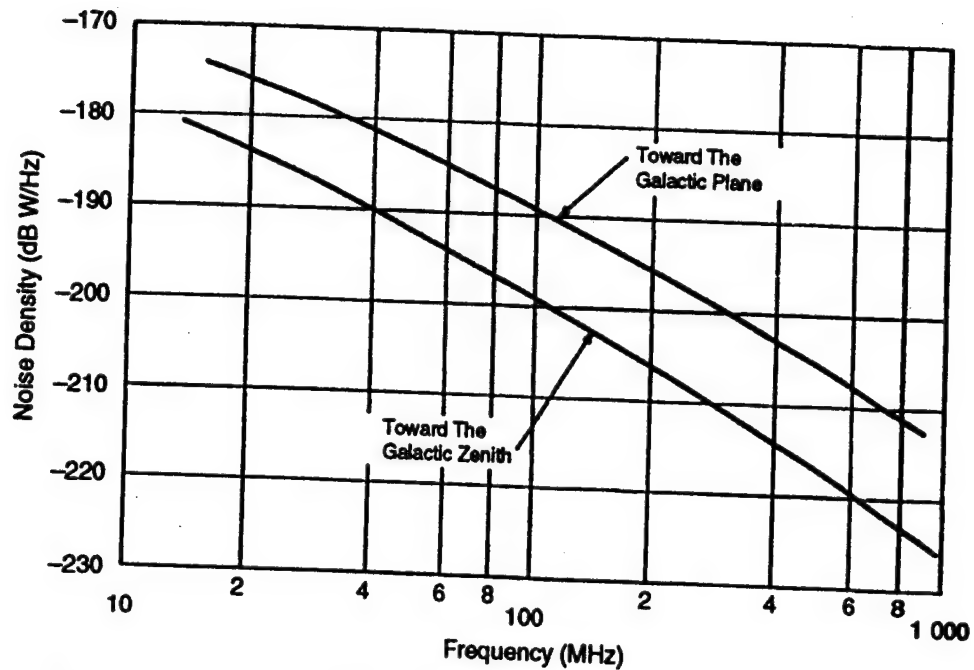


Figure 6-1. Levels of galactic radio noise as a function of frequency (ref. 23).

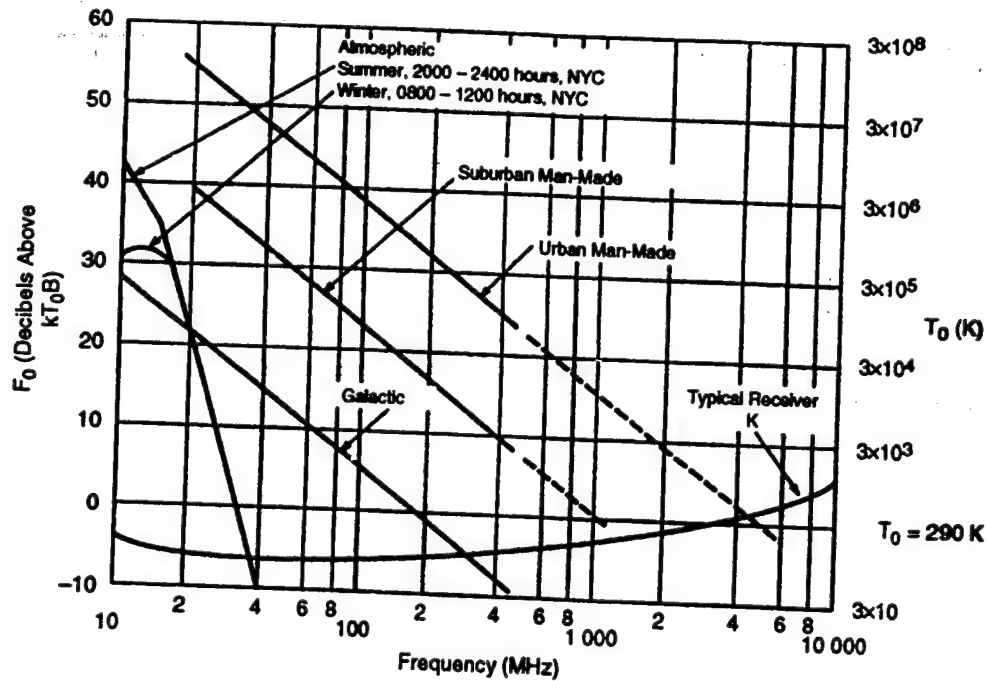


Figure 6-2. Median values of average noise power expected from various sources (omnidirectional antenna near surface) (ref. 23).

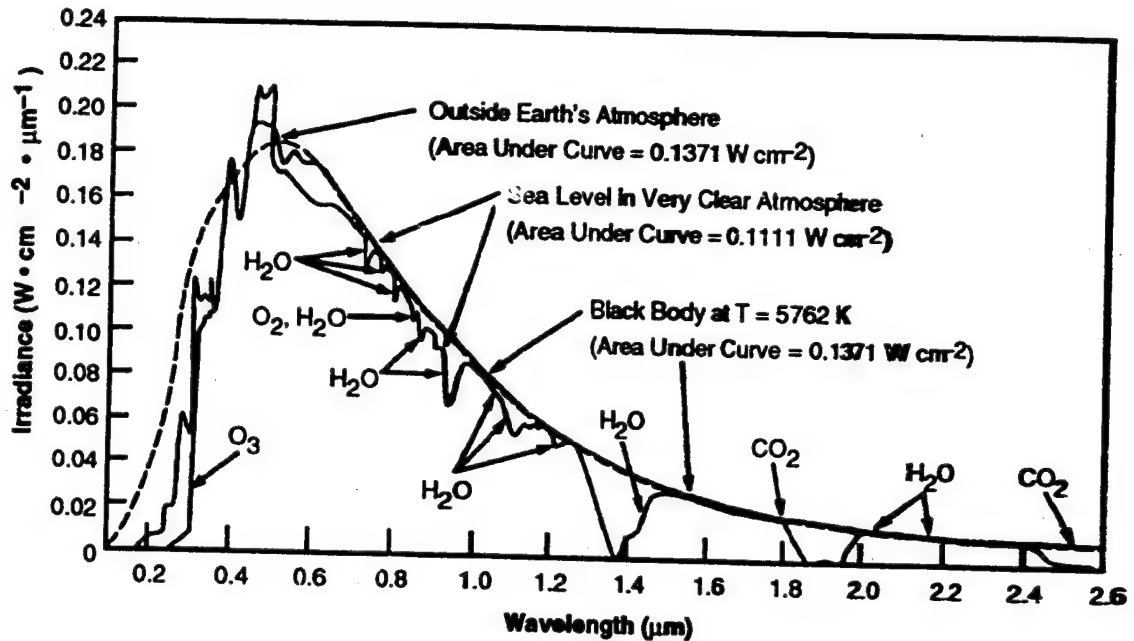


Figure 6-3. Normally incident solar radiation at sea level on very clear days, solar spectral irradiance outside the Earth's atmosphere at 1 AU, and blackbody spectral irradiance curve at $T = 5762\text{ K}$ (normalized to 1 AU).

Recent measurements have greatly improved the data base for this portion of the spectrum. These results, derived from the review in reference 22, have been incorporated into this specification table 6-2). They provide data that give a good indication of the irradiance variability over the 27-day solar rotation period and somewhat longer time scales; however, the time span covered by good quality data is still too short to provide high confidence in estimates of irradiance variations over the 11-year solar cycle.

Table 6-1. Solar electromagnetic radiation.

Type	Wavelength (nm)	Level (W/m^2)
UV	100-150	$7.5\text{E-}3$
EUV	10-100	$2\text{E-}3$
X-Rays	1-10	$5\text{E-}5$
Flare X Rays	0.1-1	$1\text{E-}4$
Cosmic Rays*		$1\text{E-}3$
Solar Wind*		$1\text{E-}4$

*Not electromagnetic but included for comparison ²⁴

Table 6-2. Parameters for estimating irradiance variability over the 11-year solar cycle.²²

Wavelength Range (nm)	R_{sc} (max/min)	R_{27}
175-190	1.020 (± 0.020)	1.07
190-210	1.030 (± 0.020)	1.06
210-240	1.026 (± 0.020)	1.03
240-300	1.005 (± 0.020)	1.01

R_{sc} is the ratio of a 27-day mean irradiance near solar maximum to a 27-day mean at solar minimum. R_{27} is the ratio of the maximum irradiance observed during a typical 27-day solar rotation to the minimum irradiance during this rotation.

The Lyman-alpha ($\text{Ly-}\alpha$) emission line at 0.1216 μm is the primary emission line below 0.1300 μm , and its integrated irradiance varies by roughly a factor of 2 over the 11-year solar cycle with an uncertainty of ± 15 percent. For estimates of the $\text{Ly-}\alpha$ flux at any level of solar activity, the following relationship is the best available:

$$q(\text{Ly-}\alpha) = 2.25\text{E}^{11} + 0.014\text{E}^{11} (F_{10.7} - 65) \quad (6-1)$$

where q is expressed in photons $\cdot\text{cm}^{-2}\cdot\text{s}^{-1}$.

The variation in the integrated 0.130 to 0.175 μm wavelength flux over the solar cycle is a factor of 2 with error bars on the recent measurements of ± 20 percent. The percent change of the short-term variation is less than that at $\text{Ly-}\alpha$, and most values lie between 7.6E^{11} and 8.7E^{11} photons $\cdot\text{cm}^{-2}\cdot\text{s}^{-1}$ for solar activity levels prevailing in 1982 to 1984.

It is now generally accepted that the spectral region 0.175 to 0.210 μm varies with the 27-day solar rotation and the 11-year solar cycle. In this spectral region, the root mean square deviations from the Reference Solar Irradiance Spectrum in table 6-3 are less than 10 percent in most cases although the quoted uncertainty in any single measurement is typically ± 15 to ± 20 percent.

Typical uncertainty limits for the measurements in the 0.210 to 0.3275 μm spectral region are ± 15 to 20 percent; however, once again root mean square deviations from the reference solar irradiance spectrum (RSIS) are less than 10 percent. Between 0.175 and 0.210 μm , the maximum irradiance tends to be 1.05 to 1.07 times the minimum value with a peak ratio approaching 1.10. Between 0.210 and 0.250 μm , the maximum to minimum irradiance ratio is typically 1.03 and, beyond 0.260 μm , drops to 1.01 or less. Table 6-2 presents estimates of the solar cycle variability in selected wavelength bins spanning the region 0.175 to 0.300 μm . The quantity, R_{sc} , is a measure of the ratio of solar maximum irradiance to solar minimum irradiance. R_{27} is an estimate of the 27-day irradiance variation. The ratio of the maximum to minimum irradiance during a solar cycle is the product of R_{27} and R_{sc} . The maximum and minimum irradiances over a solar cycle are related to the mean reference cycle of table 6-3 by:

$$F_{\max}(i) = F_{\text{ref}}(i) \frac{2R_{27}(i)R_{sc}(i)}{1+R_{27}(i)R_{sc}(i)} \quad (6-2)$$

and

$$F_{\min}(i) = F_{\text{ref}}(i) \frac{2}{1+R_{27}(i)R_{sc}(i)} \quad (6-3)$$

where R_{27} and R_{sc} are obtained from table 6-2.

Table 6-3. Reference solar irradiance, Rayleigh scattering, oxygen, ozone cross sections, and energy flux (page 1 of 6).*

Wavelength Range† (nm)	Solar Irradiance (phot/cm ² -s)	Rayleigh Scatter σ_{RS} (cm ²)	Oxygen Herzberg σ_{Hz} (O ₂) (cm ²)	Ozone†† σ (O ₃) (cm ²)	Energy Flux (W/m ²)
1 175.439-176.991	1.74E+11	6.79E-25	4.61E-24	8.11E-19	1.96E-3
2 176.991-178.571	2.10E+11	6.49E-25	5.03E-24	7.99E-19	2.34E-3
3 178.571-180.180	2.38E+11	6.20E-25	5.46E-24	7.86E-19	2.64E-3
4 180.180-181.818	3.04E+11	5.93E-25	5.88E-24	7.63E-19	3.35E-3
5 181.818-183.486	3.19E+11	5.66E-25	6.29E-24	7.29E-19	3.47E-3
6 183.486-185.185	2.93E+11	5.41E-25	6.68E-24	6.88E-19	3.16E-3
7 185.185-186.916	3.62E+11	5.16E-25	7.04E-24	6.40E-19	3.87E-3
8 186.916-188.679	4.73E+11	4.93E-25	7.36E-24	5.88E-19	5.00E-3
9 188.679-190.476	5.61E+11	4.70E-25	7.64E-24	5.31E-19	5.88E-3
10 190.476-192.308	6.63E+11	4.49E-25	7.87E-24	4.80E-19	6.88E-3
11 192.308-194.175	6.90E+11	4.28E-25	8.04E-24	4.38E-19	7.09E-3
12 194.175-196.078	9.56E+11	4.08E-25	8.14E-24	4.11E-19	9.74E-3
13 196.078-198.020	1.15E+12	3.89E-25	8.17E-24	3.69E-19	1.16E-2
14 198.020-200.000	1.27E+12	3.71E-25	8.13E-24	3.30E-19	1.27E-2
15 200.000-202.020	1.52E+12	3.53E-25	8.01E-24	3.26E-19	1.50E-2
16 202.020-204.082	1.78E+12	3.36E-25	7.84E-24	3.26E-19	1.74E-2
17 204.082-206.186	2.20E+12	3.20E-25	7.63E-24	3.51E-19	2.13E-2
18 206.186-208.333	2.69E+12	3.05E-25	7.33E-24	4.11E-19	2.58E-2
19 208.333-210.526	4.54E+12	2.90E-25	6.99E-24	4.84E-19	4.31E-2
20 210.526-212.766	7.14E+12	2.76E-25	6.45E-24	6.26E-19	6.70E-2
21 212.766-215.054	8.35E+12	2.62E-25	5.81E-24	8.57E-19	7.75E-2
22 215.054-217.391	8.39E+12	2.49E-25	5.23E-24	1.17E-18	7.71E-2
23 217.391-219.780	1.08E+13	2.36E-25	4.71E-24	1.52E-18	9.82E-2
24 219.780-222.222	1.18E+13	2.24E-25	4.26E-24	1.97E-18	1.06E-1
25 222.222-224.719	1.60E+13	2.13E-25	3.80E-24	2.55E-18	1.42E-1
26 224.719-227.273	1.34E+13	2.02E-25	3.35E-24	3.24E-18	1.18E-1
27 227.273-229.885	1.41E+13	1.92E-25	2.90E-24	4.00E-18	1.23E-1

From reference 22.

Wavelength range for spectral intervals 1 to 49 corresponds to 500 wavenumbers. Wavelength range for remainder of spectral intervals is 5 nm.

$T = 203$ K and $T = 273$ K.

Table 6-3. Reference solar irradiance, Rayleigh scattering, oxygen, ozone cross sections, and energy flux (page 2 of 6).*

Wavelength Range† (nm)	Solar Irradiance (phot/cm ² -s)	Rayleigh Scatter σ_{RS} (cm ²)	Oxygen Herzberg σ_{Hz} (O ₂) (cm ²)	Ozone†† σ (O ₃) (cm ²)	Energy Flux (W/m ²)
28 229.885–232.558	1.57E+13	1.82E–25	2.45E–24	4.83E–18	1.35E–1
29 232.558–235.294	1.38E+13	1.72E–25	2.05E–24	5.79E–18	1.17E–1
30 235.294–238.095	1.60E+13	1.63E–25	1.69E–24	6.86E–18	1.34E–1
31 238.095–240.964	1.45E+13	1.54E–25	1.30E–24	7.97E–18	1.20E–1
32 240.964–243.902	2.20E+13	1.46E–25	0.93E–24	9.00E–18	1.80E–1
33 243.902–246.914	1.99E+13	1.38E–25	0.00E–00	1.00E–17	1.61E–1
34 246.914–250.000	1.97E+13	1.31E–25	–	1.08E–17	1.58E–1
35 250.000–253.165	1.94E+13	1.23E–25	–	1.13E–17	1.53E–1
36 253.165–256.410	2.91E+13	1.17E–25	–	1.15E–17	2.27E–1
37 256.410–259.740	4.95E+13	1.10E–25	–	1.12E–17	3.81E–1
38 259.740–263.158	4.53E+13	1.04E–25	–	1.06E–17	3.44E–1

* From reference 22.

† Wavelength range for spectral intervals 1 to 49 corresponds to 500 wavenumbers. Wavelength range for remainder of spectral intervals is 5 nm.

†† $T = 203$ K and $T = 273$ K.

Table 6-3. Reference solar irradiance, Rayleigh scattering, oxygen, ozone cross sections, and energy flux (page 3 of 6).*

Wavelength Range† (nm)	Solar Irradiance (phot/cm ² -s)	Rayleigh Scatter σ_{RS} (cm ²)	Ozone $\alpha(O_3)$ $T = 203\text{ K}$ (cm ²)	Ozone $\alpha(O_3)$ $T = 273\text{ K}$ (cm ²)	Energy Flux (W/m ²)
39 263.158–266.667	1.07E+14	9.78E-26	9.59E-18	9.65E-18	8.02E-1
40 266.667–270.270	1.20E+14	9.22E-26	8.31E-18	8.34E-18	8.88E-1
41 270.270–273.973	1.10E+14	8.68E-26	6.89E-18	6.92E-18	8.03E-1
42 273.973–277.778	1.04E+14	8.17E-26	5.35E-18	5.42E-18	7.49E-1
43 277.778–281.690	8.24E+13	7.68E-26	3.91E-18	4.02E-18	5.85E-1
44 281.690–285.714	1.52E+14	7.22E-26	2.67E-18	2.77E-18	1.06
45 285.714–289.855	2.15E+14	6.78E-26	1.73E-18	1.79E-18	1.48
46 289.855–294.118	3.48E+14	6.36E-26	1.04E-18	1.09E-18	2.37
47 294.118–298.507	3.40E+14	5.97E-26	5.85E-19	6.24E-19	2.28
48 298.507–303.030	3.22E+14	5.59E-26	3.16E-19	3.43E-19	2.13
49 303.030–307.692	4.23E+14	5.24E-26	1.66E-19	1.85E-19	2.75
50 307.692–312.5	4.95E+14	4.90E-26	8.67E-20	9.80E-20	3.17
51 312.5–317.5	5.44E+14	4.58E-26	4.33E-20	5.01E-20	3.43
52 317.5–322.5	5.93E+14	4.28E-26	2.09E-20	2.49E-20	3.68
53 322.5–327.5	6.95E+14	4.01E-26	9.37E-21	1.20E-20	4.25
54 327.5–332.5	8.15E+14	3.75E-26	4.71E-21	6.17E-21	4.91
55 332.5–337.5	7.81E+14	3.52E-26	1.98E-21	2.74E-21	4.63
56 337.5–342.5	8.35E+14	3.31E-26	7.77E-22	1.17E-21	4.88
57 342.5–347.5	8.14E+14	3.11E-26	1.77E-22	5.88E-22	4.69
58 347.5–352.5	8.53E+14	2.92E-26	–	2.66E-22	4.84
59 352.5–357.5	9.17E+14	2.75E-26	–	1.09E-22	5.13
60 357.5–362.5	8.38E+14	2.60E-26	–	5.49E-23	4.62
61 362.5–367.5	1.04E+15	2.45E-26	–	–	5.66
62 367.5–372.5	1.10E+15	2.31E-26	–	–	5.91
63 372.5–377.5	9.79E+14	2.19E-26	–	–	5.19
64 377.5–382.5	1.13E+15	2.07E-25	–	–	5.91

* From reference 22.

† Wavelength range for spectral intervals 1 to 49 corresponds to 500 wavenumbers. Wavelength range for remainder of spectral intervals is 5 nm.

Table 6-3. Reference solar irradiance, Rayleigh scattering, oxygen, ozone cross sections, and energy flux (page 4 of 6).*

Wavelength Range† (nm)	Solar Irradiance (phot/cm ² -s)	Rayleigh Scatter σ_{RS} (cm ²)	Ozone†† $\sigma(O_3)$ (cm ²)	Energy Flux (W/m ²)
65 382.5–387.5	8.89E+14	1.96E–26	–	4.59
66 387.5–392.5	1.14E+15	1.86E–26	–	5.81
67 392.5–397.5	9.17E+14	1.76E–26	–	4.61
68 397.5–402.5	1.69E+15	1.67E–26	–	8.39
69 402.5–407.5	1.70E+15	1.59E–26	–	8.34
70 407.5–412.5	1.84E+15	1.51E–26	2.91E–23	8.91
71 412.5–417.5	1.87E+15	1.44E–26	3.14E–23	8.95
72 417.5–422.5	1.95E+15	1.37E–26	3.99E–23	9.22
73 422.5–427.5	1.81E+15	1.30E–26	6.54E–23	8.46
74 427.5–432.5	1.67E+15	1.24E–26	6.83E–23	7.72
75 432.5–437.5	1.98E+15	1.18E–26	8.66E–23	9.04
76 437.5–442.5	2.02E+15	1.13E–26	1.25E–22	9.12
77 442.5–447.5	2.18E+15	1.08E–26	1.49E–22	9.73
78 447.5–452.5	2.36E+15	1.03E–26	1.71E–22	1.04E+1
79 452.5–457.5	2.31E+15	9.85E–27	2.12E–22	1.01E+1
80 457.5–462.5	2.39E+15	9.42E–27	3.57E–22	1.03E+1
81 462.5–467.5	2.38E+15	9.01E–27	3.68E–22	1.02E+1
82 467.5–472.5	2.39E+15	8.63E–27	4.06E–22	1.01E+1
83 472.5–477.5	2.44E+15	8.26E–27	4.89E–22	1.02E+1
84 477.5–482.5	2.51E+15	7.92E–27	7.11E–22	1.04E+1
85 482.5–487.5	2.30E+15	7.59E–27	8.43E–22	9.42
86 487.5–492.5	2.39E+15	7.28E–27	8.28E–22	9.69
87 492.5–497.5	2.48E+15	6.99E–27	9.09E–22	9.95
88 497.5–502.5	2.40E+15	6.71E–27	1.22E–21	9.54
89 502.5–507.5	2.46E+15	6.44E–27	1.62E–21	9.68
90 507.5–512.5	2.49E+15	6.19E–27	1.58E–21	9.70
91 512.5–517.5	2.32E+15	5.95E–27	1.60E–21	8.95
92 517.5–522.5	2.39E+15	5.72E–27	1.78E–21	9.13
93 522.5–527.5	2.42E+15	5.50E–27	2.07E–21	9.16
94 527.5–532.5	2.55E+15	5.30E–27	2.55E–21	9.56
95 532.5–537.5	2.51E+15	5.10E–27	2.74E–21	9.32

* From reference 22.

† Wavelength range for spectral intervals 1 to 49 corresponds to 500 wavenumbers. Wavelength range for remainder of spectral intervals is 5 nm.

†† $T = 203$ K and $T = 273$ K.

Table 6-3. Reference solar irradiance, Rayleigh scattering, oxygen, ozone cross sections, and energy flux (page 5 of 6).*

Wavelength Range† (nm)	Solar Irradiance (phot/cm ² -s)	Rayleigh Scatter σ_{RS} (cm ²)	Ozone†† $\sigma(O_3)$ (cm ²)	Energy Flux (W/m ²)
96 537.5-542.5	2.49E+15	4.91E-27	2.88E-21	9.16
97 542.5-547.5	2.55E+15	4.73E-27	3.07E-21	9.30
98 547.5-552.5	2.53E+15	4.56E-27	3.17E-21	9.14
99 552.5-557.5	2.54E+15	4.34E-27	3.36E-21	9.09
100 557.5-562.5	2.50E+15	4.18E-27	3.88E-21	8.87
101 562.5-567.5	2.57E+15	4.04E-27	4.31E-21	9.04
102 567.5-572.5	2.58E+15	3.90E-27	4.67E-21	8.99
103 572.5-577.5	2.67E+15	3.76E-27	4.75E-21	9.22
104 577.5-582.5	2.67E+15	3.63E-27	4.55E-21	9.14
105 582.5-587.5	2.70E+15	3.51E-27	4.35E-21	9.17
106 587.5-592.5	2.62E+15	3.39E-27	4.42E-21	8.82
107 592.5-597.5	2.69E+15	3.28E-27	4.61E-21	8.98
108 597.5-602.5	2.63E+15	3.17E-27	4.89E-21	8.71
109 602.5-607.5	2.68E+15	3.06E-27	4.84E-21	8.80
110 607.5-612.5	2.66E+15	2.96E-27	4.54E-21	8.66
111 612.5-617.5	2.59E+15	2.87E-27	4.24E-21	8.37
112 617.5-622.5	2.69E+15	2.77E-27	3.90E-21	8.62
113 622.5-627.5	2.61E+15	2.68E-27	3.60E-21	8.30
114 627.5-632.5	2.62E+15	2.60E-27	3.43E-21	8.26
115 632.5-637.5	2.62E+15	2.52E-27	3.17E-21	8.20
116 637.5-642.5	2.63E+15	2.44E-27	2.74E-21	8.17
117 642.5-647.5	2.60E+15	2.36E-27	2.61E-21	8.01
118 647.5-652.5	2.55E+15	2.29E-27	2.42E-21	7.79
119 652.5-657.5	2.48E+15	2.22E-27	2.20E-21	7.52
120 657.5-662.5	2.57E+15	2.15E-27	2.20E-21	7.73
121 662.5-667.5	2.61E+15	2.09E-27	1.85E-21	7.80
122 667.5-672.5	2.61E+15	2.03E-27	1.67E-21	7.74
123 672.5-677.5	2.62E+15	1.97E-27	1.54E-21	7.71
124 677.5-682.5	2.62E+15	1.91E-27	1.42E-21	7.66
125 682.5-687.5	2.57E+15	1.85E-27	1.25E-21	7.45
126 687.5-692.5	2.52E+15	1.80E-27	1.12E-21	7.25

* From reference 22.

† Wavelength range for spectral intervals 1 to 49 corresponds to 500 wavenumbers. Wavelength range for remainder of spectral intervals is 5 nm.

†† $T = 203$ K and $T = 273$ K.

Table 6-3. Reference solar irradiance, Rayleigh scattering, oxygen, ozone cross sections, and energy flux (page 6 of 6).*

Wavelength Range† (nm)	Solar Irradiance (phot/cm ² -s)	Rayleigh Scatter σ_{RS} (cm ²)	Ozone†† $\sigma(O_3)$ (cm ²)	Energy Flux (W/m ²)
127 692.5-697.5	2.60E+15	1.75E-27	1.02E-21	7.43
128 697.5-702.5	2.58E+15	1.70E-27	9.20E-22	7.32
129 702.5-707.5	2.52E+15	1.65E-27	8.40E-22	7.10
130 707.5-712.5	2.51E+15	1.60E-27	7.70E-22	7.02
131 712.5-717.5	2.48E+15	1.56E-27	6.90E-22	6.89
132 717.5-722.5	2.45E+15	1.52E-27	6.30E-22	6.76
133 722.5-727.5	2.48E+15	1.47E-27	5.70E-22	6.79
134 727.5-732.5	2.45E+15	1.43E-27	5.25E-22	6.67
135 732.5-737.5	2.44E+15	1.39E-27	4.75E-22	6.60
136 737.5-742.5	2.39E+15	1.36E-27	4.47E-22	6.41
137 742.5-747.5	2.40E+15	1.32E-27	4.20E-22	6.40
138 747.5-752.5	2.41E+15	1.29E-27	3.75E-22	6.38
139 752.5-757.5	2.40E+15	1.25E-27	3.25E-22	6.32
140 757.5-762.5	2.38E+15	1.22E-27	2.92E-22	6.22
141 762.5-767.5	2.34E+15	1.19E-27	2.76E-22	6.08
142 767.5-772.5	2.32E+15	1.16E-27	2.70E-22	5.99
143 772.5-777.5	2.30E+15	1.13E-27	2.80E-22	5.89
144 777.5-782.5	2.33E+15	1.10E-27	2.85E-22	5.93
145 782.5-787.5	2.34E+15	1.07E-27	2.52E-22	5.92
146 787.5-792.5	2.29E+15	1.04E-27	2.20E-22	5.76
147 792.5-797.5	2.29E+15	1.02E-27	1.82E-22	5.72
148 797.5-802.5	2.27E+15	9.90E-28	1.63E-22	5.64
149 802.5-807.5	2.27E+15	9.66E-28	1.75E-22	5.60
150 807.5-812.5	2.20E+15	9.42E-28	1.90E-22	5.40
151 812.5-817.5	2.22E+15	9.19E-28	1.85E-22	5.41
152 817.5-822.5	2.18E+15	8.96E-28	1.70E-22	5.28
153 822.5-827.5	2.20E+15	8.75E-28	1.52E-22	5.30
154 827.5-832.5	2.14E+15	8.53E-28	1.42E-22	5.12
155 832.5-837.5	2.14E+15	8.33E-28	1.40E-22	5.09
156 837.5-842.5	2.13E+15	8.13E-28	1.40E-22	5.04
157 842.5-847.5	2.09E+15	7.94E-28	1.42E-22	4.91
158 847.5-852.5	2.05E+15	7.75E-28	1.45E-22	4.79

* From reference 22.

† Wavelength range for spectral intervals 1 to 49 corresponds to 500 wavenumbers. Wavelength range for remainder of spectral intervals is 5 nm.

†† $T = 203$ K and $T = 273$ K.

6.3 Natural Environmental Electromagnetic Radiation

The magnetosphere-ionosphere system is filled with natural plasma emission sources which greatly from the poles to the equator. The frequencies of these emissions generally extend down from the peak electron plasma frequencies (1 to 10 MHz) to direct current. The electron plasma frequency is found simply from the electron density as:

$$f_p = \left| \frac{n_e e^2}{m_e \pi} \right|^{1/2} \text{ (cgs)} = 0.90 \text{ MHz} \left| \frac{n_e}{10^4/\text{cm}^3} \right|^{1/2},$$

where n_e is the electron density per cm^3 , e^2 is square of the electronic charge, $94.8\text{E-}10$, and m_e is the electron mass in grams ($0.911\text{E-}27$).

Note that the electron plasma frequency is independent of temperature. A wide variety of natural electromagnetic emissions are related to electron cyclotron waves from wave-particle phenomena in Earth's dipole magnetic field. These emissions are generally in the frequency range of 0.5 to 30 kHz and include very low-frequency whistler-mode noise such as hiss and chorus. They are highly position dependent since, although they are electromagnetic waves, they have a plasma component which affects the wave propagation vector. At typical LEO velocities in the 5 to 10 km/s range, one can expect natural plasma structures of small scale size (i.e., 0.01 to 10 km) to introduce an effective noise source at space vehicle receivers. This noise source is due to natural phenomena such as auroral arcs and ionospheric irregularities. Figure 6-4 presents an overview of the natural plasma noise levels from near-Earth, solar and cosmic sources. The figure shows power flux levels for various frequency ranges of naturally occurring electromagnetic and plasma waves in the Earth's environment and in astrophysical sources observed at the Earth.

As mentioned above, noise sources below about 1 MHz are likely to be negligible at the space vehicle if they have sources below 200 km. However, it is possible for certain impulsive radiation bursts such as lightning-generated sferics to penetrate the ionosphere. In particular, recent indications are that direct lightning-generated waveforms with frequencies above about 1 Hz can result in transient electric fields up to about 50 mV/m in the ionosphere. In general, all EMR field strengths are smaller at higher frequencies. The largest field strengths are for quasi-static field structures which occasionally reach 0.1 to 0.5 V/m but usually range between 10 to 50 mV/m. Such large quasi-static fields are generally found poleward of 50° latitude in association with the aurora. These direct current fields should be compared to the apparent direct current electric field due to the Lorentz transformation of the motion of the vehicle across magnetic field lines. This field, on the order of a few hundred mV/m, can create significant potential drops across large objects.

6.4 Manmade Noise

Although manmade noise sources below the peak plasma frequency of 1 to 10 MHz will not likely be a problem at orbital altitudes above the ionospheric peak because they cannot propagate through the lower ionosphere without significant attenuation, it is likely that many narrow-band sources from 1 MHz to 300 GHz will be detectable and perhaps important noise sources for an orbiting space vehicle.

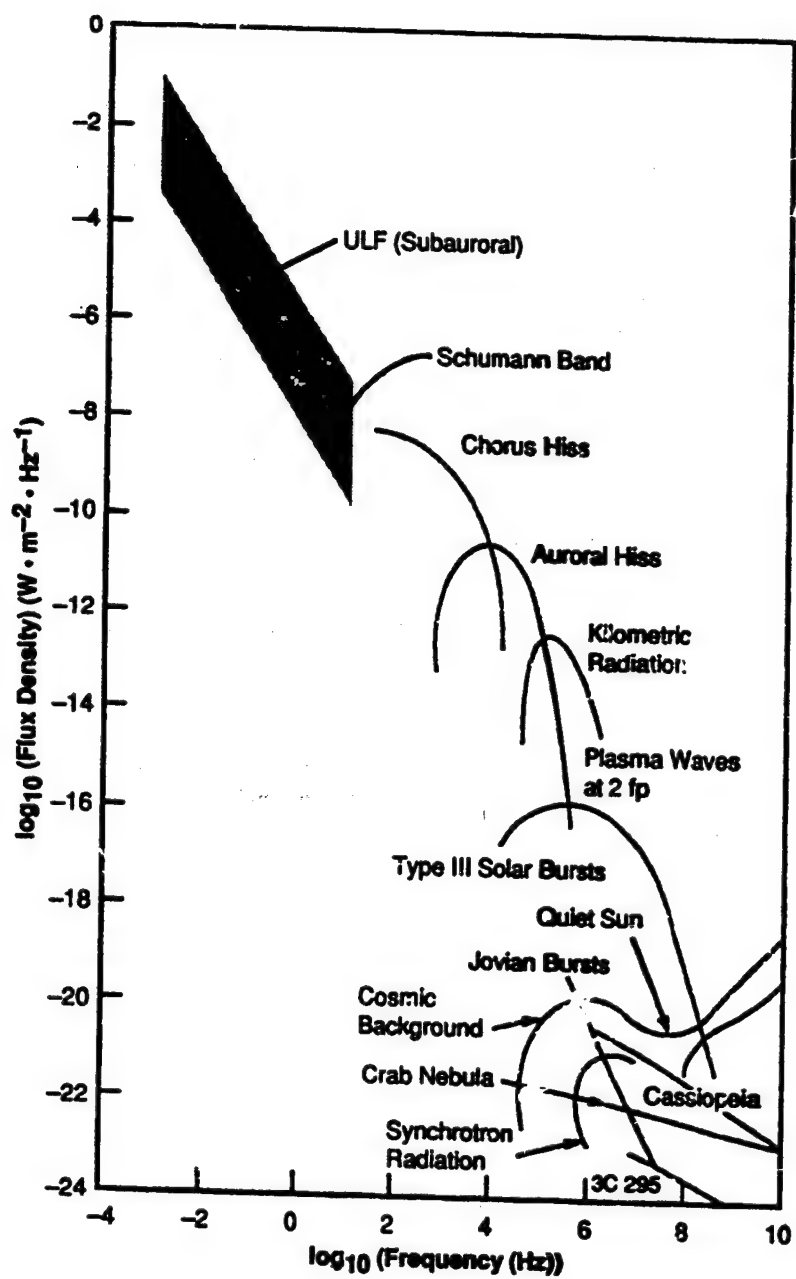


Figure 6-4. Power flux levels for various frequency ranges of naturally occurring electromagnetic and plasma waves.²⁵

The electric field E (mV/m) at a distance z (kilometers) from any RF transmitter can be estimated with the formula:

$$E = (30 \text{ ERP})^{1/2} / z, \quad (6-5)$$

where ERP (watts) is the effective radiated power which equals the product of the transmitter power and the antenna gain.

Thus, a radar with a power of 10 kW and an antenna gain of 40 dB (10 000) will result in fields of over 100 mV/m at 500 km altitude. Presumably a source such as a radar will have a very narrow beam width (perhaps less than a degree) but will be wept over wide loci of look directions. Occasionally, ionosphere research transmitters are also operated which produce measurable heating of the ionospheric plasma and have power levels in the same range as the defense radars but wider beam patterns.

In June 1983, the U.S. Air Force Space Division requested the Department of Defense Electromagnetic Compatibility Analysis Center (ECAC) to identify the worldwide RF electromagnetic environment (EME) for hypothetical spacecraft at various LEO's. The results of this task are documented in the "Worldwide Spacecraft EME Definition," report number ECAC-CR-85-065, USAF Space Division (refs. B and I).

VII. METEORIODS AND ORBITAL DEBRIS

Once in orbit, a space vehicle will encounter meteoroids and orbital debris. Either object can pose a serious damage or decompression threat to the vehicle. Meteoroids are natural in origin, and debris is the result of manmade material remaining in Earth orbit. General information and discussion appears in references 26 and 27. The debris model presented here has been recommended for most, if not all, NASA engineering applications since mid-1990. Comments have been added where recent measurements or studies have confirmed or raised issues with model results. The model is still recognized as the best available and valid within stated uncertainties; no improvements or updates are expected in the near future.

For historical reasons related to measurement method, the meteoroid and debris environments are usually specified as a time-averaged flux, F_r , against a single-sided, randomly tumbling surface. Flux is defined as number of intercepted objects per unit time and area. For F_r , the relevant area is the actual surface area of the satellite. One may also define a "cross-sectional area flux," F_c , for a randomly tumbling satellite, where the relevant area is the time-averaged cross sectional area. A useful theorem which is obvious for a tumbling sphere but which holds for objects of arbitrary non-self-shielding shape (no concave surfaces), is that $F_c = 4 F_r$.

For spacecraft which fly with a fixed orientation, the meteoroid and orbital debris fluxes are treated as vector quantities, F , and the effects of directionality must be carefully evaluated. Some effects of impact will be direction dependent. To simply evaluate the expected number, N , or probability of impacts from either meteoroids or debris (or both), one may use a "k-factor" method and the appropriate F_r , such that:

$$N = \int_0^T \sum_i k_i F_r A_i dt, \quad (7-1)$$

where the summation is over the i surfaces of the spacecraft, each of area A_i , and $k_i F_r$ is the actual flux on surface A_i . The calculation of k_i is discussed in section 7.3.

Once an N has been determined, the probability of exactly n impacts occurring on a surface in the corresponding time interval is found from Poisson statistics, thus;

$$P_n = \frac{N^n}{n!} \cdot e^{-N}. \quad (7-2)$$

7.1 Meteoroids

The meteoroid environment encompasses only particles of natural origin. Nearly all meteoroids originate from comets or asteroids. Meteoroids that retain their parent body orbit and create periods of high flux are called streams. Random fluxes with no apparent pattern are called sporadic.

The average total meteoroid environment presented is comprised of the average sporadic meteoroids and a yearly average of stream meteoroids. The mass density for meteoroids spans a wide range, from approximately 0.2 g/cm³ or less for a portion of the population to values as large as 8 g/cm³. The values for average mass density vary widely, so that a value can only be estimated. Recommended

mean values are 2 g/cm^3 for meteoroids smaller than 10^{-6} g , 1 g/cm^3 for meteoroids between 10^{-6} and 0.01 g , and 0.5 g/cm^3 for masses above 0.01 g . The uncertainty in density is not too serious because the model presented below was derived from crater and impact data and will provide a good representation of expected damage even though absolute mass calibration could conceivably be in error by as much as a factor of 10 for the smallest sizes.

Because of the precession of a satellite's orbit and the tilt of the Earth's equatorial plane with respect to the ecliptic plane, the meteoroid environment can be assumed to be omnidirectional relative to Earth for design applications. However, it becomes directional relative to a spacecraft moving through the environment with most meteoroids coming from the direction of motion. The directionality derives from the vector summation of the spacecraft velocity vector with the meteoroid velocity distribution. An additional directionality factor is introduced by the shielding provided by Earth.

The normalized meteoroid velocity distribution with respect to Earth is illustrated by figure 7-1. It is given by the expressions (number per km/s):

$$\begin{aligned} n(v) &= 0.112, & 11.1 \leq v < 16.3 \text{ km/s}, \\ n(v) &= 3.328 \times 10^5 v^{-5.34}, & 16.3 \leq v < 55 \text{ km/s}, \\ n(v) &= 1.695 \times 10^{-4}, & 55 \leq v \leq 72.2 \text{ km/s}. \end{aligned} \quad (7-3)$$

This distribution has an average velocity of about 17 km/s; relative to an orbiting spacecraft the average velocity is about 19 km/s. To determine the velocity and direction distributions relative to any surface on an orbiting spacecraft, the vector relationship between the meteoroid velocity and the spacecraft velocity should be used as discussed in paragraph 7.3.

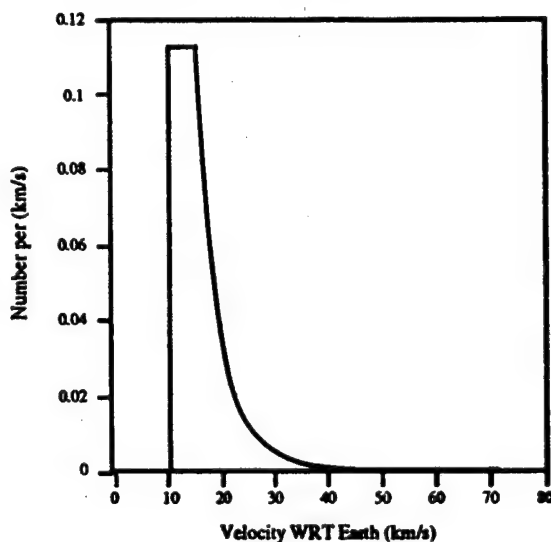


Figure 7-1. Normalized meteoroid velocity distribution from equation (7-3).

Meteoroid flux is given in terms of the integral flux F_r , the number of particles/m²/year of mass m or greater against a randomly tumbling surface. F_{ip_r} , the interplanetary flux at 1 au is described mathematically as follows (for $m \leq 10$ g):

$$F_{ip_r}(m) = c_0 \{ (c_1 m^{0.306} + c_2)^{-4.38} + c_3 (m + c_4 m^2 + c_5 m^4)^{-0.36} + c_6 (m + c_7 m^2)^{-0.85} \}, \quad (7-4)$$

where:

$$c_0 = 3.156 \times 10^7,$$

$$c_1 = 2.2 \times 10^3,$$

$$c_2 = 15,$$

$$c_3 = 1.3 \times 10^{-9},$$

$$c_4 = 10^{11},$$

$$c_5 = 10^{27},$$

$$c_6 = 1.3 \times 10^{-16},$$

$$c_7 = 10^6.$$

To convert the meteoroid flux, F_{ip_r} , stated above to that in Earth orbit, F_r , both Earth shielding and focusing factors must be applied, $F_r = s_f G_E F_{ip_r}$. The formula for shielding is:

$$\text{shielding factor} = s_f = (1 + \cos \eta)/2, \quad (7-5)$$

where

$$\sin \eta = R_E / (R_E + H),$$

where R_E = Earth radius + 100 km atmosphere (6478 km) and H = height above Earth's atmosphere (Earth's atmosphere height to be taken as 100 km for this purpose). Consequently, the Earth shielding factor varies from 0.5 just above the atmosphere to 1.0 in deep space.

The factor G_E represents the focusing effect of Earth's gravitational field which attracts meteoroids and increases their flux. The factor ranges from a value of 2.0 just above the atmosphere to a value of 1.0 in deep space. The focusing factor is represented by the following equation:

$$\text{focusing factor} = G_E = 1 + (R_E/r) \quad (7-6)$$

where R_E = Earth radius + 100 km atmosphere (6478 km) and r = orbit radius. The meteoroid environment at 500 km is illustrated in figure 7-2.

7.1.1 Uncertainty in the Meteoroid Environment. Except for small cosmic dust grains directly collected from the stratosphere, the physical properties of meteoroids must be determined by relatively indirect means, examination of impact craters, optical scattering, etc. They are also known to originate from comets (apparently composed of low density "ices" and dust) and asteroids which are rock-like. Therefore, there is considerable uncertainty in their properties. In particular, the uncertainty in mass tends to dominate the uncertainties in the flux measurement. For meteoroids less than 10^{-6} g, the mass is uncertain to within a factor from about 0.2 to 5 times the estimated value, which implies the flux is

ncertain to within a factor of 0.33 to 3 at a given mass. For meteoroids above this size, the flux is well efined but the associated mass is even more uncertain. This implies an effective uncertainty in the flux at a set mass) of a factor from 0.1 to 10 (because of the slope of the functional relationship).

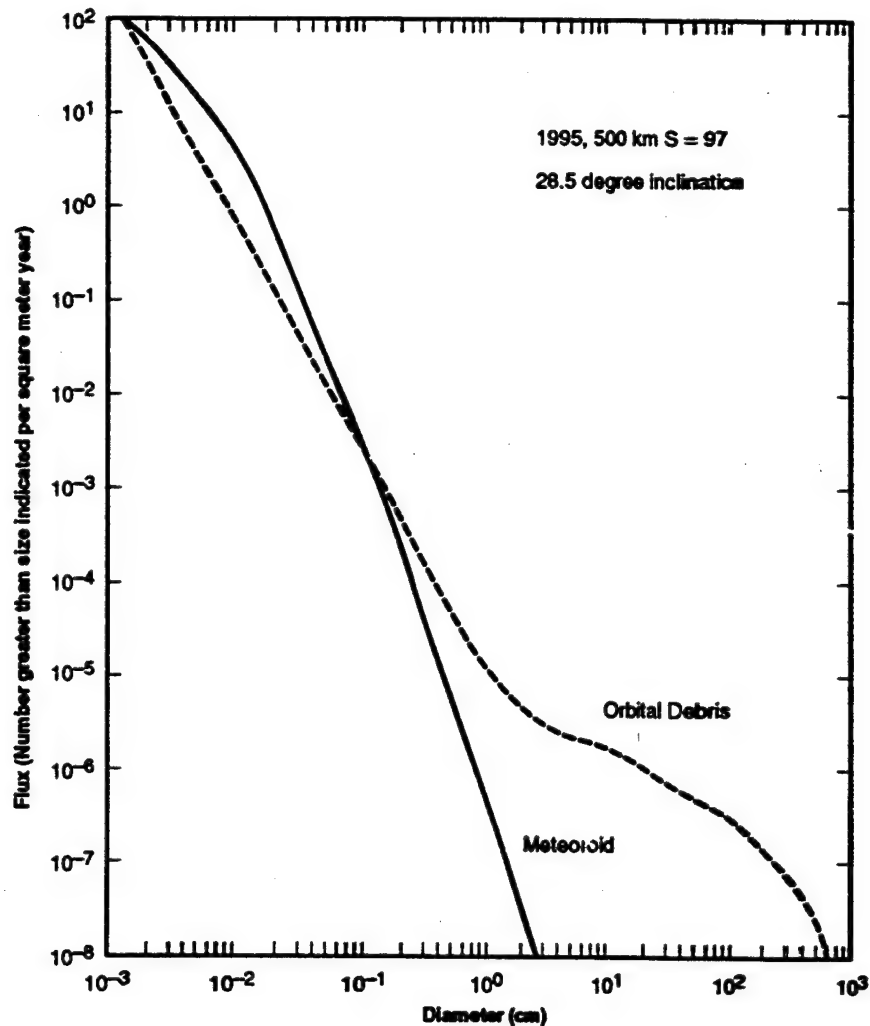


Figure 7-2. Comparison of meteoroid and orbital debris fluxes, F_p , as a function of size.

2 Orbital Debris

7.2.1 Background. The natural meteoroid flux discussed above represents, at any instant, a total about 200 kg of mass within 2000 km of the Earth's surface, most of it concentrated in the 0.1 mm meteoroids. Within this same 2000 km, there is an estimated 1.5 to 3 million kg of manmade orbiting objects as of mid-1988. Most of these are in high inclination orbits where they sweep past each other at average speed of 10 km/s. About 1500 spent rocket stages, inactive payloads, and a few active payloads account for most of this mass. These objects are currently tracked by the USAF Space Command, are about 4500 others totaling 20 000 kg, mostly fragments of satellites or other orbiting hardware.

Recent observations indicate a total mass of about 1000 kg for orbital debris with diameters of 1 cm or smaller and about 300 kg for orbital debris sizes smaller than 1 mm. This distribution of mass makes the orbital debris environment more hazardous than the meteoroid environment in most spacecraft applications below 2000 km altitude.

The debris model presented in the following represents an extension of the model presented by Kessler et al.²⁷ First, a curve fit to the "current" debris environment was developed based on the best experimental data available. This was then coupled with additional terms which represent a projection of the expected environment change into the future. The year 1988 was selected as the base year for the "current" environment. The applicable data sets include those referenced by Kessler et al.,²⁷ i.e., the analysis of panels returned from the Solar Max satellite, data from the MIT ETS telescopes, and USAF Space Command cataloged and uncataloged data sets. In addition, updates were added from recent optical measurements made with the GEODSS telescope systems and from biphasic radar measurements made with the Arecibo and Goldstone radars. Quick-look data from the Long Duration Exposure Facility (LDEF) appears to be consistent with these data sets, but analysis was not sufficiently complete to allow incorporation of this information. The model is valid for debris diameters of 1 μ m and larger (although it is known that some debris smaller than 1 μ m does exist). Measurements made with the Haystack radar after this model was developed, through 1992, fit well within the uncertainty bands of the model. However, they do seem to indicate that there is some additional debris in low inclination orbit that was not accounted for, and that the size of the material in the 3- to 10-cm size range was overestimated by a factor of about 1.4. These data are still being studied so that no changes in the current model are expected in the near future.

Model development, especially prediction of future trends in the debris environment, is difficult and subject to substantial uncertainty. The problems may be grouped into two categories which must be treated somewhat differently. The categories are:

- (a) Uncertainties in the current environment. These uncertainties shift the flux by a factor which is independent of time (a change in intercept on a flux versus time plot). They include uncertainties of measurement, statistical limitations of the data sets, and voids in the data sets, i.e., size and altitude ranges where no measurements have been made, limitations of debris shape and density information, etc.
- (b) Uncertainties related to trend projection. These factors alter the slope of a flux versus time plot. They derive primarily from the assumptions which must be made to predict future trends in human activities (launch rate for example, which historically has deviated significantly from the traffic model projections) and from assumptions needed to overcome the technical uncertainties listed above. The state-of-the-art is such that understanding is still lacking in several important areas necessary for complete engineering analysis and numerical modeling of the environment. Key examples include incomplete knowledge of satellite and rocket body fragmentation mechanics (e.g., fragment size and velocity distributions) and uncertainty in the cause and intensity of many fragmentation events. There are also important limitations in modeling capability due to the necessity of keeping computation time and model complexity within reasonable limits. These all have important influence on the final results.

Before discussing these issues in detail, we present the numerical formalism of the model in the following three sections. Then, in section 7.2.5, the uncertainties and assumptions are listed in detail along with a quantitative estimate of their importance.

7.2.2 Orbital Debris Flux to a Tumbling Surface. A vectorial description of the orbital debris environment is presented in section 7.3. However, the description is based on the flux to a randomly tumbling surface and the velocity distribution, so these concepts are presented first.

The cumulative flux of orbital debris of diameter, d , and larger on a randomly tumbling spacecraft orbiting at altitude, h , inclination, i , in the year, t , when the solar activity was S 1 year prior to t , is given by the following equation:

$$F_c(d, h, i, t, S) = H(d) \phi(h, S) \psi(i) [F_1(d) g_1(t) + F_2(d) g_2(t)] \quad (7-7)$$

where

F_c = flux, impacts per square meter of surface per year,

d = orbital debris diameter in cm, ($10^{-4} \leq d \leq 500$)

t = date (year),

h = altitude in km ($h \leq 2000$ km),

S = 13-month smoothed solar radio flux $F_{10.7}$ for $t-1$ year, expressed in 10^4 Jy; for future applications select from the Min column in table 3-1 (this will produce a conservative design),

i = inclination in degrees,

and

$$H(d) = [10^{\exp(-0.000104 - 0.707/0.037^2)}]^{1/2}$$

$$\phi(h, S) = \phi_1(h, S) / (\phi_1(h, S) + 1)$$

$$\phi_1(h, S) = 10^{0.000200 - S/140 - 1.5}$$

$$F_1(d) = 1.22 \times 10^{-5} d^{-2.5}$$

$$F_2(d) = 8.1 \times 10^{-10} (d + 700)^{-6}$$

p = the assumed annual growth rate of mass in orbit = 0.05,

q and q' = the estimated growth rate of fragment mass; $q = 0.02$; $q' = 0.04$. The q' term is only used for 2011 and later dates.

$$g_1(t) = (1+q)^{(t-1988)} \quad \text{for } t < 2011,$$

$$g_1(t) = (1+q)^{23} (1+q')^{(t-2011)} \quad \text{for } t \geq 2011,$$

$$g_2(t) = 1 + p(t-1988).$$

The inclination-dependent function, $\psi(i)$, defines the relationship between the flux on a spacecraft in an orbit of inclination, i , and the flux incident on a spacecraft in the current population's average inclination of about 50° . Values for $\psi(i)$ are as follows:

Inclination i (degrees)	$\psi(i)$
28.5	0.91
30	0.92
40	0.96
50	1.02
60	1.09
70	1.26
80	1.71
90	1.37
100	1.78
120	1.18

An example orbital debris flux is compared with the meteoroid flux from equation (7-4) in figure 7-2 for $h = 500$ km, $t = 1995$, $i = 28.5^\circ$, and $S(t-1 \text{ yr}) = 97.0$.

7.2.3 Average Shape and Mass Density. The state of knowledge of debris shape and density is very scant. Actual shapes are irregular, including flat plates, rods, hollow structures, and crumpled metal. As size decreases, the objects tend to be somewhat less irregular. For the purposes of this model, the objects are assumed to be spherical, with a size-dependent mass density function to approximate these irregularities and the probability that they may impact with any orientation.

The average mass density for debris 0.62 cm and larger is:

$$\rho = 2.8 d^{-0.74} \quad (\text{g/cm}^3, d \text{ in cm}) \quad (7-8)$$

or debris smaller than 0.62 cm,

$$\rho = 4.0 \text{ g/cm}^3 \quad (d < 0.62 \text{ cm}) .$$

That is, for small objects the mean density should be assumed to be a constant, 4.0 g/cm^3 , independent of size. Actual shape and density distributions are very broad. This issue, in particular material density as opposed to object density, is addressed further in section 7.2.5.3.

7.2.4 Velocity and Direction Distribution. Averaged over all altitudes, the non-normalized collision velocity distribution, i.e., the number of impacts with velocities between v and $v+dv$, relative to spacecraft with orbital inclination, i , and considering the debris is in a locally horizontal plane, is given by the following equations:

$$f(v) = \{2v v_0 - v^2\} \{G \exp[-((v - Av_0)/(Bv_0))^2] + F \exp[-((v - Dv_0)/(Ev_0))^2]\} + HC(4v v_0 - v^2) \quad (7-9)$$

where v is the collision velocity in km/s, A is constant, and B, C, D, E, F, G, H , and v_0 are functions of orbital inclination of the spacecraft. The values for these constants and parameters are as follows:

$$A = 2.5$$

$$B = \begin{cases} 0.5 & i < 60 \\ 0.5 - 0.01(i-60) & 60 < i < 80 \\ 0.3 & i > 80 \end{cases}$$

$$C = \begin{cases} 0.0125 & i < 100 \\ 0.0125 + 0.00125(i-100) & i > 100 \end{cases}$$

$$D = 1.3 - 0.01(i-30)$$

$$E = 0.55 + 0.005(i-30)$$

$$F = \begin{cases} 0.3 + 0.0008(i-50)^2 & i < 50 \\ 0.3 - 0.01(i-50) & 50 < i < 80 \\ 0.0 & i > 80 \end{cases}$$

$$G = \begin{cases} 18.7 & i < 60 \\ 18.7 + 0.0289(i-60)^3 & 60 < i < 80 \\ 250.0 & i > 80 \end{cases}$$

$$H = 1.0 - 0.0000757(i-60)^2$$

$$v_0 = \begin{cases} 7.25 + 0.015(i-30) & i < 60 \\ 7.7 & i > 60 \end{cases}$$

When $f(v)$ is less than zero, the function is to be reset equal to zero. The user may find it convenient to numerically normalize $f(v)$ so that;

$$f'(v) = \frac{f(v)}{\int f(v)dv} \quad (7-10)$$

When normalized in this manner, $f'(v)$ over any 1 km/s velocity interval becomes the fraction of debris impacts within a 1 km/s incremental velocity band. The function is illustrated in figure 7-3. Any n^{th} velocity moment may be defined as

$$v^n = \int_0^7 v^n f'(v) dv \quad (7-11)$$

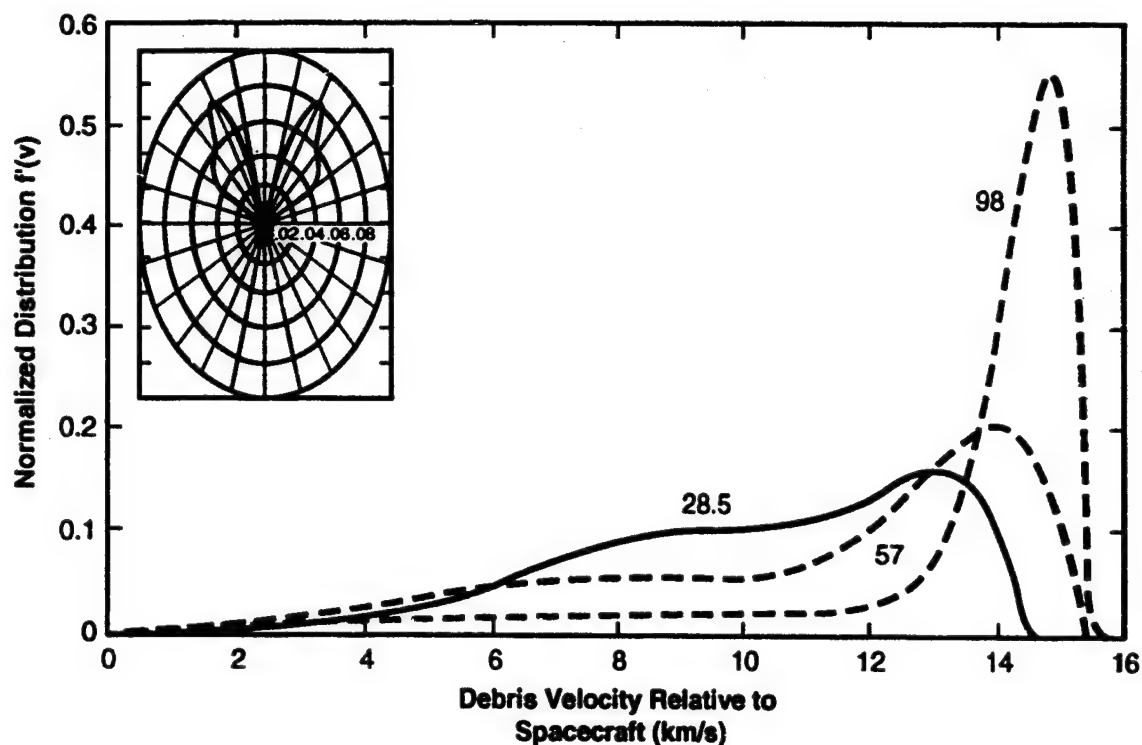
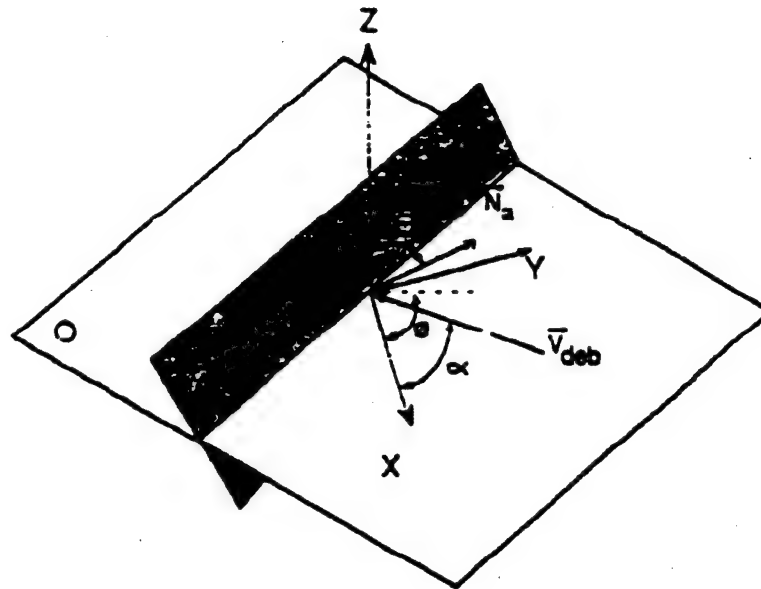


Figure 7-3. Normalized collision velocity distribution as function of the debris velocity for a spacecraft with orbital inclinations of 28.5°, 57°, and 98°.

Frequency of impact from a given direction can be estimated by using this velocity distribution. *Direction of impact is assumed to be specified by the intersection of the spacecraft velocity vector and another circular orbit.* That is, the relative velocity vectors may be obtained by vector addition in a plane tangent to the Earth's surface. Since a spacecraft velocity of 7.7 km/s was used to calculate relative velocity, the direction of the relative velocity vector is given by the relationship:

$$\cos(\pm\alpha) = \frac{v}{v_{\max}} = \frac{v}{15.4} \quad (7-12)$$

where α is the angle between the impact velocity vector and the spacecraft velocity vector in a coordinate system fixed with respect to the space vehicle, v is the impact velocity, and v_{\max} is the maximum possible velocity difference between the debris and the spacecraft. The coordinate system is illustrated in figure 7-4.



DEFINITIONS:

Plane A represents a surface of the spacecraft.

N_a is the unit vector normal to the plane A.

x is the direction of travel of the spacecraft.

V_{deb} is the debris velocity relative to the spacecraft.

O is the tangent plane (horizontal) to the spacecraft's orbit.

A right-handed coordinate system (positive x, y, z) is defined in plane O as:

x: direction of spacecraft travel

y: 90° from x and in plane O (port direction)

z: Earth vertical (up)

ANGLES:

α is the angle between x and V_{deb} .

θ is the zenith of N_a with respect to the Z axis in this reference frame.

ϕ is the azimuth of N_a with respect to the spacecraft direction of travel.

Figure 7-4. Orbital debris reference frame.

7.2.5 Limitations and Uncertainty in the Debris Flux Model

7.2.5.1 Measurements of the Current Environment (Factors Which Alter the Intercept of Flux Growth Curves). For orbital debris sizes larger than 10 cm in diameter, the environment is generally measured by ground radars. The most extensive measurements are made by the USAF Space Command, which also maintains a catalog of the debris population. While these data provide an adequate description of the distributions of large debris with respect to altitude and inclination, and of historical trends, analysis of GEODSS optical telescope data has shown that the radars are detecting, and the Space Command

is cataloging, less than half of the population in this size range. This information has been incorporated in the model presented here, so that the model represents the current environment in this size range accurately to within the range 1.5 to 0.5 times the flux, i.e., the "90-percent confidence" upper limit flux equals 1.5 times the flux from equation (7-7), etc. Table 7-1 summarizes the uncertainties and accuracy limitations in the orbital debris flux model.

Measurement of the debris flux at the other size extreme, sizes smaller than 0.05 cm, is made by analysis of impact craters on pieces of space hardware returned from orbit. Meteoroid impacts are distinguished from debris impacts by analysis of the chemical elements retained in the crater. For these sizes, the flux has only been measured on hardware flown at about 500 km; at this altitude the environment is known within the range 2 to 0.5 times the flux.

Until recently, the only measurements between the two debris size extremes was a limited set of optical telescope data from the MIT ETS telescopes. This provided an indication of the cumulative flux for objects believed to be 2 cm and larger. For intermediate sizes, the environment was estimated by a simple straight line interpolation on a log-log, flux versus size plot, as in figure 7-2. This practice was retained for the current model, but in this case the interpolation is confirmed by recent measurements by Arecibo and Goldstone radars in the important midrange between 0.2 and 2 cm. These show a detection rate which is consistent with the current model, but both systematic and random errors in these measurements leave the environment uncertain within 3 to 0.33 times the flux for these sizes. Measurements were only made between 500 and 600 km altitude. Between 2 and 10 cm, no measurements exist, but interpolation of the data from either side and modeling this region also yielded an estimated uncertainty between 3 and 0.33 times the best estimate.

7.2.5.2 Trend Projection (Factors Which Alter the Slope of Flux Growth Curves). As is the case with any analysis or model, the results hold only so long as the underlying assumptions remain valid. The following are the key assumptions upon which the model rests:

(1) It is assumed that the rate of accumulation of mass in LEO is constant, with the annual increase equal to 5 percent of the amount accumulated by 1988. This matches the historical trend over the last few decades.

(2) The relative use of different orbits is assumed to remain constant. For example, the history of launches by the USSR has been such that 80 percent of their payloads re-enter within 2 years of launch. These do not contribute significantly to the debris environment. If this practice changed with increased use of higher, longer life orbits, the population of objects in orbit would grow at a proportionally increased rate.

(3) It is assumed that the efforts to minimize fragmentation of satellites in orbit will continue such that fragmentation events will continue at the rate of only one per year in LEO (29 percent of past practice). In the last decade, intentional (or apparently intentional) fragmentation of satellites accounted for about 71 percent of the known fragmentation events. Apparently, recent publicity and increased awareness of the hazards associated with orbital debris has generated policy shifts among the space-faring nations. No intentional fragmentation events above 300 km have been observed in the last 5 years. Indeed, for a period of about 2 years, there were no significant events at all. However, from October 1990 through February 1991 there have been 14 unintentional breakup events, about half of which must be considered significant. This is roughly equivalent to the breakup rate observed in the early 1980's.

Table 7-1. Uncertainties and accuracy limitations.

Uncertainty in Current Environment (Intercept Shift)			
	Treatment	"90 Percent Confidence"	Notes
Flux Measurements ($d > 10$ cm)	Best Est	1.5 to 0.5×(1988 Flux)	
Flux Measurements (0.05 cm $< d < 10$ cm)	Best Est	3 to 0.33×(1988 Flux) in this size range	Due to statistical and measurement limitations in portions of range, data missing (interpolation used) in rest of range.
Flux Measurements ($d < 0.05$ cm)	Best Est	2 to 0.5×(1988 Flux) in this size range	
Altitude Distribution ($d < 10$ cm)	Best Est	5 to 0.2×(1988 Flux) per 200 km away from 500 km	Due to difficulty in determining flux in highly elliptical orbits
Altitude Distribution ($d \geq 10$ cm)	Smoothed Best Est	2 to 0.5×(1988 Flux) See Figure 7-5	Uncertainty is somewhat worse in 800 and 1000 km regions
Debris Density ($d < 1$ cm)	Simplified Best Est	0.10 @ 1.8/0.5 @ 2.8 0.10 @ 4.5/0.3 @ 8.9	Estimated typical "heavy" distribution. Insufficient data to develop a true uncertainty limit estimate.
Debris Density ($d > 1$ cm)	Simplified Best Est	2 to 0.5 Mean Density	Mean values are fairly well defined but number vs. density distribution is broad
Debris Shape	Simplified Nonconserv.		Spherical shape is assumed, actual debris will be irregular.
Velocity Distribution, Fraction < 5 km/s	Best Est	0.5 to 3×(Slow Fraction)	Distribution of orbit inclinations could be in error or change with time.
Uncertainty in Trend Projection (Slope Shift)			
	Treatment	"90 Percent Confidence"	Notes
Launch Rate	Best Est	} $p = 0.04$ to "comp p" = 0.1 $q = 0$ to 2p	"comp p" implies $g_2 = (1+p)^{(t-1988)}$. Worst case assumes combined effect of increased traffic and increased use of LEO above 400 km
Orbit Use Profile	Best Est		
Fragmentation Rate	Best Est	} $q = 0$ to 0.10	Assuming no changes in projected launch rate and orbit use profile.
Fragmentation Mechanics	Best Est		
Statistical Variation of Fragmentation	Best Est	0.5 to 1.5×(Current Flux)	
Solar Activity	Best Est	Substitute "Max" and "Min" values from Table 3-1	Model tends to overestimate variation with solar cycle so these would be extreme limits
"Local" Fragmentation Events	Nonconserv.	+4×(1988 Flux) for 1 Year	Difficult to assess, depends strongly on type of event and proximity to station orbit. Ignored in current model.

(4) It is assumed that the debris size distribution is independent of altitude. One would expect small debris in circular orbits to decay faster than large debris, implying an altitude-dependent distribution. However, consideration of the population of small fragments in elliptical orbits, assuming a trend similar to the one for large fragments, leads to a dependent distribution with the opposite trend. Therefore, pending further measurements and research, an intermediate assumption has been made.

(5) It is assumed that future solar cycles will affect debris orbit decay uniformly for all sizes. The uncertainties associated with these factors differ from those discussed above in that they alter the growth terms in equation (7-7) rather than entering as multipliers of the total flux. Thus, the variations are expressed as variations of the p , q , and S terms.

The first two of these assumptions relate to the predicted future accumulation of objects in LEO. This is a key determinant of the expected debris growth rate—the value of p . The combination of a decreasing launch rate for the United States with an increasing rate for the rest of the world has led to the relatively constant historical trend. It is not clear, however, that this trend will continue. Expected launch rates are subject to political and economic influences which may change unpredictably, and many new countries are becoming involved in space activities. Current traffic models extended to the year 2010 predict that future growth will be at a compounded rate between 5 and 10 percent per year. The lower limit of these models corresponds to a value of $p = 0.05$ compounded annually. These models represent the projects that are planned, and since some projects are either canceled or postponed, the actual rate has always fallen below the traffic models. Therefore the baselined rate is a constant (not compounded) $p = 0.05$. A substantially lower rate would only be expected in the case of a worldwide economic depression or similar event. A higher rate is possible, especially if an increased launch rate is coupled with an increased use of higher, long-life orbits. A compounded 10 percent per year increase, or $p = 0.1$, represents the "90-percent confidence level" upper limit.

The value of q , which represents the expected growth rate of small debris, primarily depends on the frequency of expected satellite breakup—assumption (3). Breakups may be intentional, or they may result from accidents and random collisions. Thus, the breakup rate is partially controllable, partially not. The value selected for this model, $q = 0.02$, assumes no intentional breakups, and an accidental breakup rate of 1 per year. The range of possible q values is from 0.0 (random collisions are not important and improved precautions lower the accidental rate below historical values) to 0.06 (both accidental and intentional fragmentation rates match the 1980 to 1987 rates). Technically, negative values of q are possible if all fragmentation events are prevented, but this is not considered a credible possibility. At the other extreme, if fragmentation rates rise above the 1 per year and the rate of accumulation of mass in orbit increases, on-orbit collisions become important, and q will approach $2p$.

Unintentional fragmentation events can result from either explosions or collisions between objects. The first of these represents a simple linear source: the population growth is directly related to the fragmentation rate. The second is exponential in nature, since the number of fragmentation events is a function of the square of the population. Thus, the coupling between p and q uncertainty limits noted above. Modeling these processes indicates that the first process will be dominant until about the year 2010. About that time, under the assumptions of the current model, the second process becomes significant, and the small particle population will grow at an increasing rate. If the assumptions of the current model hold and current practices continue, q is expected to increase to 0.04 beginning about the year 2010.

Uncertainties in the mechanics of fragmentation events, i.e., fragment size, number, and velocity distribution, impact the capability to model and analyze the debris environment. Fragmentation events have multiple possible causes and may vary widely in intensity. Direct data from simulations of these processes are quite limited. In the analysis supporting the current model, these limitations were overcome by tuning the fragmentation model so that the historical fragmentation record reproduced the current environment. This approach provides the "best estimate" fragmentation models for the analysis, but it is very limiting in the sense that there is no independent check of the analysis. Since there are only

recent measurements of the small fragment environment, there is no second point to check the analysis against. The associated uncertainty has been included within the $2p$ factor described above.

Assumption (4) is necessary because there were no measurements of debris smaller than 2 cm at other than in the 500 to 600 km altitude range when this model was developed, and because poor knowledge of the fragment velocity distributions (and computer run-time limitations) makes it impractical to model small fragments in highly elliptical orbits. The recent Haystack measurements indicate this assumption is good up to 1000 km, but falls apart for higher altitudes. No data are available at 1500 km or above. Additional study is needed in this area. Analysis indicates that the actual flux of small material could trend either above or below the large object distribution with altitude, depending upon the assumptions used. The model presented here assumes that the distribution with altitude for the small material matches the catalog distribution. The actual amount that these fluxes differ could be as high as a factor from 5 to 0.2 for every 200 km away from the 500 km altitude. The distribution with respect to altitude is also assumed to be smooth. Actually, the USAF Space Command data (sizes larger than 10 cm) give fluxes at 800 and 1000 km, which approach the level predicted by the recommended flux model, as shown in figure 7-5, not allowing for the correction factor from the GEODSS telescope study.

With respect to assumption (5), the possible variance of solar activity can be well defined based on the historical record. A high solar cycle will increase the depletion rate for debris in low-altitude orbits, compared to a mean or low cycle, but prediction of the solar activity level beyond about 1 year is highly uncertain. Table 3-1 provides profiles of maximum and minimum solar activity, and these values may be used in equation (7-7) to estimate the range of variation.

An important short-term factor that is not included in the model and thus contributes an additional uncertainty is the flux arising from the intentional or inadvertent fragmentation of a satellite in an orbit at or near the proposed space vehicle operating altitude. In the region of the breakup, an enhanced flux may be apparent for a considerable period of time, depending upon the altitude of the breakup and the size and velocity distribution of the debris. Analysis and modeling of various scenarios indicates that such an event would probably cause increases in the flux environment by factors of a few tens of a percent for a year or more, although a factor of 4 may be possible as an extreme worst case.

7.2.5.3 Uncertainties in Direction, Velocity Distribution, and Density. The fact that orbital debris objects are not in exactly circular orbits will introduce a small error in direction. As a result of the currently small eccentricities of debris orbits, the actual directions of impacts are within 1° for most velocities derived from section 7.2.4. For velocities less than 2 km/s, the uncertainty is much larger, with a significant fraction being more than 20° from the direction derived from section 7.2.4. These errors in direction can be in the local horizontal plane, or they can appear as direction errors above or below this plane.

Uncertainty in the distribution of debris orbit inclinations leads to an uncertainty in the velocity distribution which can affect penetration analysis. Since inclinations are only known for large (cataloged) debris, the small fragments may have a different distribution, or the distribution may change with time as a result of orbit selection and fragmentation events. These considerations imply the slow fraction of the population, i.e., the fraction of debris objects with a relative speed less than 5 km/s with respect to a vehicle, could shift or be in error by a factor from 0.5 to 3.

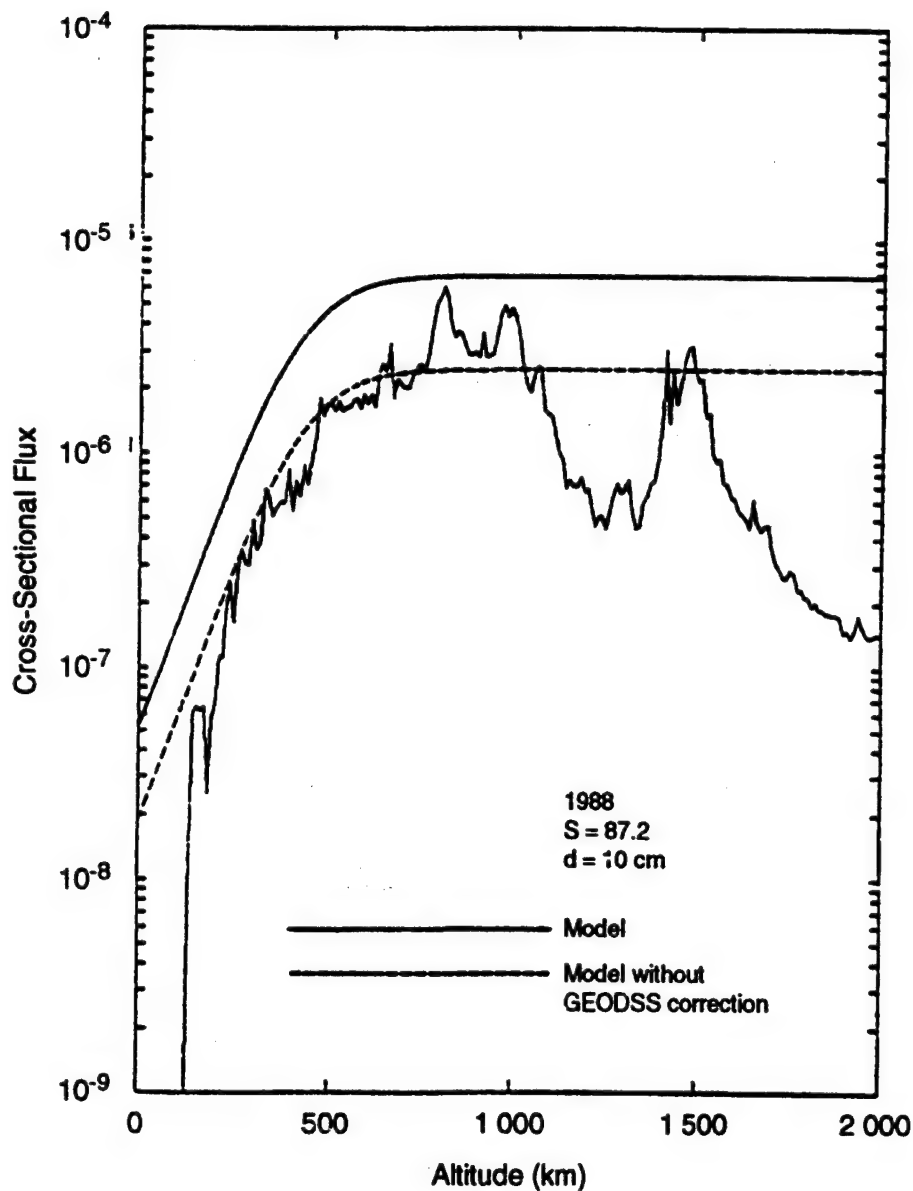


Figure 7-5. Comparison of model flux, F_c , with catalog flux not corrected for GEODSS results.

The expression for debris density given in section 7.2.3 for objects larger than 0.5 cm has been verified by direct measurements of actual objects, studies of orbit decay, and fragmentation experiments. Thus, it is believed to be a good representation of the mean density of the debris population (within a factor of 0.5 to 2), especially for sizes above 30 cm. However, it represents the mean of a broad distribution; the density of individual objects can vary widely.

For small fragments, the density issue is more difficult because information is extremely scant. To illustrate the problem, consider the following materials density profile based on a summary review of space shuttle materials usage (neglecting tiles):

Estimated Volume Fraction	Specific Gravity	Representative Materials
0.65	2.8	Aluminum, Glass
0.15	1.8	Epoxy-Glass, Rubber
0.05	4.5	Titanium
0.15	7.8 to 8.9	Copper, Steel

One might expect that this would be typical of many spacecraft, but it may underestimate the fraction of dense materials for several reasons. First, many objects involved in fragmentation events are believed to have had a higher fraction of dense materials used in their construction. The Delta second stages, for example, contain about 70-percent steel, 20-percent aluminum, and 10-percent titanium. Second, low-density objects are more affected by drag and, thus, decay from orbit more rapidly. However, fragment shape is also an important determinant of effective density. The thickness of the Delta walls is between 0.2 and 0.5 cm, so fragments larger than this would be irregular in shape with an effective density less than that of steel. Since definitive studies have not been done, uncertainty bounds cannot be defined at this time. For study purposes the recommended "heavy" distribution is: 10 percent (by volume) at 1.8, 50 percent at 2.8, 10 percent at 4.5, and 30 percent at 8.9 g/cm³. This gives a mean density of 4.7 g/cm³ for solid spheres.

7.3 Evaluation of Directionality Effects

The parameter k which appears in equation (7-1) is defined as the ratio of the flux against an oriented surface to the flux against a randomly tumbling surface. Introduction of the k factor allows application of the flux (equation (7-7)) to evaluate the expected number and probability of impacts on surfaces flying with fixed orientation. Evaluation of penetration probability should be by numerical techniques which account for the directional dependence of both the penetration equations and the meteoroid and debris fluxes, although the k factor may be useful for quick approximations. The value of k can theoretically range from 0 to 4; a value of 4 can only be achieved when a surface normal vector is oriented in the direction of a monodirectional flux. It depends on the orientation of the surface with respect to the Earth vertical and the spacecraft velocity vector. If the surface is randomly oriented, then $k = 1$.

Care must be taken in evaluating k factors and other directional effects because of the complex directional nature of the meteoroid and debris fluxes. Unlike most fluxes with which the engineer and physicist deals, the meteoroid and debris fluxes do not have a unique direction associated with them at any given point in space. Meteoroids are equally likely to appear from any direction (except where the Earth provides shielding) in a reference frame fixed with respect to the Earth; they tend to appear from the ram direction on an orbiting satellite. The relative velocity with respect to a randomly tumbling spacecraft is about 20 km/s. The approach for evaluating k for meteoroids will be similar to the approach for debris which is presented below. As an illustration of the expected effect, the ram-to-lee ratio of the number of impacts was found to be about 7 to 1 in preliminary analysis of LDEF data for constant particle size, or about 18 to 1 for constant crater size.²⁸ It is expected that meteoroids were dominant in this case.

For orbital debris the directionality in a reference frame fixed with respect to the space vehicle is defined by combining equations (7-10) and (7-12). That is, the directionality can be written as a function of velocity alone, so differential pseudo-vector fluxes can be defined in terms of the velocity distributions such that:

$$\begin{aligned} -dF_+(v) &= F \{ (f'(v)/2) dv_+ \} \\ \text{and} \\ -dF_-(v) &= F \{ (f'(v)/2) dv_- \} , \end{aligned} \quad (7-13)$$

where $f'(v)$ is defined by equation (7-10) and the + and - subscripts are associated with the $+\alpha$ and $-\alpha$ angles of equation (7-12), i.e., the left and right lobes of the "butterfly-shaped" debris distribution (symmetric about the direction of flight). Our sign convention is such that dF is positive in the minus dv direction (fig. 7-4). By solving the problem of the flux against a sphere, it can be shown that $F = 4 F_r = F_c$, where F_r is defined by equation (7-7).

To find the expected rate of impacts on a surface, A , flying with fixed orientation one must solve the following:

$$R(A) = \int_v \int_A dF_+(v) \cdot N_a da + \int_v \int_A dF_-(v) \cdot N_a da , \quad (7-14)$$

where N_a is the outward unit vector normal to the surface element, da . **IMPORTANT:** The limits on the surface integrals must be such that all of the surface where the dot product is positive is included, and portions where it is negative are excluded. (A negative dot product corresponds to flux leaving the surface.) The k factor for the surface A is simply:

$$k = \frac{R(A)}{AF_r} .$$

Figures 7-6a and b and 7-7 illustrate k factors for a flat plate and a right circular cylinder at various orientations and inclinations.

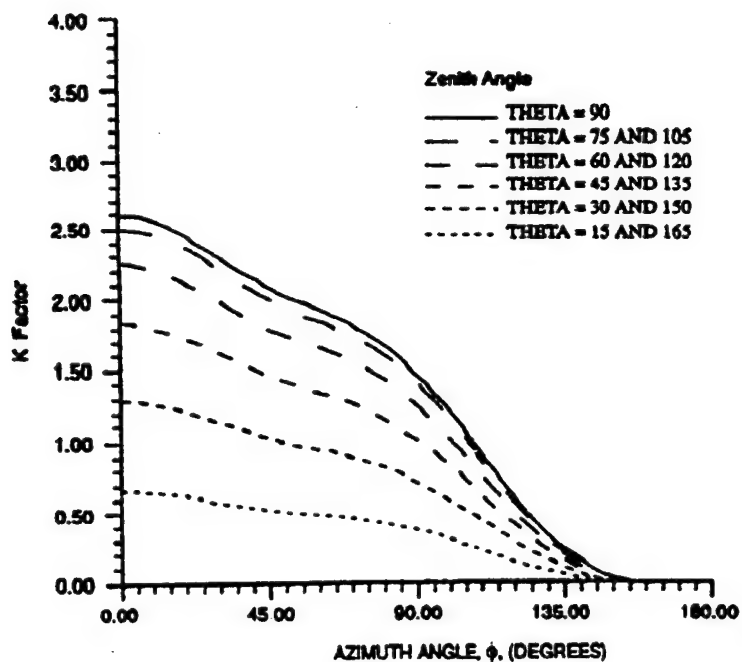


Figure 7-6a. K factor for single-sided flat plates for 28.5° inclination orbit.

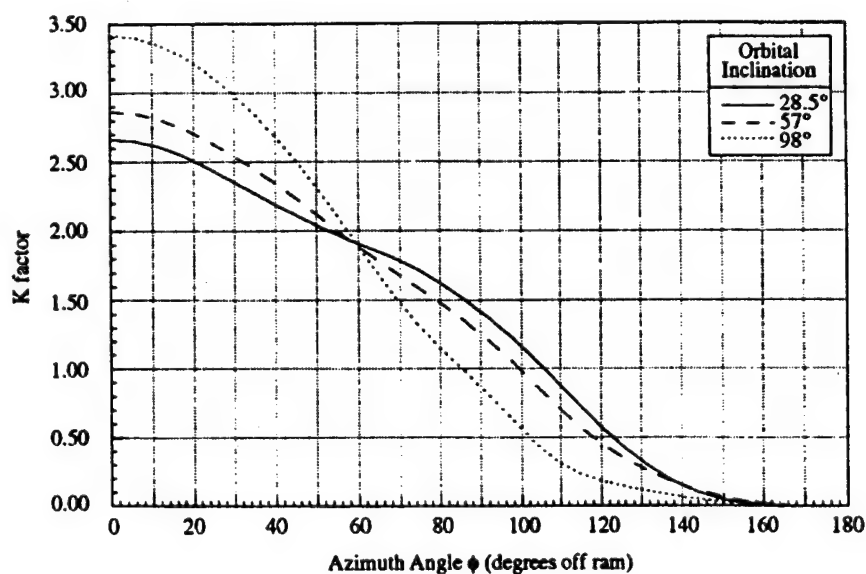


Figure 7-6b. K factor for a single-sided flat plate for 28.5° , 57° , and 98° inclination orbits ($\theta = 90^\circ$).

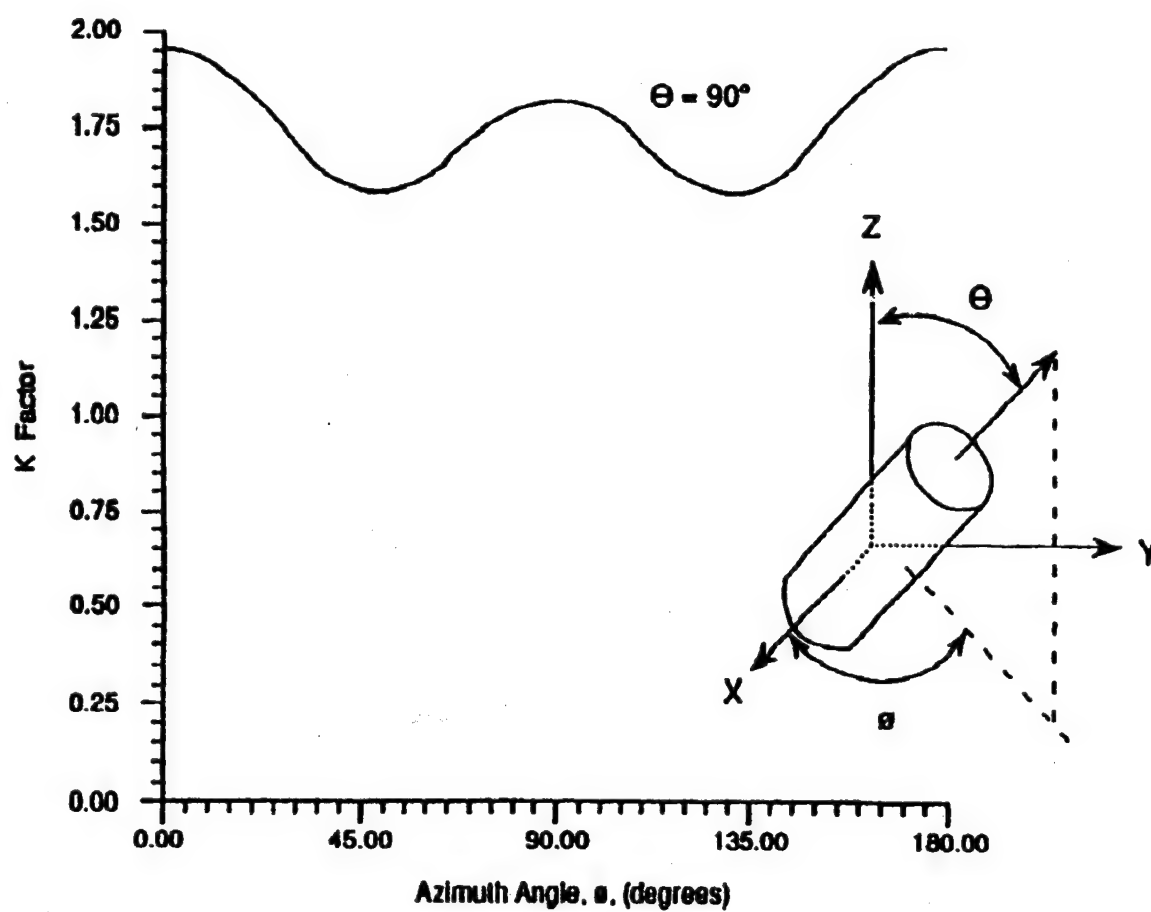


Figure 7-7. K factor for a right circular cylinder, length to diameter ratio = 3.1, $\theta = 90^\circ$.

VIII. MAGNETIC FIELD

As discussed in previous sections, the Earth has a magnetic field which greatly affects the environment in the LEO region. The magnetic field traps charged particles (discussed in sections IV and V) and deflects low-energy cosmic rays. The field is basically a dipole field, but the magnetic axis is not coincident with the rotation axis. The south (north seeking) pole of the magnetic field is rotated 11.7° along the 69° west longitude line from the rotational north pole. The strength of the dipole results in a field strength at the Earth's surface of approximately 0.3 gauss (G) at the equator and 0.6 G at the poles. The magnetic field direction at the equator is horizontal pointing north. At the magnetic south (north seeking) pole it points down into the Earth. Beyond an altitude of approximately 2000 km, strong currents in the magnetosphere cause deviations from the near-Earth field.

The particle L -shell is most simply defined for a dipole field like the Earth's by the equation for a magnetic field line

$$r = L R_E \cos^2 \lambda , \quad (8-1)$$

where λ is the magnetic latitude, r the radial distance to the L -shell, and R_E the radius of the Earth. Thus, the L value of a field line is its distance in the magnetic equatorial plane from the center of the Earth expressed in Earth radii. The L -shell is a surface of revolution of this line about the dipole axis.

Unlike most Earth/Sun parameters which remain constant for hundreds of years, the magnetic field strength changes significantly on the scale of 5 to 10 years. At present, the magnetic field strength is decreasing at approximately 0.1 percent per year. Thus, it is important to use a recent version of the model to correctly determine the magnetic field. Note, however, that as mentioned in section V of this document, the current magnetic field (IGRF, 1991) should not be used to calculate trapped radiation with the AP8 and AE8 radiation models because they do not correctly account for the effect of the atmosphere at orbital altitudes.

In addition to the general decrease in the magnetic field strength, geomagnetic storms caused by solar activity can change the magnetic field by hundreds of gamma (1 gamma (Γ) is 10^{-5} G).

The magnetic field can be accurately represented using a spherical harmonic expansion. The expansion in terms of the Earth's rotational coordinate system (i.e., normal latitude, longitude) requires more terms than a simple dipole because the axes of the coordinate system are not coincident with the axes of the field. However, this coordinate system is so familiar that it is the usual choice. The specification is given in terms of magnetic potential, U , and the field is derived from the potential by taking the negative gradient (which is the vector derivative):

$$\vec{B} = -\vec{\nabla}U . \quad (8-2)$$

In particular:

$$B_{\text{north}} = (1/r) dU/d\theta , \quad (8-3)$$

$$B_{\text{east}} = [-1/(r \sin \theta)] dU/d\phi , \quad (8-4)$$

$$B_{\text{down}} = dU/dr , \quad (8-5)$$

where U is the magnetic potential; r , θ , and ϕ are the spherical coordinates; and down means toward the center of the Earth.

Given that representation, the potential is expressed as Schmidt-normalized Legendre polynomials with the following form:

$$U = R_E \sum_{n=1}^{\infty} \sum_{m=0}^n P_n^m(\cos \theta) (R_E/r)^{n+1} [g_n^m \cos(m\phi) + h_n^m \sin(m\phi)] \quad (8-6)$$

where

θ = co-latitude (i.e., measured from the pole)

ϕ = east longitude

R_E = Earth radius = (6371.2 km)

r = radial distance

P_n^m = Schmidt-normalized associated Legendre polynomials

g_n^m and h_n^m = Schmidt-normalized coefficients.

The Schmidt-normalized Legendre polynomials are related to the normal associated Legendre polynomials as follows:

$$P_n^m = [\varepsilon_m (n-m)! / (n+m)!]^{1/2} P_{nm} \quad (8-7)$$

where

P_{nm} = regular associated Legendre polynomial

$$\varepsilon_m = \begin{cases} 2 & \text{for } m \neq 0 \\ 1 & \text{for } m = 0 \end{cases}$$

Given this formalism, the coefficients g and h can be stated. Note that the h coefficient for $m = 0$ is not stated because the sine function of 0° is zero. The coefficients are given in units of gamma (Γ) which is 10^{-5} G. Note also that the value of each coefficient depends on the radius of the Earth, so the stated radius (6371.2 km) must be used with these coefficients. The coefficients, according to the current International Geomagnetic Reference Field (IGRF, 1991), are listed in table 8-1.

Since the polynomials P_n^m are of order unity, the coefficients in table 8-2 terms will represent the field to approximately 1 percent in the worst case. The complete model has been calculated to degree and order 10 which is more accurate. Computer programs for determining the field values are available.

Table 8-1. Spherical harmonic coefficients of the IGRF 1991 (from references. 29 and J) (page 1 of 2).

n	m	g_n^m	h_n^m	gt_n^m	ht_n^m
1	0	-29 775	0	18	0
1	1	-1 851	5 411	11	-16
2	0	-2 136	0	-13	0
2	1	3 058	-2 278	2	-16
2	2	1 693	-380	0	-14
3	0	1 315	0	3	0
3	1	-2 240	-287	-7	4
3	2	1 246	293	0	2
3	3	807	-348	-6	-11
4	0	939	0	1	0
4	1	782	248	1	3
4	2	324	-240	-7	2
4	3	-423	87	1	3
4	4	142	-299	-6	-1
5	0	-211	0	1	0
5	1	353	47	0	0
5	2	244	153	-2	1
5	3	-111	-154	-3	0
5	4	-166	-69	0	2
5	5	-37	98	2	0
6	0	61	0	1	0
6	1	64	-16	0	0
6	2	60	83	2	-1
6	3	-178	68	1	0
6	4	2	-52	0	-1
6	5	17	2	0	1
6	6	-96	27	1	1
7	0	77	0	1	0
7	1	-64	-81	-1	1
7	2	4	-27	0	0
7	3	28	1	1	1
7	4	1	20	2	-1
7	5	6	16	0	0

Table 8-1. Spherical harmonic coefficients of the IGRF 1991 (from references 29 and J)
(page 2 of 2).

n	m	g_n^m	h_n^m	g_t^m	h_t^m
7	6	10	-23	0	0
7	7	0	-5	0	0
8	0	22	0	0	0
8	1	5	10	-1	1
8	2	-1	-20	0	0
8	3	-11	7	0	0
8	4	-12	-22	-1	0
8	5	4	12	0	0
8	6	4	11	0	-1
8	7	3	-16	-1	0
8	8	-6	-11	-1	1
9	0	4	0		
9	1	10	-21		
9	2	1	15		
9	3	-12	10		
9	4	9	-6		
9	5	-4	-6		
9	6	-1	9		
9	7	7	9		
9	8	2	-7		
9	9	-6	2		
10	0	-4	0		
10	1	-4	1		
10	2	2	0		
10	3	-5	3		
10	4	-2	6		
10	5	4	-4		
10	6	3	0		
10	7	1	-1		
10	8	2	4		
10	9	3	-0		
10	10	0	-6		

Table 8-2. Schmidt coefficients.

n	m	g_n^m	h_n^m
Dipole Terms			
1	0	-29 988	
1	1	-1 957	5 606
Quadrupole Terms			
2	0	-1 997	
2	1	3 028	-2 129
2	2	1 662	- 199
Octupole Terms			
3	0	1 279	
3	1	-2 181	- 335
3	2	1 251	271
3	3	833	- 252

IX. THERMAL ENVIRONMENT

9.1 General Discussion

A vehicle in LEO will receive radiant thermal energy from three primary sources; the incoming solar radiation (described by the solar constant), reflected solar energy (Earth albedo energy), and outgoing longwave radiation (OLR) emitted by the Earth and atmosphere. Portions of this energy will be reflected by the vehicle, and the vehicle radiates energy into the cold sink of space at 3 K. Spacecraft surfaces will tend toward a temperature which balances these energy fluxes with any energy produced internally within the vehicle. A similar thermal balance process applies to the Earth itself. If one considers the Earth and its atmosphere as a whole and averages over long time periods, the incoming solar energy and OLR energy are essentially in balance; the Earth/atmosphere is very nearly in radiative equilibrium with the Sun. However, it is not in balance everywhere on the globe, and there are important variations with respect to local time, geography, and atmospheric conditions. A space vehicle's motion with respect to the Earth results in its viewing only a "swath" across the full global thermal profile; so it sees these variations as functions of time in accord with the thermal time constants of the hardware systems. Thus, the thermal environment is, to some extent, dependent upon the orbit parameters selected for the mission. The data in this section have been tailored to allow selection of a statistically correct description of this environment and its variations for most common LEOs.

9.1.1 Solar Constant. The direct solar flux is the greatest source of heating for most spacecraft. The mean value of this solar flux at mean Earth-Sun distance is termed the "solar constant." Specifically, the solar constant is defined as the radiation that falls on a unit area of surface normal to the line from the Sun, per unit time, outside the atmosphere, at one astronomical unit (the mean Earth-Sun distance). In actuality, the incoming solar flux which impinges on an Earth-orbiting spacecraft is not quite constant. There are two factors influencing its variability. First, the amount of radiant energy that is emitted by the Sun is known to vary slightly throughout the 11-yr solar cycle and differs from cycle to cycle. The exact amount of this variation is still being studied, but it is estimated to be less than half a percent. Second, the slightly elliptical orbit of the Earth about the Sun also results in a variation of approximately ± 3.4 percent; the maximum occurring at the winter solstice when the Earth-Sun distance is a minimum. The solar constant defined in this document is $1371 \pm 10 \text{ W/m}^2$. The $\pm 10 \text{ W/m}^2$ allows for the slight solar cycle variation and, much more importantly, the measurement uncertainty. The variation with respect to Earth-Sun distance must be added. It may be calculated by standard methods dependent upon which season of the year is of interest to the user. Extreme values are listed in table 9-1.

9.1.2 Albedo. The fraction of incident sunlight which is reflected off a planet is termed albedo. Albedo values typically are given as a fraction, but may also be given as a percent. This parameter gives a measure of the amount of solar energy which is reflected back to space. Therefore, albedo values are only applicable when a portion of the Earth-atmosphere system that is seen by the spacecraft is sunlit. Albedo values vary with solar zenith angle, and care must be taken to correctly account for this effect, especially near the terminator. (See paragraph 9.2.2.) Albedo radiation has approximately the same spectral shape as the Sun's spectrum, which approximates a blackbody with a characteristic temperature of 5762 K. As used in this document, albedo refers to the total solar spectrum albedo. Albedo values have a wide range, and the range would be even greater if smaller bandwidths were considered.

Albedo is highly variable across the globe and is dependent on the distribution of reflective properties of the surface and the amount and type of cloud cover. Albedo is generally highest over cloudy regions such as the intertropical convergence zone, deserts, and ice- and snow-covered areas. If the sky is clear, the albedo over ocean areas is generally low. Albedo also increases as the solar zenith angle increases. Because of the snow and ice cover, decreasing solar elevation angle, and increasing cloud coverage, albedo tends to increase slightly with latitude if viewed on a large scale.

9.1.3 Outgoing Longwave Radiation. The third component of a spacecraft's thermal environment is the OLR emitted by the Earth itself. This Earth-emitted thermal radiation has a spectrum of a blackbody with a characteristic temperature of 288 K. OLR is not constant over the globe, but the localized variations are much less severe than for albedo. OLR is principally influenced by the temperature of the Earth's surface and the amount of cloud cover. A warmer region of the Earth's surface will emit more radiation than a colder area. On a large scale, highest values of OLR will occur in tropical regions (as these are the regions of the globe receiving the maximum solar heating) and will decrease with latitude. Increasing cloud cover tends to lower OLR by absorbing up-welling radiation from the Earth's surface. The solar elevation angle may also affect OLR because of its influence on the temperature of the surface and lower atmosphere. Thus, both diurnal and seasonal variations may be detected. This diurnal variation is small over the oceans, but for local regions over the continents, especially desert areas, it can amount to about 20 percent.

9.1.4 The Earth Radiation Budget Experiment. The data used to define the thermal environment were collected by the Earth Radiation Budget Experiment (ERBE). ERBE began in the 1980's and is still ongoing. ERBE is a multisatellite experiment which has as its primary objective global data collection of such Earth radiation budget parameters as incident sunlight, reflected sunlight (albedo), and OLR. This experiment was selected because of its thorough coverage and its up-to-date information. The experiment consisted of three satellites, the low-inclination Earth Radiation Budget Satellite (ERBS) and two NOAA Sun-synchronous satellites. The data used here are from the active cavity, flat plate radiometers in the fixed, nonscanning, wide field of view (FOV) mode. This type of instrument was chosen to most closely approximate the albedo and OLR variations that a spacecraft surface would encounter. The data are available in three separate sets, daily averaged values (S-4), hourly averaged values (S-10), and the direct 16-s instrument measurements along the ERBS or NOAA satellite trajectory (S-7). The S-4 and S-10 data products were evaluated but were deemed inappropriate for this application; the averaging times are much too long compared to the thermal time constant of most satellite systems. Therefore, the following design criteria are based on 28 files, representing 1 mo of 16-s data each, of S-7 data. The measurements were made from November of 1984 through July of 1987, with all seasons represented.

9.2 Thermal Environment Criteria

9.2.1 Temporal Variations. Satellite systems have thermal response times ranging from a few minutes to hours. To enable the analyst to model the thermal response of a particular system as simply as possible, a running mean analysis was developed for the albedo and OLR variations as a vehicle would view them moving along its orbit track. Data are presented for 30°, 60°, and 90° orbit inclinations. The dependence on orbit inclination is not especially strong, so the data presented here are expected to be adequate for most applications. Running averages were computed for averaging times ranging from a few seconds to an hour and a half. Percentile* statistics of the running means describe the low and high extremes, 1, 3, 5, 95, 97, and 99 percentile, and the expectation value (50 percentile) for each parameter as a function of averaging time periods along an orbit track. The data

* A percentile value is the probability that this value will not be exceeded (i.e., is equal to or less than this value).

are adjusted to the top of the atmosphere (30 km) and, for albedo, zero solar zenith angle.[†] (The diurnal (solar zenith angle) variations of OLR were not significant enough to warrant similar treatment.) These statistics are presented in tables 9-2 through 9-4 and are illustrated by figures 9-2 through 9-4.

9.2.2 Solar Zenith Angle Correction for Albedo. To a first approximation, albedo may be assumed to be independent of the solar zenith angle; that is, the scattering is "Lambertian" or equal in all directions. This approximation has been assumed for most engineering applications in the past. However, the data quality and the capability of current engineering analysis methods warrant an improved approach. Albedo actually exhibits an appreciable solar zenith angle dependence. Treatment of this topic in the scientific literature (ref. 30) is generally "scene specific," e.g., it depends on the geographic features in the FOV, data which are not readily available to the design engineer, and the general algorithms tested did not fully remove the zenith angle dependence from this data set. Therefore, a zenith angle correction (fig. 9-1) was derived specifically for this data set in a manner which is specifically matched to the analysis tools most commonly used for engineering analysis, the Thermal Radiation Analysis System (TRASYS) and Thermal Synthesizer System (TSS).

Most satellite orbits encounter all solar zenith angles. The exceptions are certain Sun-synchronous orbits which never reach the smaller angles. The standard TRASYS and TSS codes contain the primary solar zenith angle dependence, the cosine dependence of the view factor, but they treat albedo as a constant. Since maximum albedo energy occurs at small zenith angles (near but not at local noon) when the correction factor is small and not rapidly changing, it will often be satisfactory to calculate an upper limit albedo and use it as a constant in the TRASYS or TSS code for estimating the extreme hot case. This is especially true for subsystems with short thermal time constants. For analysis of the temporal variations and time integrated effects of the thermal environment, the thermal analysis code should be modified to account for the albedo variations. Orbital average solar zenith angles for the daylight portion of several orbits are illustrated in figure 9-5. For any single orbit:

$$|\beta| \leq \text{sza} \leq \pi/2,$$

that is, the solar zenith angle is limited by the beta angle at local noon and $\pi/2$ at ground sunrise/sunset.

The correction term was derived from 4 mo of data restricted to the -30 to +30 latitude band. It was verified by testing another 4 mo of data and testing to wider latitude bands. It removes the solar zenith angle dependence to within ± 0.04 . The correction is expressed as an additive term, thus:

$$\text{Albedo}(\text{SZA}) = \text{Albedo}(\text{SZA} = 0) + \text{Correction}$$

$$\text{Correction} = [C_4(\text{SZA})^4 + C_3(\text{SZA})^3 + C_2(\text{SZA})^2 + C_1(\text{SZA})]$$

where SZA is the Solar Zenith Angle in degrees and the albedo is expressed as a fraction.

$$C_4 = +4.9115 \text{ E-9,}$$

$$C_3 = +6.0372 \text{ E-8,}$$

$$C_2 = -2.1793 \text{ E-5,}$$

$$C_1 = +1.3798 \text{ E-3.}$$

[†] Solar zenith angle is the angle between the Earth center-satellite vector and the Earth center-Sun vector.

Figure 9-1 illustrates the correction. This term must be added to the albedo from tables 9-2 through 9-4 and figures 9-2 through 9-4.

9.2.3 Correlation Analysis. Figures 9-6 through 9-8 show plots of the running mean albedo against the running mean OLR from simultaneous measurements. The two parameters are not strongly correlated in the sense that, for almost any value of one parameter, a substantial range of values is encountered for the other, even though there is clearly some relationship between them. For many applications, the albedo and emitted thermal radiation may be considered as independent parameters, both of which vary across a range of values. The range is quite large for systems with short thermal time constants, e.g., short averaging times, but as longer averaging times are considered, the range narrows toward the mean for the region covered by the spacecraft.

In selecting benchmarks for design purposes, it should be remembered that the joint probability of occurrence for independent parameters is given by the product of the individual probabilities. For example, OLR values in excess of the 95th percentile value may be expected to occur in combination with albedos in excess of the median 0.025 of the time, e.g. $(0.05)(0.50) = 0.025$. Thus, assuming these are independent parameters implies 97.5 percent of the data would lie outside this region in this example. Eventually joint probability distributions for these parameters will be developed for applications where the assumption of independence is not adequate, but this analysis is not yet available.

Table 9-1. Thermal parameters for LEO.

Solar constant at 1 AU (1 AU = mean Earth-Sun distance)	1371±10 W/m ²
Maximum solar energy flux (winter solstice) (at Perihelion, +10 W/m ² included)	1428 W/m ²
Minimum solar energy flux (summer solstice) (at Aphelion, -10 W/m ² included)	1316 W/m ²
Characteristic blackbody temperature of solar spectrum {Albedo radiation has approximately the same spectrum.}	5762 K
Space sink temperature	3 K (absolute)

Table 9-2. Running mean albedo and OLR percentile data for 30° inclination orbits.

Albedo: (top of the atmosphere, 30 km, and corrected to zero solar zenith angle.*)

Ave. Time (s)	Lowest Observed	1%	3%	5%	50%	95%	97%	99%	Highest Observed
16	0.06	0.08	0.09	0.09	0.16	0.30	0.32	0.35	0.51
64	0.06	0.08	0.09	0.09	0.17	0.30	0.32	0.35	0.49
128	0.06	0.08	0.09	0.10	0.17	0.29	0.31	0.34	0.48
256	0.06	0.08	0.09	0.10	0.17	0.28	0.30	0.33	0.44
512	0.07	0.09	0.10	0.11	0.17	0.26	0.28	0.30	0.39
896	0.08	0.10	0.11	0.12	0.18	0.24	0.26	0.28	0.37
1344	0.08	0.11	0.12	0.13	0.18	0.24	0.24	0.26	0.33
1800	0.09	0.11	0.12	0.13	0.18	0.23	0.24	0.25	0.31
2688	0.10	0.12	0.13	0.14	0.18	0.22	0.23	0.24	0.30
3600	0.10	0.13	0.14	0.14	0.18	0.22	0.22	0.23	0.29
5400	0.12	0.14	0.14	0.15	0.18	0.21	0.22	0.22	0.26

*Angle between the Earth center-satellite vector and the Earth center-Sun vector.

Outgoing Longwave Radiation: (top of the atmosphere, 30 km, units are W/m²)

Ave. Time (s)	Lowest* Observed	1%	3%	5%	50%	95%	97%	99%	Highest Observed
16	151	174	187	194	249	285	291	303	345
64	152	175	187	195	249	285	290	302	343
128	154	177	189	196	249	284	289	301	342
256	160	182	193	200	248	282	287	296	334
512	174	193	202	208	247	277	281	288	313
896	189	204	212	216	247	272	276	282	297
1344	194	209	215	219	246	270	273	279	296
1800	199	212	218	221	246	269	272	277	294
2688	206	216	221	224	246	267	270	274	289
3600	210	219	223	226	246	265	268	272	283
5400	217	223	227	229	246	263	265	269	277

*Set at 0.04 percentile, eliminating a very few, unrealistically low data points.

Note: Percentile is the probability that the indicated albedo or OLR value will not be exceeded (i.e., is equal to or less than this value).

Table 9-3. Running mean albedo and OLR percentile data for 60° inclination orbits.

Albedo: (top of the atmosphere, 30 km, and corrected to zero solar zenith angle.*)

Ave. Time (s)	Lowest Observed	1%	3%	5%	50%	95%	97%	99%	Highest Observed
16	0.06	0.09	0.10	0.11	0.23	0.39	0.41	0.44	0.53
64	0.06	0.09	0.10	0.11	0.23	0.39	0.40	0.43	0.53
128	0.06	0.09	0.10	0.11	0.23	0.38	0.40	0.43	0.53
256	0.06	0.09	0.10	0.11	0.23	0.37	0.39	0.42	0.52
512	0.07	0.10	0.12	0.13	0.23	0.36	0.37	0.40	0.48
896	0.08	0.12	0.13	0.14	0.23	0.34	0.35	0.37	0.44
1344	0.10	0.14	0.15	0.16	0.23	0.33	0.34	0.35	0.41
1800	0.11	0.15	0.16	0.16	0.23	0.32	0.33	0.34	0.40
2688	0.12	0.15	0.16	0.17	0.23	0.32	0.33	0.34	0.39
3600	0.13	0.16	0.17	0.17	0.23	0.31	0.32	0.33	0.38
5400	0.14	0.16	0.17	0.18	0.23	0.31	0.32	0.33	0.36

*Angle between the Earth center-satellite vector and the Earth center-Sun vector.

Outgoing Longwave Radiation: (top of the atmosphere, 30 km, units are W/m²)

Ave. Time (s)	Lowest * Observed	1%	3%	5%	50%	95%	97%	99%	Highest Observed
16	155	178	187	192	230	279	286	300	349
64	156	179	188	193	230	279	285	300	348
128	158	181	189	193	230	278	285	299	347
256	164	185	192	196	230	276	282	296	342
512	177	191	197	200	231	270	275	287	332
896	186	197	202	205	232	264	268	278	316
1344	191	201	206	209	232	259	263	271	303
1800	193	203	208	211	232	255	259	267	295
2688	196	204	209	211	232	255	258	265	284
3600	198	205	210	213	232	253	257	263	280
5400	200	205	211	213	233	252	255	260	278

*Set at 0.04 percentile, eliminating a very few, unrealistically low data points.

Note: Percentile is the probability that the indicated albedo or OLR value will not be exceeded (i.e., is equal to or less than this value).

Table 9-4. Running mean albedo and OLR percentile data for 90° inclination orbits.

Albedo: (top of the atmosphere, 30 km, and corrected to zero solar zenith angle. *)

Ave. Time (s)	Lowest Observed	1%	3%	5%	50%	95%	97%	99%	Highest Observed
16	0.06	0.09	0.10	0.11	0.26	0.41	0.42	0.46	0.54
64	0.06	0.09	0.10	0.11	0.26	0.40	0.42	0.46	0.53
128	0.06	0.09	0.10	0.12	0.26	0.40	0.42	0.45	0.53
256	0.06	0.10	0.11	0.12	0.26	0.39	0.41	0.44	0.52
512	0.07	0.11	0.12	0.13	0.26	0.38	0.39	0.42	0.48
896	0.08	0.12	0.14	0.15	0.26	0.36	0.37	0.39	0.46
1344	0.10	0.15	0.16	0.17	0.25	0.35	0.36	0.38	0.43
1800	0.12	0.16	0.18	0.18	0.25	0.34	0.35	0.36	0.42
2688	0.12	0.17	0.18	0.19	0.25	0.34	0.34	0.36	0.42
3600	0.14	0.17	0.18	0.19	0.25	0.33	0.34	0.35	0.40
5400	0.15	0.18	0.19	0.19	0.25	0.33	0.34	0.34	0.39

*Angle between the Earth center-satellite vector and the Earth center-Sun vector.

Outgoing Longwave Radiation: (top of the atmosphere, 30 km, units are W/m²)

Ave. Time (s)	Lowest * Observed	1%	3%	5%	50%	95%	97%	99%	Highest Observed
16	157	178	186	190	223	276	283	300	349
64	157	179	187	191	223	276	283	300	348
128	160	181	188	192	223	275	282	299	347
256	166	184	191	194	223	273	279	295	342
512	177	189	194	197	225	267	273	286	332
896	184	194	199	201	226	260	265	275	315
1344	188	198	202	204	226	254	258	267	304
1800	191	200	204	206	227	250	254	261	295
2688	194	200	204	206	227	250	253	260	283
3600	196	201	205	207	227	248	252	259	280
5400	198	202	205	208	227	247	250	257	276

*Set at 0.04 percentile, eliminating a very few, unrealistically low data points.

Note: Percentile is the probability that the indicated albedo or OLR value will not be exceeded (i.e., is equal to or less than this value).

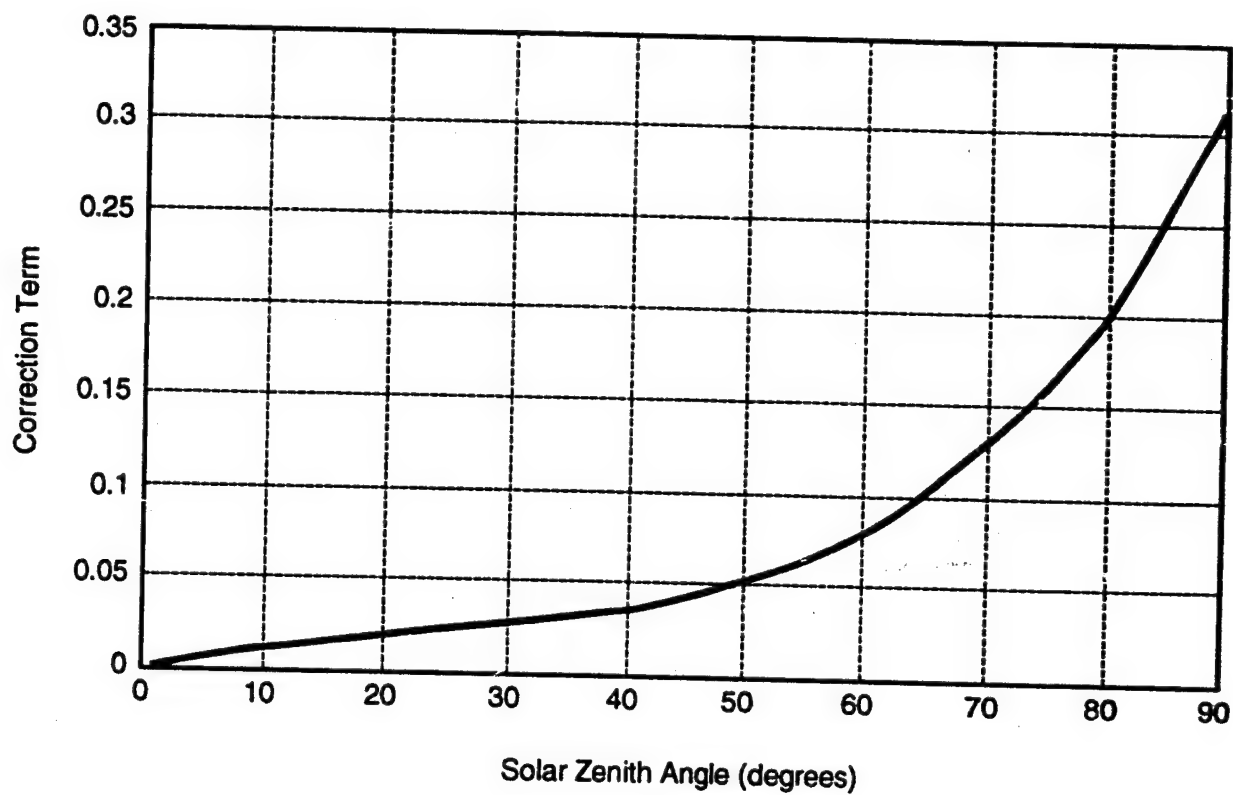


Figure 9-1. Albedo correction term.

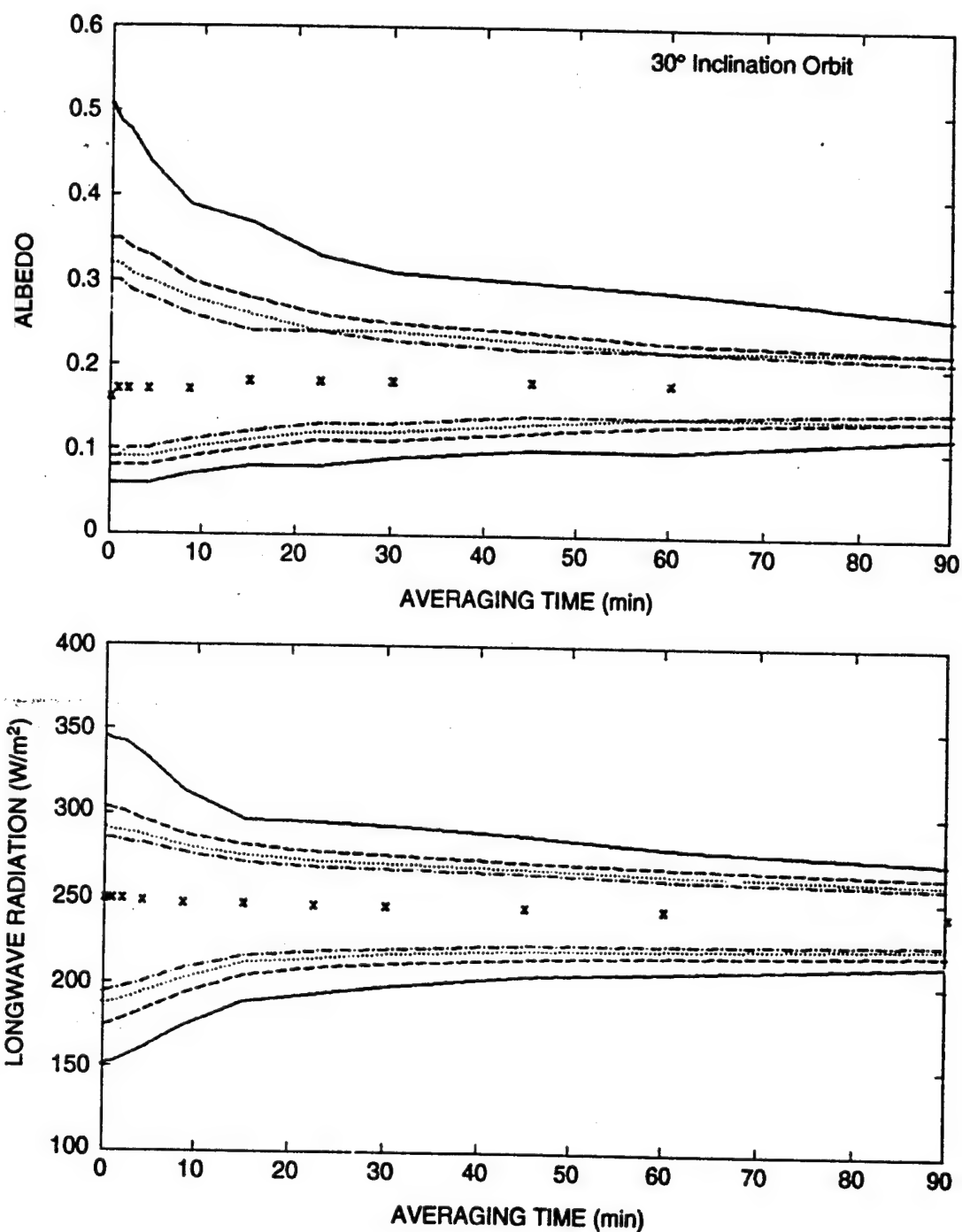


Figure 9-2. Statistical summary of albedo (top) and OLR (bottom) observations for a 30° inclination orbit. Solid lines—limiting values; dashed lines—1 and 99 percent; dotted lines—3 and 97 percent; dot dash—5 and 95 percent; and "x"—median.

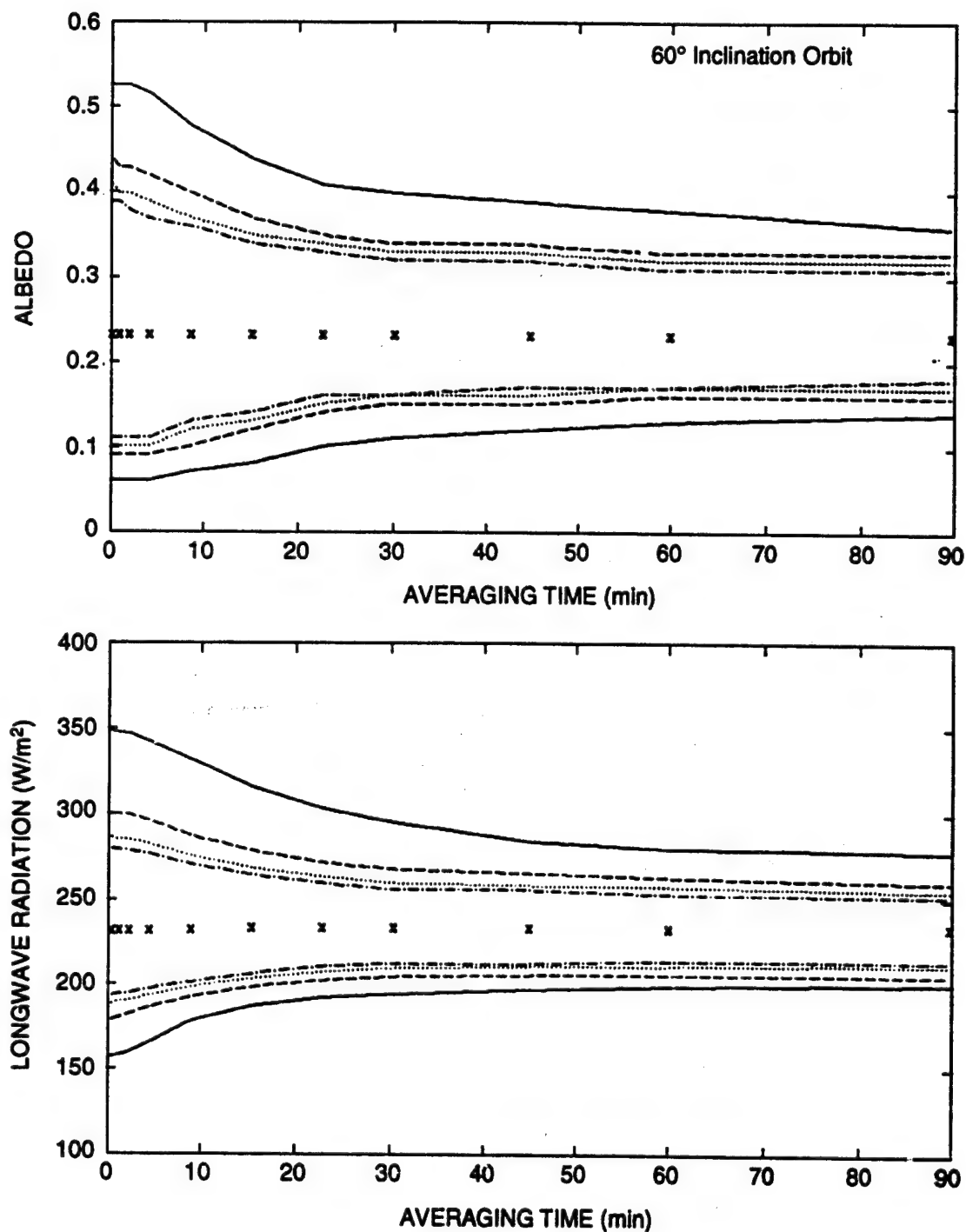


Figure 9-3. Statistical summary of albedo (top) and OLR (bottom) observations for a 60° inclination orbit. Solid lines—limiting values; dashed lines—1 and 99 percent; dotted lines—3 and 97 percent; dot dash—5 and 95 percent; and “x”—median.

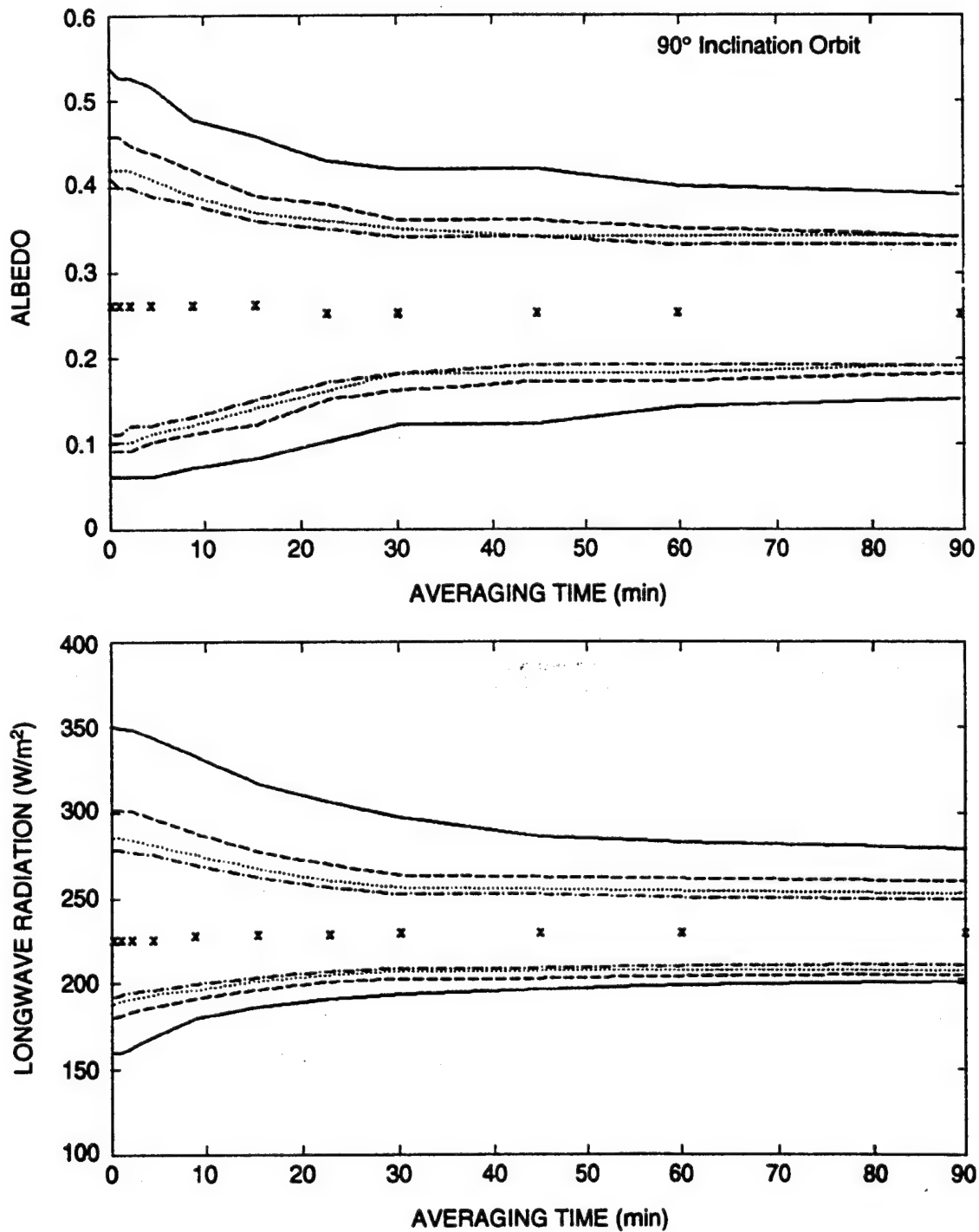


Figure 9-4. Statistical summary of albedo (top) and OLR (bottom) observations for a 90° inclination orbit. Solid lines—limiting values; dashed lines—1 and 99 percent; dotted lines—3 and 97 percent; dot dash—5 and 95 percent; and “x”—median.

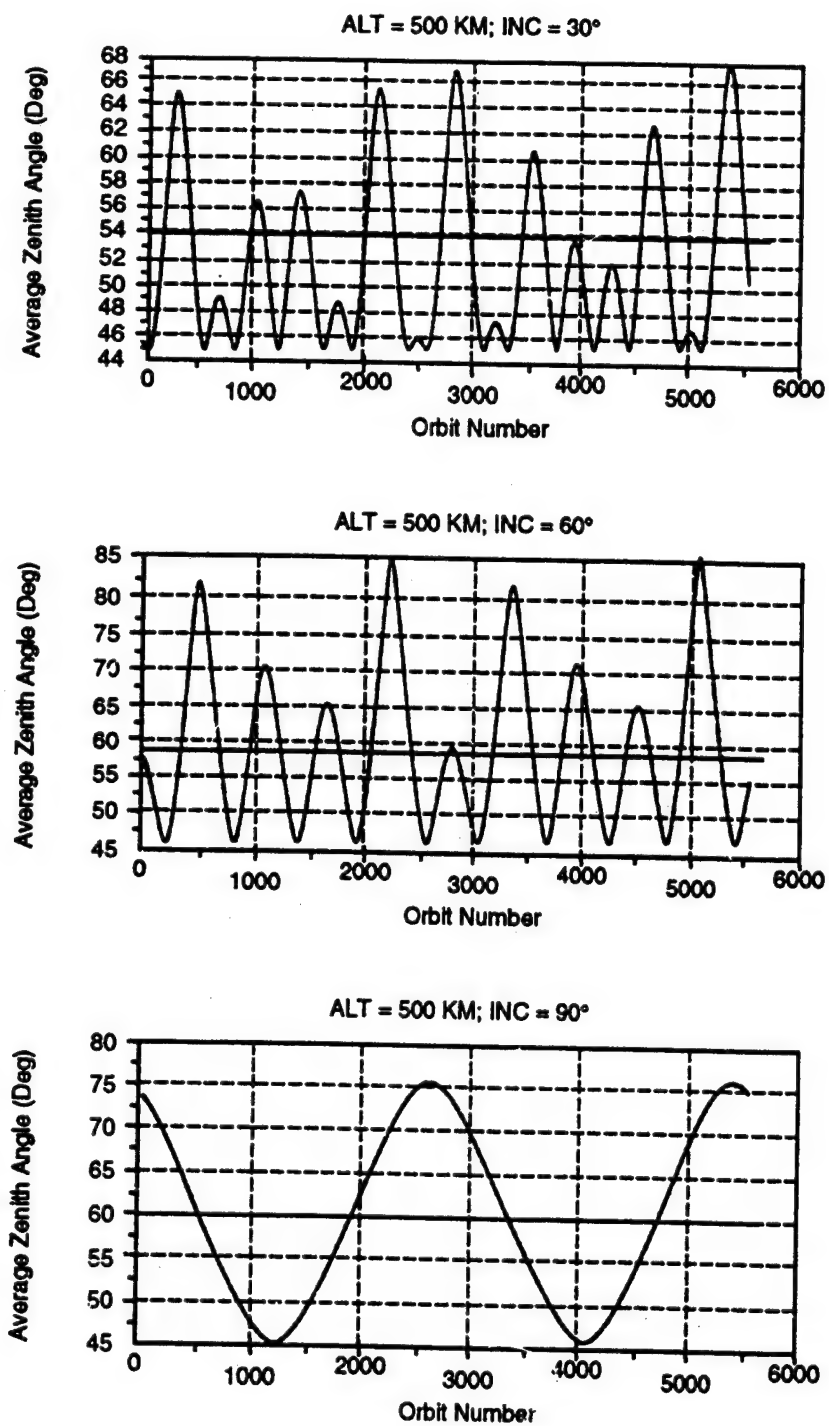


Figure 9-5. Orbit-average solar zenith angles for 30°, 60°, and 90° inclination orbits, daylight side only. Annual average is indicated by solid horizontal line. Phase of the peaks is a function of β angle.

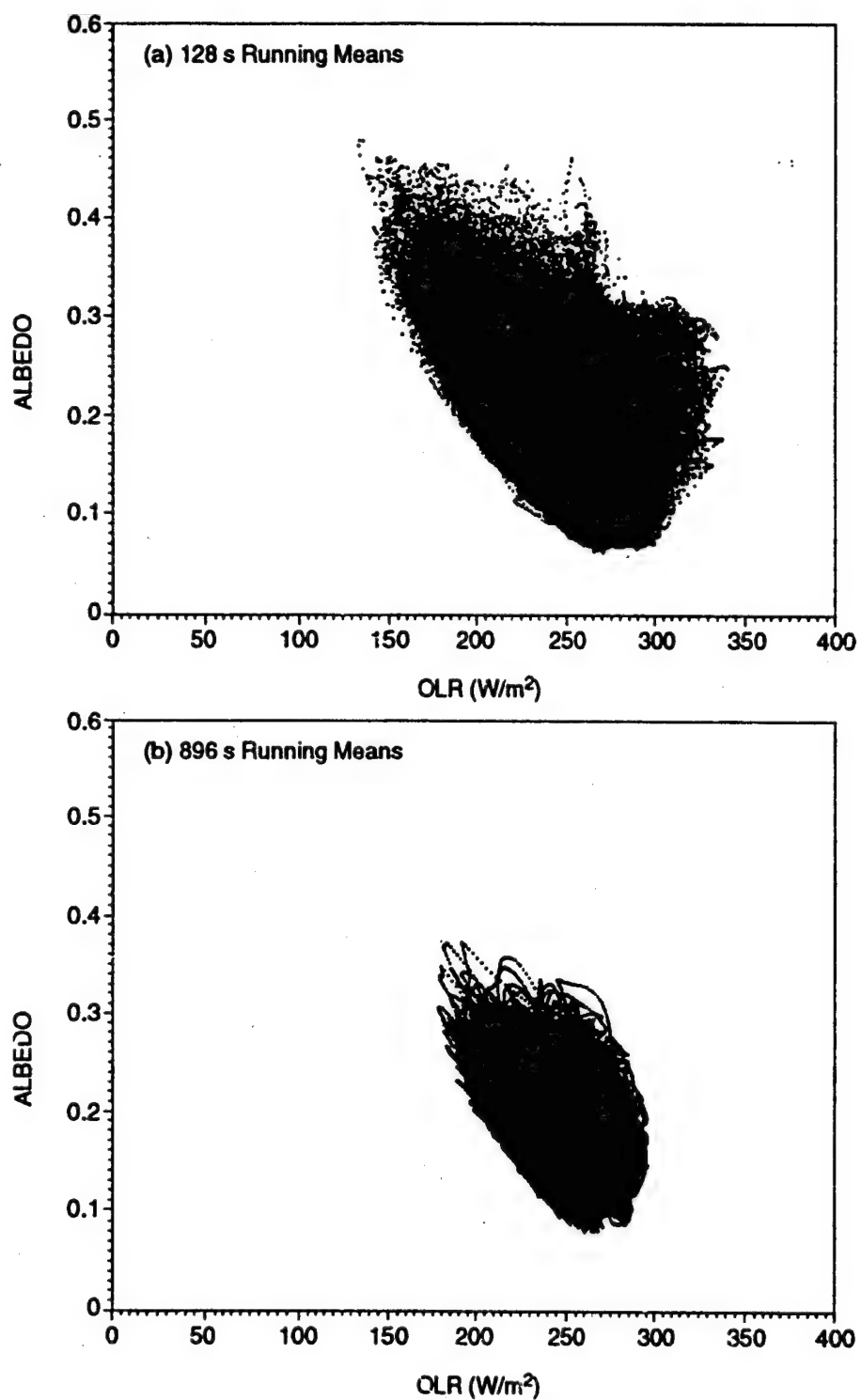


Figure 9-6. Albedo-OLR correlated pairs for 30° inclination orbits (page 1 of 2).

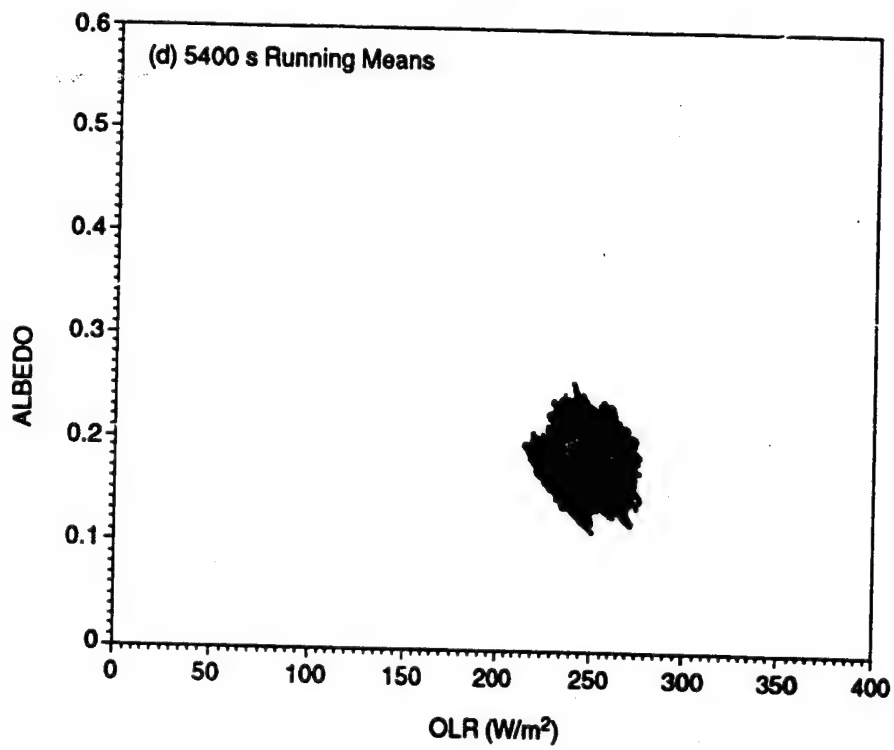
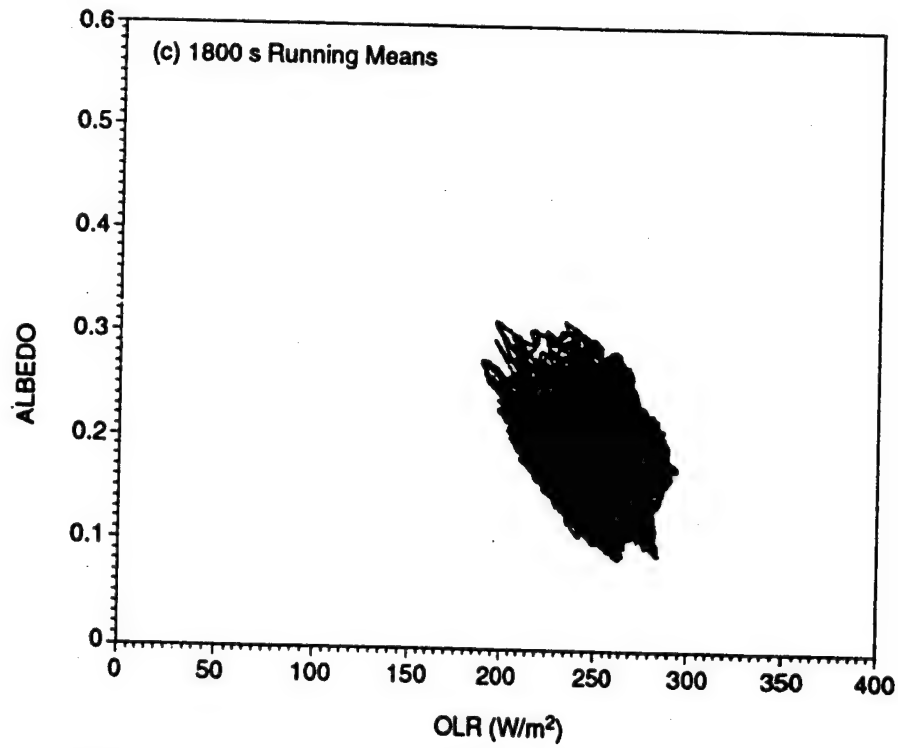


Figure 9-6. Albedo-OLR correlated pairs for 30° inclination orbits (page 2 of 2).

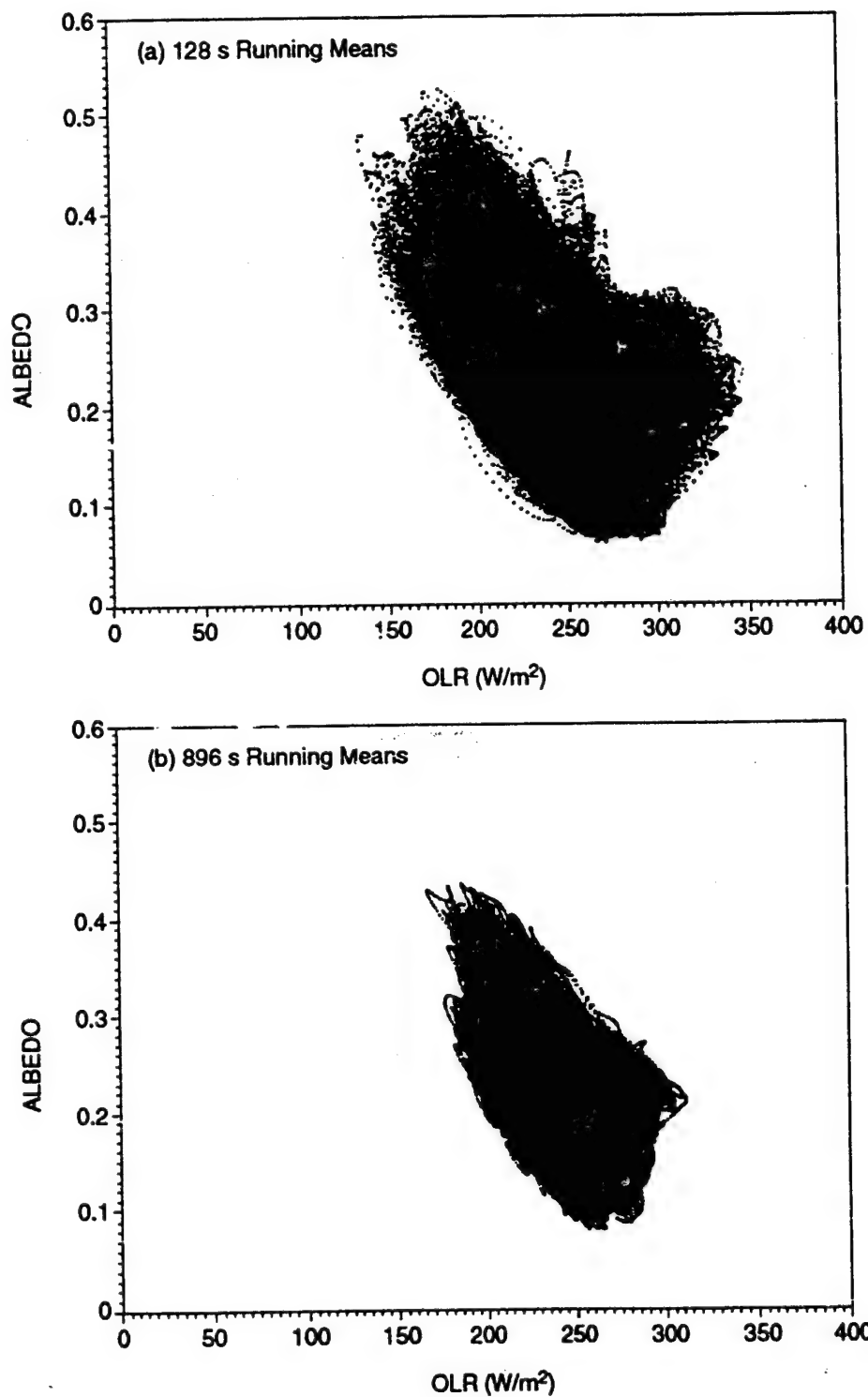


Figure 9-7. Albedo-OLR correlated pairs for 60° inclination orbits (page 1 of 2).

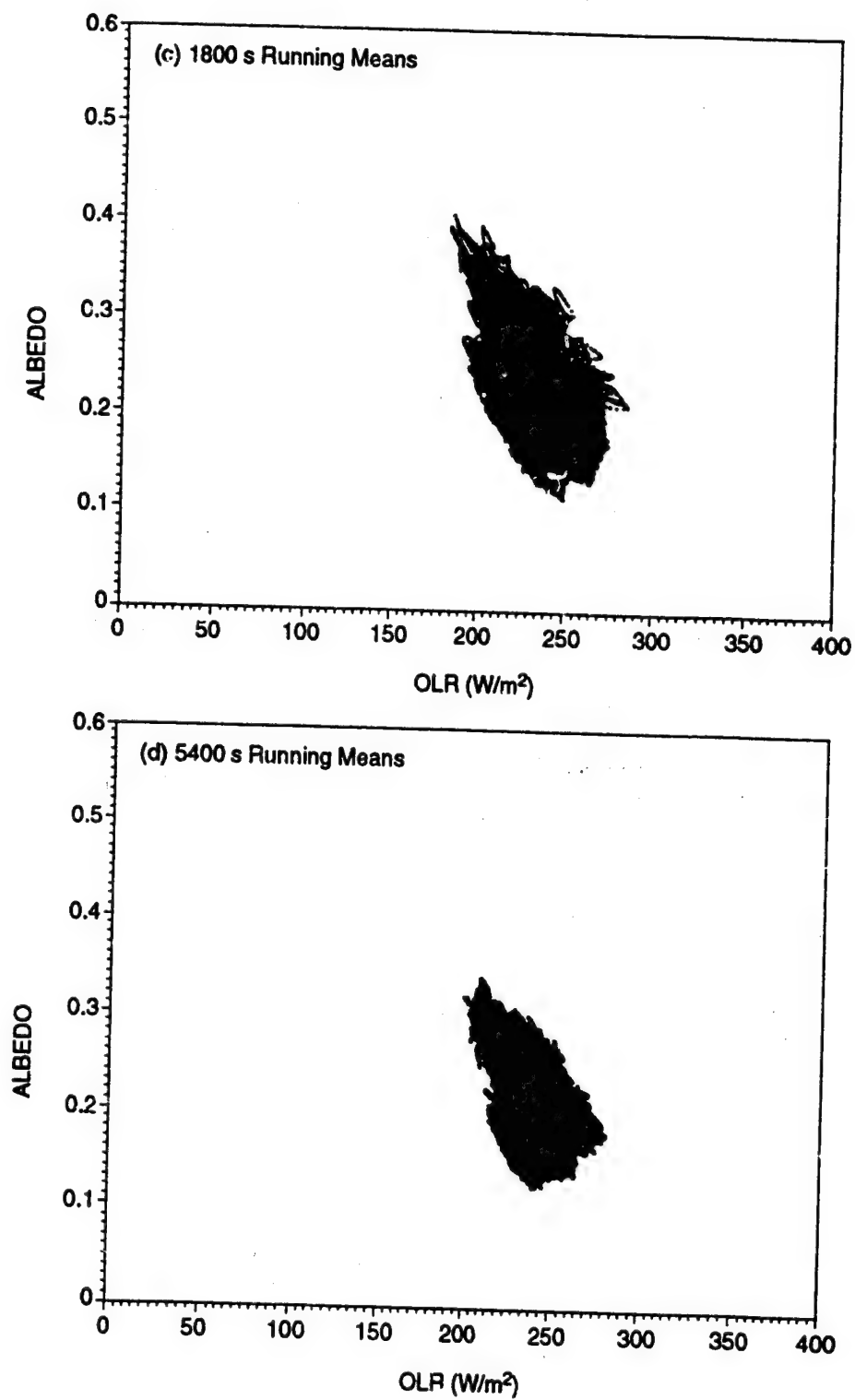


Figure 9-7. Albedo-OLR correlated pairs for 60° inclination orbits (page 2 of 2).

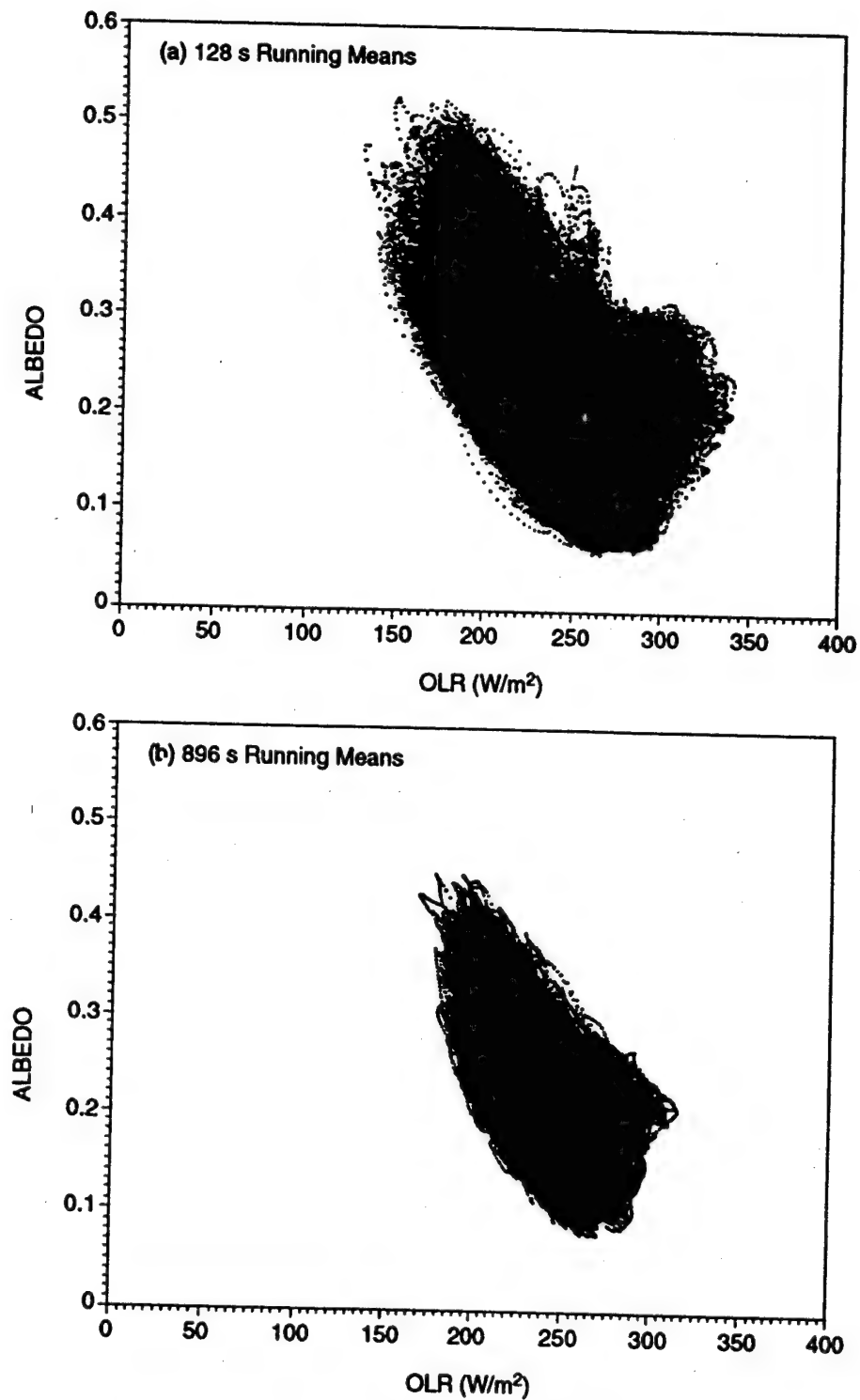


Figure 9-8. Albedo-OLR correlated pairs for 90° inclination orbits (page 1 of 2).

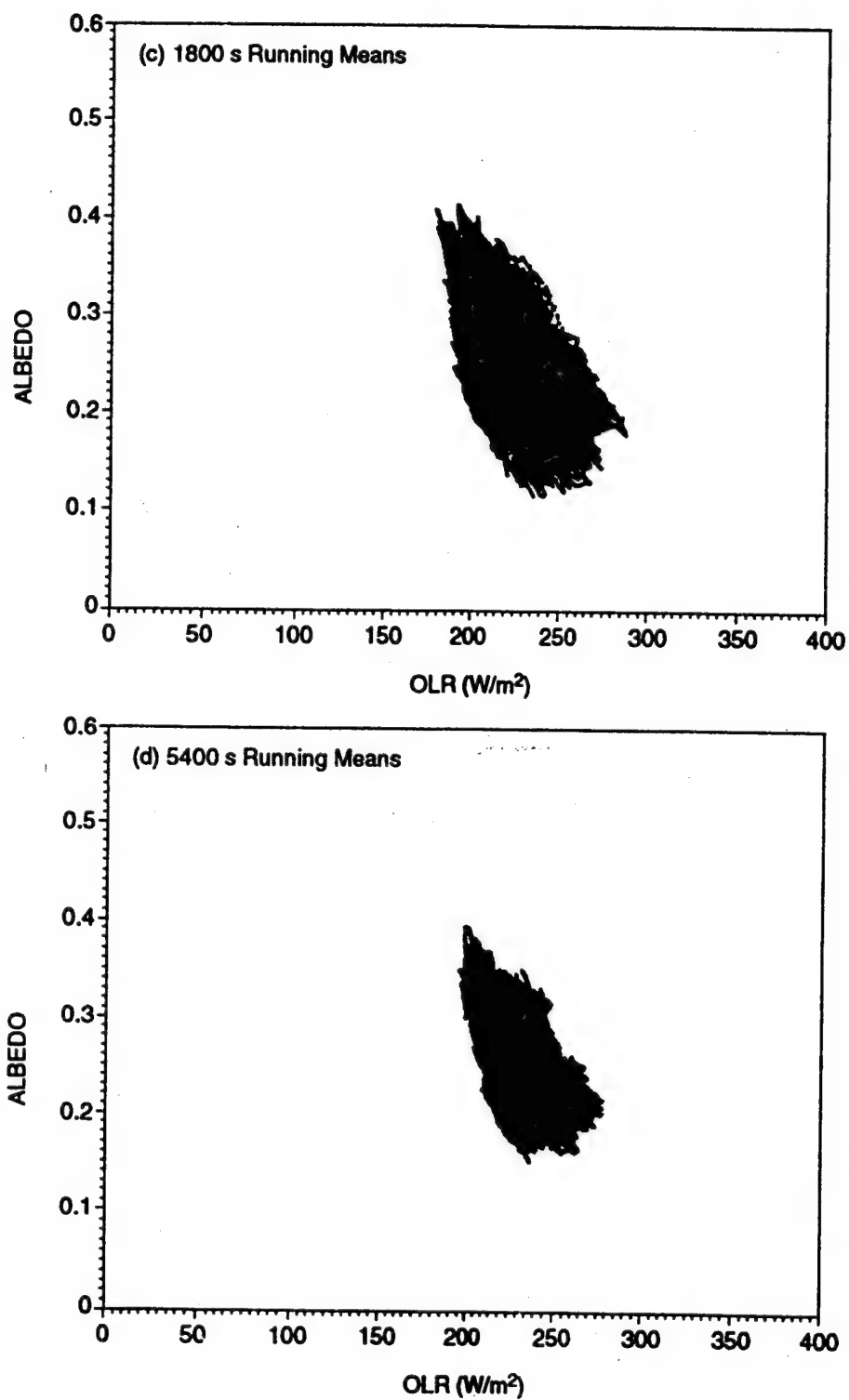


Figure 9-8. Albedo-OLR correlated pairs for 90° inclination orbits (page 2 of 2).

X. GRAVITATIONAL FIELD

With the advent of Earth satellites, there has been a considerable advance in the accurate determination of the Earth's gravitational field. The current knowledge regarding the Earth's gravitational field has advanced far beyond the normal operational requirement. Adequate accuracy for determining most space vehicle design values of gravitational interactions is obtained with the central inverse square field.

$$\vec{F} = -\frac{\mu_E m}{r^2} \hat{r}, \quad (10-1)$$

where:

\vec{F} = vector force acting on a particle in Newtons,

m = mass of particle in kg,

μ_E = gravitational constant for the Earth,

r = distance from the particle to the center of the Earth in meters,

\hat{r} = unit vector from the center of the Earth to the particle, dimensionless.

The above central force model accurately represents the gravitational field to approximately 0.1 percent. If this accuracy is insufficient, a more detailed model of the gravitational field can be used that accounts for the non-uniform mass distribution within Earth. This model gives gravitational potential, V , to an accuracy of approximately a few parts in a million. The gravitational acceleration is the negative gradient (vector derivative) of the potential and introduces nonradial gravitational forces.

$$\vec{F} = m\vec{g} = m(-\vec{\nabla}V). \quad (10-2)$$

The formula for V is shown below:

$$V(r, \phi, \lambda) = \frac{\mu_E}{r} \left(1 + \sum_{n=1}^{\infty} \sum_{m=0}^n \left(\frac{R_E}{r} \right)^n P_{nm}(\sin \phi) [C_{nm} \cos(m\lambda) + S_{nm} \sin(m\lambda)] \right), \quad (10-3)$$

where

ϕ = geocentric declination

λ = east longitude

μ_E = gravitational constant for the Earth

for the Marsh et al.³¹ model discussed below

$$\mu_E = 3.9860064 \times 10^{14} \text{ (N m}^2\text{/kg)}, *$$

$$R_E = 6378.137 \text{ km} . *$$

*Use these values only in this model. For other applications, use the values found in table 2-1.

The coefficients C_{nm} and S_{nm} are the harmonic coefficients of the potential function and P_{nm} represents the associated Legendre functions of the first kind of degree n and order m . Because $\sin \phi = Z/r = u$, it is simply a direction cosine and the associated Legendre function may be expressed as:

$$P_{nm} = \frac{(1-u^2)^{m/2}}{2^n n!} \frac{d^{n+m}(u^2-1)^n}{du^{n+m}} \quad (10-4)$$

Unnormalized Legendre functions should be used with the 4x4 coefficients given in table 10-1. They are adequate for calculation of orbit position to within a few hundred meters. Improved accuracy can be obtained by using additional terms. When computer capacity is an issue, it is best to use the model with the number of coefficients tailored to the application, rather than truncate a larger set. A recommended high accuracy set of coefficients (36x36) is presented in reference 31. Additional information on normalization can be found in Anon. (1975).

Table 10-1. Gravitational coefficients (4x4).

Zonal Harmonic Coefficients (Multiply by 10 ⁻⁶)			
C10		0.0	
C20		-1082.6258313	
C30		2.5326124	
C40		1.6161966	
Tesseral Harmonic Coefficients (Multiply by 10 ⁻⁶)			
n	m	C_{nm}	S_{nm}
1	1	0.0	0.0
2	1	0.0	0.0
2	2	+1.5743213	-0.90359264
3	1	+2.1924062	+0.2695930
3	2	+0.3086208	-0.2119137
3	3	+0.1005368	+0.1970571
4	1	-0.5060535	-0.4507374
4	2	+0.0775920	+0.1484817
4	3	+0.0592223	-0.0119894
4	4	-0.0040152	+0.0065174
(Derived from the normalized coefficients in reference 31 by the conversion defined in reference 32.)			

APPENDIX A

ABBREVIATIONS AND ACRONYMS

ac	alternating current
AL	anomalously large
AO	atomic oxygen
A_p	geomagnetic activity index (daily)
a_p	geomagnetic activity index (3-hourly)
AU	astronomical unit
C	Celsius
CCD	charge-coupled device
CH	coronal hole
cm	centimeter
CME	coronal mass ejection
CMG	control moment gyro
dc	direct current
DMSP	Defense Meteorological Satellite Program
EMI	electromagnetic interference
EMR	electromagnetic radiation
EUV	extreme ultraviolet
eV	electron volt
EVA	extravehicular activity
$F_{10.7}$	10.7 centimeter solar radio noise flux
FORTTRAN	formula translation
G	gauss
GCR	galactic cosmic ray

A-2

GEO	geosynchronous Earth orbit
GeV	gigaelectron volt
GHz	gigahertz
μ_E	gravitational constant for the Earth
GN&C	guidance, navigation, and control
GRAM	global reference atmosphere model
GSFC	Goddard Space Flight Center
GV	gigavolt
Hg	mercury
Hz	Hertz
IGRF	international geomagnetic reference field
IMF	interplanetary magnetic field
IOC	initial operational capability
IR	infrared
IRI	international reference ionosphere
JAS	Journal of Atmospheric Sciences
JGR	Journal of Geophysical Research
JSC	Johnson Space Center
K	Kelvin
keV	kiloelectron volt
kg	kilogram
kHz	kiloHertz
km	kilometer
K_p	logarithm of the geomagnetic activity index A_p
LDEF	Long Duration Exposure Facility

.LEO	low-Earth orbit
.eRC	Lewis Research Center
.SI	large-scale integration
.y- α	Lyman-alpha
n	meter
.MET	Marshall engineering thermosphere
.MeV	megaelectron volt
.MHz	megahertz
.MLT	magnetic local time
.MSFC	Marshall Space Flight Center
.mV	millivolt
.MW	megawatt
IASA	National Aeronautics and Space Administration
m	nanometer
IRL	Naval Research Laboratory
ISSDC	National Space Science Data Center
ITI	New Technology, Inc.
.R	ordinary
CA	polar cap absorption
E	radius of the Earth
F	radio frequency
	second
AM	statistical analysis mode
EU	single event upset
ZA	solar zenith angle

A-4

TID	traveling ionospheric disturbance
UAH	University of Alabama, Huntsville
UT	universal time
u	atomic mass unit
UV	ultraviolet
VLF	very low frequency
VLSID	very large-scale integrated device
W	Watt
wrt	with respect to
WTS	westward traveling surges

APPENDIX B

1.0 GALACTIC COSMIC RAYS (GCR's)*

The following paragraphs and tables present an algorithm for computing the differential energy spectra of the most important charged-particle populations in the Earth's vicinity. These equations were devised to fit the data and are intended to have no physical interpretation. This analytic formula may be easily programmed for a digital computer of almost any size and is intended to become a subroutine in a program which will be used to estimate the soft error rates in satellite-borne electronics.

GCR's consist of electrons and the nuclei of all the elements in the periodic table; the first 28 elements are the most important for cosmic ray effects on microelectronics. These particles are from outside the solar system, and their flux at low energies is anticorrelated with solar activity (i.e., more cosmic rays at solar minimum). The differential energy spectra in particles per square meter-steradian-second-Megaelectron volts per atomic mass unit (i.e., particles/(m²-sr-s-MeV/u)) are given in the following paragraphs.

The spectra for protons (hydrogen nuclei), α -particles (helium nuclei), and iron nuclei are given below for energies above 10 MeV/u:

$$F(E,t) = A(E) \sin[W(t-t_0)] + B(E) \quad (\text{B1-1})$$

where

$W = 0.576$ radian/year,

$t_0 = 1950.6$ A.D. date,

$t =$ current date in years,

$E =$ particle energy in MeV/nucleon,

$$B(E) = 0.5 [f_{\min}(E) + f_{\max}(E)] , \quad (\text{B1-2})$$

$$A(E) = 0.5 [f_{\min}(E) - f_{\max}(E)] , \quad (\text{B1-3})$$

f_{\max} and f_{\min} differ only by the choice of constants in the equation,

$$f(E) = 10^m (E/E_0)^a , \quad (\text{B1-4})$$

where

$$a = a_0 \{1 - \exp[-X_1(\log_{10} E)^b]\} , \quad (\text{B1-5})$$

and

$$m = C_1 \exp[-X_2(\log_{10} E)^2] - C_2 . \quad (\text{B1-6})$$

*Part 1, appendix B is from Adams et al.^{33 34}

The values of the constants, a_0 , E_0 , b , X_1 , X_2 , C_1 , and C_2 , are given in table B1-1 for each of the elements hydrogen (H), helium (He), and iron (Fe) for the conditions of solar maximum and solar minimum.

Table B1-1. Constants used in equations (B1-4) through (B1-6) to compute the differential energy spectra of H, He, and Fe at solar maximum and solar minimum.

Element	a_0	E_0	b	X_1	X_2	C_1	C_2
H-min	-2.20	1.1775E+5	2.685	0.117	0.80	6.52	4.00
H-max	-2.20	1.1775E+5	2.685	0.079	0.80	6.52	4.00
He-min	-2.35	8.2700E+4	2.070	0.241	0.83	4.75	5.10
He-max	-2.35	8.2700E+4	2.070	0.180	0.83	4.75	5.10
Fe-min	-2.14	1.1750E+5	2.640	0.140	0.65	6.63	7.69
Fe-max	-2.14	1.1750E+5	2.640	0.102	0.65	6.63	7.69

The differential energy spectra for carbon (C), oxygen (O), fluorine (F), neon (Ne), sodium (Na), aluminum (Al), and phosphorus (P) are obtained by multiplying the helium spectrum (obtained from equation (B1-1)) by the appropriate scaling factor in table B1-2.

Table B1-2. The ratio of the abundance of various nuclei to helium.

Element	Ratio	Element	Ratio
C	3.04E-2		
O	2.84E-2	Al	1.07E-3
F	6.06E-4		
Ne	4.63E-3	P	2.34E-4
Na	1.02E-3		

The differential energy spectra for calcium (Ca), cobalt (Co), and nickel (Ni) are obtained by multiplying the iron spectrum (obtained from equation (B1-1)) by the scaling factors listed in table B1-3.

Table B1-3. The ratios of the abundance of various elements to iron.

Element	Ratio
Ca	2.1E-1
Co	3.4E-3
Ni	5.0E-2

The spectra of the elements lithium (Li), beryllium (Be), and boron (B) are obtained from the helium spectrum, F_{He} , modified by the equation:

$$F^* = \begin{cases} 0.021 F_{\text{He}} & E < 3000 \text{ MeV/u} \\ 0.729 E^{-0.443} F_{\text{He}} & E \geq 3000 \text{ MeV/u} \end{cases} \quad (\text{B1-7})$$

to obtain the combined spectrum of (Li+Be+B). Equation (B1-7) is then multiplied by the ratio in table B1-4 to obtain the individual elemental spectra.

Table B1-4. Relative fractions of Li, Be, and B in the combined total abundance Li+Be+B.

Element	Ratio
Li	0.330
Be	0.176
B	0.480

The spectrum of the element nitrogen (N) is obtained by modifying the helium spectrum, F_{He} , as shown below:

$$F_N = \{8.7E^{-3} \exp[-0.4 (\log_{10} E - 3.15)^2] + 7.6E^{-3} \exp[-0.9 (\log_{10} E - 0.8)^2]\} F_{\text{He}} \quad (\text{B1-8})$$

where E is in MeV/u.

The spectra of the elements magnesium (Mg), silicon (Si), and sulfur (S) are obtained by modifying the helium spectrum, F_{He} , as shown:

$$F^* = \begin{cases} F_{\text{He}} & E < 2200 \\ (1 + 1.56E^{-5}(E - 2200)) F_{\text{He}} & E \geq 2200 \end{cases} \quad (\text{B1-9})$$

The individual spectra for these elements are obtained by multiplying F^* by the ratio of table B1-5.

Table B1-5. Ratios of Mg, Si, and S to an adjusted helium spectrum.

Element	Ratio
Mg	$6.02E^{-3}$
Si	$4.63E^{-3}$
S	$9.30E^{-4}$

The spectra for the elements chlorine (Cl), argon (Ar), potassium (K), scandium (Sc), titanium (Ti), vanadium (V), chromium (Cr), and manganese (Mn) are all obtained by modifying the iron spectrum, F_{Fe} , as shown below:

$$F^* = Q(E)F_{Fe}, \quad (B1-10)$$

where

$$Q(E) = 16 [1 - \exp(-0.075E^{0.4})]E^{-0.33}, \quad (B1-11)$$

where E is in MeV/u.

The F^* , from the subiron spectrum (equation (B1-10)) is multiplied by the appropriate ratio in table B1-6 to obtain the individual elemental spectra.

Table B1-6. Fractional abundance of each element in the subiron group.

Element	Ratio	Element	Ratio
Cl	0.070	Ti	0.147
Ar	0.130	V	0.070
K	0.090	Cr	0.140
Sc	0.042	Mn	0.100

The differential energy spectra for elements from copper to uranium are obtained by multiplying the iron spectrum (from equation (B1-1)) by the scaling factors listed in table B1-7.

Table B1-7. Ratio of the abundances of various nuclei to iron (page 1 of 2).

Element	Ratio	Element	Ratio
Cu	6.8E-4	Pm	1.9E-7
Zn	8.8E-4	Sm	8.7E-7
Ga	6.5E-5	Eu	1.5E-7
Ge	1.4E-4	Gd	7.0E-7
As	9.9E-6	Tb	1.7E-7
Se	5.8E-5	Dy	7.0E-7
Br	8.3E-6	Ho	2.6E-7
Kr	2.3E-5	Er	4.3E-7
Rb	1.1E-5	Tm	8.9E-8
Sr	3.6E-5	Yb	4.4E-7
Y	6.8E-6	Lu	6.4E-8

Table B1-7. Ratio of the abundances of various nuclei to iron (page 2 of 2).

Element	Ratio	Element	Ratio
Zr	1.7E-5	Hf	4.0E-7
Nb	2.6E-6	Ta	3.6E-8
Mo	7.1E-6	W	3.8E-7
Tc	1.6E-6	Re	1.3E-7
Ru	5.3E-6	Os	5.6E-7
Rh	1.5E-6	Ir	3.7E-7
Pd	4.5E-6	Pt	7.2E-7
Ag	1.3E-6	Au	1.3E-7
Cd	3.6E-6	Hg	2.3E-7
In	1.4E-6	Tl	1.8E-7
Sn	7.5E-6	Pb	1.7E-6
Sb	9.9E-7	Bi	9.0E-8
Te	5.7E-6	Po	0
I	1.5E-6	At	0
Xe	3.5E-6	Rn	0
Cs	5.8E-7	Fr	0
Ba	6.0E-6	Ra	0
La	5.3E-7	Ac	0
Ce	1.6E-6	Th	9.0E-8
Pr	3.0E-7	Pa	0
Nd	1.1E-6	U	5.4E-8

The formula given above is correct for quiet periods in the interplanetary medium when only the GCRs are present. These conditions are often disturbed, especially at low energies, by small solar flares, co-rotating events, etc. To allow for typical disturbed conditions, a worst-case spectrum should be employed. With 90-percent confidence, the instantaneous particle flux should never be more intense than described by this case at any energy.

To construct the worst-case spectrum for protons, compute the "H-min" spectrum (using equation (B1-4)) and then compute as shown below:

$$F_{\text{H-worst}} = [1897e^{-E/9.66+1.64}] F_{\text{H-min}} \quad (\text{B1-12})$$

This applies for $E < 100$ MeV/u. For higher energies, use the GCR spectrum for the appropriate mission time, t , in equation (B1-1).

In like manner, the solar minimum case for helium and iron spectra (obtained from equation (B1-4)) is multiplied by:

$$28.4 e^{-E/13.84+1.64} , \quad (B1-13)$$

for $E \leq 100$ MeV/u.

The worst-case spectra of H, He, and Fe for any element for $E > 100$ MeV/u are approximated by a multiple of the solar minimum spectra:

$$F_{\text{worst}} = 1.64 F_{\text{min}} . \quad (B1-14)$$

The resulting spectra are employed as described above to obtain the other elemental spectra, i.e., in the same way as F_{He} and F_{Fe} were used.

In addition to galactic cosmic rays, some particles are believed to be accelerated in the interplanetary medium. The most important of these is called the anomalous component. The contribution of the anomalous component to the helium spectrum is important for cosmic ray effects on microelectronics. For periods of decaying or minimum solar activity the cosmic ray helium spectrum should be modified as follows:

1. Determine the maximum values of the cosmic ray spectra from equation (B1-4) using the He-max and He-min constants from table B1-1.
2. Modify equation (B1-4) so that these maximum values apply for all energies below the energy at which the maxima occurs, i.e., for solar minimum:

$$f^*_{\text{He-min}} = \begin{cases} 0.33 & E < 200 \text{ MeV/u} \\ f_{\text{He-min}} (\text{eq. (B1-4)}) & E \geq 200 \text{ MeV/u} \end{cases} \quad (B1-15)$$

3. Make the same type of modification, for solar maximum:

$$f^*_{\text{He-max}} = \begin{cases} 0.33 & E < 300 \text{ MeV/u} \\ f_{\text{He-max}} (\text{eq. (B1-4)}) & E \geq 300 \text{ MeV/u} \end{cases} \quad (B1-16)$$

4. Combine the resulting spectra as before using equations (B1-1) through (B1-3).

NOTE: This applies only to He. Use the regular He spectra of equations (B1-1) through (B1-6) for obtaining the spectra of other elements.

Besides helium, the anomalous component contributes to the oxygen and nitrogen spectra at low energies. For years with decaying or minimum solar activity these contributions should be added to the GCR oxygen and nitrogen spectra. For oxygen, use:

$$f(E) = 6E^{-2} \exp[-(\ln(E)-1.79)^2/0.70] \text{ (particles/(m}^2\text{-sr-s-MeV/u))} . \quad (B1-17)$$

This spectrum crosses over the galactic spectrum at approximately 30 MeV/u. The two spectra should be matched at that point with equation (B1-17) replacing the galactic spectrum at lower energies.

Similarly for nitrogen:

$$f(E) = 1.54E^{-2} \exp[-(\ln(E)-1.79)^2/0.70] \text{ (particles/(m}^2\text{-sr-s-MeV/u))} \quad (\text{B1-18})$$

Again, this crosses with the GCR spectrum at approximately 30 MeV/u and should replace it below this energy. The spectra of the remaining elements are unaffected or affected at too low an energy to matter.

There is a possibility that the anomalous component is singly ionized. If so, it will have an extraordinary ability to penetrate the Earth's magnetosphere. In this case, the differential energy spectra shown below are assumed for the helium, carbon, nitrogen, oxygen, neon, magnesium, silicon, argon, and iron spectra of the anomalous component. There probably are anomalous components in the spectra of the nuclei heavier than iron, but there are no data on them at this time.

For singly ionized helium,

$$F = \begin{cases} 0.4 & E < 195 \\ 1.54 \times 10^4 E^{-2} & E \geq 195 \end{cases} \quad (\text{B1-19})$$

For singly ionized carbon,

$$F = \begin{cases} 4.00 \times 10^3 \exp[-\ln(E)-1.79)^2/0.7] & E < 10 \\ 0.27 E^{-2} & E \geq 10 \end{cases} \quad (\text{B1-20})$$

For singly ionized nitrogen,

$$F = \begin{cases} 1.54 \times 10^{-2} \exp[-\ln(E)-1.79)^2/0.7] & E < 20 \\ 0.773 E^{-2} & E \geq 20 \end{cases} \quad (\text{B1-21})$$

For singly ionized oxygen,

$$F = \begin{cases} 6.00 \times 10^{-2} \exp[-\ln(E)-1.79)^2/0.7] & E < 30 \\ 1.32 E^{-2} & E \geq 30 \end{cases} \quad (\text{B1-22})$$

For singly ionized neon,

$$F = \begin{cases} 8.00 \times 10^{-3} \exp[-\ln(E)-1.79)^2/0.7] & E < 20 \\ 0.40 E^{-2} & E \geq 20 \end{cases} \quad (\text{B1-23})$$

For singly ionized magnesium,

$$F = \begin{cases} 8.00 \times 10^{-4} \exp[-\ln(E)-2.30)^2/0.7] & E < 20 \\ 0.16 E^{-2} & E \geq 20 \end{cases} \quad (\text{B1-24})$$

For singly ionized silicon,

$$F = \begin{cases} 1.00 \times 10^{-3} \exp[-\ln(E) - 2.20]^2 / 0.4] & E < 10 \\ 0.10 E^{-2} & E \geq 10 \end{cases} \quad (B1-25)$$

For singly ionized argon,

$$F = \begin{cases} 5.40 \times 10^{-4} \exp[-\ln(E) - 1.79]^2 / 0.7] & E < 20 \\ 0.28 E^{-2} & E \geq 20 \end{cases} \quad (B1-26)$$

For singly ionized iron,

$$F = \begin{cases} 6.00 \times 10^{-4} \exp[-\ln(E) - 2.48]^2 / 2.0] & E < 30 \\ 0.35 E^{-2} & E \geq 30 \end{cases} \quad (B1-27)$$

Since these anomalous component particles are assumed to be singly ionized, they will have a higher magnetic rigidity than galactic cosmic rays of the same energy. The magnetic rigidity of galactic cosmic rays is

$$R = (A/Z)(E^2 + 1862.324E)^{1/2} / 1000, \quad (B1-28)$$

in GeV/ec. The rigidity of singly ionized nuclei is

$$R = (A(E^2 + 1862.324E)^{1/2}) / 1000. \quad (B1-29)$$

To add the singly ionized anomalous component, it is necessary to modulate both the galactic cosmic ray spectra and the anomalous component spectra given above using the geomagnetic cutoff transmission function. After calculating this function (discussed in Adams et. al.^{34 35}), the resulting modulated spectra are then added together.

2.0 SOLAR FLARE PARTICLE EVENTS*

Solar flare particle events are sporadic occurrences lasting 1 to 5 days. When these events occur, they can be the dominant cause of soft errors. For statistical treatment, they are broken into two classes: ordinary (OR) and anomalously large (AL). The probability of having more than a number of events, n , in a time, t , is given by:

$$P(n, t, N, T) = 1 - \sum_{i=0}^n (i+N)! (t/T)^i / [i! N! (1+t/T)^{1+N}] , \quad (B2-1)$$

where T and t are in years, and N is the number of flares that have occurred in T years.

For ordinary events, equation (B2-1) becomes:

$$\begin{aligned} P_{OR} &= P(n, t, 24, 7) \text{ for the decreasing portion of the solar cycle} \\ \text{and} \\ P_{OR} &= P(n, t, 6, 8) \text{ for the increasing portion of the solar cycle,} \end{aligned} \quad (B2-2)$$

where there is a probability, P_{OR} , of having more than n ordinary events in t years. Similarly for anomalously large events:

$$P_{AL} = P(n, t, 1, 7) . \quad (B2-3)$$

The peak proton flux differential energy spectrum for ordinary events is, typically:

$$f_{OR} = 2.45E^4(e^{-E/27.5} + 173e^{-E/4}) \text{ protons}/(\text{m}^2 \cdot \text{sr} \cdot \text{s} \cdot \text{MeV}) , \quad (B2-4)$$

where E is in MeV, and no worse than:

$$f_{WOR} = 2.06E^5(e^{-E/24.5} + 63.6e^{-E/4}) \text{ protons}/(\text{m}^2 \cdot \text{sr} \cdot \text{s} \cdot \text{MeV}) , \quad (B2-5)$$

with a confidence of approximately 90 percent.

Using the August 1972 flare as a model AL event, the peak proton flux differential energy spectrum is:

$$f_{AL} = \begin{cases} 9.3E^9(dP/dE) \exp(-P/0.10) & E < 150 \text{ MeV} \\ 1.76E^5(dP/dE)p^{-9} & E \geq 150 \text{ MeV} \end{cases} , \quad (B2-6)$$

in protons/ $(\text{m}^2 \cdot \text{sr} \cdot \text{s} \cdot \text{MeV})$, where

$$P = [E^2 + 1863.2E]^{1/2} / 1000 , \quad (B2-7)$$

and E is in MeV.

*Part 2, appendix B is from Adams et al.^{33 34}

To model the worst flare that is ever likely to occur, use the composite of the August 1972 flare and the February 1956 flare. The composite worst-case flare proton spectrum is taken to be the peak of the 1972 spectrum, as given by equation (B2-6), and the 1956 peak spectrum, given below.

$$f_{1956} = 1.116E^{+8}(E^{-1.248})(0.248+2.5E^{+5})((1.7)(EPOW)(EXPOW)) \\ + 4.7E^{+19}(E^{-5.3})(4.3(1-EXPOW)-6.32E^{-15}((4)(EPOW)(EXPOW))) , \quad (B2-8)$$

where

$$EPOW = E^{1.7}$$

and

$$EXPOW = \exp(-2.5E^{-5} EPOW) .$$

The composition of flare particles is also highly variable from flare to flare. Table B2-1 gives the composition relative to hydrogen for the elements through nickel. Both mean and 90-percent confidence level worst cases are given. To obtain the spectrum of any element in a flare, just multiply the abundance ratio from the Table B2-1 by the appropriate flare proton spectrum.

The worst-case compositions of the elements from copper to uranium are obtained by multiplying the abundance ratios of table B2-2 by:

$$(C_w(O)/C_r(O))0.48 \exp(Z^{0.78}/6.89) , \quad (B2-9)$$

where $C_w(O)$ and $C_r(O)$ are the worst-case and mean abundance coefficients for oxygen in Table B2-1.

Table B2-1. Mean and worst-case flare compositions.

Element	Mean Case	Worst Case
H	1	1
He	1.0E-2	3.3E-2
Li	0	0
Be	0	0
B	0	0
C	1.6E-4	4.0E-4
N	3.8E-5	1.1E-4
O	3.2E-4	1.0E-3
F	0	0
Ne	5.1E-5	1.9E-4
Na	3.2E-6	1.3E-5
Mg	6.4E-5	2.5E-4
Al	3.5E-6	1.4E-5
Si	5.8E-5	1.9E-4
P	2.3E-7	1.1E-6
S	8.0E-6	5.0E-5
Cl	1.7E-7	8.0E-7
Ar	3.3E-6	1.8E-5
K	1.3E-7	6.0E-7
Ca	3.2E-6	2.0E-5
Sc	0	0
Ti	1.0E-7	5.0E-7
V	0	0
Cr	5.7E-7	4.0E-6
Mn	4.2E-7	2.3E-6
Fe	4.1E-5	4.0E-4
Co	1.0E-7	5.5E-7
Ni	2.2E-6	2.0E-5

The mean case compositions for the elements from copper to uranium are taken from reference 36. The ratios of these abundances to hydrogen are given in Table B2-2.

Table B2-2. Mean flare compositions.

Cu	2.0E-8	Pm	0
Zn	6.0E-8	Sm	1.0E-11
Ga	2.0E-9	Eu	4.0E-12
Ge	5.0E-9	Gd	2.0E-11
As	3.0E-10	Tb	3.0E-12
Se	3.0E-9	Dy	2.0E-11
Br	4.0E-10	Ho	4.0E-12
Kr	2.0E-9	Er	1.0E-11
Rb	3.0E-10	Tm	2.0E-12
Sr	1.0E-9	Yb	9.0E-12
Y	2.0E-10	Lu	2.0E-12
Zr	5.0E-10	Hf	8.0E-12
Nb	4.0E-11	Ta	9.0E-13
Mo	2.0E-10	W	1.0E-11
Tc	0	Re	2.0E-12
Ru	9.0E-11	Cs	3.0E-11
Rh	2.0E-11	Ir	3.0E-11
Pd	6.0E-11	Pt	6.0E-11
Ag	2.0E-11	Au	1.0E-11
Cd	7.0E-11	Hg	1.0E-11
In	9.0E-12	Tl	9.0E-12
Sn	2.0E-10	Pb	1.0E-10
Sb	1.4E-11	Bi	6.0E-12
Te	3.0E-10	Po	0
I	6.0E-11	At	0
Xe	2.7E-10	Rn	0
Cs	2.0E-11	Fr	0
Ba	2.0E-10	Ra	0
La	2.0E-11	Ac	0
Ce	5.0E-11	Th	2.0E-12
Pr	8.0E-12	Pa	0
Nd	4.0E-11	U	1.2E-12

3.0 GEOMAGNETIC CUTOFFS*

The modulation of cosmic ray spectra by the Earth's magnetic field requires a more thorough treatment than can be offered here, but some guidance will be provided. The geomagnetic cutoff is a value of magnetic rigidity below which cosmic rays will not reach a specified point in the magnetosphere from a specified direction. The magnetic rigidity, P , in GeV/ec, may be computed from the particles' energy using:

$$P = \frac{A}{1000 Z} [E^2 + 1863.2E]^{1/2} , \quad (B3-1)$$

where A and Z are the atomic mass and charge of the nucleus in question. The cutoff at any point for particles arriving from the zenith is most simply computed with:

$$P_c = 15.96/L^{2.005} \text{ GeV/ec} , \quad (B3-2)$$

where L is McIlwain's L parameter (i.e., the radial distance, in Earth radii, from the center of the Earth to the point in the geometric equatorial plane where it is crossed by the magnetic field line that also passes through the point of observation).

Design consideration must be given to solar flare spectra, because (1) the flare particle intensity changes on a time scale comparable to or shorter than an orbital period, (2) there is no certain proof that solar flare particles are fully ionized, and (3) the geomagnetic cutoff is suppressed to some extent during a flare. The geomagnetic cutoff during a flare, P_F , should be computed from the "quiet time" cutoff, P_0 , using:

$$\delta P/P_0 = 0.54 \exp(-P_0/2.9) , \quad (B3-3)$$

and

$$P_F = P_0 - \delta P , \quad (B3-4)$$

where P_F , P_0 , and δP are in GeV/ec.

*Part 3, Appendix B is from Adams.³⁴

APPENDIX C

Table C-1. Median value of global maximum densities for altitude and $F_{10.7}$ bin with differences between global maximum density and median value for several percentile ranges. Densities in kg/m^3 (page 1 of 6).

$F_{10.7B}$ Range	Bin 1 66-102	Bin 2 102-138	Bin 3 138-174	Bin 4 174-210	Bin 5 210-246	All 66-246
----------------------	-----------------	------------------	------------------	------------------	------------------	---------------

Altitude 250 km

Median	5.941E-11	8.411E-11	1.050E-10	1.239E-10	1.363E-10	8.629E-11
1	-1.554E-11	-2.191E-11	-2.827E-11	-3.497E-11	-2.560E-11	-4.066E-11
5	-1.209E-11	-1.707E-11	-2.063E-11	-2.481E-11	-2.000E-11	-3.559E-11
33	-3.760E-12	-4.970E-12	-5.570E-12	-6.400E-12	-5.100E-12	-1.718E-11
67	4.460E-12	5.750E-12	6.000E-12	6.100E-12	6.100E-12	1.921E-11
95	1.816E-11	2.359E-11	2.140E-11	2.090E-11	2.130E-11	5.291E-11
99	2.724E-11	3.529E-11	3.060E-11	2.940E-11	2.680E-11	6.621E-11
100	6.099E-11	6.859E-11	4.670E-11	4.590E-11	3.740E-11	8.741E-11

Altitude 275 km

Median	3.123E-11	4.721E-11	6.184E-11	7.595E-11	8.574E-11	4.869E-11
1	-9.330E-12	-1.425E-11	-1.956E-11	-2.546E-11	-1.975E-11	-2.576E-11
5	-7.310E-12	-1.119E-11	-1.446E-11	-1.837E-11	-1.554E-11	-2.277E-11
33	-2.320E-12	-3.330E-12	-4.020E-12	-4.880E-12	-4.040E-12	-1.135E-11
67	2.780E-12	3.920E-12	4.400E-12	4.780E-12	5.030E-12	1.350E-11
95	1.161E-11	1.660E-11	1.607E-11	1.683E-11	1.796E-11	3.946E-11
99	1.770E-11	2.534E-11	2.333E-11	2.405E-11	2.286E-11	5.060E-11
100	4.209E-11	5.223E-11	3.680E-11	3.875E-11	3.266E-11	6.971E-11

Altitude 300 km

Median	1.721E-11	2.767E-11	3.793E-11	4.843E-11	5.609E-11	2.868E-11
1	-5.720E-12	-9.360E-12	-1.356E-11	-1.851E-11	-1.513E-11	-1.658E-11
5	-4.510E-12	-7.410E-12	-1.014E-11	-1.355E-11	-1.201E-11	-1.476E-11
33	-1.450E-12	-2.240E-12	-2.880E-12	-3.700E-12	-3.200E-12	-7.570E-12
67	1.760E-12	2.690E-12	3.210E-12	3.700E-12	4.060E-12	9.510E-12
95	7.530E-12	1.169E-11	1.201E-11	1.336E-11	1.491E-11	2.934E-11
99	1.164E-11	1.818E-11	1.771E-11	1.940E-11	1.915E-11	3.854E-11
100	2.922E-11	3.968E-11	2.874E-11	3.232E-11	2.801E-11	5.542E-11

Altitude 325 km

Median	9.838E-12	1.679E-11	2.402E-11	3.183E-11	3.777E-11	1.748E-11
1	-3.582E-12	-6.250E-12	-9.480E-12	-1.349E-11	-1.154E-11	-1.085E-11
5	-2.839E-12	-4.970E-12	-7.150E-12	-1.000E-11	-9.230E-12	-9.725E-12
33	-9.230E-13	-1.530E-12	-2.070E-12	-2.800E-12	-2.510E-12	-5.100E-12
67	1.142E-12	1.850E-12	2.340E-12	2.840E-12	3.240E-12	6.730E-12
95	4.952E-12	8.270E-12	8.960E-12	1.051E-11	1.221E-11	2.183E-11
99	7.762E-12	1.308E-11	1.339E-11	1.549E-11	1.585E-11	2.932E-11
100	2.046E-11	3.012E-11	2.232E-11	2.662E-11	2.368E-11	4.397E-11

Table C-1. Median value of global maximum densities for altitude and $F_{10.7}$ bin with differences between global maximum density and median value for several percentile ranges. Densities in kg/m^3 (page 2 of 6).

$F_{10.7B}$ Range	Bin 1 66-102	Bin 2 102-138	Bin 3 138-174	Bin 4 174-210	Bin 5 210-246	All 66-246
Altitude 350 km						
Median	5.786E-12	1.047E-11	1.561E-11	2.142E-11	2.602E-11	1.095E-11
1	-2.283E-12	-4.223E-12	-6.687E-12	-9.880E-12	-8.790E-12	-7.212E-12
5	-1.818E-12	-3.382E-12	-5.090E-12	-7.400E-12	-7.080E-12	-6.504E-12
33	-5.980E-13	-1.057E-12	-1.500E-12	-2.110E-12	-1.960E-12	-3.488E-12
67	7.460E-13	1.290E-12	1.710E-12	2.180E-12	2.570E-12	4.790E-12
95	3.307E-12	5.900E-12	6.690E-12	8.240E-12	9.910E-12	1.628E-11
99	5.244E-12	9.470E-12	1.013E-11	1.230E-11	1.299E-11	2.234E-11
100	1.448E-11	2.291E-11	1.731E-11	2.176E-11	1.980E-11	3.487E-11

Altitude 375 km						
Median	3.479E-12	6.670E-12	1.035E-11	1.470E-11	1.826E-11	7.008E-12
1	-1.474E-12	-2.886E-12	-4.753E-12	-7.271E-12	-6.710E-12	-4.856E-12
5	-1.180E-12	-2.323E-12	-3.641E-12	-5.497E-12	-5.430E-12	-4.404E-12
33	-3.930E-13	-7.340E-13	-1.084E-12	-1.600E-12	-1.530E-12	-2.408E-12
67	4.950E-13	9.120E-13	1.270E-12	1.680E-12	2.030E-12	3.442E-12
95	2.236E-12	4.240E-12	5.020E-12	6.450E-12	8.010E-12	1.221E-11
99	3.586E-12	6.900E-12	7.690E-12	9.740E-12	1.059E-11	1.709E-11
100	1.034E-11	1.750E-11	1.344E-11	1.771E-11	1.645E-11	2.770E-11

Altitude 400 km						
Median	2.128E-12	4.327E-12	6.990E-12	1.026E-11	1.302E-11	4.567E-12
1	-9.610E-13	-1.994E-12	-3.415E-12	-5.393E-12	-5.145E-12	-3.306E-12
5	-7.730E-13	-1.613E-12	-2.635E-12	-4.114E-12	-4.186E-12	-3.015E-12
33	-2.600E-13	-5.160E-13	-7.980E-13	-1.219E-12	-1.200E-12	-1.681E-12
67	3.330E-13	6.490E-13	9.390E-13	1.290E-12	1.600E-12	2.496E-12
95	1.528E-12	3.076E-12	3.780E-12	5.050E-12	6.460E-12	9.203E-12
99	2.479E-12	5.072E-12	5.850E-12	7.710E-12	0.600E-12	1.312E-11
100	7.460E-12	1.342E-11	1.045E-11	1.438E-11	1.360E-11	2.205E-11

Altitude 425 km						
Median	1.321E-12	2.848E-12	4.788E-12	7.257E-12	9.405E-12	3.019E-12
1	-6.319E-13	-1.389E-12	-2.472E-12	-4.022E-12	-3.957E-12	-2.270E-12
5	-5.112E-13	-1.129E-12	-1.920E-12	-3.092E-12	-3.234E-12	-2.081E-12
33	-1.740E-13	-3.660E-13	-5.890E-13	-9.290E-13	-9.360E-13	-1.182E-12
67	2.250E-13	4.650E-13	7.000E-13	9.980E-13	1.275E-12	1.823E-12
95	1.052E-12	2.247E-12	2.867E-12	3.963E-12	5.205E-12	6.979E-12
99	1.727E-12	3.752E-12	4.480E-12	6.123E-12	6.985E-12	1.013E-11
100	5.424E-12	1.034E-11	8.152E-12	1.167E-11	1.123E-11	1.761E-11

Table C-1. Median value of global maximum densities for altitude and $F_{10.7}$ bin with differences between global maximum density and median value for several percentile ranges. Densities in kg/m^3 (page 2 of 6).

$F_{10.7B}$ Range	Bin 1 66-102	Bin 2 102-138	Bin 3 138-174	Bin 4 174-210	Bin 5 210-246	All 66-246
----------------------	-----------------	------------------	------------------	------------------	------------------	---------------

Altitude 450 km

Median	8.298E-13	1.898E-12	3.320E-12	5.196E-12	6.873E-12	2.021E-12
1	-4.173E-13	-9.744E-13	-1.801E-12	-3.020E-12	-3.058E-12	-1.570E-12
5	-3.393E-13	-7.960E-13	-1.408E-12	-2.339E-12	-2.510E-12	-1.446E-12
33	-1.171E-13	-2.620E-13	-4.380E-13	-7.130E-13	-7.360E-13	-8.380E-13
67	1.530E-13	3.350E-13	5.250E-13	7.750E-13	1.009E-12	1.339E-12
95	7.292E-13	1.652E-12	2.183E-12	3.123E-12	4.197E-12	5.321E-12
99	1.211E-12	2.793E-12	3.445E-12	4.864E-12	5.677E-12	7.854E-12
100	3.972E-12	8.016E-12	6.387E-12	9.494E-12	9.257E-12	1.411E-11

Altitude 475 km

Median	5.271E-13	1.277E-12	2.326E-12	3.758E-12	5.073E-12	1.366E-12
1	-2.767E-13	-6.860E-13	-1.320E-12	-2.279E-12	-2.374E-12	-1.091E-12
5	-2.262E-13	-5.634E-13	-1.038E-12	-1.778E-12	-1.956E-12	-1.010E-12
33	-7.900E-14	-1.870E-13	-3.270E-13	-5.500E-13	-5.800E-13	-5.955E-13
67	1.045E-13	2.440E-13	3.960E-13	6.040E-13	8.040E-13	9.900E-13
95	5.079E-13	1.221E-12	1.671E-12	2.469E-12	3.398E-12	4.080E-12
99	8.539E-13	2.091E-12	2.661E-12	3.883E-12	4.622E-12	6.122E-12
100	2.927E-12	6.243E-12	5.025E-12	7.732E-12	7.647E-12	1.135E-11

Altitude 500 km

Median	3.384E-13	8.677E-13	1.644E-12	2.743E-12	3.777E-12	9.322E-13
1	-1.841E-13	-4.856E-13	-9.711E-13	-1.728E-12	-1.850E-12	-7.616E-13
5	-1.512E-13	-4.009E-13	-7.689E-13	-1.358E-12	-1.531E-12	-7.087E-13
33	-5.350E-14	-1.349E-13	-2.450E-13	-4.260E-13	-4.590E-13	-4.257E-13
67	7.160E-14	1.773E-13	3.000E-13	4.720E-13	6.420E-13	7.348E-13
95	3.551E-13	9.063E-13	1.285E-12	1.958E-12	2.756E-12	3.142E-12
99	6.048E-13	1.572E-12	2.065E-12	3.107E-12	3.771E-12	4.793E-12
100	2.168E-12	4.883E-12	3.970E-12	6.314E-12	6.323E-12	9.168E-12

Altitude 550 km

Median	1.445E-13	4.091E-13	8.387E-13	1.493E-12	2.134E-12	4.442E-13
1	-8.213E-14	-2.445E-13	-5.309E-13	-1.005E-12	-1.131E-12	-3.751E-13
5	-6.842E-14	-2.037E-13	-4.255E-13	-8.012E-13	-9.42E-13	-3.521E-13
33	-2.53E-14	-7E-14	-1.39E-13	-2.57E-13	-2.85E-13	-2.197E-13
67	1.778E-13	5.04E-13	1.014E-12	1.785E-12	2.554E-12	8.521E-13
95	3.185E-13	9.147E-13	1.607E-12	2.738E-12	3.966E-12	1.038E-12
99	4.503E-13	1.309E-12	2.091E-12	3.5E-12	4.667E-12	3.413E-12
100	1.348E-12	3.435E-12	3.343E-12	5.744E-12	5.415E-12	7.105E-12

Table C-1. Median value of global maximum densities for altitude and $F_{10.7}$ bin with differences between global maximum density and median value for several percentile ranges. Densities in kg/m^3 (page 4 of 6).

$F_{10.7B}$ Range	Bin 1 66-102	Bin 2 102-138	Bin 3 138-174	Bin 4 174-210	Bin 5 210-246	All 66-246
----------------------	-----------------	------------------	------------------	------------------	------------------	---------------

Altitude 600 km

Median	6.534E-14	1.995E-13	4.4E-13	8.325E-13	1.243E-12	2.181E-13
1	-3.759E-14	-1.247E-13	-2.935E-13	-5.907E-13	-7.072E-13	-1.874E-13
5	-3.151E-14	-1.048E-13	-2.384E-13	-4.772E-13	-5.945E-13	-1.771E-13
33	-1.184E-14	-3.68E-14	-8.03E-14	-1.579E-13	-1.87E-13	-1.139E-13
67	8.125E-14	2.506E-13	5.421E-13	1.015E-12	1.512E-12	4.479E-13
95	1.52E-13	4.844E-13	9.033E-13	1.635E-12	2.468E-12	5.578E-13
99	2.213E-13	7.191E-13	1.214E-12	2.148E-12	2.955E-12	2.091E-12
100	7.434E-13	2.103E-12	2.04E-12	3.719E-12	4.267E-12	5.292E-12

Altitude 650 km

Median	3.179E-14	1.009E-13	2.366E-13	4.755E-13	7.37E-13	1.11E-13
1	-1.763E-14	-6.447E-14	-1.638E-13	-3.515E-13	-4.436E-13	-7.215E-13
5	-1.482E-14	-5.461E-14	-1.345E-13	-2.877E-13	-3.755E-13	-9.077E-14
33	-5.64E-15	-1.966E-14	-4.63E-14	-9.81E-14	-1.205E-13	-5.992E-14
67	3.962E-14	1.289E-13	2.971E-13	5.907E-13	9.136E-13	2.411E-13
95	7.566E-14	2.626E-13	5.199E-13	9.953E-13	1.909E-12	3.083E-13
99	1.128E-13	4.049E-13	7.186E-13	1.343E-12	2.041E-12	1.304E-12
100	4.199E-13	1.313E-12	1.269E-12	2.43E-12	2.821E-12	3.447E-12

Altitude 700 km

Median	1.696E-14	5.319E-14	1.302E-13	2.76E-13	4.445E-13	5.872E-14
1	-8.687E-15	-3.39E-14	-9.212E-14	-2.101E-13	-2.804E-13	-4.976E-14
5	-7.289E-15	-2.894E-14	-7.638E-14	-1.741E-13	-2.391E-13	-4.746E-14
33	-2.78E-15	-1.063E-14	-2.68E-14	-6.09E-14	-7.81E-14	-3.199E-14
67	2.088E-14	6.859E-14	1.664E-13	3.495E-13	5.617E-13	1.329E-13
95	3.961E-14	1.456E-13	3.041E-13	6.16E-13	1.008E-12	1.752E-13
99	5.967E-14	2.32E-13	4.326E-13	8.539E-13	1.253E-12	8.267E-13
100	2.413E-13	8.323E-13	8.026E-13	1.647E-12	1.941E-12	2.326E-12

Altitude 750 km

Median	1.011E-14	2.965E-14	7.412E-14	1.637E-13	2.724E-13	3.269E-14
1	-4.63E-15	-1.83E-14	-5.275E-14	-1.27E-13	-1.781E-13	-2.683E-14
5	-3.868E-15	-1.57E-14	-4.412E-14	-1.063E-13	-1.528E-13	-2.561E-14
33	-1.463E-15	-5.84E-15	-1.588E-14	-3.81E-14	-5.08E-14	-1.741E-14
67	1.218E-14	3.824E-14	9.57E-14	2.108E-13	3.505E-13	7.57E-14
95	2.22E-14	8.327E-14	1.816E-13	3.878E-13	6.593E-13	1.028E-13
99	3.322E-14	1.361E-13	2.646E-13	5.515E-13	8.328E-13	5.33E-13
100	1.419E-13	5.368E-13	5.163E-13	1.11E-12	1.323E-12	1.563E-12

Table C-1. Median value of global maximum densities for altitude and $F_{10.7}$ bin with differences between global maximum density and median value for several percentile ranges. Densities in kg/m^3 (page 5 of 6).

$F_{10.7B}$ Range	Bin 1 66-102	Bin 2 102-138	Bin 3 138-174	Bin 4 174-210	Bin 5 210-246	All 66-246
----------------------	-----------------	------------------	------------------	------------------	------------------	---------------

Altitude 800 km

Median	6.631E-15	1.758E-14	4.354E-14	9.912E-14	1.7E-13	1.931E-14
1	-2.69E-15	-1.025E-14	-3.061E-14	-7.752E-14	-1.142E-13	-1.514E-14
5	-2.232E-15	-8.788E-15	-2.576E-14	-6.551E-14	-9.864E-14	-1.441E-14
33	-8.29E-16	-3.3E-15	-9.44E-15	-2.401E-14	-3.38E-14	-9.775E-15
67	7.803E-15	2.248E-14	5.663E-14	1.292E-13	2.221E-13	4.449E-14
95	1.339E-14	4.905E-14	1.105E-13	2.475E-13	4.363E-13	6.268E-14
99	1.961E-14	8.168E-14	1.647E-13	3.606E-13	5.612E-13	3.477E-13
100	8.534E-14	3.503E-13	3.361E-13	7.713E-13	9.331E-13	1.084E-12

Altitude 850 km

Median	4.735E-15	1.122E-14	2.67E-14	6.153E-14	1.079E-13	1.223E-14
1	-1.747E-15	-6.052E-15	-1.821E-14	-4.795E-14	-7.371E-14	-9.087E-15
5	-1.434E-15	-5.17E-15	-1.536E-14	-4.082E-14	-6.401E-14	-8.594E-15
33	-5.19E-16	-1.941E-15	-5.69E-15	-1.529E-14	-2.228E-14	-5.737E-15
67	5.454E-15	1.41E-14	3.471E-14	8.102E-14	1.43E-13	2.727E-14
95	8.761E-15	3.004E-14	6.885E-14	1.601E-13	2.927E-13	3.99E-14
99	1.24E-14	5.04E-14	1.044E-13	2.388E-13	3.824E-13	2.297E-13
100	5.272E-14	2.316E-13	2.216E-13	5.322E-13	6.51E-13	7.466E-13

Altitude 900 km

Median	3.576E-15	7.671E-15	1.713E-14	3.916E-14	6.967E-14	8.284E-15
1	-1.243E-15	-3.81E-15	-1.115E-14	-3.006E-14	-4.788E-14	-5.837E-15
5	-1.014E-15	-3.236E-15	-9.388E-15	-2.571E-14	-4.176E-14	-5.478E-15
33	-3.59E-16	-1.196E-15	-3.5E-15	-9.75E-15	-1.47E-14	-3.565E-15
67	4.048E-15	9.423E-15	2.211E-14	5.194E-14	9.359E-14	1.748E-14
95	6.152E-15	1.92E-14	4.395E-14	1.052E-13	1.986E-13	2.65E-14
99	8.389E-15	3.206E-14	6.737E-14	1.6E-13	2.635E-13	1.535E-13
100	3.354E-14	1.548E-13	1.478E-13	3.773E-13	4.681E-13	5.294E-13

Altitude 950 km

Median	2.804E-15	5.518E-15	1.16E-14	2.578E-14	4.609E-14	5.977E-15
1	-9.44E-16	-2.505E-15	-7.122E-15	-1.927E-14	-3.152E-14	-4.028E-15
5	-7.66E-16	-2.09E-15	-5.973E-15	-1.652E-14	-2.762E-14	-3.75E-15
33	-2.67E-16	-7.17E-16	-2.228E-15	-6.35E-15	-9.88E-15	-2.352E-15
67	3.15E-15	6.711E-15	1.477E-14	3.419E-14	6.233E-14	1.182E-14
95	4.589E-15	1.292E-14	2.892E-14	7.044E-14	1.363E-13	1.834E-14
99	6.044E-15	2.114E-14	4.453E-14	1.089E-13	1.833E-13	1.043E-13
100	2.211E-14	1.053E-13	1.003E-13	2.654E-13	3.33E-13	3.731E-13

Table C-1. Median value of global maximum densities for altitude and $F_{10.7}$ bin with differences between global maximum density and median value for several percentile ranges. Densities in kg/m^3 (page 6 of 6).

$F_{10.7B}$ Range	Bin 1 66-102	Bin 2 102-138	Bin 3 138-174	Bin 4 174-210	Bin 5 210-246	All 66-246
Altitude 1000 km						
Median	2.251E-15	4.267E-15	8.26E-15	1.756E-14	3.122E-14	4.535E-15
1	-7.55E-16	-1.855E-15	-4.763E-15	-1.267E-14	-2.103E-14	-2.967E-15
5	-6.1E-16	-1.54E-15	-3.962E-15	-1.083E-14	-1.849E-14	-2.74E-15
33	-2.1E-16	-5.38E-16	-1.454E-15	-4.21E-15	-6.72E-15	-1.662E-15
67	2.517E-15	5.032E-15	1.032E-14	2.315E-14	4.233E-14	8.405E-15
95	3.577E-15	9.117E-15	1.964E-14	4.794E-14	9.48E-14	1.316E-14
99	4.58E-15	1.448E-14	3.015E-14	7.505E-14	1.29E-13	7.175E-14
100	1.512E-14	7.243E-14	6.886E-14	1.918E-13	2.435E-13	2.702E-13

Table C-2. Probabilities of achieving a time interval without encountering a thermospheric density level above a given percentile value.

C-2-1. Probability of going at least 10 days without exceeding the indicated percentile density level (Random Start)

13-month Smoothed $F_{10.7}$ Range	Percentile Level			
	66 Percent	90 Percent	95 Percent	99 Percent
66 to 102	0.13	0.46	0.63	0.86
102 to 138	0.21	0.55	0.71	0.90
138 to 174	0.28	0.55	0.68	0.89
174 to 210	0.35	0.60	0.75	0.93
210 to 246	0.38	0.65	0.76	0.87

C-2-2. Probability of going at least 30 days without exceeding the indicated percentile density level (Random Start)

13-month Smoothed $F_{10.7}$ Range	Percentile Level			
	66 Percent	90 Percent	95 Percent	99 Percent
66 to 102	0.03	0.23	0.40	0.72
102 to 138	0.05	0.28	0.48	0.76
138 to 174	0.08	0.33	0.44	0.77
174 to 210	0.12	0.37	0.52	0.82
210 to 246	0.12	0.38	0.57	0.75

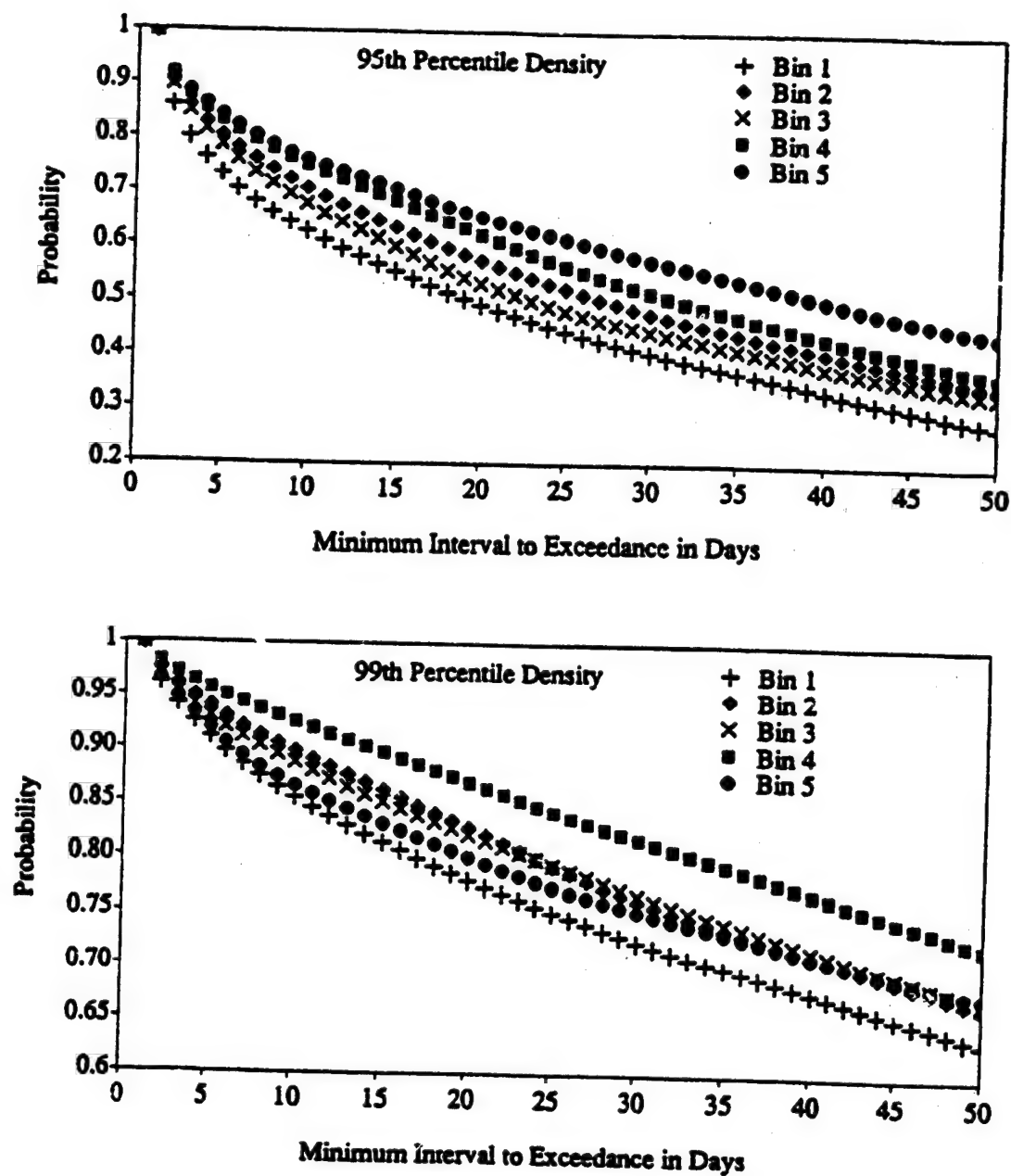


Figure C-1. Probability of meeting or exceeding a given time interval without exceeding the 95th percentile density (top) or 99th percentile density (bottom). The bins represent a range of $F_{10,7}$: (1) 66–102, (2) 102–138, (3) 138–174, (4) 174–210, and (5) 210–246.

APPENDIX D**REFERENCES**

1. Smith, R.E., and West, G.S., Compilers: "Space and Planetary Environment Criteria Guidelines for Use in Space Vehicle Development, 1982 Revision (Volume 1)." NASA TM-82478, 1983.
2. Johnson, D.L., Editor: "Terrestrial Environment (Climatic) Criteria Guidelines for Use in Aerospace Vehicle Development, 1993 Revision." NASA TM-4511, 1993.
3. Anon: "Space Shuttle Level II Program Definition and Requirements." National Space Transportation System Space Shuttle Flight and Ground System Specification, NSTS 07700, vol. X, rev. G, NASA Johnson Space Center, Houston, TX, July 13, 1988.
4. Heikkila, W.J., "Aurora." EOS, vol. 54, 1973, p. 764.
5. Roble, R.G.: "Global Dynamic Models of the Earth's Thermosphere and Ionosphere." ESA Journal, vol. 7, Netherlands, 1983, pp. 405-429.
6. Hernandez, G., McCormac, F.G., and Smith, R.W.: "Austral Thermospheric Wind Circulation and Interplanetary Magnetic Field Orientation." J. Geophys. Res., vol. 96(A4), 1991, pp. 5777-5783.
7. Hecht, J.H., Strickland, D.J., Christensen, A.B., Kayser, D.C., and Walterscheid, R.L.: "Lower Thermospheric Composition Changes Derived From Optical and Radar Data Taken at Sondre Stromfjord During the Great Magnetic Storm of February 1986." J. Geophys. Res., vol. 96(A4), 1991, pp. 5757-5776.
8. Johnson, D.L., and Smith, R.E.: "The 1985 MSFC/J70 Orbital Atmosphere Model and Data Bases for the MSFC Solar Activity Prediction Technique." NASA TM-86522, 1985.
9. Hickey, M.P.: "The NASA Marshall Engineering Thermosphere Model." NASA CR-179359, 1988.
10. Hickey, M.P.: "An Improvement in the Integration Procedure Used in the NASA Marshall Engineering Thermosphere Model." NASA CR-179389, 1988.
11. Hedin, A.E.: "MSIS-86 Thermospheric Model." J. Geophys. Res., vol. 92(A5), 1987, pp. 4649-4662.
12. Bilitza, D.: "The Worldwide Ionospheric Data Base." NSSDC/WDC-A-R&S 89-03, April 1989.
13. McNeil, W.J., Hardy, D.A., and O'Neal, R.R.: "Auroral Event Probability Based on Defense Meteorological Satellite Program (DMSP) 2 and 4 Data." Air Force Geophysics Laboratory, TM-105, 1984.
14. Robinson, R.M.: "Simultaneous Ground and Rocket-Based Measurements of Electric Fields and Currents in an Auroral Arc." Ph.D. thesis, Rice University, Houston, TX, 1980.

15. Hardy, D.A., Gussenhoven, M.S., and Holeman, E.: "A Statistical Model of Auroral Electron Precipitation." *J. Geophys. Res.*, vol. 90(A5), 1985, pp. 4229-4248.
16. Purvis, C.K., Garrett, H.B., Whittlesey, A.C., and Stevens, N.J.: "Design Guidelines for Assessing and Controlling Spacecraft Charging Effects." NASA TP-2361, 1984.
17. Pulliam, D.M., Anderson, H.R., Stammes, K., and Rees, M.H.: "Auroral Electron Acceleration and Atmospheric Interactions." *J. Geophys. Res.*, vol. 86(A4), 1981, pp. 2397-2404.
18. Gussenhoven, M.S., Hardy, D.A., Rich, F., and Burke, W.J.: "High-Level Spacecraft Charging in the Low-Altitude Polar Auroral Environment." *J. Geophys. Res.*, vol. 90(A11), 1985, pp. 11009-11023.
19. Teague, M.J., and Vette, J.I.: "A Model of the Trapped Electron Population for Solar Minimum." National Space Science Data Center, Goddard Space Flight Center, NSSDC 74-03, 1974.
20. Teague, M.J., Chan, K.W., and Vette, J.I.: "AE6: A Model Environment of the Trapped Electrons for Solar Maximum." National Space Science Data Center, Goddard Space Flight Center, NSSDC/WDC-A-R&S 76-04, 1976.
21. Stassinopoulos, E.G., and Mead, G.D.: ALLMAG, GDALMG, LINTRA: Computer Programs for Geomagnetic Field and Field-Line Calculations." National Space Science Data Center, Goddard Space Flight Center, NSSDC 72-12, 1972.
22. World Meteorological Organization, Compiler: "Atmospheric Ozone 1985, Assessment of Our Understanding of the Processes Controlling Its Present Distribution and Change." World Meteorological Organization Report, No. 16, vol. 1, Ch. 7, 1985.
23. Anon.: "Reference Data for Radio Engineers." *Intl. Telephone and Telegraph*, vol. 34, 1981, pp. 1-13.
24. Anon.: "Solar-Terrestrial Research for the 1980's." Committee on Solar-Terrestrial Research, National Research Council, 1981, pp. 164.
25. Kelley, M.C.: "Electrical Measurements in the Atmosphere and the Ionosphere Over an Active Thunderstorm: 1, Campaign Overview and Initial Results." *J. Geophys. Res.*, vol. 90(A12), 1985, pp. 9815-9823.
26. Grun, E., Zook, H.A., Fectig, H., and Giese, R.H.: "Collisional Balance of the Meteoritic Complex." *Icarus*, vol. 62, 1985, pp. 244-272.
27. Kessler, D.J., Reynolds, R.C., and Anz-Meador, P.: "Orbital Debris Environment for Spacecraft Designed to Operate in Low-Earth Orbit." NASA TM-100471, Johnson Space Center, Houston, TX, April 1989.
28. Zook, H.A.: "Flux Versus Direction of Impacts on LDEF by Meteoroids and Orbital Debris." *Proc. 21st Lunar and Planetary Science Conference*, 1990, pp. 1385-1386.

29. Barraclough, D.R.: "International Geomagnetic Reference Field: The Fourth Generation." *Physics of the Earth and Planetary Interiors*, vol. 48, 1987, pp. 279-292.
 30. Green, R.N., and Smith, G.L.: "Shortwave Shape Factor Inversion of Earth Radiation Budget Observations." *J. Atmospheric Sciences*, vol. 48, No. 3, 1991, pp. 390-402.
 31. Marsh, J.G., Lerch, F.J., Putney, B.H., Christodoulidis, D.C., Smith, D.E., Pelsentreger, T.L., and Sanchez, B.V.: "A New Gravitational Model for the Earth From Satellite Tracking Data: GEM-T1." *J. Geophys. Res.*, vol. 93(B6), 1988, pp. 6169-6215.
 32. Zendell, A., Brown, R.D., and Vincent, S.: "Gravity Fields of the Solar System." NASA SP-8117, 1975.
 33. Adams, J.H., Jr., Silberberg, R., and Tsao, C.H.: "Cosmic Ray Effects on Microelectronics, Part I: The Near-Earth Particle Environment." NRL Memorandum Report 4506, August 25, 1981.
 34. Adams, J.H., Jr.: "Cosmic Ray Effects on Microelectronics, Part IV." NRL Memorandum Report 5901, 1986.
 35. Adams, J.H., Jr., Letaw, J.R., and Smart, D.F.: "Cosmic Ray Effects on Microelectronics, Part II: The Geomagnetic Cutoff Effects." NRL Memorandum Report 5099, May 26, 1983.
 36. Cameron, A.G.W.: "Elementary and Nuclidic Abundances in the Solar System." Harvard-Smithsonian Center for Astrophysics, Preprint Series No. 1357, 1980.
- A. Anon: "U.S. Standard Atmosphere, 1976," NOAA-S/T 76-1562, National Oceanic and Atmospheric Administration, National Aeronautics and Space Administration, U.S. Air Force, Washington, DC, October 1976.
 - B. Ba'immer, P., and Gross, A.: "Worldwide Spacecraft EME Definition." Supplement 1, ECAC-CR-85-065, Department of Defense, Electromagnetic Compatibility Analysis Center, Annapolis, MD, November 1988.
 - C. Bilitza, D.: "International Reference Ionosphere 1990," NSSDC/WDC-A-R&S 90-22, November 1990.
 - D. Hickey, M.P., and Smith, R.E.: "Ninety-Day Solar and Geomagnetic Activity Input Files for Thermospheric Variation Simulation: Simulation Data Files/Research 2," NASA Contractor Report PHY-92R031, Contract NAS8-38333.
 - E. Holland, R.L., and Vaughan, W.W.: "Lagrangian Least-Squares Prediction of Solar Flux ($F_{10.7}$)." *Journal of Geophysical Research*, vol. 89, No. A1, January 1, 1984, pp. 11-16.
 - F. Jursa, A.S., Sci. Ed.: "Handbook of Geophysics and the Space Environment." Air Force Geophysics Laboratory, Air Force Systems Command, 1985.
 - G. Justus, C.G., Alyea, F.N., Cunnold, D.M., Jeffries, W.R. III, and Johnson, D.L.: "The NASA/MSFC Global Reference Atmosphere Model—1990 Version (GRAM-90), Part I: Technical/User's Manual," NASA TM-4268, Part I, April 1991.

- H. Justus, C.G., Alyea, F.N., Cunnold, D.M., Jeffries, W.R. III, and Johnson, D.L.: "The NASA/MSFC Global Reference Atmosphere Model—1990 Version (GRAM-90), Part II: Program/Data Listings," NASA TM-4268, Part II, June 1991.
- I. Klaips, D.G., Dean, G., and Mullen, R.L.: "Worldwide Spacecraft EME Definition." ECAC-CR-85-065, Department of Defense, Electromagnetic Compatibility Analysis Center, Annapolis, MD, July 1985.
- J. Langel, L.A., Mundt, W., Barraclough, D.R., Barton, C.E., Golovkov, V.P., Hood, P.J., Lowes, F.J., Peddie, N.W., Qi, G.-Z., and Quinn, J.M.: "International Geomagnetic Reference Field, 1991 Revision." Journal of Geomagnetism and Geoelectricity, vol. 43, No. 12, 1991, pp. 1007-1012.

APPENDIX E

BIBLIOGRAPHY

- Comstock, G.M.: "Propagation and Source Characteristics Derived From the Low-Energy, Multiply Charged, Cosmic Ray Nuclei." *Astrophys. J.*, vol. 155, 1969, pp. 619-643.
- Cour-Palais, B.G., Whipple, F.L., D'Airolto, C.T., Dalton, C.C., Dohnanyi, J.S., Dubin, M., Frost, V.C., Kinard, W.H., Loeffler, I.J., Naumann, R.J., Nysmith, C.R., and Savin, R.C.: "Meteoroid Environment Model—1969 (Near Earth to Lunar Surface)." NASA SP-8013, Washington, DC, 1969.
- Crowley, G.: "Dynamics of the Earth's Thermosphere: A Review." U.S. National Report to International Union of Geodesy and Geophysics 1987-1990, Review of Geophysics, Supplement, April 1991, pp. 1143-1165.
- Fan, C.Y., Gloeckler, G., and Simpson, J.A.: "Galactic Deuterium and Its Energy Above 20 MeV per Nucleon (Measured by IMP-III Satellite Near Minimum Solar Activity)." *Phys. Rev. Letters*, vol. 17, 1966, pp. 329-333.
- Freier, P.S., and Waddington, C.J.: "Very Heavy Nuclei in the Primary Cosmic Radiation I, Observation on the Energy Spectrum." *Phys. Rev.*, vol. 175, 1968, pp. 1641-1648.
- Freier, P.S., Young, J., Waddington, C.J., Fickle, R., Gilman, C., and Scarlett, W.R.: "Charge Distribution of Heavy Cosmic Ray Nuclei." 16th International Cosmic Ray Conference, Kyoto, Japan, vol. 1, 1979, pp. 316-321.
- Garcia-Munoz, M., Mason, G.M., and Simpson, J.A.: "The Anomalous ISUP 4/HE Component in the Cosmic Ray Spectrum at 50 MeV per Nucleon During 1972-1974." *Astrophys. J.*, vol. 202, 1975, pp. 265-275.
- Guliusson, E.: "Charge Composition and Energy Spectrum of Cosmic-Ray Nuclei at Energies Above 20 GeV per Nucleon." *Astrophys. J.*, vol. 191, 1974, pp. 331-348.
- Guliusson, E., Engelmann, J.J., Jorrand, J., Koch-Miramond, L., Masse, P., Petrou, N., Lund, N., Rasmussen, I.L., and Rotenberg, M.: "The Galactic Cosmic Ray Energy Spectra as Measured by the French-Danish Instrument on HEAO-3." 18th International Cosmic Ray Conference, vol. 2, 1983, pp. 21-24.
- Leech, H.W., and O'Gallagher, J.J.: "The Isotopic Composition of Cosmic-Ray Helium From 123 to 279 MeV per Nucleon: A New Measurement and Analysis." *Astrophys. J.*, vol. 221, 1978, pp. 1110-1123.
- Lezniak, J.A., and Webber, W.R.: "Nuclei From 3000 MeV per Nucleon to 50 GeV per Nucleon." *Astrophys. J.*, vol. 223, 1978, pp. 676-696.
- Lincoln, J.V., and Conkright, R.O. (Eds.): "International Reference Ionosphere—IRI 79." Rept. UAG-82, World Data Center A for Solar-Terrestrial Physics, NOAA, Boulder, CO, 1981.

- McDonald, F.B., Van Hollebeke, M.A.I., Trainor, J.H., Lal, N., and Webber, W.R.: "Galactic Cosmic Ray Observation in the Distant Heliosphere." 16th International Cosmic Ray Conference, Japan, vol. 12, 1979, pp. 330-334.
- Meng, C.-L., and Mauk, B.H.: "Global Auroral Morphology: Quadrennial Report to the I.U.G.G. on U.S. Contributions." U.S. National Report to International Union of Geodesy and Geophysics 1987-1990, Reviews of Geophys., Supplement, April 1991, pp. 1028-1038.
- Ormes, J.F., and Webber, W.R.: "Measurements of the Primary Proton and Helium Spectra and Their Modulations Using a Balloon-Borne Cherenkov-Scintillation Counter." Proc. 9th International Conference on Cosmic Rays, London, 1965, p. 349.
- Orth, C.D., Buffington, A., Smoot, G.F., and Mast, T.S.: "Abundance and Spectra for Cosmic-Ray Nuclei From Lithium to Iron for 2 to 150 GeV per Nucleon." *Astrophys. J.*, vol. 226, 1978, pp. 1147-1161.
- Price, W.E., Pickel, J.C., Ellis, T., and Frazee, F.G.: "Cosmic Ray Induced Errors in I2L Microprocessors and Logic Devices." *IEEE Trans. on Nucl. Sci.*, NS-38, 1981, pp. 3946-3954.
- Reames, D.V., and Fichtel, C.E.: "Low-Energy Cosmic-Ray Composition and Energy Spectra Measured in June 1965 (Low Energy Cosmic Ray Composition and Energy Spectra Measured by Sounding Rockets Carrying Nuclear Emulsions)." *Phys. Rev.*, vol. 162, 1967, pp. 1291-1295.
- Ryan, M.R., Ormes, J.F., and Balasubrahmanyam, V.K.: "Cosmic-Ray Proton and Helium Spectra Above 50 GeV." *Phys. Rev. Letters*, vol. 28, 1972, pp. 985-988.
- Sawyer, D.M., and Vette, J.I.: "AP-8 Trapped Proton Environment for Solar Maximum and Solar Minimum." National Space Science Data Center, Goddard Space Flight Center, NSSDC/WDC-A-R&S 76-06, 1976.
- Scarlett, W.R., Freier, P.S., and Waddington, C.J.: "The Charge Energy Spectra of Heavy Cosmic-Ray Nuclei." *Astrophys. and Space Sci.*, Netherlands, vol. 59, 1978, pp. 301-311.
- Simon, M., Spiegelhauer, H., Schmidt, W.K.H., Siohan, F., Ormes, J.F., Balasubrahmanyam, V.K., and Arens, J.F.: "Cosmic Ray Spectra of Boron to Iron Nuclei to Above 100 GeV per Nucleon." 16th International Cosmic Ray Conference, vol. 1, 1979, pp. 352-357.
- Smith, L.H., Buffington, A., Smoot, G.F., Alvarez, L.W., and Wahlig, W.A.: "A Measurement of Cosmic-Ray Rigidity Spectra Above 6 GV/C of Elements From Hydrogen to Iron." *Astrophys. J.*, vol. 180, 1973, pp. 987-1010.
- Sojka, J.J.: "Ionospheric Physics, U.S. National Report to International Union of Geodesy and Geophysics 1987-1990." *Reviews of Geophysics*, Supplement, April 1991, pp. 1166-1186.
- Von Rosenvinge, T.T., Webber, W.R., and Ormes, J.F.: "A Comparison of the Energy Spectra of Cosmic Ray Helium and Heavy Nuclei." *Astrophys. Space Sci.*, vol. 5, 1969, pp. 342-359.

Webber, W.R., and Lezniak, J.A.: "Interplanetary Radial Gradients of Galactic Cosmic-Ray Protons and Helium Nuclei: Pioneer 8 and 9 Measurements From 0.75 to 1.10 AU." J. Geophys. Res., vol. 78, 1973, pp. 1979-2000.

Webber, W.R., and Ormes, J.F.: "Cerenkov-Scintillation Counter Measurements of Nuclei Heavier Than Helium in the Primary Cosmic Radiation I. Energy Spectra and Charge Composition of Nuclei Heavier Than Helium in Primary Cosmic Radiation From Cerenkov-Scintillation Counter Measurements." J. Geophys. Res., vol. 72, 1967, pp. 5957-5976.

Webber, W.R., Lezniak, J.A., and Kish, J.: "Differences in the Spectra of Cosmic Ray Nuclear Species Below Approximately 5 GeV/nuc." Proc. 13th Intl. Cosmic Ray Conf., vol. 1, 1973, pp. 248-253.

Webber, W.R., Stone, E.C., and Vogt, R.E.: "The Elemental Composition of Quiet Time Low Energy Cosmic Rays Measured on the Voyager Spacecraft." 16th Intl. Cosmic Ray Conf., vol. 5, 1979, pp. 357-362.

Zook, H.A.: "The State of Meteoritic Material on the Moon." Proc. 6th Lunar Science Conference, 1975, pp. 1653-1672.

REPORT DOCUMENTATION PAGE

Form Approved
OMB No. 0704-0188

Public reporting burden for this collection of information is estimated to average 1 hour per response, including the time for reviewing instructions, searching existing data sources, gathering and maintaining the data needed, and completing and reviewing the collection of information. Send comments regarding this burden estimate or any other aspect of this collection of information, including suggestions for reducing this burden, to Washington Headquarters Services, Directorate for Information Operations and Reports, 1215 Jefferson Davis Highway, Suite 1204, Arlington, VA 22202-4302, and to the Office of Management and Budget, Paperwork Reduction Project (0704-0188), Washington, DC 20503.

1. AGENCY USE ONLY (Leave blank)		2. REPORT DATE June 1994		3. REPORT TYPE AND DATES COVERED Technical Memorandum	
4. TITLE AND SUBTITLE Natural Orbital Environment Definition Guidelines for Use in Aerospace Vehicle Development				5. FUNDING NUMBERS	
6. AUTHOR(S) B. Jeffrey Anderson, Editor Robert E. Smith,* Compiler					
7. PERFORMING ORGANIZATION NAME(S) AND ADDRESS(ES) George C. Marshall Space Flight Center Marshall Space Flight Center, Alabama 35812				8. PERFORMING ORGANIZATION REPORT NUMBER M-729	
9. SPONSORING/MONITORING AGENCY NAME(S) AND ADDRESS(ES) National Aeronautics and Space Administration Washington, DC 20546				10. SPONSORING/MONITORING AGENCY REPORT NUMBER NASA TM - 4527	
11. SUPPLEMENTARY NOTES Prepared by Systems Analysis and Integration Laboratory, Science and Engineering Directorate *Physitron, Inc., Huntsville, Alabama					
12a. DISTRIBUTION/AVAILABILITY STATEMENT Unclassified—Unlimited Subject Category: 46				12b. DISTRIBUTION CODE	
13. ABSTRACT (Maximum 200 words) This document provides definitions of the natural near-Earth space environment suitable for use in the initial development/design phase of any space vehicle. The natural environment includes the neutral atmosphere, plasma, charged particle radiation, electromagnetic radiation (EMR), meteoroids, orbital debris, magnetic field, physical and thermal constants, and gravitational field. Communications and other unmanned satellites operate in geosynchronous-Earth orbit (GEO); therefore, some data are given for GEO, but emphasis is on altitudes from 200 km to 1000 km (low-Earth orbit (LEO)). This document does not cover the induced environment or other effects resulting from presence of the space vehicle. Manmade factors are included as part of the ambient natural environment; i.e., orbital debris and radio frequency (RF) noise generated on Earth, because they are not caused by the presence of the space vehicle but form part of the ambient environment that the space vehicle experiences.					
14. SUBJECT TERMS orbital environment, space environment, thermosphere, low-Earth orbit, satellite design, ionosphere, geophysics				15. NUMBER OF PAGES 165	
				16. PRICE CODE A08	
17. SECURITY CLASSIFICATION OF REPORT Unclassified	18. SECURITY CLASSIFICATION OF THIS PAGE Unclassified	19. SECURITY CLASSIFICATION OF ABSTRACT Unclassified	20. LIMITATION OF ABSTRACT Unlimited		